

University of Louisville

ThinkIR: The University of Louisville's Institutional Repository

Electronic Theses and Dissertations

8-2015

Optimization of support structures for selective laser melting.

Kai Zeng

University of Louisville

Follow this and additional works at: <https://ir.library.louisville.edu/etd>



Part of the [Industrial Engineering Commons](#)

Recommended Citation

Zeng, Kai, "Optimization of support structures for selective laser melting." (2015). *Electronic Theses and Dissertations*. Paper 2221.

<https://doi.org/10.18297/etd/2221>

This Doctoral Dissertation is brought to you for free and open access by ThinkIR: The University of Louisville's Institutional Repository. It has been accepted for inclusion in Electronic Theses and Dissertations by an authorized administrator of ThinkIR: The University of Louisville's Institutional Repository. This title appears here courtesy of the author, who has retained all other copyrights. For more information, please contact thinkir@louisville.edu.

OPTIMIZATION OF SUPPORT STRUCTURES FOR SELECTIVE LASER MELTING

By

Kai Zeng

A Dissertation
Submitted to the Faculty of the
J. B. Speed School of Engineering of the University of Louisville
in Partial Fulfillment of the Requirements
for the Degree of

Doctor of Philosophy in Industrial Engineering

Department of Industrial Engineering

University of Louisville

Louisville, Kentucky

August 2015

Copyright 2015 by Kai Zeng

All rights reserved

OPTIMIZATION OF SUPPORT STRUCTURES FOR SELECTIVE LASER MELTING

By

Kai Zeng

A Dissertation Approved on

July 20, 2015

by the following Dissertation Committee:

Dissertation Director: Dr. Brent E. Stucker

Dr. Tim Hardin

Dr. Kevin Murphy

Dr. Deepankar Pal

Dr. Li Yang

DEDICATION

*This dissertation is dedicated to my parents and sister
for their endless love, support and encouragement.*

ACKNOWLEDGMENTS

I wish to express my deepest gratitude to my advisor, Dr. Brent Stucker, for his generous guidance and support during my research at the University of Louisville and internship at 3DSIM. I would like to thank other committee members, Dr. Tim Hardin, Dr. Kevin Murphy, Dr. Deepankar Pal and Dr. Li Yang for sharing their expertise and offering constructive advice and continuous encouragements that were necessary to complete my work.

I place on record, my sincere thanks to the staff of the Industrial Engineering Department for their support and the staff of the Rapid Prototyping Center at the University of Louisville for providing me with all the necessary facilities for my research.

I am grateful to all the fellows in my research group for their generous help and support. Special thanks go to Dr. Deepankar Pal who provided his valuable insights into my work and Dr. Haijun Gong who offered me sincere help for my experiment. Many thanks to Nachiket Patil, Dr. Xiaodong Xing and Shanshan Zhang for their warm assistance.

I am thankful to my colleagues Tim Sublette, Chong Teng and Sally Xu at 3DSIM, for letting me experience my research beyond the textbooks.

I would also like to thank the Air Force Research Laboratory for funding this research.

Last but not the least, I would like to take this opportunity to acknowledge my parents and sister, who always supported me with their best wishes and stood by me through thick and thin.

ABSTRACT

OPTIMIZATION OF SUPPORT STRUCTURES FOR SELECTIVE LASER MELTING

Kai Zeng

July 20, 2015

Additive Manufacturing (AM) users rely on experiments and experience to predict the performance of AM processes. This trial and error approach for qualifying AM parts takes significant time and money. Simulation tools are an urgent need for today's AM industry. One area of need is the automatic generation of optimized support structures based upon the scan patterns used to produce those structures. This research seeks to develop support structure generation tools based on real scan pattern and thermo-mechanical simulation tools for Selective Laser Melting (SLM) developed at the University of Louisville and being commercialized by 3DSIM, LLC.

In order to benchmark the 3DSIM thermo-mechanical simulation tool, a thermal finite element model has been developed in ANSYS which uses the similar multi-scale meshing strategies as 3DSIM. The use of the sub-modeling approach for dynamic meshing was verified by comparing it against a uniform fine mesh model. The results of the two models match within an acceptable tolerance. Also, a mesh sensitivity analysis was carried out in order to show solution convergence as a function of increasing mesh density. The results of this analysis were also validated using experiments to show a match between experimental and simulated melt pools. Finally, the ANSYS solution was

compared with 3DSIM results. The result of 3DSIM for a simple represented model is validated compared against the ANSYS model. What is more, it was significantly faster than their ANSYS counterparts for solving problems using a dynamic mesh.

A scan pattern generation tool has been implemented to enable the input of real scan patterns as it is used in fabrication. The scan pattern is arbitrarily varied using user-defined parameters including hatching space, orientation angle, scanning start point, etc. Several types of scan patterns such as traditional S and chessboard are included in the tool.

A simplified representation of the thermomechanical properties of support structures in order to accelerate the simulation of supports has been formulated. The effective thermal properties of support structures are represented using thermal homogenization. The effective thermal properties of the support structures have been found to be a function of their geometry, anisotropy and constituent independent thermal properties. The results from this study have been compared against standard models and a good match has been found.

A novel framework for a support structure generation and optimization tool has been developed to overcome the difficulty of dealing with support structures in SLM. Supports are optimized and designed based on the thermal stress accumulated in parts as they are made as well as geometrical rules. The support structure is designed to be withstand the thermal stress at locations where it could cause damage to the part and support structure, while minimizing the overall need for support structure materials. The support structure is designed with non-uniform parameters so as to make it flexible to

alter based upon thermal stress. Experiments were conducted to explore the threshold for block support structure parameters and results were applied to adjust and verify the tool.

TABLE OF CONTENTS

	PAGE
ACKNOWLEDGEMENTS	iv
ABSTRACT	vi
LIST OF TABLES	viii
LIST OF FIGURES	xvii
CHAPTER 1 RESEARCH MOTIVATION AND PROBLEM STATEMENT	1
1.1 Introduction and Motivation	1
1.2 Problem Statement	4
CHAPTER 2 LITERATURE REVIEW	6
2.1 Additive Manufacturing	6
2.2 Selective Laser Melting (SLM) process	8
2.2.1 SLM Process Mechanism	8
2.2.2 SLM Process Parameters	8
2.2.3 SLM Part Defects	9
2.2.4 SLM Post-processing	10
2.3 Thermo-mechanical Simulation Study in SLM	10
2.3.1 SLM Thermal Phenomenon	10
2.3.2 Governing Equations and Boundary Conditions	11
2.3.3 Laser Beam Approximation Modeling	12
2.3.4 SLM Thermal Modeling Techniques	14

2.3.4.1 Analytical Solution	15
2.3.4.2 Numerical Models	16
2.4 Scan Strategies in SLM	21
2.4.1 Scan Strategies in SLM processing	21
2.4.2 Scan Strategies in Modeling	26
2.4.3 Hatching Algorithm	28
2.5 Support Strategies in SLM	29
2.5.1 Support Structures in AM processing	29
2.5.2 Importance of Support in SLM processing	30
2.5.3 Cost Estimation for Support Structures	32
2.5.4 Support Strategies for SLM	34
2.5.4.1 Support Structure Generation Software	34
2.5.4.2 Types of Support Structure	35
2.5.4.3 Metrics of Optimum Support Structure	37
2.5.5 Support Structure Optimization Design	38
2.5.5.1 Support Structure Orientation	38
2.5.5.2 Support Structure Weight/Volume Minimization	39
2.5.6 Support Structure in Thermal Modeling	40
2.6 Structural Optimization Design	41
2.6.1 Structural Optimization Design Method	41
2.6.2 Structural Optimization Design in Additive Manufacturing	45
2.7 Conclusions	45
CHAPTER 3 RESEARCH OBJECTIVE AND DISSERTATION FORMAT	48

3.1 Research Objective	48
3.2 Dissertation Format	50
CHAPTER 4 SCAN PATTERN GENERATION	52
4.1 Introduction	52
4.2 STL File	54
4.2.1 STL Format	54
4.2.2 STL File Slicing	54
4.3 Sliced File	56
4.3.1 CLI File	56
4.3.2 CLI and SLI Comparison	57
4.3.3 Template Matching Method	58
4.3.4 Example	59
4.4 Scan Pattern	60
4.4.1 Introduction	60
4.4.2 Reverse Engineering of the Scan Pattern	62
4.4.2.1 Line Detection: Hough Transform	62
4.4.2.2 Rotation Angle Estimation	65
4.4.3 Other Scan Pattern Examples and Application	66
4.5 Conclusion	67
CHAPTER 5 COMPARISON OF 3DSIM THERMAL MODELING OF SELECTIVE LASER MELTING USING A NEW DYNAMIC MESHING METHOD TO ANSY.	68
5.1 Introduction	68
5.2 Modeling	70

5.2.1 Thermal Phenomena in SLM	70
5.2.2 Governing Equation and Boundary Conditions (BCs)	71
5.2.3 Material Properties	71
5.2.4 Laser Beam Approximation	72
5.2.5 Sensitivity Analysis of the Number of Elements in the HAZ	72
5.2.6 Dynamic Meshing Method and ANSYS Techniques	73
5.3 Results and Discussions	75
5.3.1 Single Time-Step Temperature Distribution Calculation	75
5.3.2 Interpolation Results	77
5.3.3 Dynamic and Uniform Meshing Model Results	81
5.4 Multi Time-Step Temperature Distribution Calculation	82
5.5 Experimental Validation	87
5.6 Computational Expense Analysis	89
5.6.1 Computational Time between Dynamic and Uniformly Meshed Model.	89
5.6.2 Computational Cost Comparison between an ANSYS Dynamic Mesh Model and FFDAMRD	91
5.6.2.1 Convergence Study	91
5.6.2.2 Computational Time Study	91
5.6.2.3 Results and Discussion	93
5.7 Conclusions and Future Work	98
CHAPTER 6 EVALUATION OF EFFECTIVE THERMAL CONDUCTIVITY APPROACHES FOR SUPPORT STRUCTURES	99
6.1 Introduction	99

6.2 Background	99
6.3 Description of the Problem	102
6.4 Numerical Method	105
6.4.1 Linear Temperature-Independent Material Property Case Study Results.	106
6.4.2 Nonlinear Temperature-Dependent Material Property Case Study Results	109
6.5 Validation of the Results of Effective Thermal Properties	114
6.6 Conclusion and Future Work	115
CHAPTER 7 SUPPORT STRUCTURE DESIGN AND OPTIMIZATION FRAMEWORK	117
7.1 Introduction	117
7.2 The Support Structure Optimization and Design Framework	119
7.2.1 Supporting Area Detection	121
7.2.2 Support Structure Default Parameters Determination	122
7.2.3 Support Structure Volume Calculation	123
7.2.4 Non-uniform Localized Support Design	125
7.2.5 Linear Programming (LP) Method	126
7.2.6 Minimal Cross-Section Area	128
7.2.7 Thermal Stress Mapping to Support Structure	129
7.2.8 t/l Ratio Calculation Based On Thermal Stress	129
7.2.8.1 Simple Structure Surface (SSS) Method	129
7.2.8.2 Analytical Solutions for Calculation of t/l	131
7.2.9 t/l Interpolation	134

7.2.10 Post-processing	134
7.2.11 STL Output	135
7.2.12 Example	135
7.3 FEM Based Support Structure Optimization	138
7.3.1 FEM Formulation	138
7.3.1.1 1D Formulation	139
7.3.1.2 2D Formulation	139
7.3.1.3 3D Formulation	139
7.3.1.4 B-Bar Method	140
7.3.2 Sensitivity Analysis	142
7.3.3 Support Structure Optimization Example Based On FEM Results	145
7.4 Conclusion	152
CHAPTER 8 SUPPORT STRUCTURE EXPERIMENTS WITH TI64	154
8.1 Introduction	154
8.2 Design of Experiment and Observation of Results	154
8.2.1 Experiment 1: Investigation the Support Structure for a 40x5x2mm Part	154
8.2.1.1 Experimental Design	154
8.2.1.2 Result Observation for Experiment 1	156
8.2.2 Experiments 2&3: Uniform Hatch Spacing Support Structure Design for the 40x5x2mm Part	158
8.2.2.1 Experimental Design	158
8.2.2.2 Experimental Results	160
8.2.3 Experiment 4: Refinement of Experiments 2&3	161

8.2.4	Experiment 5: Non-uniform Supports Design for a 40x5x2mm Part . . .	162
8.2.5	Experiment 6: Non-uniform Wall Thickness Support Structure for 40x5x2mm Part	164
8.2.5.1	EOS Default Support Structure Wall Thickness	164
8.2.5.2	Experimental Design and Result	165
8.2.6	Experiment 7: Support Structure Investigation for a 20x20x2mm part	166
8.2.6.1	Experimental Design	166
8.2.6.2	Experimental Result	167
8.3	Conclusion	169
CHAPTER 9 CONCLUSION AND FUTURE WORK		171
9.1	Conclusion	171
9.1.1	Scan Pattern Generation Tool	171
9.1.2	A Dynamic Moving Mesh Model in ANSYS and 3DSIM against ANSYS Benchmark	172
9.1.3	Support Structure Optimization and Design Framework	173
9.1.4	Experiment to Investigate the Block Support Structure for Ti64	173
9.2	Future Work	174
REFERENCES		176
APPENDICES		192
CURRICULUM VITA		199

LIST OF TABLES

TABLE	PAGE
1. 3DSIM Processing Time for the model with 3 elements in the Z direction	97
2. Configurations for design of experiment	156
3. Support spacing in the length and width direction	159
4. Hatch spacing in the width and length direction	162
5. Parameters for experiment design	163
6. Support structure wall thickness measurement data (unit: mm)	165
7. Parameters for experimental design	165
8. Support spacing	167

LIST OF FIGURES

FIGURE	PAGE
1. The eight stages of the AM process [3].	2
2. (a) Support structure for different building orientations and (b) Cross-section of one part with a block support structure.	2
3. Scan pattern from EOS M270	3
4. Classification of additive manufacturing processes defined by the additive manufacturing special interest group (AM SIG)-adapted from ASTM classifications [6].	7
5. SLM process diagram [7]	9
6. Schematic representation of heat transfer [14]	11
7. 2D illustration of the RC model: simulation over a depth of 1mm and width of 1mm of powder bed [19]	14
8. Six different scan strategies tested [47]	22
9. Five different scan strategies tested [49]	23
10. Four different scan strategies tested [50].	24
11. Four different scan strategies tested [53].	26
12. Cracking and delamination in SLM [59]	30
13. Distortion and delamination in SLM processing [60].	30
14. Curling in SLM [11]	31
15. Overhang failure in SLM.	32

16. Cost splitting for each geometry according to the cost model [67].	33
17. Different types of Magics' generated support structures [60]	35
18. Grid support structure [71].	36
19. Gyroid and Diamond lattice support structures [70].	37
20. Typical optimization design flow chart.	43
21. Steps of operation for a typical metal laser sintering machine	53
22. Thick hemispherical dome structure	55
23. STL model of hemisphere	55
24. Intersection of triangles and plane [96]	56
25. Distance of point to plane [96]	56
26. Points in the cross section of 200th layer from CLI file	59
27. Correlation between two cross-sections corresponding to CLI and SLI	59
28. Exposure strategy and process parameters [98]	61
29. Real scan pattern from AM machine	62
30. Line representation in Cartesian (left) and Polar (right) coordinates.	63
31. Point in Cartesian (left) and Polar (right) coordinates	64
32. Scan pattern extracted from picture	64
33. Angle difference between two consecutive layers.	65
34. Angle difference every 27 layers.	66
35. Scan pattern for a crescent structure and chessboard scan pattern	66
36. Influence of number of divisions to the maximal heat flux for a Gaussian heat source	73
37. Flow chart for establishing the dynamic model.	74

38. Geometry of physical model	76
39. Temperature contour plot of the first time step of the dynamic model.	78
40. Temperature results before and after interpolation	79
41. Dynamic and uniform mesh model temperature distribution comparison	80
42. Influence of mesh density on the peak temperature	81
43. Scan pattern.	82
44. Temperature contour plots of melt pools in different locations	83
45. Melt pool for locations A,B,C of Figure 44 shown respectively in (a),(b) and (c) .	85
46. Melt pool temperature contour distribution	86
47. Temperature distribution through the melt pool	87
48. Tracks of laser beam on the surface	88
49. Melt pool curvature and width	89
50. Computational comparison of dynamic and uniform meshing model	90
51. Convergence study for peak temperature comparing 3DSIM and ANSYS results . .	92
52. Problem definition showing the part, mesh and scan strategy employed in the simulation	93
53. ANSYS sub-model run time on an ordinary desktop computer	95
54. Different computational configurations comparison	96
55. ANSYS model running time for multiple GPU processors	97
56. Support structure built using an EOS M270 machine	103
57. 3D model with support structure and RVE of support structure	103
58. View of the XY plane of an example mesh	104

59. Representative Volume Element for the support structure with defined boundary conditions	105
60. Temperature distribution along the z direction.	107
61. $K_{\text{effective}}/K_{\text{solidified}}$ vs the fraction of solidified material.	109
62. Effective conductivity vs temperature for temperature-dependent Ti64 properties at various temperature gradients	110
63. Effective conductivity ratio vs temperature for temperature dependent Ti64 properties at different temperature gradients	111
64. Effective thermal conductivity vs Temperature for temperature-dependent Ti64 properties at different support structure space distances	112
65. Effective thermal conductivity vs Volume fraction for temperature-dependent Ti64 properties	113
66. Temperature distribution of the RVE for linear material property.	114
67. Temperature distribution of the RVE for nonlinear thermal conductivity	115
68. Support structure optimization and design flowchart for incorporation with 3DSIM	118
69. support structure optimization and design framework	120
70. STL file representation of the part in 2D	122
71. Square honeycomb structure [127]	123
72. Flow chart for finding the support wall and triangle intersection line	124
73. Line and triangle intersections	125

74. Non-uniform support structure where blue represents the part boundary, green/red represent thermal stress contour plot lines and yellow represents the support structure walls.	126
75. Static equivalency for a distributed force on a surface [129]	129
76. Load distribution for each wall [131].	130
77. Spreading of the twin cantilever depending on bar thickness (h) and measurement point (n) [134]	136
78. Assumed quadratic thermal stress	136
79. Optimized wall thickness in the X direction	137
80. Optimized wall thickness in the Y direction	137
81. Flow chart of FEM analysis for support structure optimization.	138
82. 1D representation of the structure	139
83. 2D representation of the structure	139
84. 3D representation of the structure	140
85. Sensitivity analysis of 1D FEM result	143
86. Sensitivity analysis of 2D FEM result.	144
87. Sensitivity analysis of 3D FEM result	144
88. The uniform distributed force cantilever beam.	145
89. 1st step for a 1D support structure (Unit: mm).	146
90. 2nd step for a 1D support structure (Unit: mm)	147
91. 3rd step for a 1D support structure (Unit: mm)	148
92. 4th step for a 1D support structure (Unit: mm).	148
93. 1st step for support structure design in 2D (Unit: mm)	149

94. 2nd step for support structure design in 2D (Unit: mm)	149
95. 3rd step for support structure design in 2D (Unit: mm)	150
96. 4th step for support structure design in 2D (Unit: mm)	150
97. Beam deformation in 3D (Unit: mm)	151
98. 1st step for support structure design in 3D (Unit: mm)	151
99. 2nd step for support structure design in 3D (Unit: mm).	152
100. 3rd step for support structure design in 3D (Unit: mm)	152
101. 4th step for support structure design in 3D (Unit: mm)	153
102. Experiment 1 layout.	155
103. Defects observed for different support structures	157
104. Surface defects during scanning of parts with large hatch spacing	158
105. Uniform support structure design layout	159
106. Support structure cracking at the bottom	160
107. Uniform support structure design layout	162
108. Non-uniform support structure layout	164
109. Customized support structure design layout	166
110. Uniform hatch space support structure cracking at the bottom	167
111. Non-uniform support structures	168

CHAPTER 1 RESEARCH MOTIVATION AND PROBLEM STATEMENT

1.1 Introduction and Research Motivation

Additive Manufacturing (AM) was first developed in the 1980's to enable rapid prototyping of objects using a layer by layer fabrication technique [1]. AM has transformed from its early days in rapid prototyping to find application in industries ranging from aerospace to orthodontic [2].

Figure 1 [3] shows the typical eight steps for fabricating a part from a CAD model using AM. AM technologies are able to directly transform a digital CAD file to a real product, so creating a CAD file to represent the physical part is the first step in the production design and development process. In the second step, the CAD file is approximated using triangles in the STL file format before commencing the layer by layer fabrication process. The STL file is thereafter sliced into multiple layers at a prescribed thickness. Part slicing is processed in the system software of the AM machine; or third party software such as Magics from Materialise can do pre-processing, such as for metal melting AM processes. Some general pre-processing includes correcting and slicing the STL file, adding support structures, etc. Support structures are necessary for printing key features such as overhanging surfaces in photopolymer processes or to resist thermal stress induced distortion in powder bed processes. Figure 2(a) shows different supporting strategies for building the same part for different orientations and Figure 2 (b) is the cross-section of a part using block supports. Process parameters such as laser

power, speed and scan pattern are set up in the machine in step 4. The scan pattern shown in Figure 3 is a typical type for an EOS M270 machine. After finishing the build in step 5, post-processing including removal of the support structure, surface cleaning and heat treatment may be done before using a part.

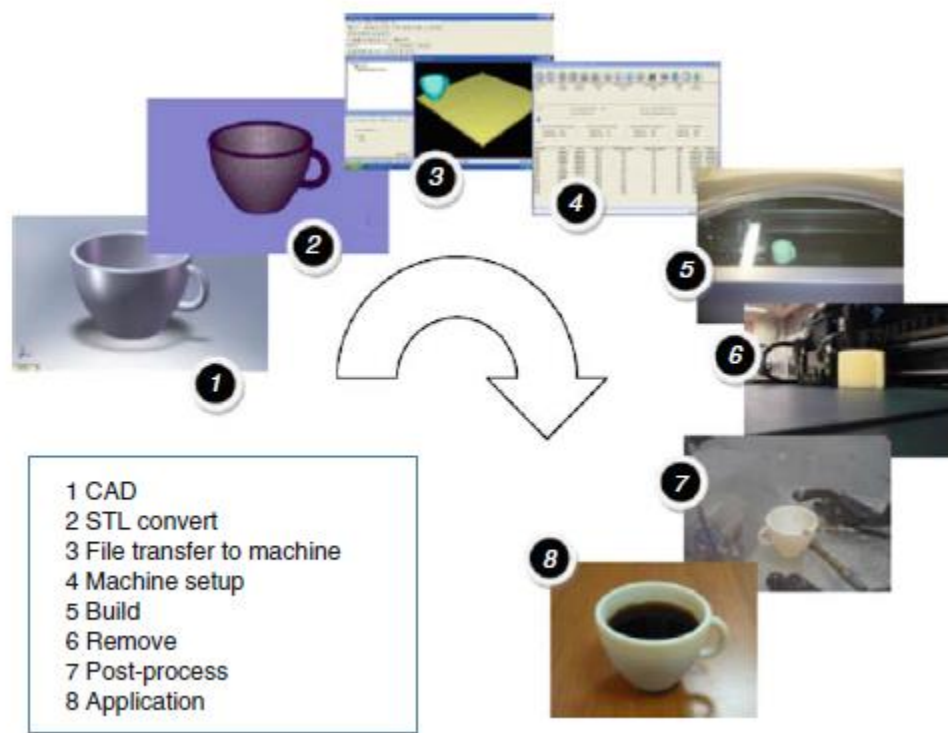


Figure 1 The eight stages of the AM process [3]

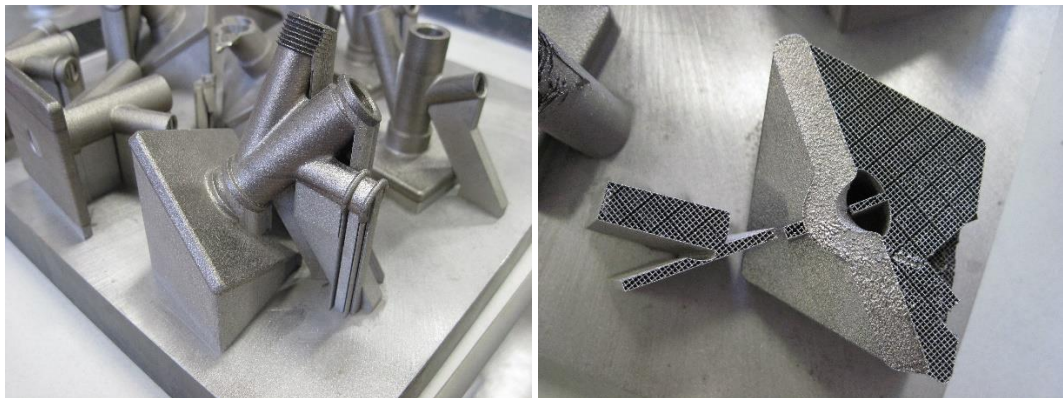


Figure 2 (a) Support structure for different building orientations and (b) Cross-section of one part with a block support structure

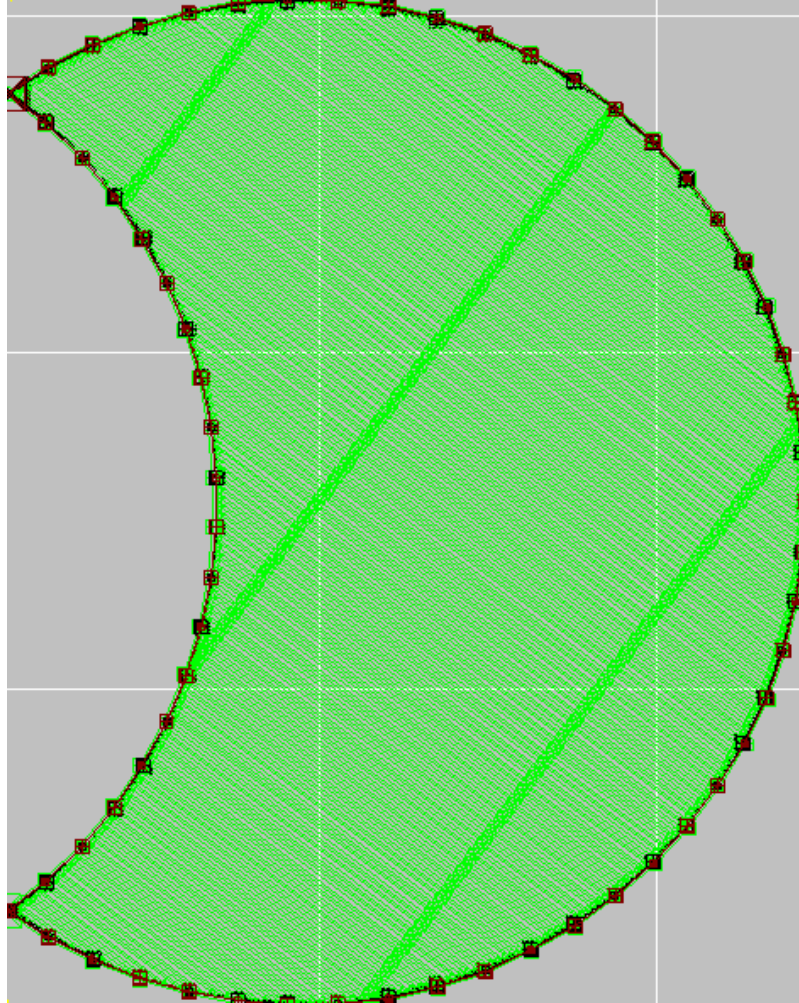


Figure 3 Scan pattern from EOS M270

Although AM technologies have existed for almost 30 years, technical challenges related to materials, equipment, process control, modeling and process understanding remain [2]. AM users rely on a large number of repeated experiments and experience to understand the performance of AM processes. This trial and error approach to producing a qualified AM part is costly for both time and money. As seen in Figure 2 and Figure 3, scan pattern and support structure are two complex aspects in AM. Therefore, simulation tools are critically needed for today's AM industry to aid understanding and further prediction of material behavior and AM part properties. These motivate the research in

this proposal to build new tools to investigate the influence of scan pattern on thermal stress and to generate optimal support structures for AM processes.

1.2 Problem Statement

The Selective Laser Melting (SLM) process involves the moving of a laser beam across a powder bed to melt material layer by layer. SLM involves very high laser intensity values, on the order of 10^{10} W/m² and a Heat Affected Zone (HAZ) that is orders of magnitude less than the dimensions of the platform. Comprehensive literature review in chapter 2 will show many computational models developed to study temperature evolution in SLM. However most of these models are not able to simulate the complete problem, but only simulate a small part of the problem with a fine mesh or the entire problem using a coarse mesh to avoid the computational burdens of meshing the full problem with a fine mesh. A thermo-mechanical simulation tool for SLM developed at the University of Louisville is being commercialized by 3DSIM, LLC. It is able to simulate the temperature and thermal stress distribution in the SLM process in a fine-scale [4]. The model utilizes a spatiotemporal adaptive meshing technique where the fine mesh domain moves along with the laser scan path. This tool has been shown to provide significant computational enhancements over other solution methodologies and makes possible simulating the complete problem for an SLM process.

In order to adopt this tool as a thermal stress predictor for support structure design in SLM, the first goal of this research is to validate the thermal results of the 3DSIM thermo-mechanical simulation tools. A finite element method (FEM) model with a similar dynamic moving mesh has been developed in the commercialized standard FEM software ANSYS. The ANSYS model is used to compare against the 3DSIM model. The

second goal of the research is to make the 3DSIM model able to simulate the SLM process using the same scan pattern as used in an SLM machine to study the influence of various scan patterns on the temperature, stress distribution and microstructure of parts made using SLM. A scan pattern generation module has been created and integrated into the 3DSIM model. The third goal is to add the influence of support structure into the model. An effective thermal conductivity for the support structure has been studied and implemented. The fourth goal is to develop a novel framework for a support structure optimization and design tool which is able to create optimal support structures based on both stress and geometry of the part. The support structure generation tool has been focused on optimization of block support structure density for a given part built with a specific orientation and scan pattern. What is more, the experiment has been carried out to explore the threshold of block support structure parameters which can be applied to the model.

CHAPTER 2 LITERATURE REVIEW

In this chapter, an introduction to SLM followed by a comprehensive literature review of thermal modeling of SLM technology, scan strategies and support structures is presented.

2.1 Additive Manufacturing

Additive Manufacturing (AM) technologies have been improved, re-innovated and extended tremendously since the idea of layer-by-layer fabrication from a CAD model was first developed in the 1970s [3, 5]. There are seven major categories of AM technologies according to the ASTM classification as shown in Figure 4 [6]. Figure 4 also summarizes the materials that different AM technologies are able to process and examples of companies that produce AM machines worldwide. AM technologies are categorized mainly by the mechanism of processing and each classification has been divided into several other processes according to the materials and/or energy source. Metals and polymers (including photopolymers) are widely used materials in AM. As shown in Figure 4, AM is being utilized all over the world, with the United States and Europe as the main pioneers.

Classification	Material	Process description	Commercial systems (country)	Developmental system (country)
Powder Bed Fusion	Metal	Direct metal laser sintering Selective laser melting Selective laser melting Selective laser melting Selective laser melting Selective laser melting Selective laser melting Electron beam melting	EOS (Germany) Concept Laser (Germany) Renishaw (UK) Realizer (Germany) Phenix (France) SLM Solutions (Germany) Matsuura (Japan) ARCAM (Sweden)	
	Polymer	Selective Laser Sintering Selective Laser Sintering Selective Heat Sintering Selective Mask Sintering High speed sintering Selective Laser Printing	EOS (Germany) 3D Systems (USA)	Blue Printer (Denmark) FIT (Germany) Sheffield Uni (UK) Renishaw / DMU (UK)
	Ceramic	Selective Laser Sintering Selective Laser Sintering	Phenix (France) EOS (Germany)	
Directed Energy Deposition	Metal (powder feed)	Direct Metal Deposition Laser Engineer Net shaping Laser Consolidation Laser Deposition Laser Deposition* Laser Deposition* Ion Fusion Formation	POM (USA) Optomec (USA) Accufusion (Canada) Irepa Laser (France) Trumpf (Germany) Huffnan (USA)	Honeywell (USA)
	Metal (wire feed)	Electron Beam Direct Melting Wire & arc deposition (WAAM) Shape Metal Deposition (SMD)	Sciaky (USA)	Cranfield Uni (UK) Nuclear AMRC / RR (UK)
Material Jetting	Photopolymer	Polyjet Projet Ink-jetting	Objet (Israel) 3D Systems (USA) LUXeXcel (Netherlands)	
	Wax	Thermojet / Projet T-Benchtop	3D Systems (USA) SolidScape-Stratasys (USA)	
Binder Jetting	Metal	M-Print / M-Lab	ExOne (USA)	
	Polymer	3DP	Voxel Jet (Germany)	
	Ceramic	3DP (models & parts) 3DP (medical implant) S-Print (sand cores)	3D Systems (Z-Corp) Therics (USA) ExOne (USA)	
Material extrusion	Polymer	FDM (Dimension & Fortus) FDM (Replicator) FDM (UP) FDM (Cube & BFB)	Stratasys (USA) MakerBot (USA) Delta Microfactory (China) 3D Systems (USA)	
Vat photopolymerisation	Photopolymer	Stereolithography Digital Light processing Digital Light processing SLA / DLP	3D Systems (USA) Envisiontec (Germany) Asiga (USA) DWS (Italy)	
	Photopolymer (ceramic)	CeraFab CeramPilot	Lithoz (Austria) 3DCeram (France)	
Sheet lamination	Hybrids	Ultrasonic Consolidation	Fabrisonic / Solidica (USA)	
	Metallic	Ultrasonic Consolidation	Fabrisonic / Solidica (USA)	
	Ceramic	Laminated Objet Manufacture	CAMLEM (USA)	

Figure 4 Classification of additive manufacturing processes defined by the additive manufacturing special interest group (AM SIG)-adapted from ASTM classifications [6]

* Technology typically associated with turbine blade repair, but also used for AM applications

2.2 Selective Laser Melting (SLM) Process

As seen from Figure 4, SLM is one of the processes under Powder Bed Fusion (PBF). SLM is a metal based PBF process and is similar to Selective Laser Sintering (SLS). A wide range of metals have been used in SLM, such as stainless steel, titanium, cobalt chrome, etc.

2.2.1 SLM Process

Figure 5 [7] shows a schematic diagram of a typical SLM process mechanism. It consists of the building platform system, powder delivery system and laser system. The part is built upon the building plate which is fastened to the build platform and adjusted to be horizontal. Then the powder is delivered and spread over the plate by the recoater blade. The thickness of each powder layer is usually at least the diameter of the powder and can be flexibly set by the user. Laser scanning begins with predefined tracks after the powder has been spread over the plate. After layer scanning is finished, the build platform is lowered the depth of a layer and new powder is spread over the previous layer. The process is repeated continuously and the new layer is built upon the old ones until the part has been finished.

2.2.2 SLM Process Parameters

In SLM the basic process parameters include laser related parameters and geometry/scanning related parameters. Laser related parameters include laser power, beam diameter and scanning speed. Geometry/scanning related parameters include hatch spacing, beam offset and layer thickness. Besides these, different scan patterns, such as strip, chessboard, and skin/contour settings can be selected for the part. Parameter setup is usually tedious in the machine, but very critical to the success of the build since the

microstructure, mechanical properties, deformation, geometric accuracy and surface roughness of the part are influenced by process parameters [8] .

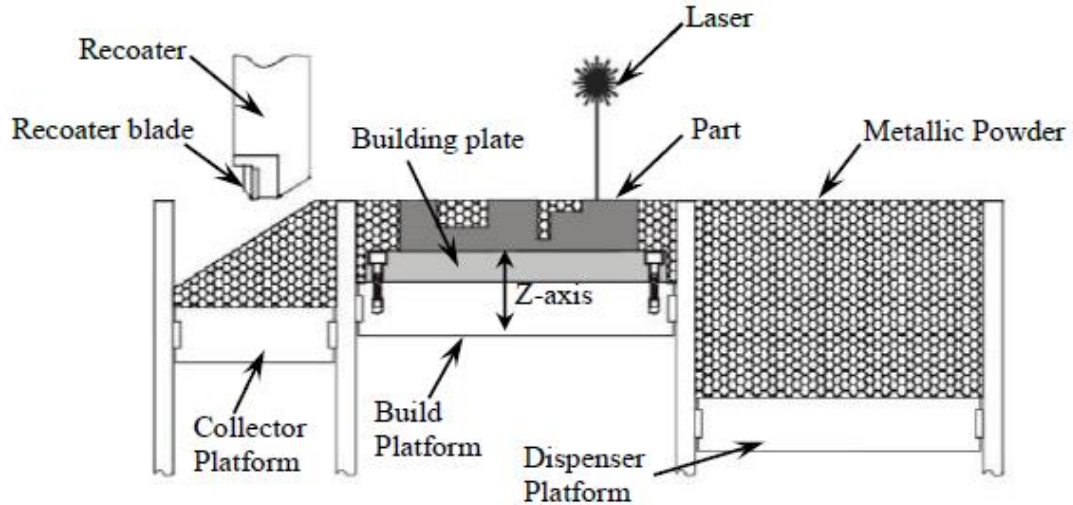


Figure 5 SLM process diagram [7]

2.2.3 SLM Defects

The highly concentrated laser energy input in SLM results in large thermal gradients, which result in thermal stress in the part. Deformation, cracking, internal porosity and dimensional inaccuracy are four of the most common defects. A bridge structure [9] and a T-shaped cantilever structure [10] were fabricated using SLM and the bending deformation was measured in both cases. The bridge structure shows bending of the two ends into the positive vertical direction and the T-shaped cantilever structure bent in the negative vertical direction after cooling down to ambient temperature and removal of the support structures. A structure with overhanging features on both sides was built in the experiment and overhanging structures bent and broke away from the support structure because of the thermal stress [11]. Cracks and delamination can occur during fabrication of M2 Tool Steel parts in SLM [12]. Pre-heating the base plate and re-melting

every layer were studied in order to reduce cracking and delamination. Cracks were also observed in Titanium parts produced with SLM [13].

2.2.4 SLM Post-processing

The major work of post-processing in SLM is support removal and finishing. There are two types of support materials: (a) material which surrounds the part as a naturally-occurring by-product of the build process (natural supports), and (b) rigid structures which are designed and built to support, restrain or attach the part being built to a build platform (synthetic support) [3]. In SLM, the surrounding powder behaves as a natural support and provides support for the part in the build process. The part could be easily removed from the loose powder in SLM. In most cases, extra synthetic support structures need to be designed and fabricated to reduce deformation caused by thermal stress. This type of support structure needs to be removed from the part during SLM post processing. Surface finishing is usually required after support removal.

2.3 Thermo-mechanical simulation studies in SLM

2.3.1 SLM Thermal Phenomenon

A high energy density laser beam is applied in SLM to melt the powder material. The melt pool solidifies quickly to form the bulk part. Figure 6 [14] shows a schematic representation of a laser melting the surface of a powder bed. The laser source moves on the top of the powder bed following a prescribed scan pattern. The laser energy is dissipated in several ways as shown in Figure 6. A big portion of energy is reflected by the powder surface. In a typical SLM process, such as an EOS M270 machine, the build takes place in a closed chamber in which convection across the surface carries away a

certain amount of energy. Most of the remaining energy is conducted by the powder and

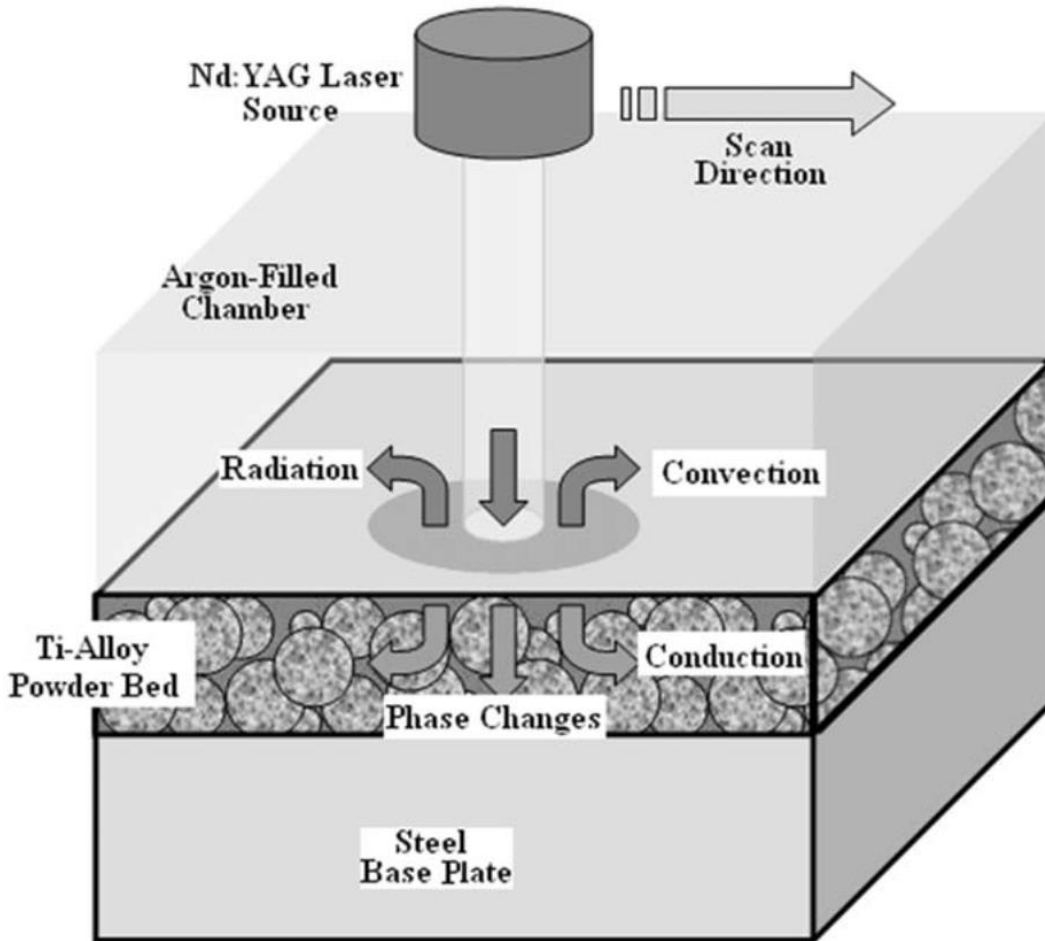


Figure 6 Schematic representation of heat transfer [14]

air trapped among powder particles through the powder bed and the base plate. During the heating and cooling process, the material undergoes phase changes from solid to liquid and back to solid, and can include solid state phase changes as well. Vaporization occurs if the temperature exceeds the material's vaporization point. In such a situation, heat radiation is significant due to the high temperature.

2.3.2 Governing Equations and Boundary Conditions

Fourier heat conduction theory is the most common theory used to describe the various heat conduction problems. It is also adopted for simulation of the moving heat

source problem in order to study thermal evolution in SLM processes. Most researchers utilize the heat conduction equation (Equation (1)) as the governing equation [15], Equation (2) represents an initial boundary condition of a constant temperature throughout the domain and Equations (3) and (4) are example convection and constraint boundary conditions respectively.

$$\lambda(T) \left(\frac{\partial^2 T}{\partial x^2} + \frac{\partial^2 T}{\partial y^2} + \frac{\partial^2 T}{\partial z^2} \right) + q = \rho(T)c(T) \frac{\partial T}{\partial t} \quad (1)$$

Initial condition:

Initial temperature:

$$T(x, y, z, 0) = T_0 \quad (2)$$

Boundary conditions:

Surface convection:

$$-\lambda(T) \frac{\partial T}{\partial z} = h(T - T_e) \quad (3)$$

No heat loss at the bottom:

$$-\lambda \frac{\partial T}{\partial z} \Big|_{z=0} = 0 \quad (4)$$

In these equations T is temperature, λ conductivity coefficient, ρ density, c heat capacity, q internal heat source, T_0 powder bed initial temperature, T_e environment temperature, and h convection heat transfer coefficient. The thermal coefficients λ , ρ , and c are considered temperature dependent for SLM.

2.3.3 Laser Beam Approximation Modeling

Surface Heat Source

A laser beam can be assumed to be a point or line source, but this is not in conjunction with reality. The Gaussian model, which is the most widely adopted model, utilizes a symmetrical distribution of laser irradiance across the beam [14, 16]. There are three basic modes for the Gaussian model: TEM₀₀, TEM₀₁, and TEM₀₂ [17]. Equation (5) describe the Gaussian laser beam distribution for the fundamental mode TEM₀₀,

$$I(r) = I_0 e^{-\frac{d^2}{d_1^2}} \quad (5)$$

where d_1 is the beam diameter and corresponds to the point where the irradiance (I_0) diminishes by a factor of $1/e^2$, and d is the radial distance of a point from the center.

The thermal heat flux is defined as the thermal energy per unit area and is modeled using Equation (6)[18],

$$q(r) = \frac{2P}{\pi r_0^2} e^{-\frac{2r^2}{r_0^2}} \quad (6)$$

where P is the laser power, r_0 the spot radius and r the radial distance. Similarly, the average heat flux on the laser spot is shown in Equation (7) by using the same definition as thermal heat flux,

$$q_m = \frac{1}{\pi r_0^2} \int_0^{r_0} q(2\pi r) dr = \frac{0.865\alpha P}{\pi r_0^2} \quad (7)$$

where α is the absorption rate (e.g. laser absorptivity).

Volumetric Heat Source

The surface heat source model is commonly assumed for simulation of the laser beam in SLM processes. There are also other models which consider laser beam penetration into the powder bed due to its porosity.

A ray tracing (RC) model has been simulated considering the geometry and structure of the powder [19]. The laser beam is simulated as a ray and it is reflected and absorbed by the surface of powder particles until the energy of the 'ray' decays to zero, as shown in Figure 7 [19]. Each ray has been traced and the simulation has been run with a large number of rays penetrating into the powder bed. Based on the large number of simulation results, the ratio of energy absorption can be calculated.

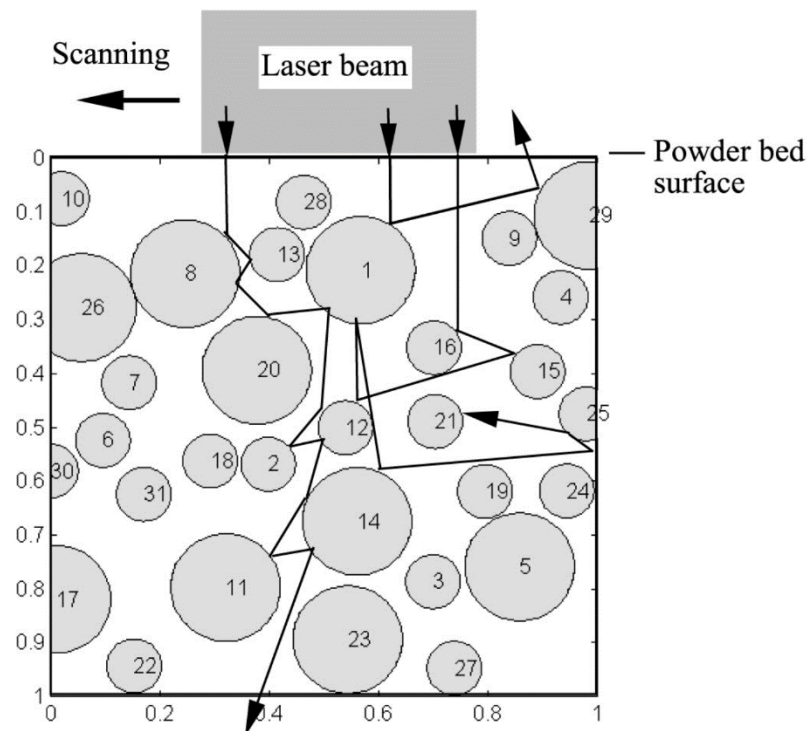


Figure 7 2D illustration of the RC model: simulation over a depth of 1mm and width of 1mm of powder bed [19]

2.3.4 SLM Thermal Modeling Techniques

The core problem when simulating heat transfer in SLM is to solve the governing Equation (1) under various specific boundary conditions. Analytical solutions and numerical method such as the finite element method (FEM) are two ways to find thermal results.

2.3.4.1 Analytical Solutions

An analytical solution has not been derived from the heat transfer model governed by Equation (1) under boundary condition Equations (2), (3), (4) with temperature dependent thermal coefficients. However, there are some solutions associated with constant coefficients and simplified boundary conditions. The Rosenthal solution is considered the basic formulation for simulating a traveling point heat source in welding [20]. Many welding studies focusing on different heat sources and calculation domains for one-dimensional (1D), two-dimensional (2D) and three-dimensional (3D) problems are based on the Rosenthal solution [21]. Rosenthal's solution plays an important role in the study of SLM temperature distribution as well since SLM processes and welding have a lot in common.

The solution for 1D steady state problems with point and line heat sources is derived analytically in [22]. The 3D Rosenthal analytical solution has been applied to solve the steady state temperature distribution by a moving point heat source in a semi-infinite plate domain for SLM [3]. A more complicated analytical solution with consideration of the Gaussian distribution heat source has also been derived [21, 23, 24]. The solution is in a form of an integral without a concise closed form [21]. The analytical closed form solution for the maximum temperature of a stationary laser beam, an extremely fast moving laser beam and a laser beam with intermediate velocity has

been derived [24]. From the literature, there are no analytical solutions for the problem with consideration of the nonlinearity of thermal properties.

2.3.4.2 Numerical Models

Uniform mesh FEM model

The effects of volume shrinkage during laser densification processes for ceramics have been analyzed using a finite element model [18, 25, 26]. A domain with dimensions of 10x6x2mm was created and meshed with element size of 0.25mm in ANSYS [18]. The thermal distribution caused by a laser beam with a radius of 0.5mm moving at a speed of 0.24mm/s has been calculated. The volumetric shrinkage was determined by the changing of porosity for powder and liquid which are 40% and 0% respectively. The shrinkage is implemented to the model by shrinking the Y coordinates of the fully melted elements. The results show that shrinkage has critical effects on the temperature distribution.

A numerical model of coupled radiation and heat transfer was built to analyze and explain observed instability such as ‘balling’ effects for processing 316 L stainless steel in SLM [27]. The simulation results suggest that decreasing the scanning velocity, reducing the length-to-width ratio of the melt pool and increasing the width of contact with the substrate will make the SLM process more stable. Single track scanning was simulated and compared against experiment results.

A heat equation solver using FEM was built in Matlab and the node, element information and connectivity matrix was imported from ANSYS [28]. This model was used to analyze the temperature distribution in a single metallic powder layer during SLM processing. The temperature distribution of a 2D domain with dimension of less than 1x1mm was calculated. The domain was divided into 64 elements and four area

elements were assumed under the Gaussian laser beam distribution. The temperature distribution was compared against experimental results [29] and numerical results [30].

A cubic specimen with the dimension of 5x0.8x0.1mm and meshed with 40000 hexahedral eight elements was modeled to study the thermal distribution of polycarbonate in Selective Laser Sintering (SLS) [31]. The model simulates the temperature distribution of the laser beam scanning the powder bed in the longitudinal direction for a total length of 4mm. The density distribution for simulation and experimental results were found to be in good agreement.

An ANSYS model was built to study the temperature distribution and thermal stress for laser melting of W-Ni-Fe powders [32]. A powder bed domain with dimension of 1x2x0.05mm was built upon a substrate with dimension of 2x3x1.5mm. The powder bed was hexahedron meshed with an element size of 0.05mm and the substrate was meshed by a free grid tetrahedron. The Gaussian heat flux zone was represented by 2x2 mesh matrices. The influences of various process parameters have been investigated using the FEM model in order to understand the SLM process.

A recent SLM model introduces a FEM model to simulate single bead scans of Titanium powder [33]. It was used to study the influence of process parameters and thus investigate the optimal parameters for fabricating denser Ti64 parts without post-processing. A powder bed with dimension of 2x1x0.05mm was sintered on a block with dimension of 25x10x5mm. Subsequently the solid model was meshed with an element size of 5 μ m for a laser diameter of 34 μ m.

Non-uniform mesh FEM model

A 2D model was developed to solve the SLS thermal problem for polymers and metals respectively, known as Childs' model and developed in Fortran [34-37]. These models have the ability to solve the transient thermal problem, accounting for various material states. It has been used to predict the track mass per unit length melted by the laser beam using the thermal and post-processing calculation for M2, H13 tool steels and 314S stainless steel powder [36] and crystalline polymer [34]. A boat-shaped track with a crescent cross-section is simulated by the Childs' model [35]. Reasonable agreement in melt pool shape and dimension with experimental results at low scan speed (0.5mm/s) for M2 and H13 tool steel was achieved. The 3D metal version of Childs's model is known as stmet3d [37]. The mesh in that 3D model is coarsened with distance from a heat source and it is represented by a 10x10 elements matrix zone. The local fine mesh is formed by intensifying the discretization in the heat flux zone. This localized fine discretization also inevitably increases the number of elements in the surrounding area. The process maps are constructed to relate modelled part qualities to input power, speed and hatch spacing, approximately 90 parts were modeled using stmet3d [37].

A FEM model simulates the temperature and thermal stress distribution of a simple geometry block with dimension of 20x20x9mm of H13 hot work tool steel in the SLM process. The size of each element depends on the melting depth and track width of the fused powder. The melting depth and width are determined experimentally. In the model, the latent heat is ignored because of the small melt pool. The new manner of using Element death and birth to deal with the powder deposition was first adopted in the Finite Element model in ANSYS [38].

Another coarse-fine mesh FEM model used to study SLM processing of Titanium powder was introduced [30]. The computational domain of the model is 5x5x2mm and the fine mesh domain is 2x2x0.5mm, in which the associated mesh size is 0.1mm and 0.01mm respectively. It is able to reduce the number of elements using two types of elements: coarse and fine mesh. However, the boundary between fine and coarse mesh needs to be coupled, and the associated FE method is non-conforming along the interface between the coarsely and finely meshed regions in this case, which is easily built compared to conformal meshes[30].

A recent thermal model using a coarse and fine mesh strategy to simulate the temperature distribution in SLM has been developed [14, 39]. The computational domain consists of five layers of 1x1x0.03mm Titanium powder deposited on the mild steel substrate with dimension of 3x3x3mm. The element type in this model is hexahedron for the substrate and powder bed compared against the tetrahedron model in [32]. The powder bed is uniformly divided in a fine mesh size of 0.025x0.025x0.03mm. A smarter manner was used to reduce the model size. The mesh for areas surrounding the finely meshed zone is coarse. And the mesh is coarser and coarser when it is further away from the finely meshed zone. The model was also built in ANSYS and the functionality of element death and birth is applied for new layer deposition.

Adaptive moving mesh FEM model

Adaptive moving mesh FEM is categorized in this dissertation based on whether the mesh is updated during the time/calculation steps in the thermal simulation. There are a lot of physical situations where temperature, stress, strain or point of interest is

highly concentrated in a tiny local area and changes with time. The thermal problem in the SLM process is one such phenomenon.

There are a series of effective, mesh-adaptation-based approaches aiming to numerically solve the mathematical differential equations [40]. There are three main mesh adaption strategies: mesh subdivision, local high order approximation, and mesh movement, which has not been well studied.

The commercial software ANSYS Fluent has the functionality for applying dynamic and moving meshes for solving fluid dynamics problem. It is used to model flows for which the domain is changing with time [41]. Besides ANSYS Fluent, there are no other tools fully capable of simulating thermo-mechanical problem in a moving mesh fashion so far.

There are a few models in the literature for using adaptive moving meshes to simulate temperature distributions in SLM. A FEM model was developed to simulate the melting and solidifying process and calculate the amount of solidified mass during SLM processing [42]. The solidified part is assumed to be a hemisphere due to surface tension, therefore the mesh for the melted/solidified powder is updated to the assumed shape after each heating in the simulation.

An innovative generalized feed forward dynamic adaptive mesh refinement and de-refinement finite element framework for SLM has been established most recently [43-45]. A fine-coarse mesh strategy is applied to quickly calculate the temperature distribution. The heat affected zone (HAZ) is meshed into an ultrafine scale in order to capture the temperature under the laser beam. The area surrounding the HAZ is meshed using a relatively coarse mesh to reduce the number of elements. The fine mesh

representing the HAZ moves at the scanning speed of the laser beam, therefore, the global temperature in the SLM process can be calculated using a really fine scale.

In conclusion most of the works from the literature try to give insights about the SLM process through simulation of the simplified problem. Since the traditional uniform meshing FEM method are not capable of fully simulating the multi-scale thermal problem for an SLM process under normal computational capacity. Non-uniform meshing strategies are beneficial to reduce the problem size for solving larger, but still limited, problems. However, more effective and smart algorithms such as multi scale dynamic meshing are necessary to adopt to dramatically reduce the level of computational burden and potentially simulate the SLM process in the near future.

2.4 Scan Strategies in SLM

2.4.1 Scan Strategies in SLM processing

A study of the sintering and melting behavior of stainless steel 314S powder in SLM was undertaken [46]. The study included building tracks from a single layer to multiple layers. Single track scanning and traditional raster scanning strategies were used in the experiments. A combination of different scan speed and power were applied to the experiment and a process map correlated scan speed, power and melt pool shape based on a massive experimental data.

Thermal stress is influenced by both material properties and process parameters, such as scanning strategies. In order to optimize the scanning strategy, a closer look was taken at the thermal deformation and other mechanism involved in SLM. Six different scanning strategies were used in the experiment and performed in the self-developed machine at the University of Leuven with a maximum output power of 300W [47]. The

six scan strategies include two parallel line scanning through the X and Y direction and other four sector patterns where the part is divided into small square sections as shown in Figure 8. Two of the sector patterns have dimension of 5x5mm for the square section. And the other two have dimension of 2.5x2.5mm. For the sector strategies, there are two scanning orders (1) scanning successively or (2) according to the least heat influence (LHI) for the neighboring sectors. So all the six scanning strategies performed in the experiment are (1) line X, (2) line Y, (3) sector 5-suc., (4) sector 5-LHI, (5) sector 2.5-suc. And (6) sector 2.5-LHI. Some conclusions are drawn for the six different scan strategies. In general, the stresses perpendicular to the scan direction are larger than along the scan direction. Scanning along the X/Y-direction results in the smallest curvature in that direction, but the largest curvature in the other direction. Sector strategies result in less deformation. The same six scan strategies [47] with different square section dimensions were used to study their influence on thermal stress. And the experimental results for four of the scan patterns were also compared against the residual stress results from a theoretical model which was described in the paper [48]. The paper indicated that both results have similar tendency although large deviation exists in some area.

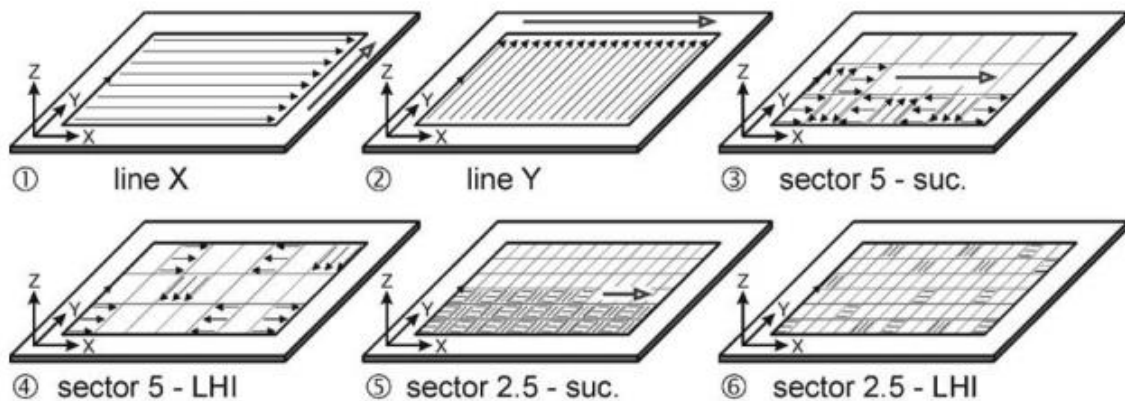


Figure 8 Six different scan strategies tested [47]

A fine microstructure and controllable texture AlSi10Mg part is obtainable through SLM [49]. A modified Concept Laser M1 machine with maximum 200W fiber laser was used to fabricate the AlSi10Mg part. A cubical sample with dimensions of 15x15x15mm was fabricated using five different scan strategies, which are (a) uni-direction, (b) bi-direction, (c) alternate bi-direction, (d) island with 90° rotation and (e) island with 90° rotation and 1mm shift between layers as it shown in Figure 9. The melt pool width for sample (a, b) is $170 \pm 15\mu\text{m}$ and (d, e) is $180 \pm 30\mu\text{m}$. The crystallographic texture of samples (a) and (b) are similar and the normalized texture difference was calculated to be 0.64%. However, the overall crystallographic texture was reduced significantly by 35% when the scanning direction is rotated by 90° every layer. The normalized texture difference between samples (c) and (d) was about 3.5%, and about 1% between samples (d) and (e).

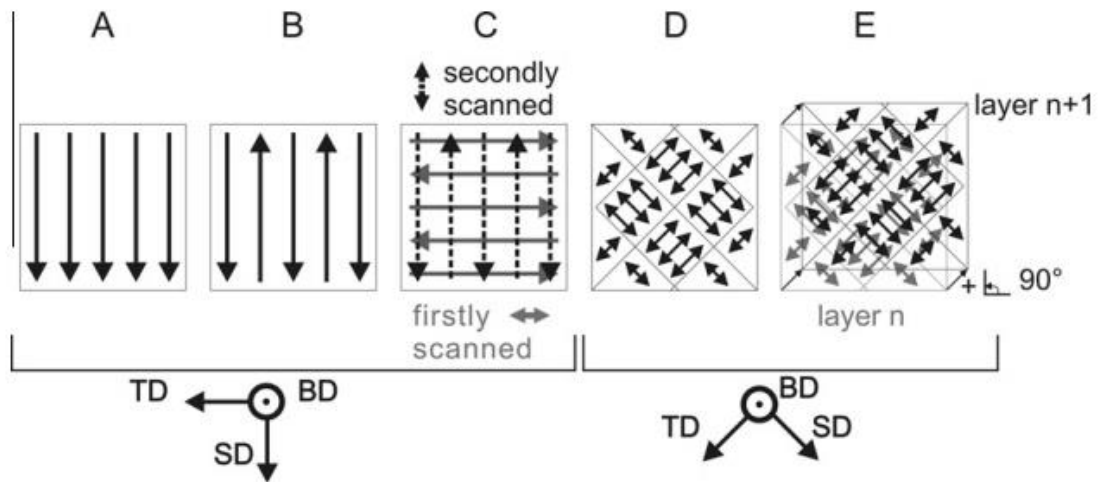


Figure 9 Five different scan strategies tested [49]

Another experiment [9] was performed in order to understand the influence of scan strategy on the thermal stress and curling angle from the same research group [47, 48]. The relative density for a Ti64 part was measured for three different scan strategies: uni-

direction, bi-direction and alternating bi-direction for two layers. The results showed that part scanning using alternating bi-direction achieves the highest relative density. On the other hand, the uni-direction scanned part has the lowest density. The experimental results also show that re-melting the scanned layer or top surface can improve the density and surface quality. By reducing the scan vector length in bi-direction scanning from 10mm to 2mm, the thermal stress is improved by 13%. Also the island scanning strategy is able to reduce the curling angle, but island section size did not influence the curling angle. When the scanning direction angle is 45° with respect to the x axis, the largest improvement for the curling angle is 36%.

Porosity and layer distortion was compared for four different scan strategies for H13 tool steel built in a 550 W pulsed Nd:YAG laser SLM machine [50]. The four scanning strategies are: filling, sequential, alternating, and refill. The alternating strategy produced specimens with a more uniform temperature and surface quality as shown in Figure 10. Alternating strategy specimens show the highest porosity. The specimen fabricated using the refill strategy showed the lowest porosity and volume reduction. The spacing change for the strategies showed little influence by cross-section of the sample.

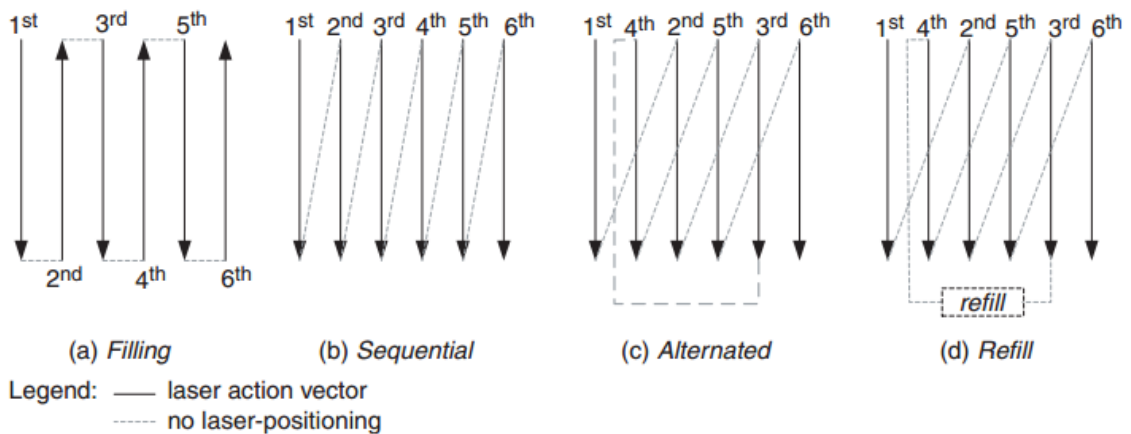


Figure 10 Four different scan strategies tested [50]

A consecutive sub-sector scan strategy, also known as a chessboard scan strategy [7], has been created and tested for stainless steel 316L inner complex structures in a self-developed HRPM II SLM machine with maximum 200W laser output [51]. The sub-sector scan strategy with adjusted short scan vectors shows its advantage for melting powder more effectively.

In the same SLM machine, a new helix scan strategy was tested by fabricating 316L to reduce thermal deformation [52]. The helix scan strategy was compared against a bi-direction scan pattern. The helix scan strategy when fabricating complex geometrical parts resulted in a lower maximum deformation. It was also shown that the helix scan strategy is not appropriate to for scanning a ring geometry.

Adjusting the scanning strategy was proposed to control defects such as balling effects and thermal deformation caused by thermal gradients in SLM. Four different types of scanning strategies were performed to fabricate selected alloy powders such as gold and stainless steel 304L in a maximum 100W Nd:YAG laser platform[53]. The four selected scanning strategies were: parallel, spiral, paintbrush and chessboard scanning. The four scanning strategies showed different influences on part quality. The parallel scanning parts normally have balling and cracks on the two sides that are perpendicular to the scanning direction even at high speed. Spiral scanning was able to produce better thermal results than parallel line scanning for very high scan speeds. Spiral scanning was able to avoid overheating near the sides perpendicular to the scanning direction, however, serious overheat happens in the center of the part. Paintbrush scanning can limit overheating and high temperature gradients for both low and high conductivity powder, resulting in dense parts. However, bonding is not perfect for the first layer and

delamination is foreseen for tall parts. Chessboard scanning was found to be the best among them to reduce thermal gradients and deformation, though it was difficult to create suitable CAD files.

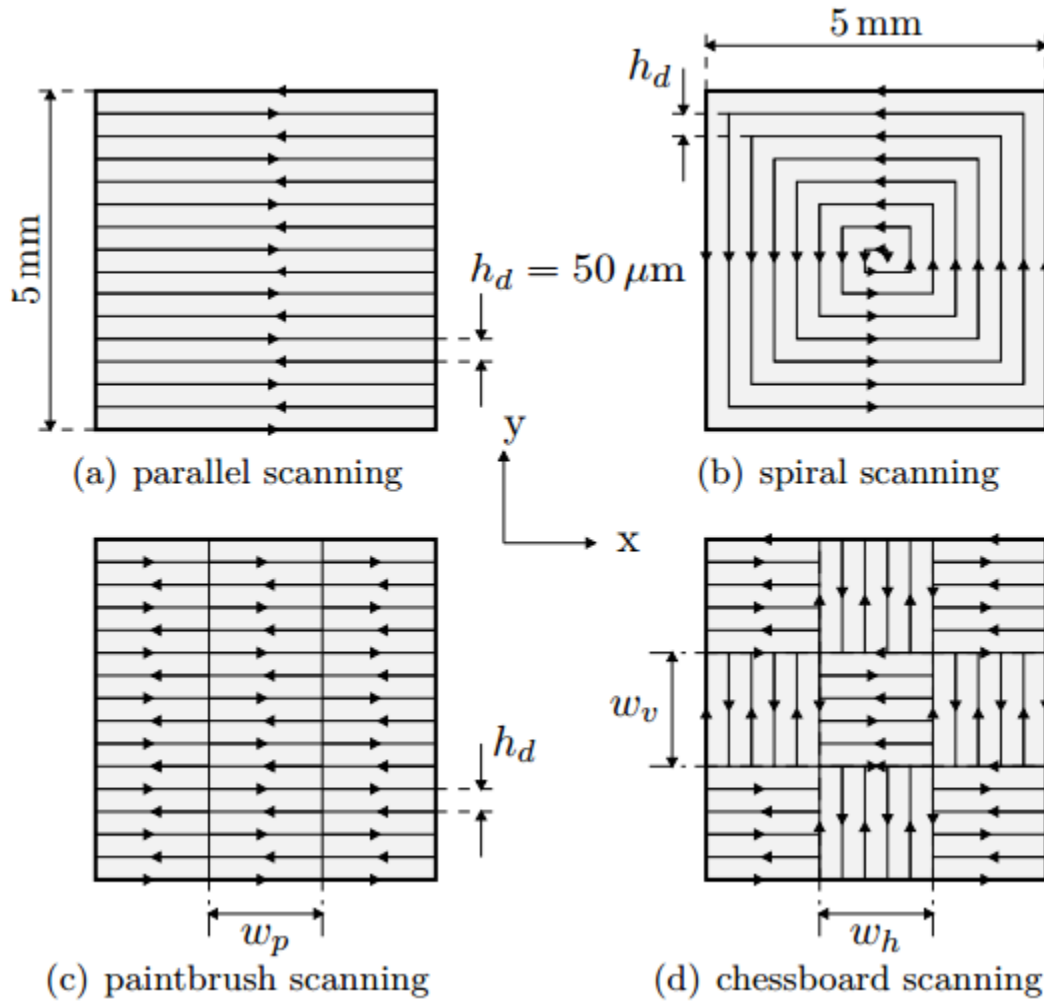


Figure 11 Four different scan strategies tested [53]

In conclusion, the literatures shows that scan strategies do influence thermal evolution and result in different deformation behavior in SLM fabricated parts. Better scan strategies by reducing the scan length could help to reduce thermal gradients, deformation and even improve the density of the part.

2.4.2 Scan Strategies in Modeling

A FEM analysis of temperature and thermal stress of a single layer formed on a nickel based alloy powder bed in SLM was investigated [54]. The thermal results for five tracks of scanning was simulated for a single layer under a Gaussian laser source. According to the simulation results, warping can be reduced by shortening the long scanning track and dividing the scanning area into small sections to avoid cracking.

The influence of two different scan strategies on the temperature distribution and thermal stress were tested in a FEM model which allows for nonlinear thermal properties [55]. A newly developed fractal scanning pattern was compared against traditional raster scanning. A flat nickel plate with dimensions of 60x60x2mm was scanned by a traveling laser beam in this FEM model. The temperature distribution was more uniform for the fractal scanning plate. The final thermal distortion of the plate was 55.7% smaller than the traditional raster scanning plate.

A combination of a pseudo-analytical model and empirical FEM model built in ABAQUS was used to test and validate existing scan strategies [56]. In spiral, out spiral, traditional raster and uni-direction scan strategies were first tested in this model. According to the ABAQUS and pseudo-analytical results, high temperature was reached at the center and edge of the part in the in and out spiral scanning strategies respectively. The high thermal gradient and stress appears in the perpendicular scanning direction for traditional raster and uni-direction scanning. The interlaced traditional raster and uni-direction scanning pattern leads to better thermal homogeneity. What's more, a dimensionless parameter θ is calculated for evaluating the thermal results of each scanning pattern, however, there is no definition for θ in the paper. A new grid-based scan strategy using a genetic algorithm to create the scanning strategy has been

developed in order to reduce thermal asymmetries. The scanning area is divided into small squares. The genetic algorithm is used to choose the scan strategy for each unit square from the mentioned existing patterns above in order to minimize the dimensionless parameter θ as the objective function. The simulation results show that the optimized scan strategy produces the best thermal homogeneity among all the scan patterns.

A numerical model was used to evaluate the drawbacks and benefits of different scanning strategies [53]. It was concluded that the numerical model could find overheating zones. However, the paper does not present many results of simulation but instead experimental results. It also pointed out that genetic algorithms could be combined to generate more intelligent scanning strategies.

2.4.3 Hatching Algorithm

A traditional raster scan path was generated for a complex concave polygon using the theory of rectangular hull [57]. There is a minimum rectangle area enclosing the cross-section of any polygon. The scanning parallel lines intersects with the rectangle hull first to find out the hatching segment first. Then these sets of segments are intersected with the polyline in the original polygon and form the scanning vectors.

An intersection points computing algorithm has been developed for generating a new sub-sector scan pattern with variable scan lengths in SLM [51]. There are three steps for hatching the contours in this algorithm: (1) group the internal and external contours, (2) calculate intersection points between contours and parallel lines and (3) break up the intersection lines into new paths in sub-sectors. In the first step, all the contours are stored in a depth tree in a sliced file in which external contours are indexed in even

numbers and internal contours in odd numbers. The geometry with multi internal and external contours can be divided into groups with only one external and one/multi internals pair. Each group of contours can be further divided into subdomains depending on the size of the sub-sector. And hatch lines obtained for the contour group can be broken and generated for each sub-sector to implement the consecutive sub-sector scan pattern.

In order to reduce the scanning time in SLM, an area division scan pattern generation algorithm is proposed [58]. All the intersection points between contours and scanning parallel lines are found in the first step and each hatch line consists of a start and end point. It is not always true that the scanning line will intersect with the internal contours for the geometry with holes, a bounding rectangle of loop (BRLp) which contains the internal contour exactly is defined. If the scanning line has no intersection with the BRLp, the calculation will be ignored so as to improve the efficiency of the algorithm. A concave polygon is selected to test the scan pattern generation algorithm.

In conclusion the most basic scan strategies were explored most extensively in the experiment although simulation tools were also applied to study the behavior of different scan patterns in SLM. Restricted by the limited capability of simulation tools for SLM, the real scan pattern used in SLM processing has never been implemented in simulation. Most of the work were using simplified models with basic scan patterns. However, there are well developed algorithms in the field of geometrical modeling which could be adopted to build a real scan pattern generation tool.

2.5 Support Strategies in SLM

2.5.1 Support Structures in AM Processing

As shown in Figure 4, AM processes are generally categorized into seven main processes and supports exist in all processes in different forms. Many AM-produced parts can be supported by their surrounding materials such as the powder in the SLS, PBF process and sheet material in sheet lamination processes. However, several other AM processes, such as extrusion based systems and direct printing, are not be able to be supported by surrounding materials. They require extra supports for overhanging structures and to connect the part to the build platform. In some cases with large distortion, such as when using PBF techniques for metal in SLM, supports are required to resist distortion

2.5.2 Importance of Support in SLM Processing

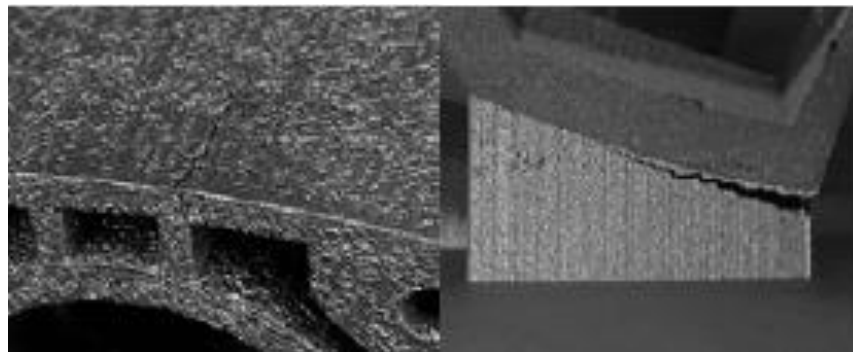


Figure 12 Cracking and delamination in SLM [59]



Figure 13 Distortion and delamination in SLM processing [60]

Support structures are critical to successfully finish building a part in many AM processes. Besides holding a layer in place, support structures play an important role in

resisting the thermal stress. Thermal stress can cause huge deformations to the part and can lead to build failure due to delamination of the part from the base plate [61], as shown in Figure 12 [59], Figure 13 [60] and Figure 14 [11]. Thermal stress also can induce cracks during processing before the part is complete, as shown in Figure 12. The part may break without enough supports as shown in Figure 15. A series of articles about 3D printing of titanium and its inherent challenges was published on 3dprintingindustry.com [62-64]. One of the articles illustrated an example of the design of support structures for one of parts took six iterations in order to build successfully, however, it was still not a functional prototype to test [64]. The need for support structures is described as one of the limitations of the SLM process because it severely restricts the geometries that the processes can make, and adds significant time and cost to production [65].

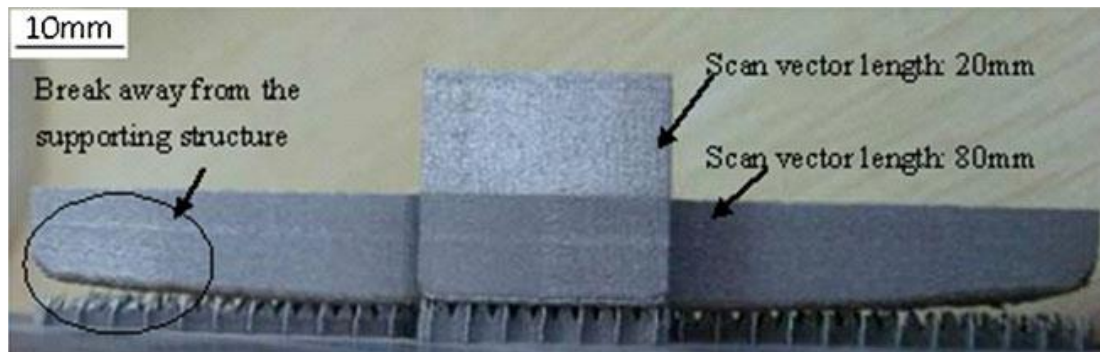


Figure 14 Curling in SLM [11]

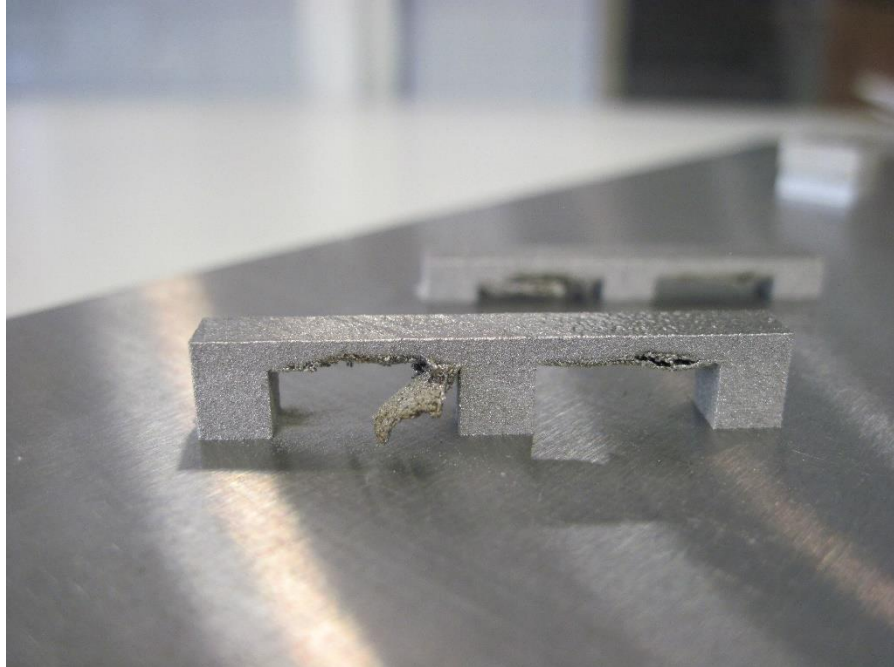


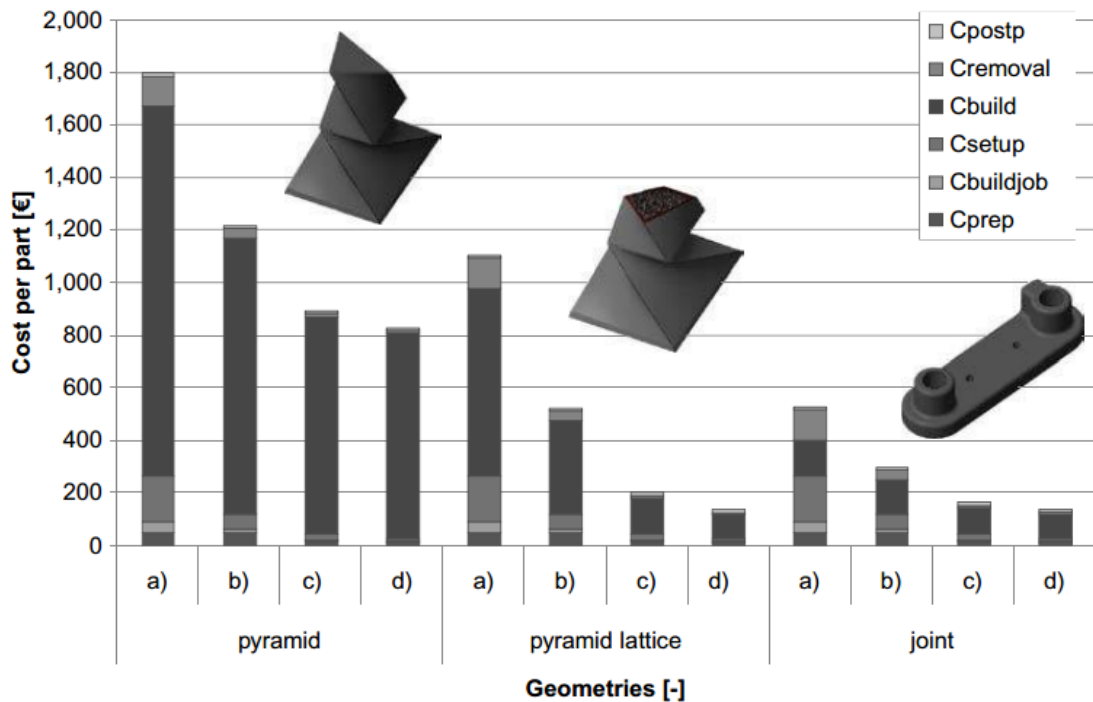
Figure 15 Overhang failure in SLM

2.5.3 Cost Estimation for Support Structures

A generic model has been developed to determine the optimal part orientation and build cost [66]. The generic cost model estimates the total cost in three aspects: cost for preprocessing, building and post-processing. The preprocessing cost consists of time used to setup process parameters, slice the STL file and generate support structures. The building cost includes machine running, part building and support building costs. The post-processing costs include part removal, cleaning and finishing costs. The model was applied to illustrate the cost of both SLA and FDM processes by fabricating simplified geometries. A simplified cup fabricated in three orientations was used to test the model to estimate the total cost, volume and contact area of supports. Results showed that the support material to total material ratio is 41.818%, 6.705% and 42.342%, and total support removal time is 0.27 hours, 0.03 hours and 0.3 hours respectively for three orientations in an FDM process. The numbers in the SLA machine are 10.864%, 3.030%,

and 6.92% for support material ratio and 0.14 hours, 0.09 hours, and 0.18 hours for support removal.

This model was adapted and extended to SLM and support material and building times were also considered in the new cost model [67]. Three parts were built and the cost estimation was analyzed for different conditions. The split cost results for each part and scenario is showing in Figure 16. It was found that the total cost per part can be significantly reduced by 41% in the presented case study by simultaneously building up multiple parts. However, the paper were not aiming to study the cost difference with different support strategies.



Notes: Case (a) separate manufacturing of each geometry; cases (b)-(d) part-costs for each geometry, when manufactured together in the same build process for one, two or five parts of each geometry, respectively

Figure 16 Cost splitting for each geometry according to the cost model [67]

In conclusion, there is little work about cost estimation of the SLM process and less work for support strategy cost analysis, although this is very crucial in the AM

industry. The model which was developed for the SLS process showed that the support material and cost could be significantly reduced with better support strategies.

2.5.4 Support Strategies for SLM

2.5.4.1 Support Structure Generation Software

Materialise Magics' support generation module is one of the most commonly used commercial software tools for designing and generating support structures for SLM. It is able to automatically generate support structures based on the 3D model and also provide flexibility for users to manually modify support structures. It allows users to choose orientation of the 3D model to attach to the support structure. Types and parameters of the support structure are also flexible for the user to select. The user can modify and tune the support structure for special features to optimize the design. Magics' support generation module provides a broad range of support structure types including block, line, point, web, contour, gusset, combi, volume, and cone support structure.

The software package Bridgeworks by Solid Concepts automatically generates support structures. The algorithm used to generate the supports utilize a number of parameters, which are well documented in the user manual [68]. The Bridgeworks program divides support structures into five categories, Gussets, Projected Features Edges, Single webs, Webs and columns.

Smart3D Supports Generator is a system for generating supports for designing and fabricating jewelry in AM machines such as SLA, SLS and SLM [69]. It is able to correct an STL file, and recognize and manage the areas to be supported. It runs in Rhino 5.4 64bit version, which is a software commonly used for industrial, architectural, and jewelry design, and is able to build 3D support structures in a 3D CAD environment.

2.5.4.2 Types of Support Structure

As mentioned above, Magics is one of most popular commercial software tools for AM. Magics' support generation module provides a broad range of support structure types including block, line, point, web, and contour support structures as shown in Figure 17 [60]. The support structures generated from Magics consisted of rectangular or circular thin walls with a large distance between walls. Among all these types of support structures, block supports, as shown in Figure 17 (a), are the most common for SLM.

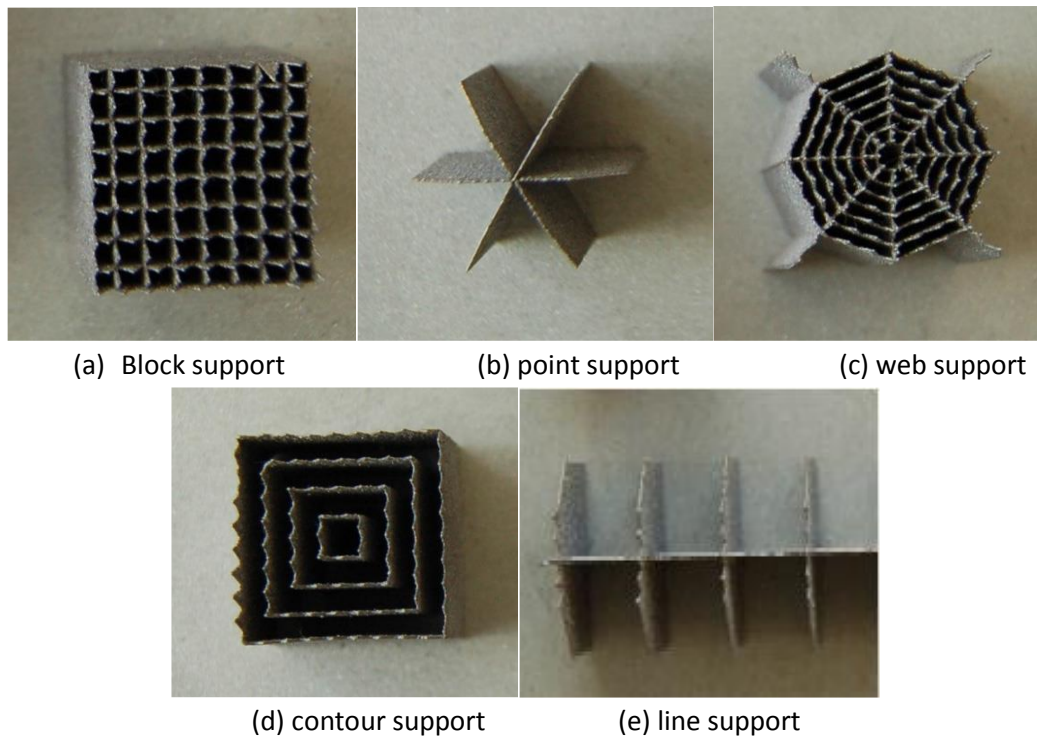


Figure 17 Different types of Magics' generated support structures [60]

There are also other less commonly used types of support structures such as gusset, combi, volume and cones available in Magics. The amount of traditional support structures is often too large for overhangs on delicate parts, which increases the difficulty to remove them and can easily cause small pieces of the part to break off [70]. There are other support structures designed by researchers shown in the literature [70-72]. A special

grid support structure shown in Figure 18 [71] has been developed to achieve the segmentation support strategy. There is no wall structure and the connection between supports and part is via fixation points for the grid support structure. The support structure was optimized using the design of experiment (DOE) method.

Figure 18 and Figure 19 [70] show a novel application of a cellular lattice with very low volume fractions to be used as an external support structure for SLM [70, 72]. First of all the lattice support structure was shown to be self-supporting [72]. The effect of percentage of volume fraction and unit cell size of the lattice structure on the manufacturability, build time, weight of support, and resulting part deformation was investigated and analyzed [70]. The lattice support structures show good manufacturability characteristics, however some of the parts failed during the build due to very thin connecting struts and large distances between the adjacent contact points. A best compromise between the best combination of cell size and volume fraction could enable the future expansion of these structures for supports.

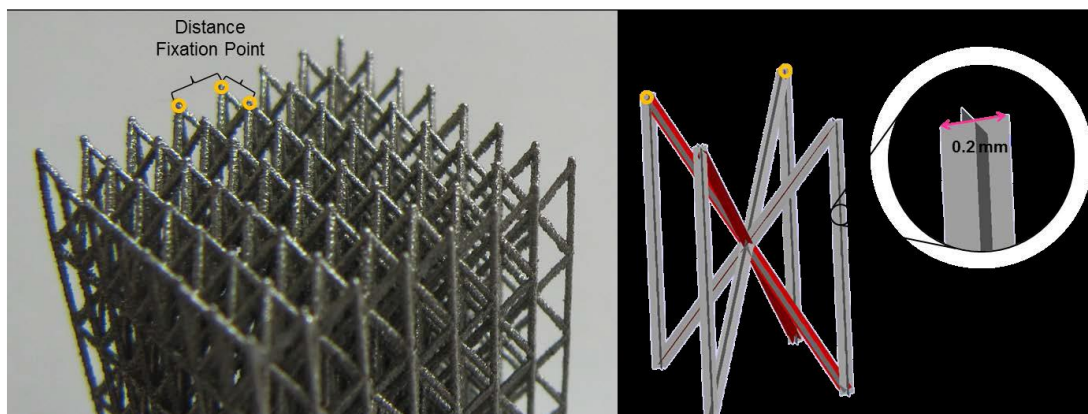


Figure 18 Grid support structure [71]

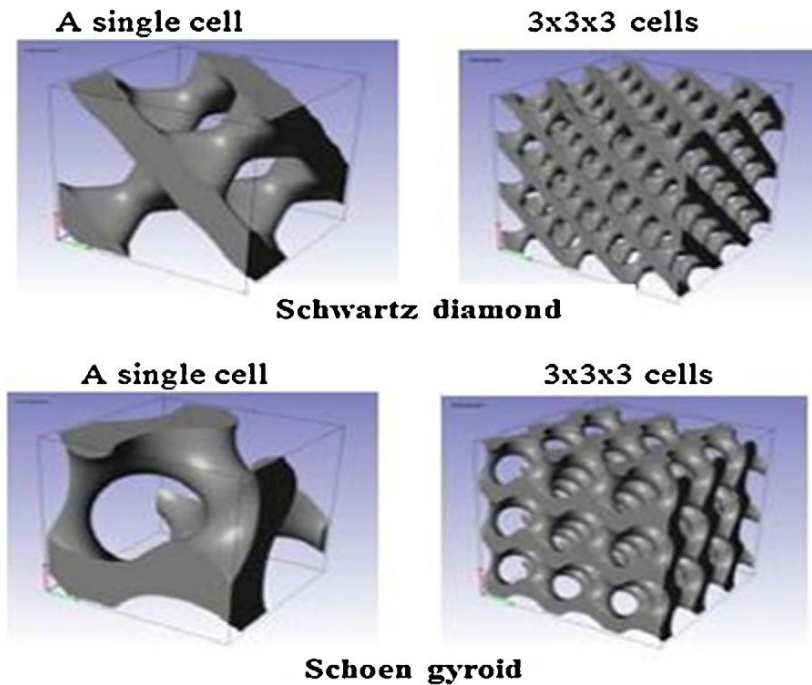


Figure 19 Gyroid and Diamond lattice support structures [70]

2.5.4.3 Metrics for an Optimum Support Strategy

The rule of thumb for good SLM support structure design is that it should be the minimum amount of supports which avoids the risk of fabrication failure. A good support design should also fulfil the following vital functions: restraining the part to a maximal amount of distortion and keeping the part from crashing into the blade, avoid breaking of the support structure, raise the part off the platform for easy removal, anchor the overhanging and floating sections introduced during the build to the platform, and strengthen thin and tall parts during the build to prevent them from bending by the forces of the powder wiper [70].

Too many supports increases the amount of material used and leads to an increase in difficulty for removing supports. The orientation of a part with respect to the primary build direction significantly affects support generation and removal [3]. The

selection of the orientation of the part should balance usage of support material, easy removal and least build time.

Orientation also affects which surface will be attached to the support structure and the volume of support material. The surface with the lowest requirement for finish is a good option for the bottom surface since the surface attached to the support structure will have poor surface finish after removal of the support structure. So a good support strategy should also avoid interfering with key geometrical features. Complex parts with features like channels, holes, and overhanging structures need careful support structure design and modification to make sure these are successfully built in SLM.

2.5.5 Support Structure Optimization Design

2.5.5.1 Support Structure Orientation

A multi-objective function can be used to optimize the number of layers, volume and contact-area of support structures as well as build time, and surface finish. An expert system-based method has been developed to select the optimal building direction [73]. In another paper, several efficient geometric algorithms were developed to solve this multi-criteria problem and find the optimal build orientation [74].

An algorithm has been developed to determine the optimal orientation when the part will have maximal tensile strength and was tested in a tensile bar experiment [75]. The calculated results from the developed algorithm were validated experimentally. The experiment showed that optimum part orientation for Polyamide tensile specimens is for rotation with respect to the X, Y and Z-axes of 90° , 45° and 90° respectively. A multi-objective criteria decision making method was suggested as future work for including surface finish and build time optimization in the model.

A preliminary design rule for selecting the build angle and process parameters for fabricating parts with overhanging surfaces in SLM was developed [11]. The critical angle is defined when the inclined angle is smaller than the critical angle for which the overhanging surface will warp more easily. A large inclined angle means the overhanging surface length is long. The overhanging surface has to be smaller than the beam radius in order to guarantee a high quality overhanging surface. The inclined angle can be decided using the theoretical formula derived from overhanging surfaces for the staircase effect. The build orientation of the part has been studied to reduce the need for manually-added supports, especially for production of complex parts with overhanging surfaces. By adjusting a part's orientation, the inclined angle for overhanging surfaces can be altered as well and the important surfaces can be built without manual support so as to improve the surface finish. Therefore, the manual support can be shifted to other surfaces which are less important overall.

2.5.5.2 Support Structure Topology Minimization

The potential for using cellular support structures with a low volume fraction to reduce the volume of support material and build time in SLM has been investigated [70, 76]. Two types of cellular structures, Schoen gyroid and Schwartz diamond, were tested and experimental results show that they can be used as support structures in SLM.

A new approach using an implicit mathematical function to generate cellular structures has been developed [77]. The approach is able to optimize the build direction and create a cellular support structure with minimal support material.

A specific component segmentation strategy has been developed to minimize the support structure based on the method of Design of Experiment (DoE) [71]. The part is

divided into critical and non-critical areas first and critical areas are scanned with a specific appropriate energy input and optimized supporting strategies. The method of DoE is applied to find the optimum value for three normalized process parameters. There will be connected layers between the support structure and part. A special lattice support structure with optimized connected layers was applied for building the supported overhang and unsupported overhang structure (angle between part and horizontal less than 20 °) in the experiment. The experiment was conducted in a Concept Laser M2 SLM machine. Results show that supports can generally be reduced by using this specific component segmentation strategy.

2.5.6 Support Structures in Thermal Modeling

A T-shaped cantilever model was built in ANSYS and the support structure for the cantilever was modeled as small pillars in a FEM model to simulate the temperature and thermal stress in SLM [10].

The influence of support structure parameters such as supporting lattice distance on the thermal stress has been analyzed in a similar model [59]. Rather than considering the real geometry of block supports, the support structure is defined as a continuum model. However, its material properties have been adjusted according to the developed and qualified method [10]. A tool steel twin-cantilever structure with dimensions of 70x15x12mm was modeled. Two block structures support the wings of the cantilever part with dimensions of 30x15x8mm. The neutron diffraction method was used to measure the thermal stress and verify the simulation results. What is more, the thermal stress relaxation of the cantilever geometry after cutting the support structure has been achieved in another FEM model.

Another continuum-mechanical FEM model has been built to optimize support structures in ANSYS [60, 78]. The block support structure is modeled as a $2\frac{1}{2}$ dimensional shell element in the FEM model. Contact elements are used to couple the substrate-support structure and support structure-part respectively to overcome the discontinuity of element alignment. An optimization procedure of fractal adaption of the support layout has been adopted to optimize the stiffness of the support structure according to the thermal stress calculated in the model. The unit cell for block supports is divided into two triangles and additional stiffening of each fractal triangle is updated if the average stress value of a cell is more than the total value of the whole support structure. A typical tilde geometry supported by block structures has been studied in the paper. Two optimization runs of support structure stiffening led to a reduction of thermal stress of about 72% which also resulted in an increase of 72% to solidified support volume.

Simulation results have been validated against experimental thermal stress measured using neutron diffraction [79]. Both tilde specimens with optimized and standard block support structures were fabricated in the experiment and several groups of experiments were carried out using different process parameters. The experimental results clearly show that the specimens with standard block supports have a higher stress level than the optimized support designed specimens.

2.6 Structural optimization design

2.6.1 Structural Optimization Design Methods

Structural optimization is the minimization of mass by varying or determining dimensional variables such as shape parameters in the classical sense [80]. The first

known attempt to seek the optimal shape of structural elements via a mathematical formulation for shape minimization dates back to Galileo [80, 81]. Substantial efforts have been made in the development of optimization procedures and strategies since then. The classical geometrical optimization problem by changing the size of the shape cannot change the topology during the solution searching process. However, the so called topological optimization design in literature can change the layout of the structure and result in a new topology during the optimization process [82].

The general structural optimization problem can be formulated using the typical minimization equation with constraint equations [80].

$$\begin{aligned} \text{Minimize} \quad & f(\mathbf{x}) \\ \text{Subject to} \quad & g_i(\mathbf{x}) \geq 0 \quad i = 1 \text{ to } n_g \\ & h_j(\mathbf{x}) = 0 \quad j = 1 \text{ to } n_h \end{aligned}$$

where \mathbf{x} is a vector of design variables with certain boundaries, $f(\mathbf{x})$ is the objective function, and $g_i(\mathbf{x})$ and $h_j(\mathbf{x})$ are constraint equations.

Mathematical programming methods are applied to solve the equations above. The optimal solution searching procedure generally starts with an initial design and proceeds with small steps intended to improve the objective function. The searching process ends when no more significant improvement can be made to the objective function. Discretization modeling such as FEM are commonly used in the optimization problem when an analytical solution is not available. FEM is utilized to calculate the magnitudes of stress and displacement in order to evaluate the objective function, and Figure 20 shows the flow chart of a typical optimization problem.

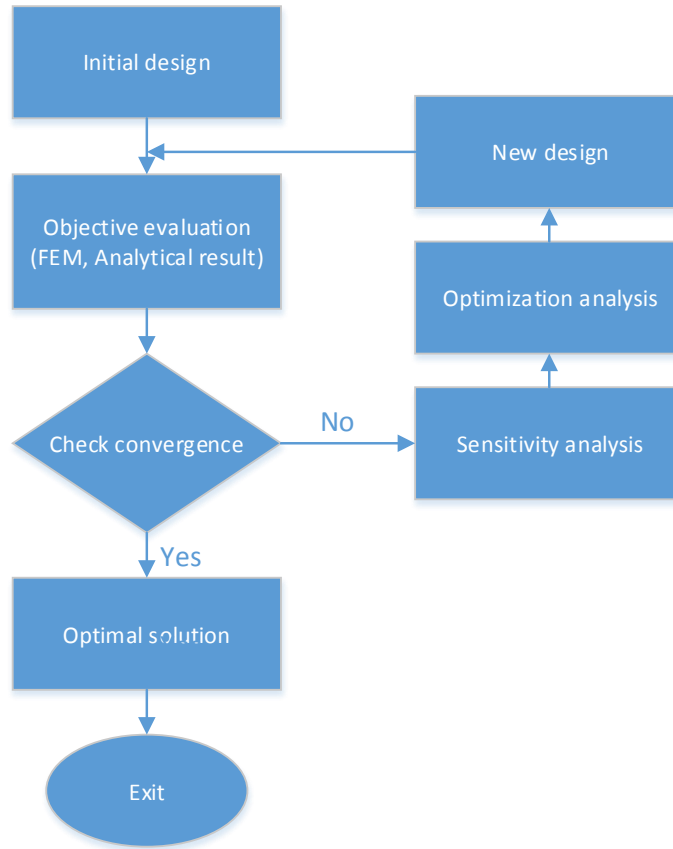


Figure 20 Typical optimization design flow chart

Geometrical optimization design

Traditional structural optimization requires the explicit definition of optimization parameters which are dependent variables to be optimized such as thickness and length of the structure [83]. The maximization of static stiffness subject to a volume constraint is a classical problem in structural design. The objective function of such types of problems can be evaluated by an analytical solution or FEM without mesh changing.

Topological optimization design

Unlike traditional structural optimization, topological optimization does not require the definition of design variables. In topological optimization, the material distribution function over a body serves as optimization parameters [83]. Since topology

is modified in the optimization procedure, if the mesh is still fixed at the one defined for the initial model, the finite elements are often distorted excessively, and then the continuity of the FEM model cannot maintain good quality. Adaptive remeshing strategies are needed in topological optimization design. However, there are also methods which don't consider the mesh of the topology in the literature.

The level set method coupled with the topological derivative can be applied to shape and topology optimization of structures [84-87]. The level set method is a numerical technique for tracking interface and shapes without having to parameterize the surface or curvature of these objects [88]. The stress for a cantilever structure bounded by three disjoint parts in a rectangular area under a single downward force is minimized by only considering the linear elasticity of material [84]. The main idea of topological optimization is to test the optimality of the domain by removing a small hole with appropriate boundary conditions by taking advantage of the level set method. A cantilever structure, L-beam, gripping mechanism and 3-D mast are tested in papers based on this method [84-87].

Homogenization can be used in topological optimization of a continuous field in order to overcome the instability of the numerical optimization method [89, 90]. Plane problems [90] and sensitivity analysis of a specific mesh have been tested to compute the homogenized elasticity tensor. The mean compliance of the structure is optimized as the objective function for the cantilever problem [89, 90].

A meshless analysis and independent density field interpolating method has been developed to study the geometrically nonlinear structure optimization problem[91]. The

method is able to overcome the convergence difficulties in large distortion problems. A center loaded planar structure was optimized as a case study.

2.6.2 Structural Optimization Design in Additive Manufacturing

The main challenges and opportunities for topology optimization in AM have been summarized [92]. According to the summary, the solid isotropic material with penalization approach (SIMP), bidirectional evolutionary structural optimization (BESO), homogenization, genetic algorithms and level set methods are the most commonly used methods in topological optimization. The paper concluded that geometrical complexity caused by topology optimization can decrease the cost of AM. There is a huge potential to use topological optimization in design of AM products and to minimize support structures [93].

A topology optimization tool was developed to design customized mesostructures in AM [94]. Homogenization and parametric smoothing functions are combined into the tool to represent material topology. The designed products using the tool were fabricated in SLS and material properties were tested.

A beam structure for AM technology was optimized using the principle stress lines method [95]. The results were compared to the homogenization and ground structure methods and showed that the method in the paper was much faster and easier to control.

2.7 Conclusions

Thermal modeling, scan pattern studies and support structure generation are three major focus areas for SLM. A predictable thermal model for SLM can play a critical role in better understanding and improving the efficiency of the process. The process of SLM

involves the moving of a laser beam across a powder bed to melt material layer by layer. However, this procedure is complicated to completely simulate accurately because of the multiscale nature of the problem. SLM uses very high laser intensity values, on the order of 10^{10} W/m², while the melt pool and Heat Affected Zone (HAZ) are several orders of magnitude smaller than the dimensions of the powder bed and part. Although many computational models have been developed to study temperature evolution in SLM, these models only either simulate a small part of the problem with a fine mesh or the entire problem using a coarse mesh to avoid the computational burdens of meshing the full problem in a really fine mesh. In order to accurately capture the details of temperature evolution anywhere in a full-sized part located anywhere in the build platform, new simulation tools are needed.

Laser scanning during metal laser sintering follows patterns developed by the various machine manufacturers. These types of patterns include, for example, parallel strips and chessboard scan strategies, such as those used in the popular EOS M270 metal laser sintering machines. Besides these, there are several types of scan patterns, which include single direction, bi-direction, traditional raster, island and their combinations. These are used in custom-developed SLM machines and experiments as well as in commercial variants. Variables related to scan strategy include input processing parameters such as hatch spacing, beam offset and scanning orientation, which critically affect thermal deformation predictions. Since thermal behavior is inhomogeneous during SLM, the scan pattern should be generated in such a fashion that the anticipated average thermal accumulation of thermal stress should be minimized. A better understanding of the influence of scan pattern in the SLM process is needed. Through the literature review,

a majority of scan pattern studies have been done using experiments and there are few studies performed using simulation tools.

A support structure is used to support a part in SLM in order to reduce deformation while providing convenient ways to remove the part from the build plate during post-processing. The support structures generated by support generation modules of AM specific design software such as Magics are geometry and pattern driven and do not place support structures based upon any knowledge of the thermal stresses generated during metal powder bed fusion processes. Thus, support structure generation becomes a trial and error process driven primarily by a user's experience with similar geometries. Support structure optimization is an area of great interest to AM researchers and designers. Most research has focused on geometrical design without considering the constraints of thermal stress and deformation. The minimization of the volume/mass and orientation of the support structure have been studied in the literature. There are few studies relevant to support structure design when considering thermal stress in SLM.

The field of structural optimization design is studied extensively and many theories are well established. Some work has focused on using structural design theories to optimize the topology of AM parts to reduce weight. There is a huge potential for using optimization design in AM in the future by taking advantage of powerful simulation tools.

CHAPTER 3 RESEARCH OBJECTIVE AND DESSERTATION FORMAT

3.1 Research Objective

According to the literature review, there is no existing powerful simulation tool which is able to accurately simulate the SLM process taking into consideration real scan patterns within a reasonable amount of computational time. What's more, support structures have not been an area of major interest in SLM simulation. Since the geometry of the support structure can be complex, simulation of the SLM process with detailed support structures increases computational time and resources. However, supports have a critical impact on the SLM fabricated part. In order to mitigate these problems, the following research objectives were proposed.

Objective 1: Scan pattern generation module development

A scan pattern generation module capable of providing various real scan patterns to the 3DSIM simulation environment will be developed. The scan pattern generation module will have the function of creating scan patterns for each layer directly from the slice file information (such as *CLI). Scan patterns used in common commercial systems, including in particular an EOS M270 machine, will be included.

Objective 2: Dynamic moving mesh model development in ANSYS

A dynamic moving mesh model will be developed using similar mesh strategies to those being developed by 3DSIM based upon prior work at the University of Louisville. The heat transfer, heat convection, material nonlinearity and phase changes

will be considered in the model. The model will be able to simulate the global temperature distribution of the SLM process with a moving laser heat source.

Objective 3: 3DSIM against ANSYS Benchmark

By using the dynamic moving mesh model developed in ANSYS, a validation of the thermal results of 3DSIM with respect to accuracy and computational behavior will be studied by applying the same parameters and inputs in both models.

Objective 4: Formulation of effective thermal conductivity for simplified modeling of support structures

In order to consider the influence of support structures on the thermal field in the thermal model, an effective thermal conductivity model will be developed. The model will reduce the computational complexity caused by the inhomogeneous material properties of the support structure. A homogeneous method combined with a representative volume element (RVE) is used to study the effective thermal conductivity.

Objective 5: Support structure optimization and design framework development

A support structure optimization and design framework will be developed. The tool will generate support structures with the minimum volume/mass needed for a given part orientation to meet a set of user-specified constraint conditions. A linear programming model will be formulated with constraint conditions includes the ability to specify maximum allowable distortion in X, Y and Z axes. The minimum volume/mass will be computed based upon the amount of support structure needed to satisfy the constraint equations for a computed thermal stress pattern resulting from a user-specified combination of process parameters, material, support structure geometry/type and scan pattern. Both analytical solutions and FEM will be applied to design the support

structure. The tool will be capable of comparing the effects of part orientation on support volume, build time, and thermal stress to enable future multi-objective optimization experiments to be conducted.

Objective 6: Experiments to investigate block support structures for Ti64

Experiments will be carried out to investigate the block support structure behavior for Ti64 in an EOS M270 machine. A threshold for support structure parameters will be explored by fabrication of two part geometries: 40x5x2mm and 20x20x2mm.

3.2 Dissertation Format

This dissertation is written in the multi-paper format. Four papers are presented which implement the identified objectives, present the methodologies and discuss the results.

Chapter 4 is modified from a paper presented in the Solid Freeform Fabrication Symposium (2013). A scan pattern generation tool has been implemented in this chapter.

Chapter 5 is a combination of two papers. One was published in Materials Science and Technology (2014) and the other was presented in the Solid Freeform Fabrication Symposium (2014). The dynamic moving mesh model has been developed in ANSYS and the 3DSIM is benchmarked against the ANSYS model.

Chapter 6 is a paper published in Additive Manufacturing (2015). It explores the effective thermal conductivity of the support structure.

Chapter 7 is prepared as a future Journal paper. It describes the methodologies applied to develop the framework for support structure design and optimization.

Chapter 8 is also prepared as a future Journal paper. It investigates the support structure design for two specific parts with Ti64 in the EOS M270.

Chapter 9 summarizes the work and future work is also proposed.

CHAPTER 4 SCAN PATTERN GENERATION

4.1 Introduction

Scan related parameters, which includes scan speed, scan spacing and scan pattern, is one of the four categories of laser parameters in for the metal laser sintering process [3]. Figure 21 shows a typical flow chart of operations for a metal laser sintering machine such as an EOS M 270. The STL files for both part and support structure are sliced using a pre-defined slicing library which has layer parameters such as layer thickness for a specific material and machine. Typical metal laser sintering machines are is able to import SLI as the layered file format. In the meanwhile, all the laser and scan parameters are set up in the machine. The scan pattern can consist of contour, inner filling, upskin and downskin scan strategies. What is more, the scan strategy for the support structure and part are different. The default support structure, such as a block support structure in an EOS machine, is scanned as a thin wall structure and each wall is scanned only once in the two perpendicular directions every other layer. The part, in contrast to the supports, is usually scanned using a raster strategy and the part contour is scanned several times followed by a filling scan. A downskin strategy is applied to the layers where part and support structure connect and overlap. An upskin strategy is used to improve the surface finish of upward-facing layers of the part. Scan pattern variations have a large influence on the results of part fabrication.

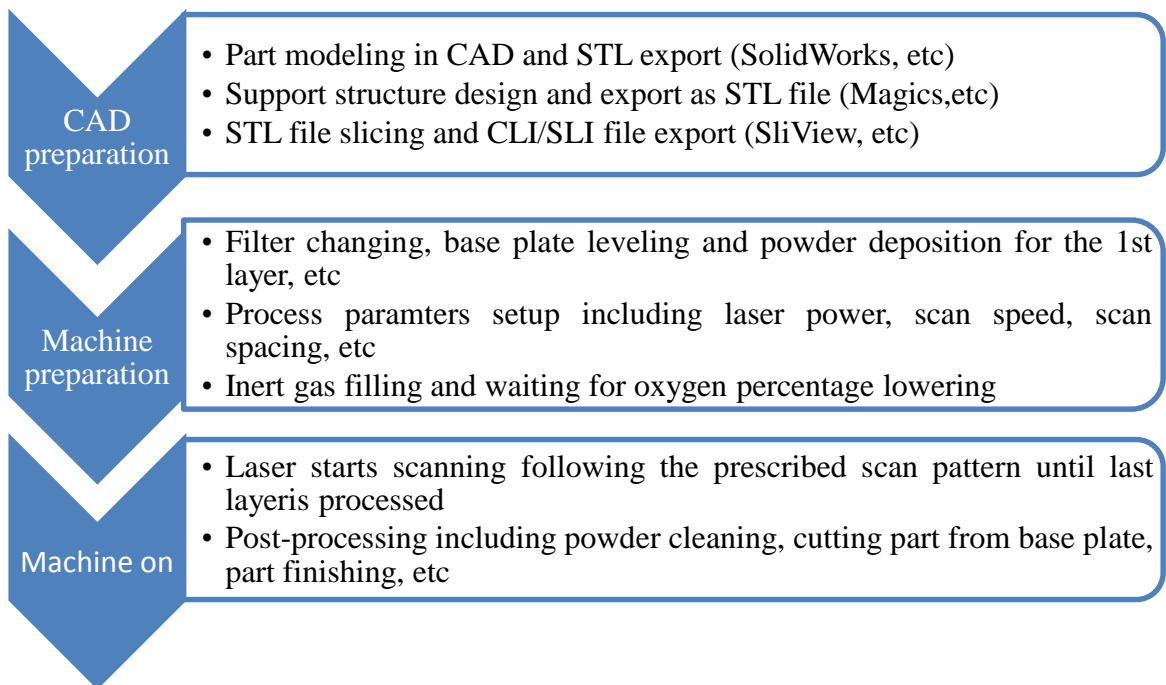


Figure 21 Steps of operation for a typical metal laser sintering machine

Laser scanning along the path of the scan pattern involves accumulation and dissipation of heat. The scan pattern has a critical impact on heat accumulation and dissipation during processing. The powder is melted and consolidated when the laser passes a region, resulting in material property transformations and phase changes within the material. If the laser scanning length is too small, an over-accumulation of heat causes very large thermal gradients so as to cause additional thermal stress. What is more, the microstructure is also dependent on the thermal gradient and porosity within the part can become worse when the scan spacing between adjacent scan vectors is too large.

Geometrical inaccuracy is induced by bad design of scan patterns as well as bad slicing of STL files. Shrinkage and thermal stress-induced deformations are two key sources of defects in SLM which can be alleviated by better design of scan patterns. To

accurately predict process outcomes, it is critical to simulate the SLM process using the exact same scan pattern as those used during the fabrication process.

In most AM processes the CAD model is represented by an STL file which is sliced into layers thereafter. The Common Layer Interface (CLI) and StereoLithography Interface (SLI) files are two layer file formats which store the sliced layer information. This chapter starts with introduction of various CAD file formats and geometrical modeling theories. Reverse engineering of the primary scan pattern used in an EOS machine is described as well as an introduction to CAD file formats.

4.2 STL File

4.2.1 STL Format

The STL file is used in nearly every AM technology today to represent the CAD model surface using triangles. The term STL was derived from STereoLithography, which was the first commercial AM technology from 3D Systems developed in the 1980s [3]. STL simply approximates the surface of the CAD model using triangles. The number of triangles is controlled by the maximal size of the triangle, such as maximal length. The accuracy of the CAD surface approximation in an STL file depends on the choosing of maximal triangle size, which can be controlled in most commercial CAD software. Figure 23 is an example of an STL file for the hemisphere structure shown in Figure 22. Each triangle is defined by a unit normal vector and three vertex coordinates which are ordered using the right hand rule.

4.2.2 STL File Slicing

The intersection of a triangle and a plane is calculated using analytic geometry theory which is widely used in computer graphics and collision detection such as ray

tracing methods. The intersection of a triangle and a plane is determined by first deciding the relative position of the triangle's three vertices against the plane. Figure 24 [96] shows the triangle T intersecting with the plane V_0 in line I_1I_2 . The triangle and plane



Figure 22 Thick hemispherical dome structure

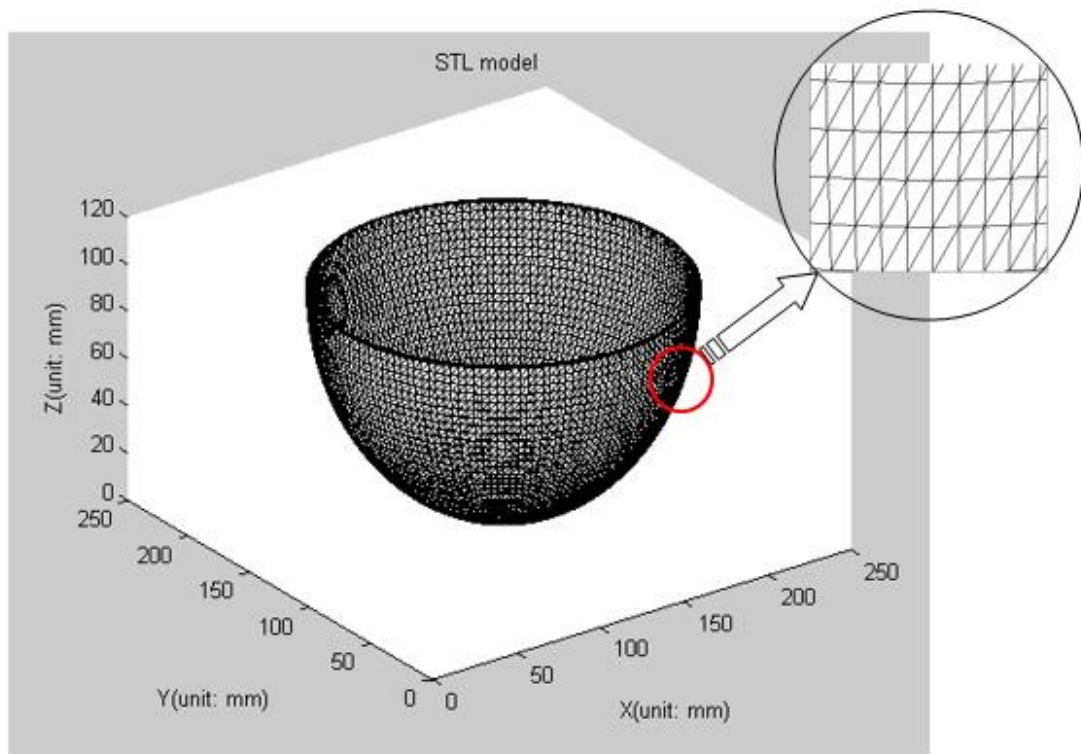


Figure 23 STL model of hemisphere

intersection problem will be converted to line and plane intersection scenarios eventually.

Line P_1P_0 and P_2P_0 clearly intersect the plane. However, the distance of a point to a plane

must be used to determine that P_1 and P_2 are on one side of V_0 and P_0 is on the other side. As shown in Figure 25, $P_0 = (x_0, y_0, z_0)$ is a random point, plane φ is described by $a*x + b*y + c*z + d = 0$. The distance from point P_0 to plane φ is calculated using equation (8).

$$d(P_0, \varphi) = |P_0 - V_0| \cos \theta = \frac{ax + by + cz + d}{\sqrt{a^2 + b^2 + c^2}} \quad (8)$$

The distance $d(P_0, \varphi)$ is a signed value. For the three vertices in a triangle, positive multiplying of either one of the two distances means those two vertices are on the same side of a plane.

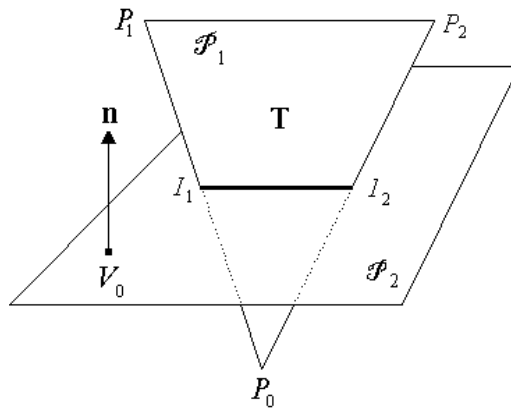


Figure 24 Intersection of triangles and plane [96]

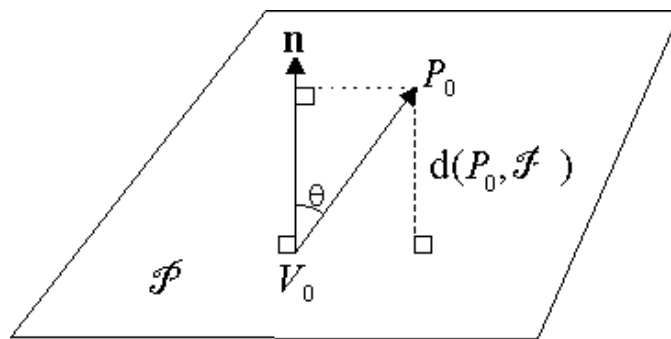


Figure 25 Distance of point to plane [96]

4.3 Sliced File

4.3.1 CLI File

CLI is short for Common Layer Interface which is a file format developed to be the interface between sliced information (such as medical scan data) and additive manufacturing machines. There are two types of CLI files: Binary and ASCII. Both of their formats are well documented [97]. The CLI file is a 2½ dimension (2½D) representation of a model. Layers are cut intermittently along the Z direction by slicing using a plane which is parallel to the XY plane of a right hand Cartesian coordinate system. A layer is the volume between two parallel slices which are represented by a contour and depth (layer thickness). Each contour consists of coordinates of vertex points which are connected continuously as a polyline. Layers are sorted in ascending order with respect to the Z direction. In order to distinguish contours for exterior surfaces and interior surfaces, clockwise and counter clockwise point orders are used to describe internal and external contours respectively. As a result an original model's characteristics in the XY plane for each layer is almost fully kept; however, the Z dimension only has layer thickness information, which is why CLI is a 2½D representation of a model.

4.3.2 CLI and SLI Comparison

CLI and SLI file format are commonly used to represent the layer information for sliced STL models. Sliced files have the contour information of each layer which includes the points' coordinates, orientation information to distinguish the inner and exterior contours, layer thickness and number, and hatches filling the contour. Different machine manufactures use different slicing strategies and file formats which increase difficulties for file exchange. Even though each file format has unique ways to represent and store the model information, the data is supposed to be the same regardless of file format. Take the EOS machine, for example; the SLI file format is the default input file

format in the EOS software. Although the SLI file format has no public and standard description of its format and structure, a CLI file has an open format and standards which makes it convenient for researchers to use. CLI permits access to the detailed layer information and it was posited that CLI file information could help us understand the proprietary SLI file. The main question to answer thus became whether the CLI and SLI files have the same information for the same model. In order to test this, the template matching method was adopted to answer this question.

4.3.3 Template Matching Method

Since there is no way to directly access the SLI file, a comparison of a snapshot of the layers produced by EOS software with CLI layers enable one to understand if they are comparable. The steps used in this comparison are as follows: input and display the same layer of the SLI and CLI file in CAD software; screenshot the images of the layer; make one of the pictures the template and calculate the normalized correlation coefficient of the other picture compared to the template.

Template matching is used to match the two images by calculating the normalized correlation coefficient. The correlation coefficient is described in equation (9)

$$\rho_{X,Y} = \frac{cov(X,Y)}{\sigma_X\sigma_Y} = \frac{E[(X - \mu_X)(Y - \mu_Y)]}{\sigma_X\sigma_Y} \quad (9)$$

Where

- $\mu_X, \mu_Y, \sigma_X, \sigma_Y$ are the mean and variance of X and Y respectively

The normalized correlation coefficient is showing in equation (10).

$$\gamma(u,v) = \frac{\sum_{x,y}[f(x,y) - \bar{f}_{u,v}][t(x-u,y-v) - \bar{t}]}{\left\{\sum_{x,y}[f(x,y) - \bar{f}_{u,v}]^2 \sum_{x,y}[t(x-u,y-v) - \bar{t}]^2\right\}^{0.5}} \quad (10)$$

Where

- f is the image
- \bar{t} is the mean of the template
- $\bar{f}_{u,v}$ is the mean of $f(x,y)$ in the region under the template

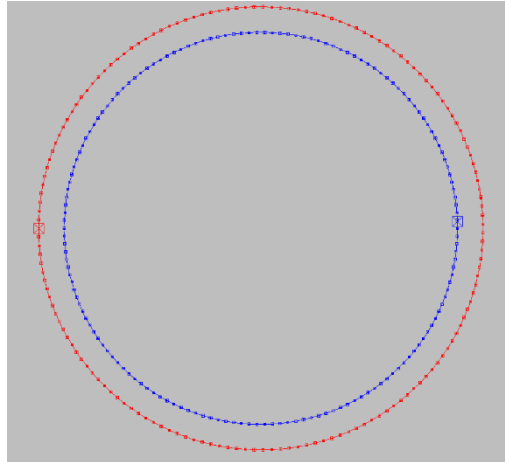


Figure 26 Points in the cross section of 200th layer from CLI file

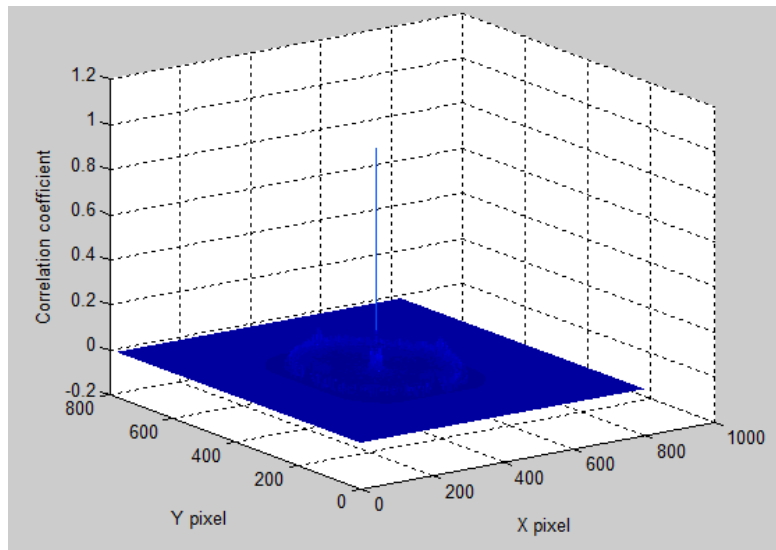


Figure 27 Correlation between two cross-sections corresponding to CLI and SLI

4.3.4 Example

Figure 26 shows the points in the cross section of 200th layer of the hemisphere structure shown in Figure 23. Pictures of the same cross section from the CLI and SLI files were captured. The normalized correlation coefficient of these two pictures is shown in Figure 27. The maximum of the correlation coefficient is 1 which means the two pictures are identical.

4.4 Scan Pattern

4.4.1 Introduction

The scan pattern and process parameters are key factors for understanding quality control in AM processes. Specific details including scanning orientation, hatch spacing, and beam offset are able to be extracted from the manufacturing process rather than assuming a certain pattern. Scan pattern plays an important role in thermal evolution, and thus deformation. By using the actual scan pattern rather than assumed pattern, the thermal model can produce more reliable simulation results.

A laser beam is usually given some dimensional shape, such as a Gaussian distribution. As shown in Figure 28 [98], the laser beam moves in a pattern which has a hatch spacing and velocity. In order to reduce the dimensional error, a beam offset is used to account for the effective diameter of the laser beam. When the laser scans the boundary, it will increase the dimension of the part by half of the beam's diameter. So the boundary contour is shifted towards the inside of the part by the radius of the beam to compensate for dimensional error.

The scan pattern shown in Figure 28 is the traditional raster pattern with scan lines parallel to the boundary. However, commercial AM machines usually scan parts in patches. Figure 29 is a real scan pattern picture taken from the EOS machine. Red lines

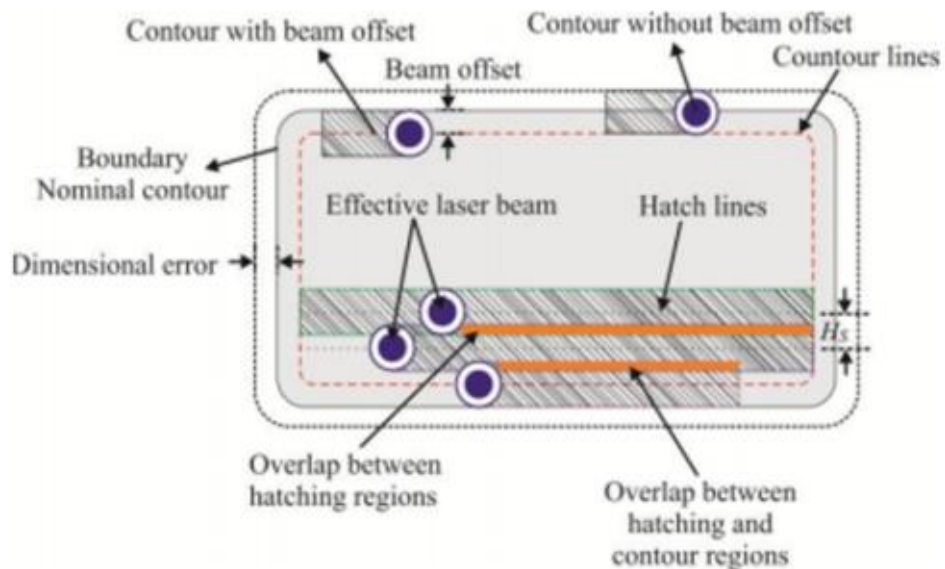
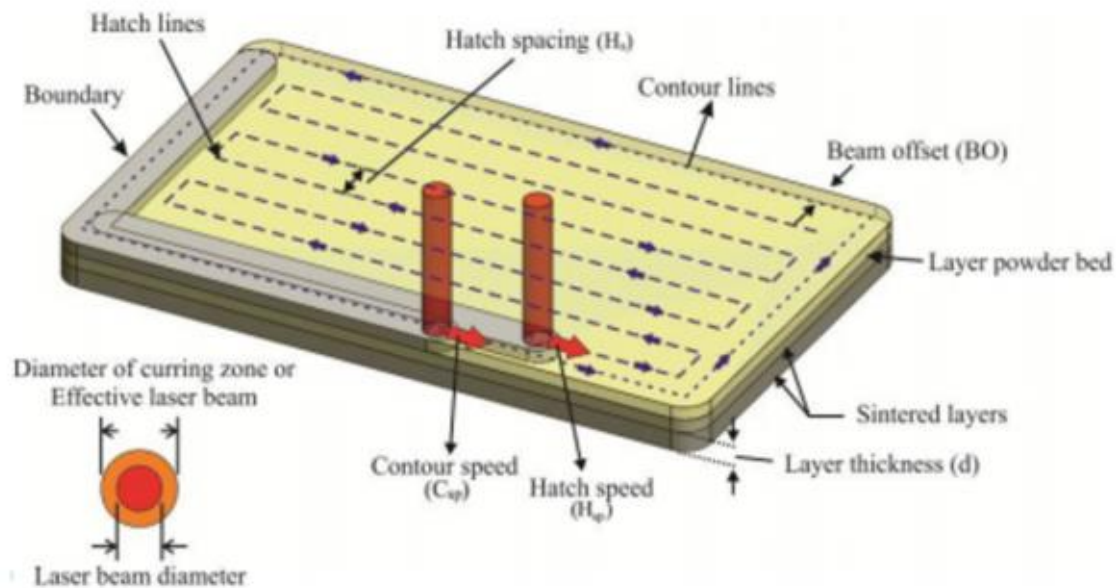


Figure 28 Exposure strategy and process parameters [98]

in the picture are the boundary contours and green lines represent scan lines. From the picture, the scan line is not parallel to either of the boundaries. The discontinuous 'bold lines' are actually junctions of the scan lines in adjacent patches. The 'bold lines' are an illusion of those junctions and 'lines' do not actually exist. The upper picture in Figure 29 indicates there are four strips which are scanned independently. The lower picture is a

magnification of the corner of the upper picture. Hatch spacing, beam offset and scan lines are shown in the picture.

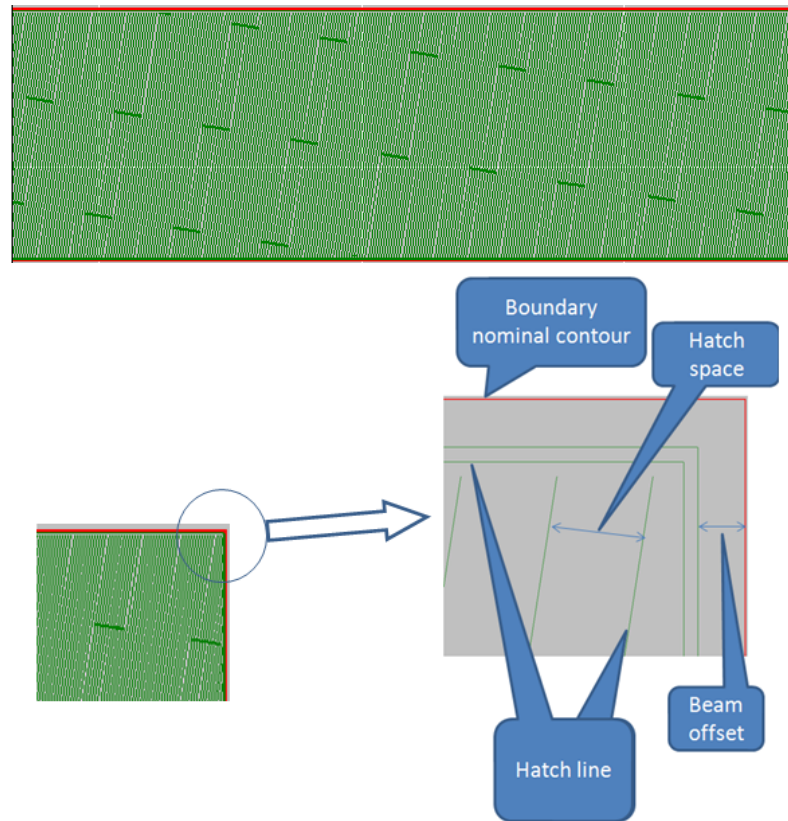


Figure 29 Real scan pattern from AM machine

4.4.2 Reverse Engineering of the Scan Pattern

4.4.2.1 Line Detection: Hough Transform

In order to extract the quantitative scan pattern from the pictures taken from an AM machine, the Hough transform line detection method can be used. It is well known that a straight line can be described using Equation (11) in Cartesian coordinates.

$$y = ax + b \tag{11}$$

The slope 'a' and intercept 'b' can characterize an equation. However, when the line is parallel to the Y axis, the slope a approaches infinity. The line in polar coordinates can avoid this problem which is shown in Equation (12). The line we see in Cartesian coordinates is a point in the polar coordinate as shown in Figure 30. What is more, one point (x, y) in the Cartesian coordinate gives a sinusoid in Polar Coordinates as shown in Figure 31. A number of m collinear points lying on the line will give the same number of sinusoidal curves which intersect at the same point in Polar coordinates. The idea of the Hough transform is to discretize the (ρ , θ) domain shown in Equation (12) and find the local point which has the maximal intersects.

$$\rho = x \cos \theta + y \sin \theta \quad (12)$$

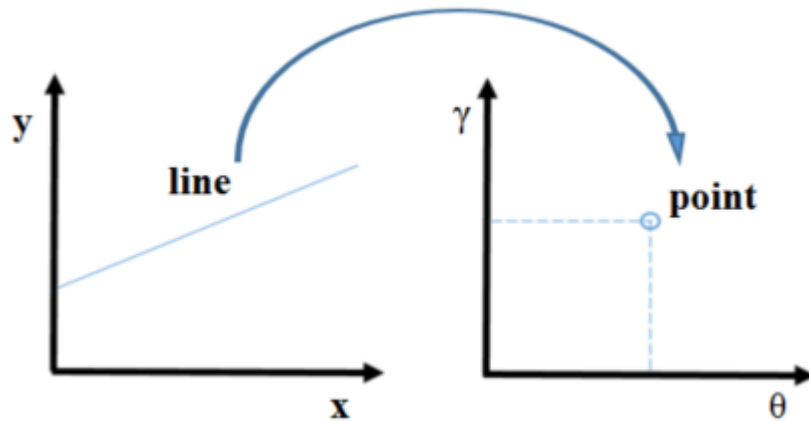


Figure 30 Line representation in Cartesian (left) and Polar (right) coordinates

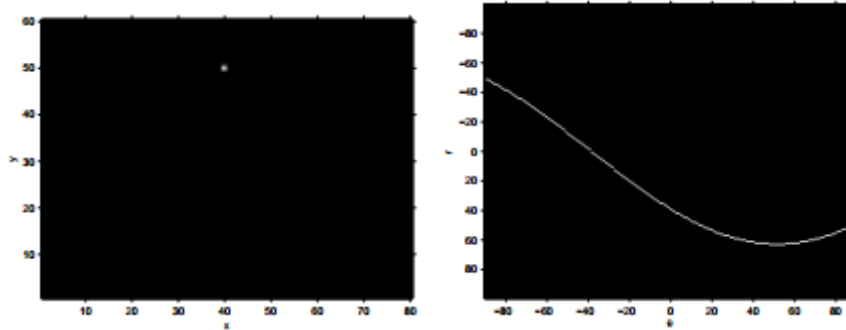


Figure 31 Point in Cartesian (left) and Polar (right) coordinates

According to the Hough transform line detection method, the scan pattern from one of the pictures snapshotted from an EOS machine is shown in Figure 32. The beam offset is 50 microns, the hatch spacing is 30 microns, and the patch distance is 5 millimeters. As shown in Figure 32, there are four scan patches/strips, and the laser scan through these four patches from 1 to 4. The laser beam will scan the boundary contour before and the inner scanning at the end to finish one layer. According to a recorded video, there will be a 12-14 seconds pause to allow the machine to bring down the platform and spread new powder.

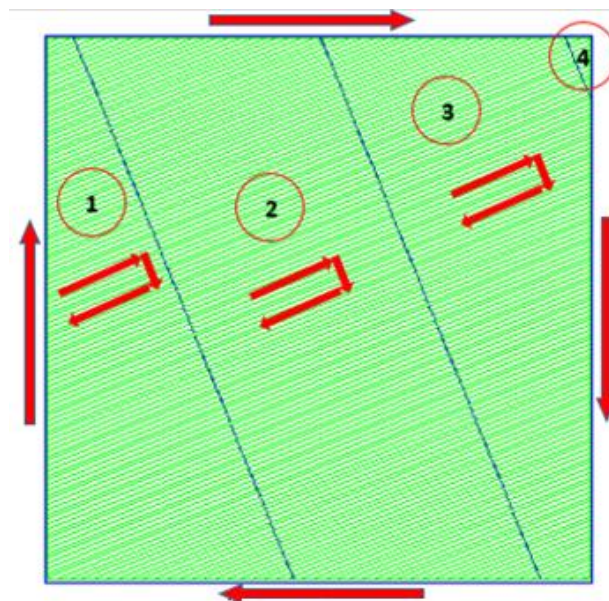


Figure 32 Scan pattern extracted from picture

4.4.2.2 Rotation Angle Estimation

It is observed that the scanning orientation is rotated a certain angle in consecutive layers in an EOS machine. Eleven consecutive layers of rotation information were collected during fabrication and the scan angle with respect to the +X axis was calculated. Figure 33 is the plot of angle difference for two consecutive layers. The average and standard deviation of the angle difference was 66.914° and 1.129° . Further verification of this calculation is carried out using the angle difference between every 27 consecutive layers. The scanning orientation is supposed to be repeating with an angle difference of 9° in every 27 consecutive layers if the angle difference is around 67° . Figure 34 is the plot of angle difference between every 27 consecutive layers. The average angle difference is 9.037° and standard deviation is 0.702° which matches the assumption.

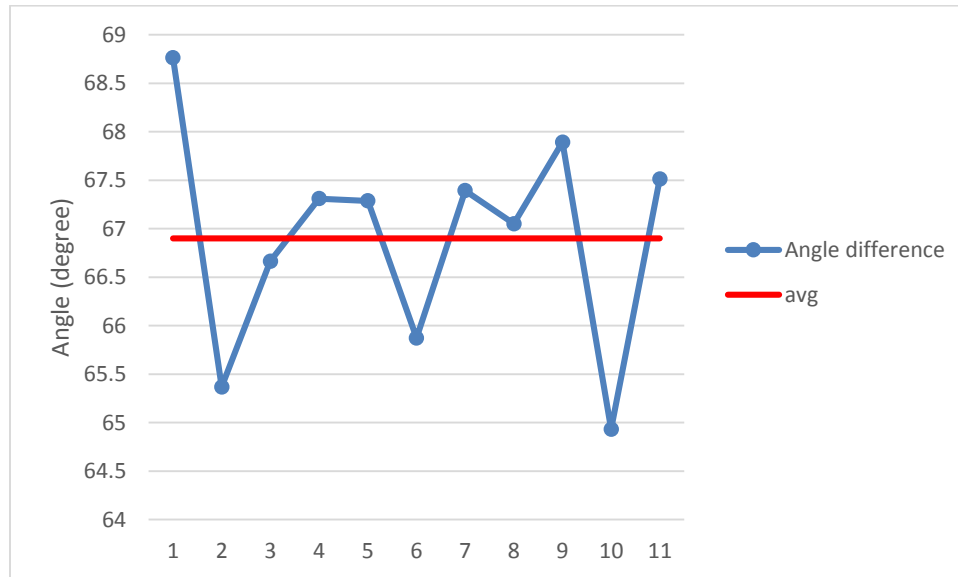


Figure 33 Angle difference between two consecutive layers

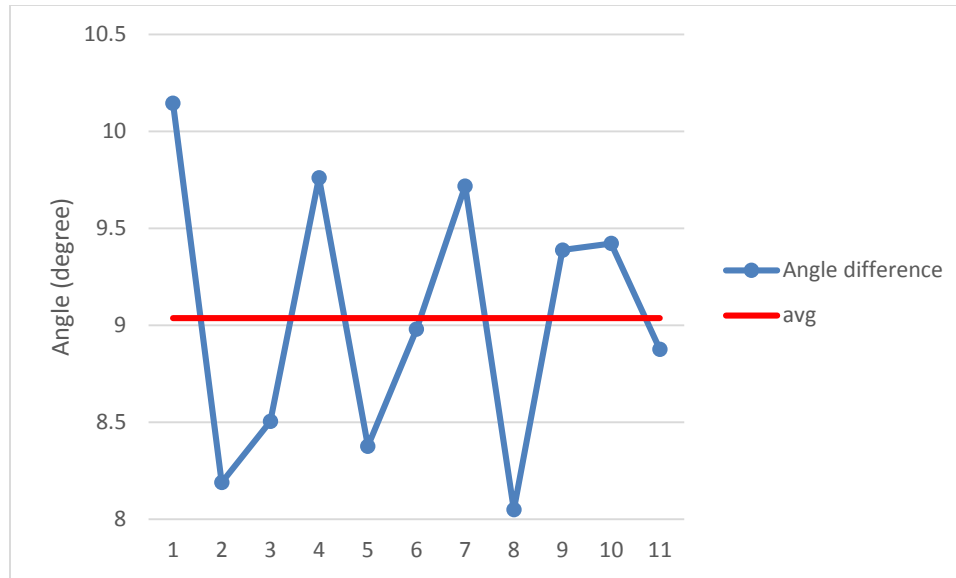


Figure 34 Angle difference every 27 layers

4.4.3 Other Scan Pattern Examples and Applications

Figure 35 (left) shows the raster scan strategy applied to a crescent structure and Figure 35 (right) shows the chessboard scan pattern. The part domain is divided into small square units in the chessboard scanning strategy. Each unit is scanned using a raster scan strategy in order to reduce the long scan path and thermal gradient especially for structures with large surface area per layer. The order of scanning each unit could be random or in sequence or using the rule of largest distance between the units.

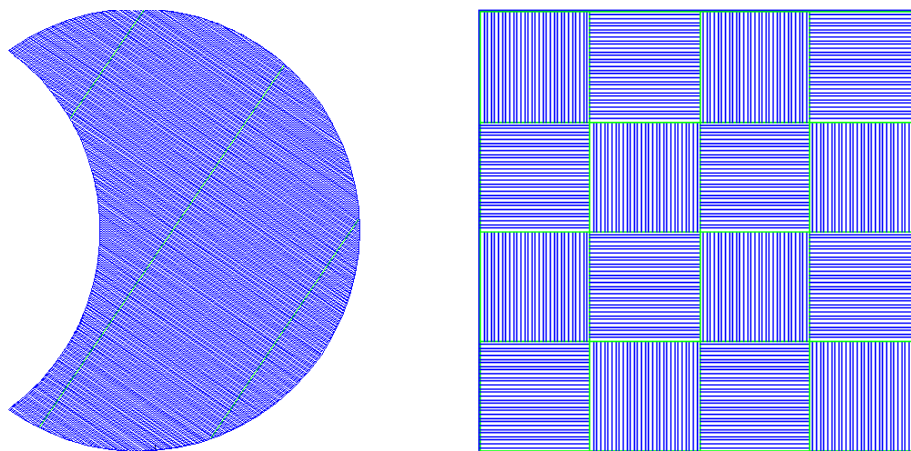


Figure 35 Scan pattern for a crescent structure and chessboard scan pattern

4.5 Conclusion

A methodology for generation of scan strategies which mimic actual build styles, including the scan orientation, scan space, scan pattern, etc, has been developed. Scan strategies were based upon a review of typical SLM process steps and empirical knowledge of scan strategies in SLM. An STL file is sliced into layers in a predefined layer thickness and there are two different slice file formats: CLI and SLI. The information stored in CLI and SLI files were compared and found to be fully correlated. The CLI file format was chosen for scan strategy generation since it has an open and standard format. The traditional raster scan strategy was reversed engineered from an EOS M270 machine based on a study of scanning orientation and scan pattern. The developed scan strategy generation tool is able to create accurate scan path information for simulation. Both traditional raster scan and other strategies such as chessboard are available in the tool. Future work should focus on exploring scan strategies in other SLM machines as well as new types of scan patterns.

CHAPTER 5 COMPARISON OF 3DSIM THERMAL MODELING OF SELECTIVE LASER MELTING USING A NEW DYNAMIC MESHING METHOD TO ANSYS

5.1 Introduction

Selective Laser Melting (SLM), also known as metal laser sintering, is a widely used Additive Manufacturing (AM) process, derived from Selective Laser Sintering (SLS) [13, 47]. SLM produces high density functional metal parts and tools. For achieving high density functional part fabrication, optimal process parameters are required such that the powder bed can melt and solidify while achieving the desired surface roughness, design geometry and mechanical properties. Poor parameter selection leads to distortion and defects, due to the thermal stresses which result from high thermal gradients. In order to avoid these defects, an experimental trial and error method is typically used across a range of process parameters. This is time-consuming and may not include all the process parameters of interest since these experiments are expensive. If a set of verified computational tools could be built to quickly test process parameter combinations, this would greatly aid in the optimization of SLM.

Various predictive models have been developed and applied to AM processes. Most of these studies used numerical methods such as the finite element method. Analytical solutions are typically not used as their derivation requires ignoring constraints/boundary mismatch and simplifying the model to be too simplistic for real problem sets. Numerical methods which take advantage of high performance computers can enable the inclusion of more realistic physics and boundary condition constraints at

ever increasing efficiencies, but current simulation tools still only enable very small problems to be solved.

Most SLM machines, such as the EOSINT M 270, focus the laser energy to a relatively small spot size of 100 μm with energy intensity values reaching $25\text{kW}/\text{mm}^2$ for a 200 W source [99]. The material thermal response to the heat source tracks the energy source as a function of both space and time. The powder exposed by the laser quickly heats up and then cools down due to the dynamics of the process. Heat dissipation is dependent on the thermal conductivity (which increases with temperature) of the previously solidified volume, previously solidified scan area lying next to the current scan track, the recently solidified portion of the current scan track, support structures and the base plate in the $-z$ direction from the melt pool. Regarding heat dissipation, multiple evolving solidification regions typically present simultaneously at various locations of the build, and generally the base plate thickness (~ 25.4 mm) is much greater than the layer thickness ($\sim 10\text{-}50$ μm), which can significantly affect heat dissipation and counteract the solidification related thermal stresses. Thus high energy intensity, short irradiation times and small melt pools along with metastable (usually diffusionless transformation) microstructures add sharp discontinuities to the non-linear temperature dependent thermal property curves (such as thermal conductivity, specific heat and density), making this a difficult and computationally expensive process to simulate. For the purpose of this study, discontinuities were smoothed to allow convergence of the ANSYS framework, and computational time was reduced using a multiscale mesh.

The concept of simultaneous coarse and fine meshing for the simulation of SLM processes using FEM has been shown in the literature [30, 36]. In these prior studies, the

fine mesh region remained stationary as a function of laser movement and the entire region of laser movement per layer has been fine meshed [44, 45]. However, the ability to move meshes as a function of laser movement in an efficient manner (with no renumbering of the fine mesh inscribed in its boundaries and intelligent matrix assembly) has not been illustrated until recently.

In this study, similar fine and coarse mesh motifs were used for the ANSYS model and the Matlab-based 3DSIM algorithms. Since intelligent matrix assembly [45, 100] is not possible in ANSYS, only the Matlab algorithms incorporated this aspect. Thus, the main objective of this paper is to study how the computational time to obtain accurate and efficient thermal solutions is affected by various types of meshing and matrix assembly methods. In specific, an ANSYS model was compared against the time for solving a similar model using Matlab-based algorithms that utilize intelligent matrix assembly and dynamic meshing. This dynamic mesh strategy is also compared against a uniform fine mesh model. Finally, simulation results were compared to experiments to ensure that the solution methodology is applicable to SLM.

5.2 Modeling

5.2.1 Thermal Phenomena in SLM

When the laser beam begins moving in SLM, the energy is transferred in four major ways: reflection, conduction, convection and radiation. Since metallic materials are lustrous in nature, a large part of the incident energy is reflected. Absorptivity depends on the material and powder morphology. Heat energy absorbed in the powder is subsequently conducted through surrounding previously solidified regions, the powder bed and/or the substrate. The ambient environment in SLM includes an inert gas such as

Argon or Nitrogen, which results in heat loss due to convection. Heat energy losses due to radiation also occur during SLM processing [18]. Heat reflection, conduction and convection are considered in this model. The radiation influence is ignored in this work since its influence is much smaller compared to other forms of heat loss based on conclusions from other literature [101-103].

5.2.2 Governing Equation and Boundary Conditions (BCs)

In SLM, the heat transfer process can be described using the Fourier thermal Equation (1) [22, 104]. The substrate is preheated to a certain temperature prior to fabrication (typically 353K in an EOS M270 machine). The prescribed temperature is described in Equation (2) as an initial condition of the problem. Heat convection between the powder bed surface and the surrounding environment is described using Equation (3). Since the bottom of the base plate is often controlled to a constant temperature, a fixed thermal boundary condition has been assumed at the bottom surface of the simulation domain which is shown in Equation (4). The x, y and z directions in the above-mentioned equations are oriented according to the ASTM F2921 standard for denoting directions inside an additive manufacturing machine.

5.2.3 Material Properties

In this paper, commonly used Ti-6Al-4V powder has been studied. Material properties such as λ , ρ and c are temperature dependent. The latent heat of fusion and vaporization are considered during phase changes. The values for thermo-physical properties such as density, thermal conductivity, enthalpy and heat capacity of Ti-6Al-4V have been adopted from existing literature values [105]. For the powder bed, a ratio is used to describe the difference between bulk and powder bed thermal conductivity. This

ratio for a powder bed of pure titanium with 30 μm diameter particles was reported to be 0.646 in one study [29] and 0.602 in another study [37]. In this model, the ratio of 0.602 has been used for simulation purposes.

5.2.4 Laser Beam Approximation

Laser beams profiles are generally approximated as Gaussian. The Gaussian mathematical form most widely used in the literature [3, 32, 33, 37, 106] is described in equations (5), (6) and (7) [14].

The laser power P and the laser beam radius r are two of the most important parameters to characterize the Gaussian model. SLM machines are able to focus the energy into a circular region with a diameter of $\sim 100\mu\text{m}$. In order to account for the fraction of energy which is absorbed, an absorptivity constant (α) is usually incorporated. For this study a value of 0.36 has been assumed [107].

5.2.5 Sensitivity Analysis of the Number of Elements in the HAZ

The accuracy and convergence of the finite element method depends on the fineness of the element [108]. For non-uniform heat flux, the maximum flux will influence the peak temperature and peak temperature will cause thermal phenomena like evaporation [107]. Figure 36 shows the convergence tendency comparing the number of element divisions in a laser beam to the maximal heat flux. The maximal heat flux converges with increasing number of division, but it varies greatly when the number of divisions is small. When a Gaussian distribution is applied in the model, the selection of the number of FEM element divisions in the heat flux input zone should be carefully

considered.

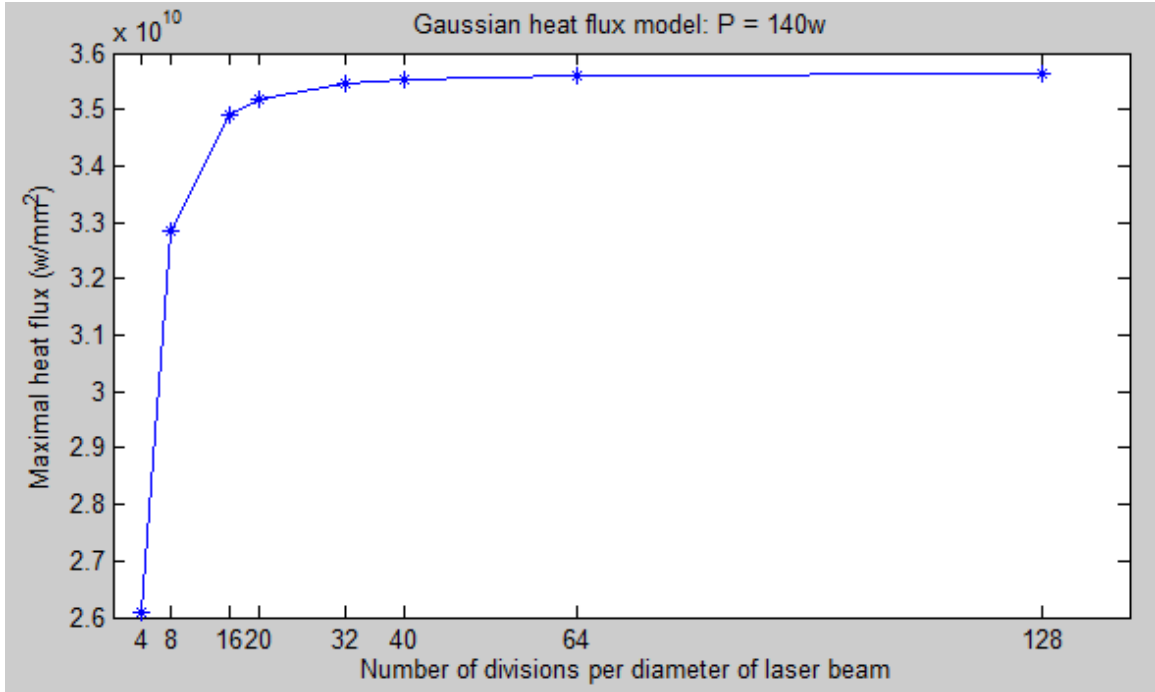


Figure 36 Influence of number of divisions to the maximal heat flux for a Gaussian heat source

5.2.6 Dynamic Meshing Method and ANSYS Techniques

The dynamic meshing method is beneficial for solving problems which require improved accuracy in a local region and reduced computational burden. There are a series of effective, mesh-adaptation-based approaches for numerically solving mathematical models of physical phenomena [40]. The commercial software ANSYS Fluent can apply dynamic and moving meshes for flows that change with time [109]. Besides ANSYS Fluent, the authors know of no other commercial tools which can fully simulate moving meshes for mechanics problems. ANSYS has the functionality for sub-modeling, which allows a user to interpolate results between different geometries. This functionality is adopted for the dynamic meshing model in ANSYS.

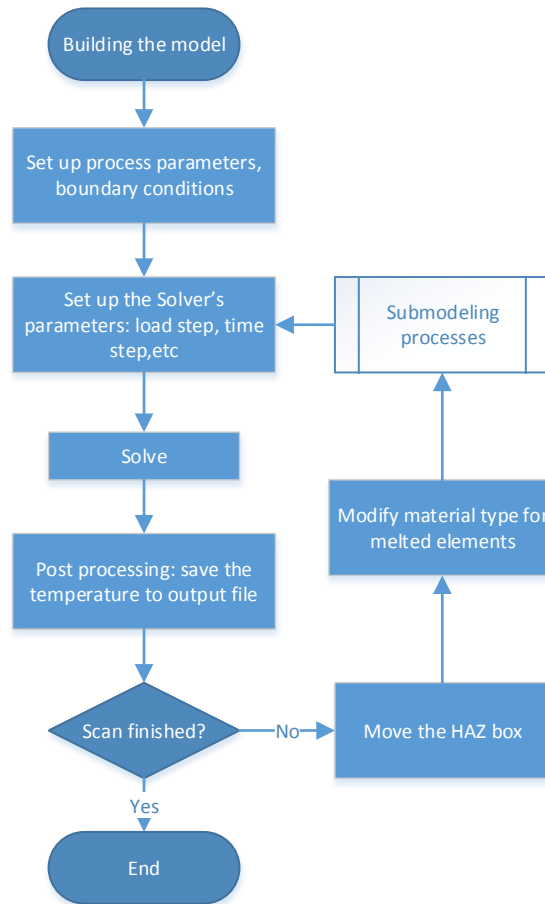


Figure 37 Flow chart for establishing the dynamic model

Figure 37 shows the flow chart for building this dynamic model in ANSYS. The flow chart starts with building the geometry model and setup of input process parameters. ANSYS has no functionality for automatically and smoothly connecting two load steps with geometry modification in between. In order to maintain this continuity, temperature interpolation has been used to keep the same boundary conditions for two different geometries. The temperature at the end of the former load step is loaded as the initial temperature of the next one. The loop for updating the geometry and interpolating the initial condition is shown in the flow chart. The sub-modeling module in the flow chart is responsible for the temperature interpolation and initial conditions establishment. Since

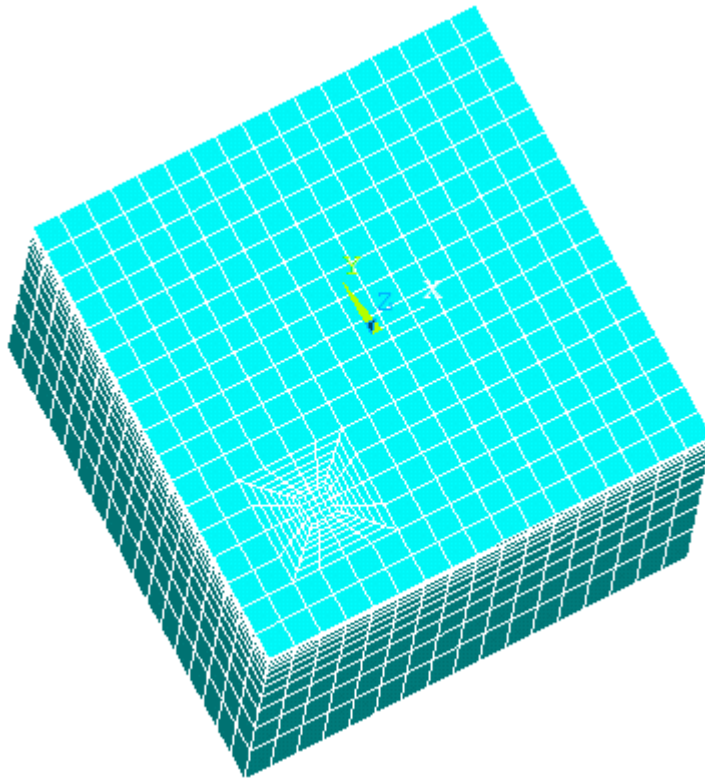
the modification of geometry in this model is flexible, the material types are able to be updated according to the element temperature at the end of each load step rather than using the element birth and death. The model ends when laser scanning is finished.

5.3 Results and Discussions

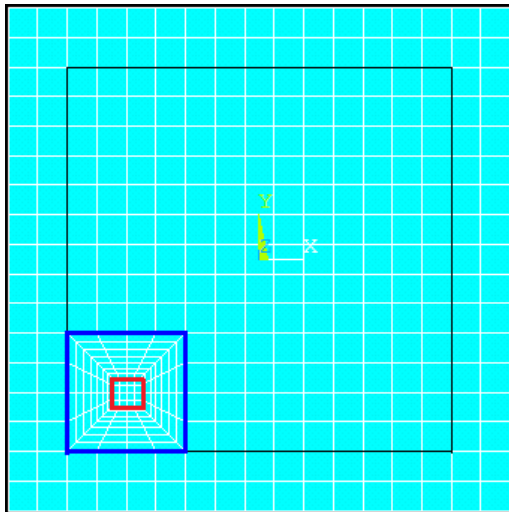
5.3.1 Single Time-Step Temperature Distribution Calculation

In order to verify the simulation results of the dynamic model, two cases were investigated. In the first case, the original thermal distribution before and the interpolated thermal distribution after fine mesh movement were compared. For the second case, the dynamic mesh thermal distribution was compared against its uniform mesh counterpart. These checks were performed to ensure that the thermal distributions converge to the same value.

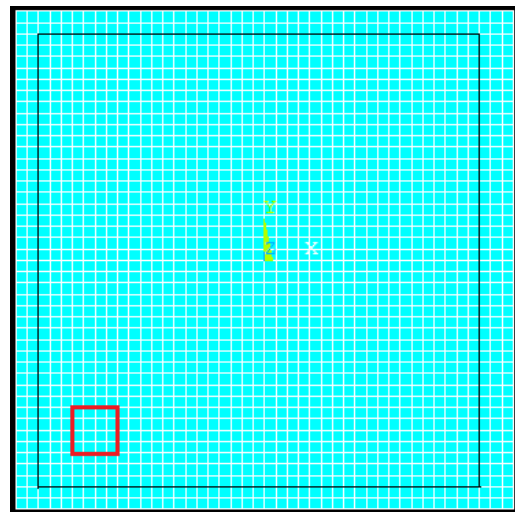
A three dimensional domain with a powder bed to beam diameter ratio of 10 has been modeled since the above-mentioned objectives are domain-size independent and a smaller domain largely reduces the computational complexity of storage, access, solution and post-processing of finite element stiffness matrices and forcing and response vectors. Figure 38 (a) shows a cubic domain with dimensions of $1 \times 1 \times 1$ mm. Figure 38 (b) shows the combined fine-coarse mesh of the top surface extruded in the z direction to arrive at a 3 Dimensional meshed domain. The laser beam diameter is assumed to be $100\mu\text{m}$ and it is accommodated within 4×4 elements marked using a red boundary in Figure 38 (b,c). The heat flux flowing into each element is calculated by integrating the Gaussian distribution over the element top surface. The inner black box shown in Figure 38 (b,c) represents the boundary of the part and the exterior black box represents the entire powder bed, which in this case has been assumed to be 1mm^2 in area. The blue box in the



(a) 3D dynamic mesh model



(b) Top surface of dynamic mesh model



(c) Top surface of uniform mesh model

Figure 38 Geometry of physical model

dynamic model (Figure 38 (b)) represents the HAZ, which is assumed to represent the thermal zone involving non-linear thermal effects. From the point of view of meshing, the region inscribed by the blue box also serves as a 'buffer' zone smoothly transitioning the highly dense mesh region close to the laser beam to a relatively coarser mesh surrounding it. This region is also beneficial for improving the accuracy and convergence of the solution by avoiding the coupling of two regions with different mesh densities.

Figure 39 shows the dynamic model results for temperature distribution in the first time step for laser scanning. A laser power of 140W and laser velocity of 1250mm/s were used to simulate temperature evolution in the model

5.3.2 Interpolation Results

An interpolation scheme has been applied for calculating the initial value thermal problem when the fine mesh is shifted by one coarse mesh spacing in the scan direction. The converged thermal solution at the final time step of the previous fine mesh location is posed as an initial thermal solution for the initial time step of the next fine mesh location. Thermal solutions are calculated for future time steps recursively based on the prior solution and continuous laser movement inside the current fine mesh location. The fine mesh moves by another coarse mesh spacing once the laser movement causes the melt pool effects to approach the boundary of the fine mesh box. Since the accuracy of the spatiotemporal thermal solution is a function of interpolation, these interpolations must not result in significant error accumulation and divergent thermal solutions. To check this, the peak temperature at the end of the previous fine mesh configuration has been compared with the initiation of the next fine mesh configuration. It has been found that the peak temperature is exactly the same before and after but the thermal distribution in

the X direction at the next fine mesh configuration varies from its previous fine mesh counterpart in the low temperature regime as shown in Figure 40 (a). The maximal variance in the thermal distribution of the Heat Affected Zone (HAZ), which is above 900K, is about 1%. Figure 40 (b) illustrates the temperature relative error in the Y direction. The small temperature variance during interpolation has a negligible effect on the overall solution outcome as these temperature errors do not accumulate and instead decay as the laser moves away from the newly solidified region.

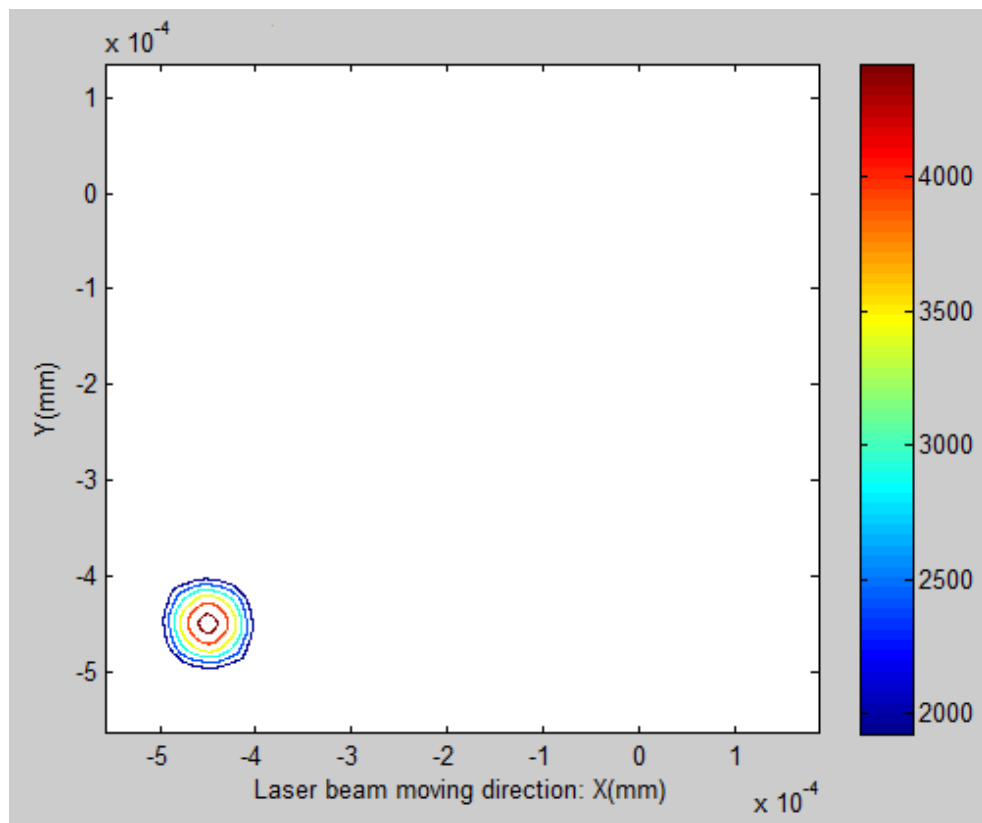
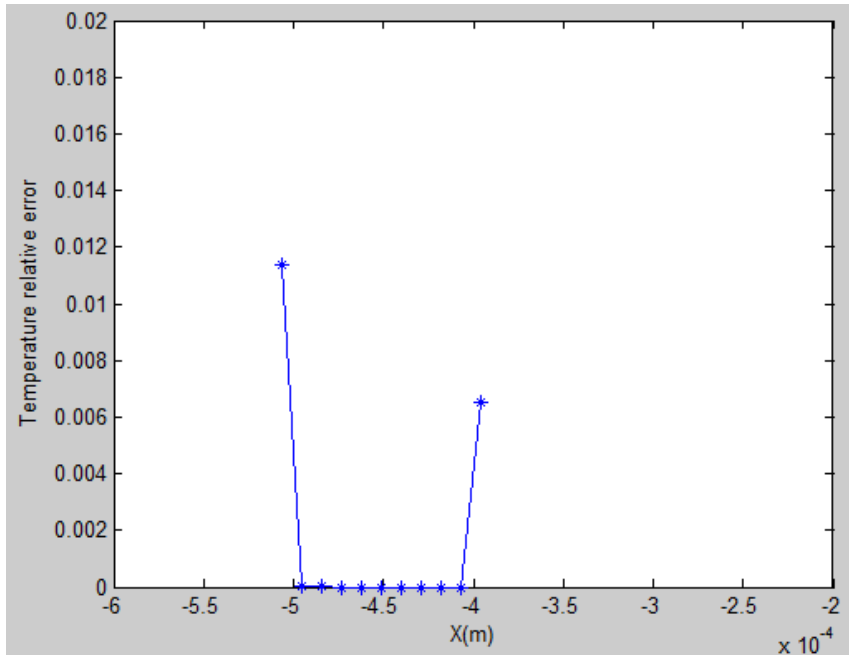
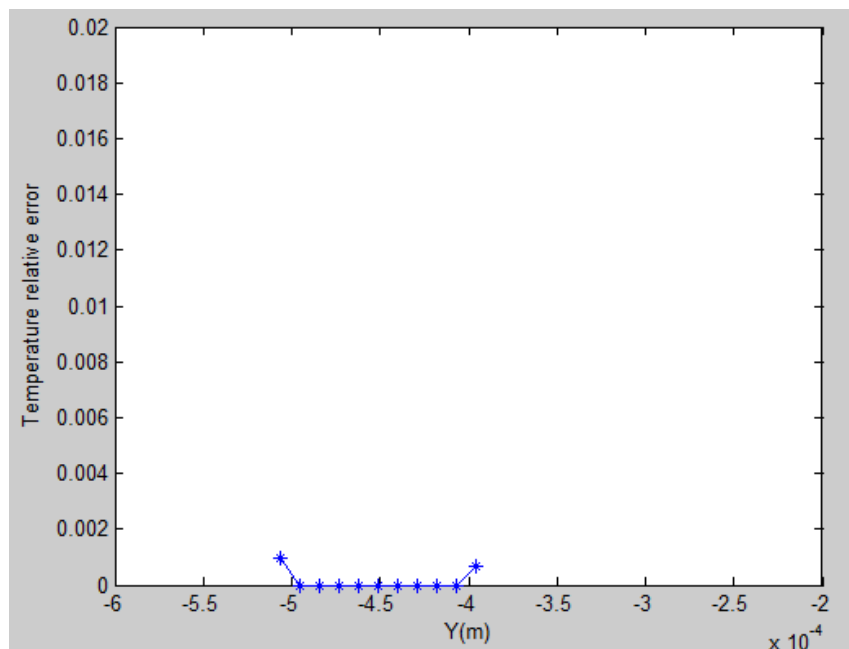


Figure 39 Temperature contour plot of the first time step of the dynamic model

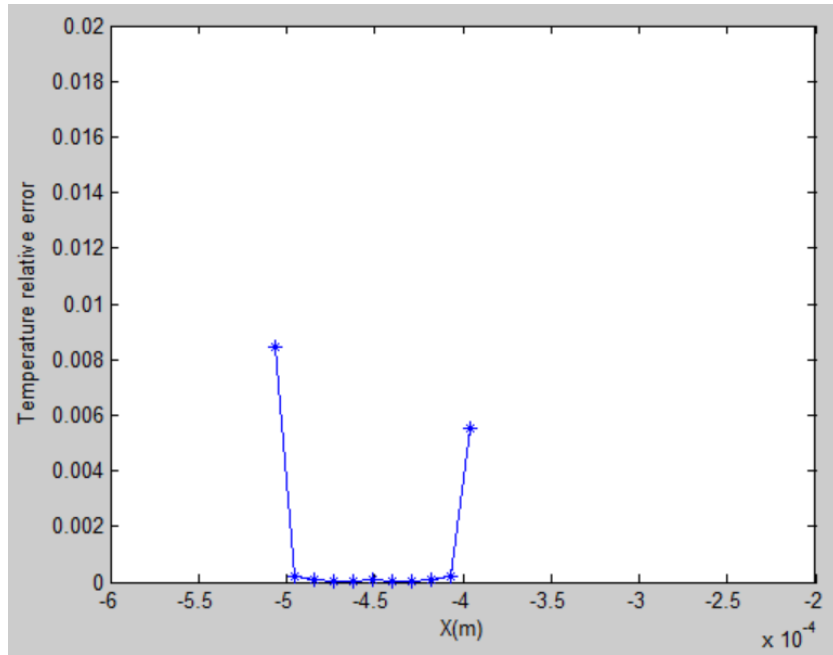


(a) Temperature distribution relative error in the X direction (scan direction)

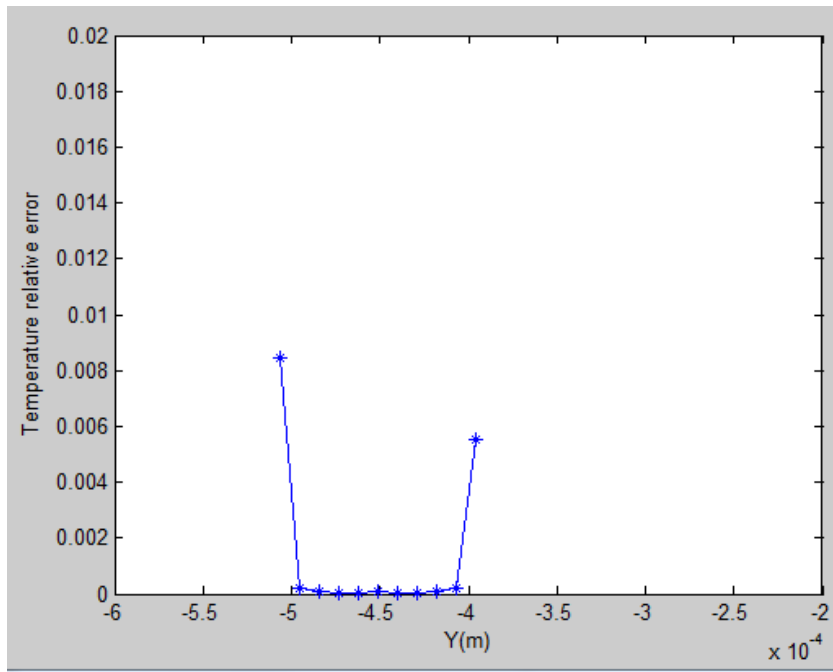


(b) Temperature distribution relative error in the Y direction

Figure 40 Temperature results before and after interpolation



(a) Temperature distribution relative error in the X direction (scan direction)



(b) Temperature distribution relative error in Y direction

Figure 41 Dynamic and uniform mesh model temperature distribution comparison

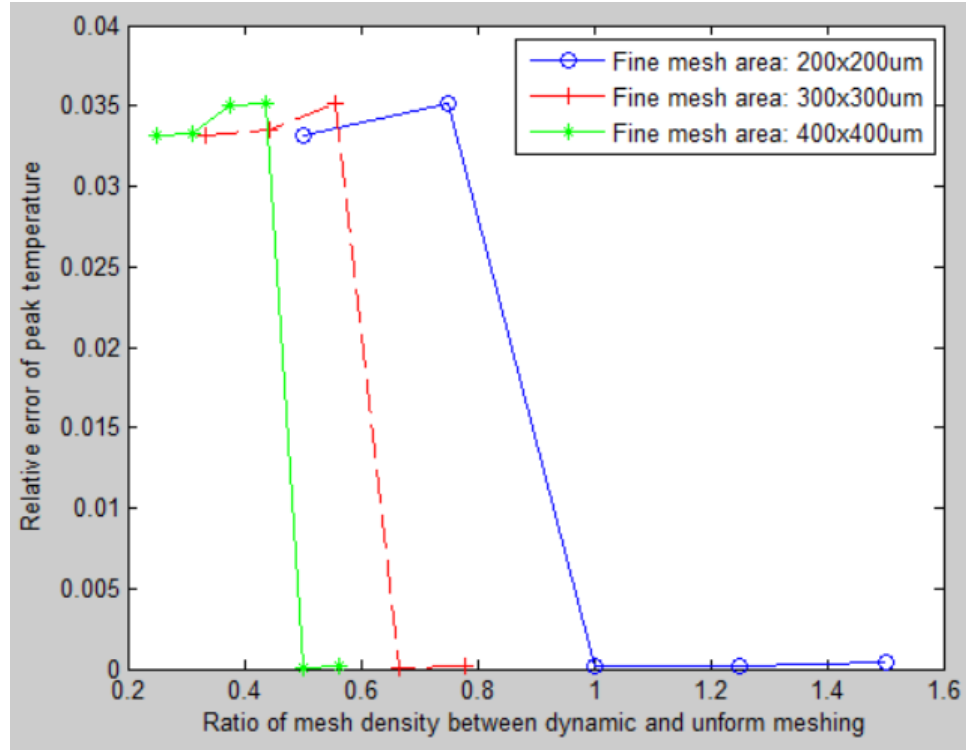


Figure 42 Influence of mesh density on the peak temperature

5.3.3 Dynamic and Uniform Meshing Model Results

In order to quantify the accuracy of the dynamic mesh model itself, it has been compared against its uniform counterpart. In order to compare the models, the mesh density of the uniform mesh has been set to be exactly the same as the mesh density within the red box in Figure 38 (b) resulting in a mesh as shown in Figure 38 (c). In both the dynamic and uniformly meshed domains the laser beam is concentrated in a small region of 4×4 elements bounded by the red box. The thermal distributions from both models have been compared against each other at exactly the same laser location and for the same time-step. The relative error of the thermal distributions in the X and Y directions for the dynamic and uniform meshing scenarios are shown in Figure 41 (a) and (b) respectively. It has been found that the relative standard deviation between the peak temperatures from both the models is zero. This illustrates that dynamic mesh modeling

is an efficient and accurate tool compared to its uniform counterpart [31, 54, 110] for modeling the thermal distributions generated by dynamic point heat energy sources.

The influence of mesh density on temperature error has been investigated and is shown in Figure 42. The mesh density is defined by the ratio of the number of elements in the fine mesh area in the dynamic meshing model to the same area in the uniform mesh model. The relative error of peak temperature for three different fine mesh areas is shown in Figure 42. The relative error of peak temperature reaches zero with increasing mesh density.

5.4 Multi time-step temperature distribution calculation

A Ti-6Al-4V cubic sample with dimensions of $10 \times 10 \times 10$ mm was built in an EOS M270 DMLS machine using input processing parameters of 80W and 360mm/s. Identical parameters were supplied as an input for simulating the thermal distribution of the above-mentioned geometry using the dynamic mesh strategy. Based upon results from the previously discussed sensitivity analysis section, a 16×16 fine element mesh



Figure 43 Scan pattern

size was used to capture the Gaussian curvature of the laser beam. The scan pattern assumption for these simulations is a raster scanning pattern as shown in Figure 43. A hatch space of 100 μm between the consecutive scan tracks was used in the experiments and for the purposes of these simulations.

In Figure 44, thermal contours at different spatiotemporal locations on the XY plane are plotted. The thermal contours shown in this illustration are higher than the solidus temperature of Ti-6Al-4V and do not capture the entire thermal spectrum, to illustrate the size of the melt pool.

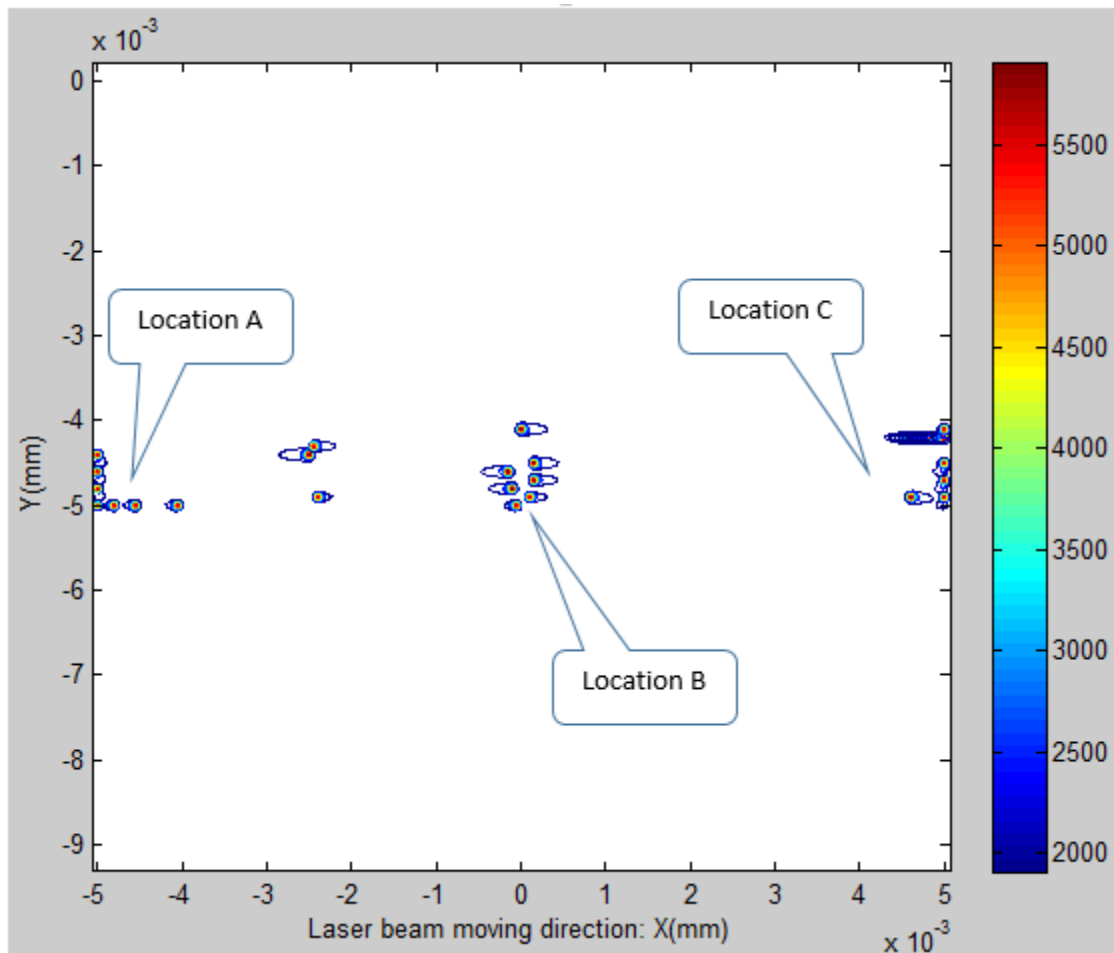


Figure 44 Temperature contour plots of melt pools in different locations

At least three types of melt pool shapes were observed for the traditional raster pattern as shown in Figure 45. Figure 45 (a) shows an enlarged illustration of melt pools from Figure 44 Location A. This location has the initiation melt pool which is comprised of circular thermal contours and symmetric contours as the laser beam moves to the right. The left edge of this figure shows contours as the laser beam turns, which have a right aligned tail since the thermal conductivity is higher towards the right side of the tail due to adjacent solidified material compared to the semi-insulating powder on the left side of the tail. Another type of melt pool occurs during the steady state laser movement in the center of the scans (away from the start and end of a scan vector) as shown in Figure 44 Location B and in its enlarged counterpart shown in Figure 45 (b). The melt pool remains symmetric about the y axis in this region with the tail enlarged in the direction behind the laser movement. The melt pool also remains constant in shape as a function of its y ordinate with respect to the simulation domain. This image shows a constant increase in the melt pool head diameter as a function of its y location due to an increase in the accumulated solid which causes the melt pool to broaden as a function of amount of solidified area compared to the area of the simulation domain. Figure 45 (c) shows yet another melt pool shape for laser scan turns on the opposite side of the scanned area, which is a mirror image of Location A melt pool shapes. Overall, Figure 45 (b) illustrates the most representative melt pools during the SLM process. Figure 46 (a) shows an enlarged view of the melt pool in the XY plane and Figure 46 (b) shows a view of melt penetration in the XZ plane for a steady state melt pool from Location B.

In Figure 44, Figure 45 and Figure 46 only the thermal contours higher than the solidus temperatures are shown to illustrate the melt pool shape. In order to obtain

complete thermal distribution information in mutually perpendicular axes, Figure 47 illustrates the thermal distribution along the +X neutral axis and Y axis passing through the melt pool center. In Figure 47 (a) the temperature gradient is high on the leading edge (the powder side) and is low on the trailing edge of the melt pool. The trailing, solidified side has a higher thermal conductivity compared to the powder side. In Figure 47 (b), the temperature is symmetric above the solidus temperature due to liquid material homogenization whereas the temperature drop is asymmetric outside the melt pool since the left side of the peak has a thermal distribution influenced by the solidified adjacent layer (with higher conductivity) compared to the right side portion with lower conductivity powder.

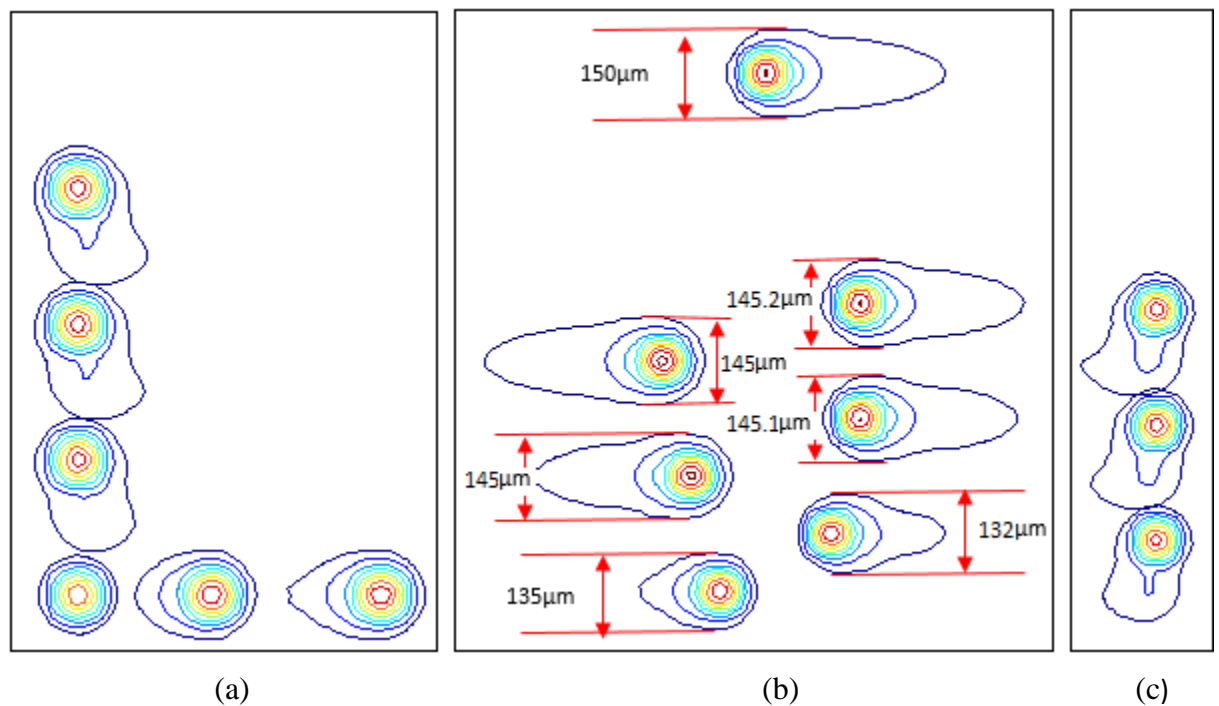
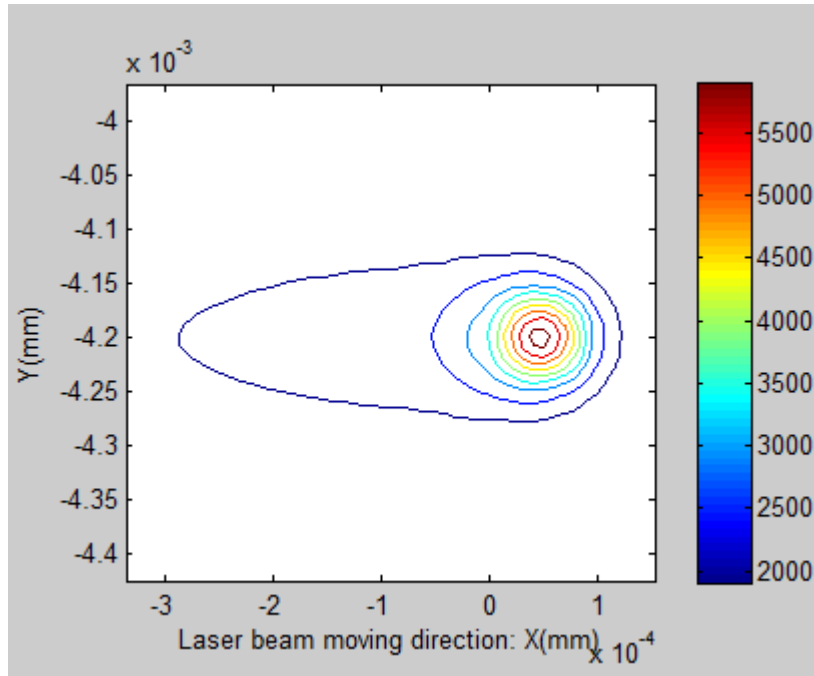
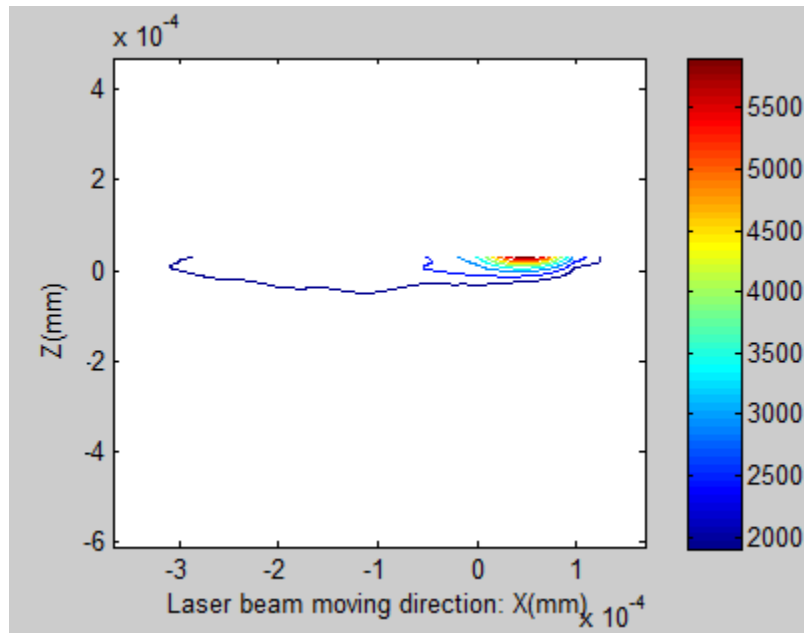


Figure 45 Melt pool for locations A,B,C of Figure 44 shown respectively in (a),(b) and (c)

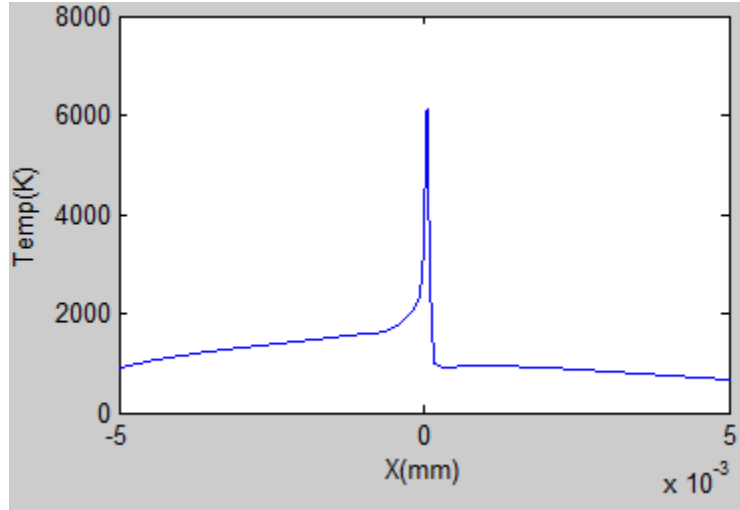


(a) Temperature contour plot in the XY plane

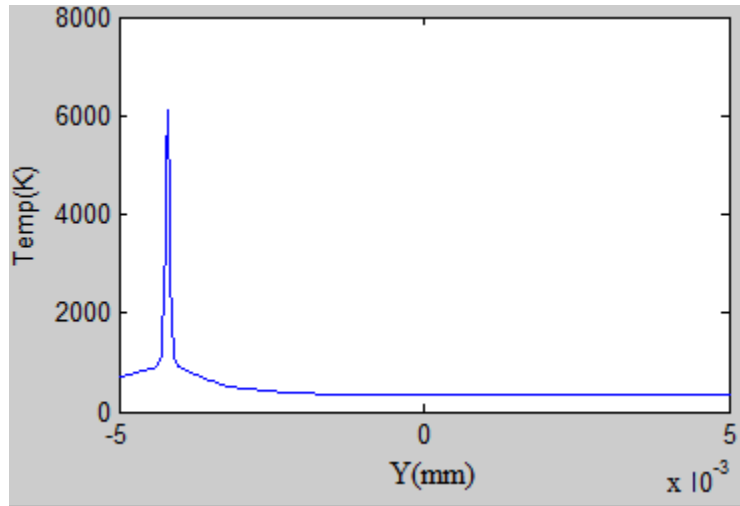


(b) Temperature contour plot in the XZ plane

Figure 46 Melt pool temperature contour distribution



(a) Temperature distribution in the X direction



(b) Temperature distribution in the Y direction

Figure 47 Temperature distribution through the melt pool

5.5 Experimental validation

Experiments were conducted to study the thermal characteristics of Ti-6Al-4V. Two melt pool scan track images are shown in Figure 48 and Figure 49 at different magnifications. In Figure 48, it can be seen that the scan track width matches closely with the input hatch space of 100 μm . Also it clearly shows the U \rightarrow D \rightarrow U (upward-

downward-upward) movement of the laser beam similar to the melt pool observations made in Figure 44.

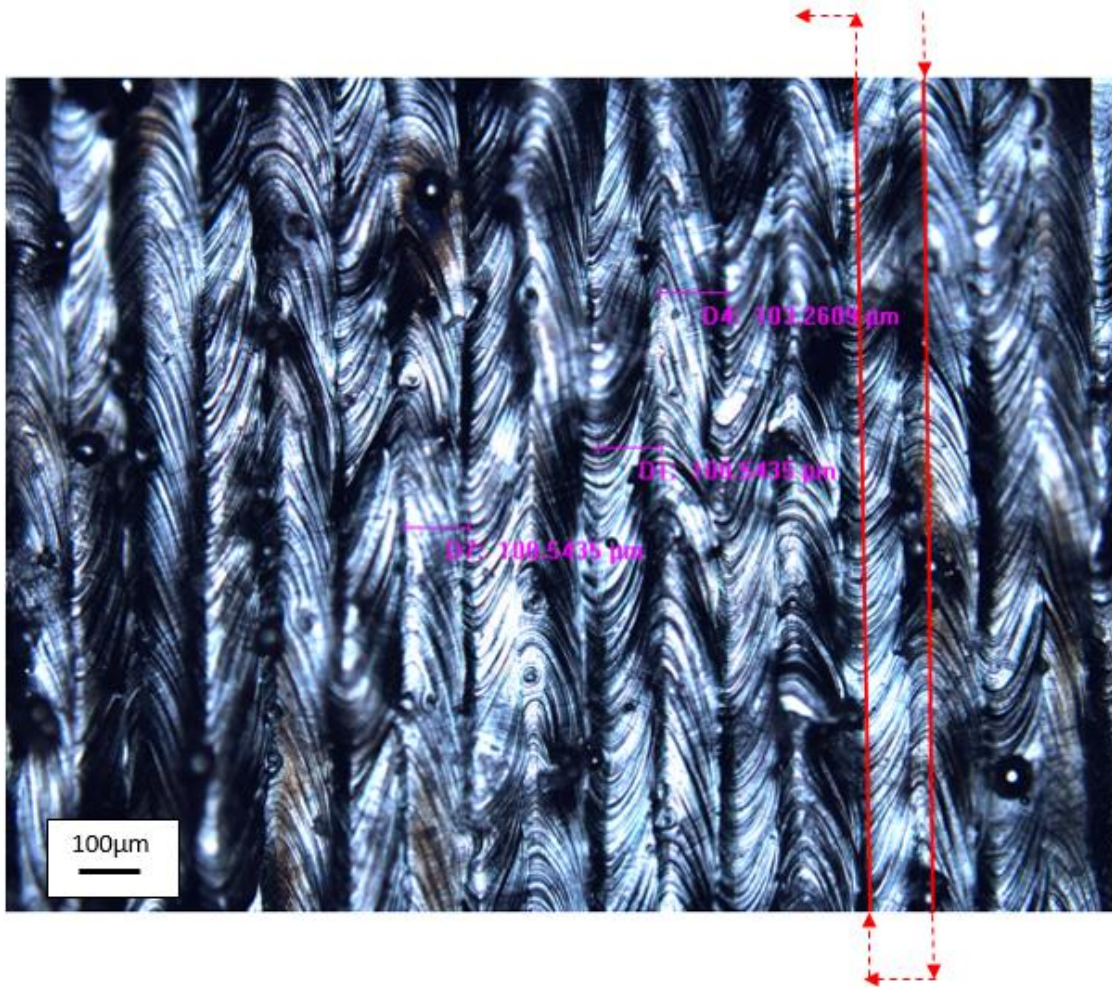


Figure 48 Tracks of laser beam on the surface

Figure 49 shows a magnified view close to the start-stop location of the scan vector. Due to melt-pool overlaps, one-half of the melt pool is clearly visible and shown to be approximately $75\ \mu\text{m}$, which corresponds well to the measurements made on simulated melt pools in Figure 45 (b). Another important aspect of these simulations is the end-of-vector instabilities in the melt pool, which are consistent in shape with the simulated melt pools shown in Figure 45.

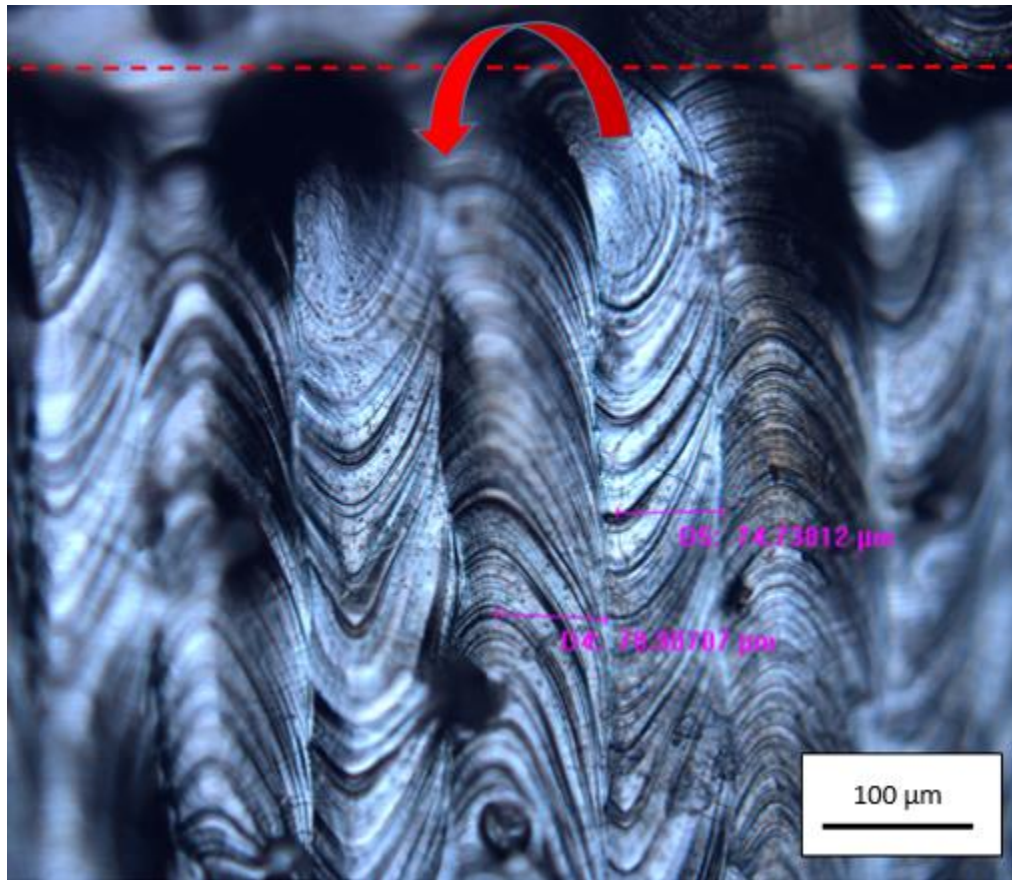


Figure 49 Melt pool curvature and width

5.6 Computational Expense Analysis

5.6.1 Computational Time Between Dynamic And Uniformly Meshed Model

In Figure 50, a computational cost comparison analysis shows the difference between the dynamic and the uniformly meshed models. The runtime of the dynamic mesh model is much less compared to the uniformly meshed model by a factor of 5. Higher factors of computational savings are anticipated as the total z height of the model increases as layers are added. The exact effect of increasing problem size on computational time is unclear, since the authors are not sure of the node renumbering schemes used in ANSYS as a function of fine mesh movement within the coarse mesh spacing. Very large savings in file size are shown in Figure 50, but these differences are partly problem dependent as ANSYS by default stores various data streams for the uniform mesh but provides options to save only the relevant data for a dynamic meshing model.

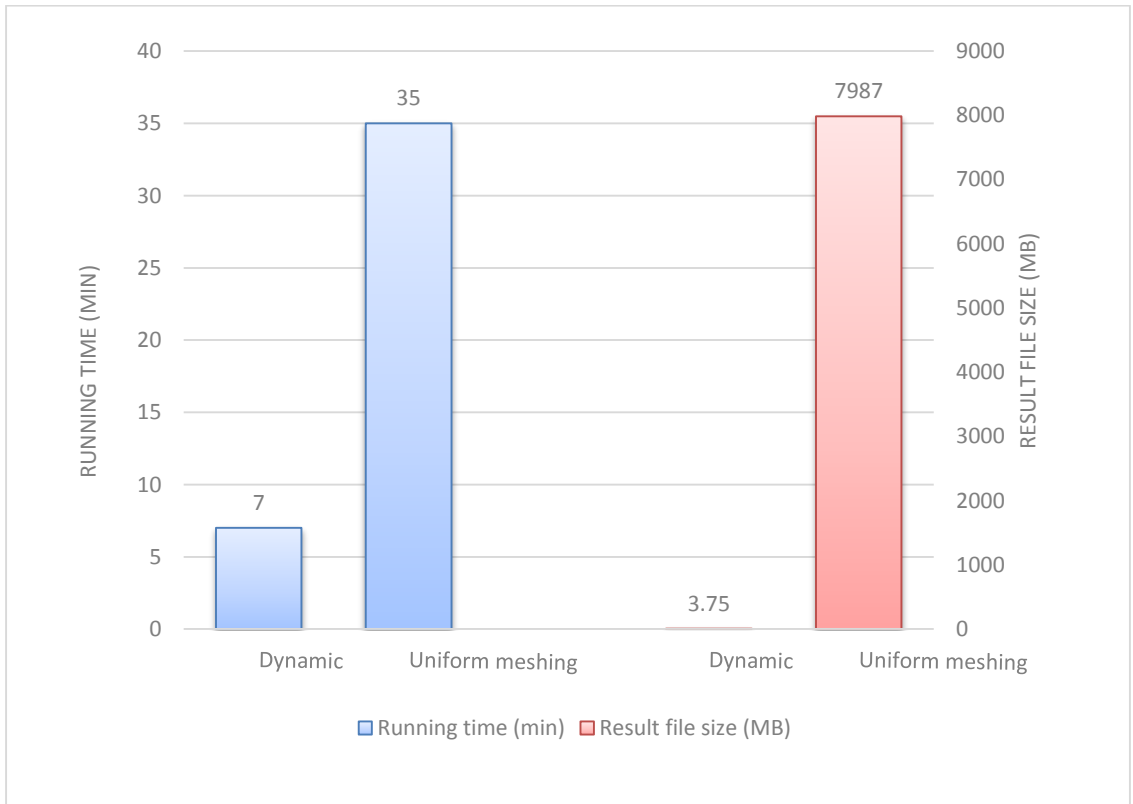


Figure 50 Computational comparison of dynamic and uniform meshing model

5.6.2 Computational Cost Comparison Between an ANSYS Dynamic Mesh Model and FFDAMRD

As mentioned in the introduction, dynamic mesh modeling using ANSYS was motivated by a Feed Forward Dynamic Adaptive Mesh Refinement and De-refinement (FFDAMRD) algorithm [44, 111]. One major purpose of this study was to compare FFDAMRD efficiency as coded in Matlab against a nearly identical ANSYS formulation for simulating SLM. Thermal distribution results and speed efficiency have been compared and reported previously [5]. Both models produce similar thermal distributions and melt pool shapes.

Improvements to FFDAMRD are underway. A commercial version of the code is being developed by 3DSIM, LLC in C++ along with code porting from CPU (Central Processing Unit) to GPU (Graphics Processing Unit). Early tests indicate this C++ version is much faster than the original Matlab code, thus enabling even better computational efficiencies. A much larger GPU-based comparison between ANSYS and FFDAMRD using 3DSIM's code is currently being planned.

5.6.2.1 Convergence Study

Figure 51 shows the convergence study using ANSYS and 3DSIM. It runs a simulation of a simple model with different number of elements in the Z direction. The 3DSIM result converged to the same value as it produced in ANSYS.

5.6.2.2 Computational Time Study

In this study, the time to simulate the small part shown in Figure 52(a) has been estimated based upon results for ANSYS and 3DSIM simulations of sub-portions of the part. The part was simulated based upon standard process parameters for Ti6/4 used in an

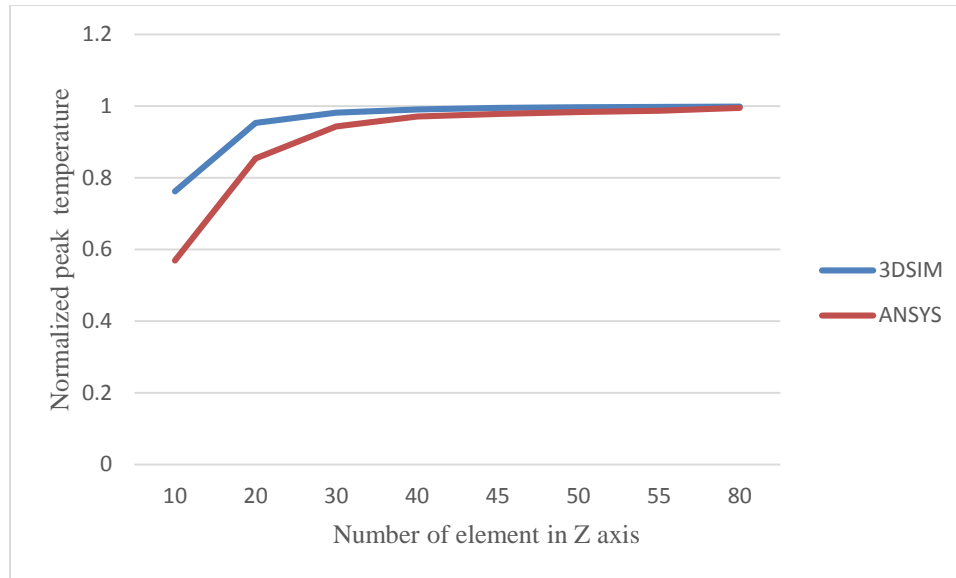
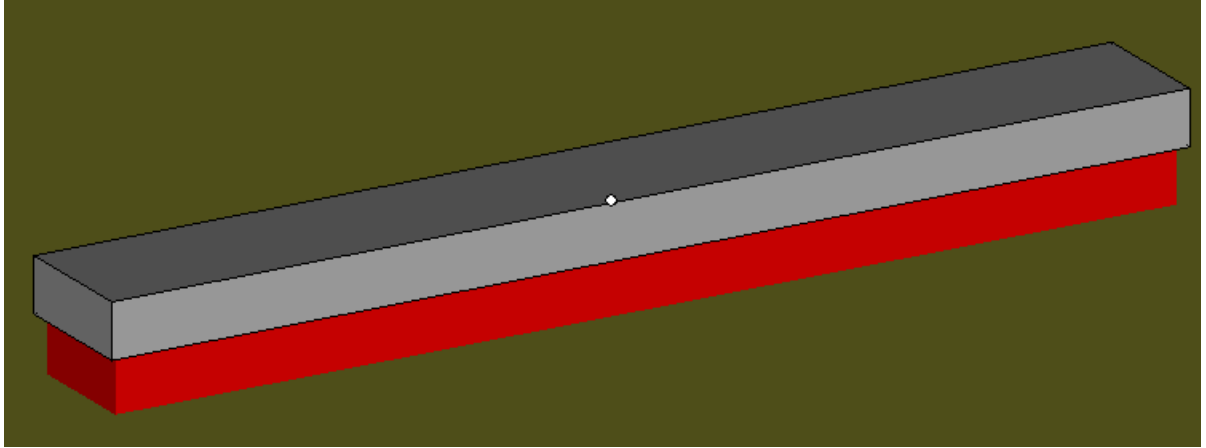
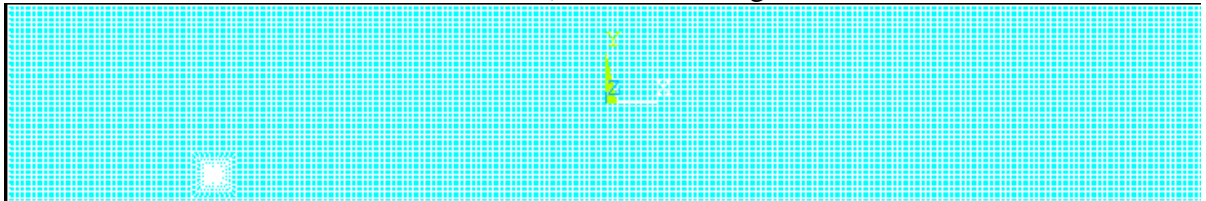


Figure 51 Convergence study for peak temperature comparing 3DSIM and ANSYS results

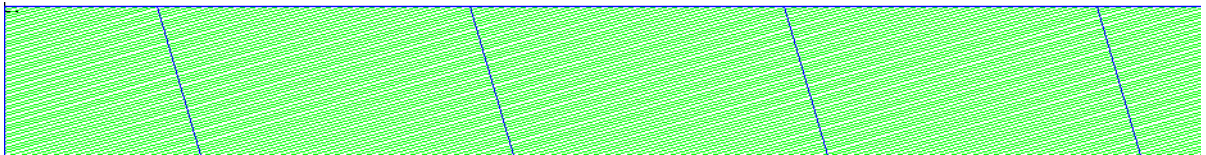
EOS M270 machine and the use of a block support structure with a 2 mm height. The simulations were set up to calculate an additional 1 mm of unmelted powder on each side of the part and 1mm of the baseplate, resulting in an FEM model size of 42 mm x7 mm in the XY plane and an initial 3 mm Z height, which increases as new layers are added in the Z direction. The mesh used for this problem, showing a uniform coarse mesh throughout and a fine discretization near the energy source, is shown in Figure 52(b). The laser beam diameter has been assumed to be 100 μm and is sub-divided into 8 elements. The coarse mesh discretization encapsulating the remaining geometry has a 200 μm spatial grid size in the XY-plane. The layer thickness and the Z direction element size were assumed to be 30 μm . The Z-direction element size for the support structure and the build plate were set at 125 μm and the existence of the support structure was assumed to be already present at time $t = 0$ with properties representative of a block support structure. The initial strip angle for scanning was observed to be 106.15° w.r.t. +X axis for an EOS M 270 machine, and this assumption has been replicated in Figure 52(c). All



(a) A plate with dimensions of 40x5x2mm, built on top of a block support structure (in red) of 2mm in height



(b) Mesh for the structure



(c) Scan pattern for the structure

Figure 52 Problem definition showing the part, mesh and scan strategy employed in the simulation

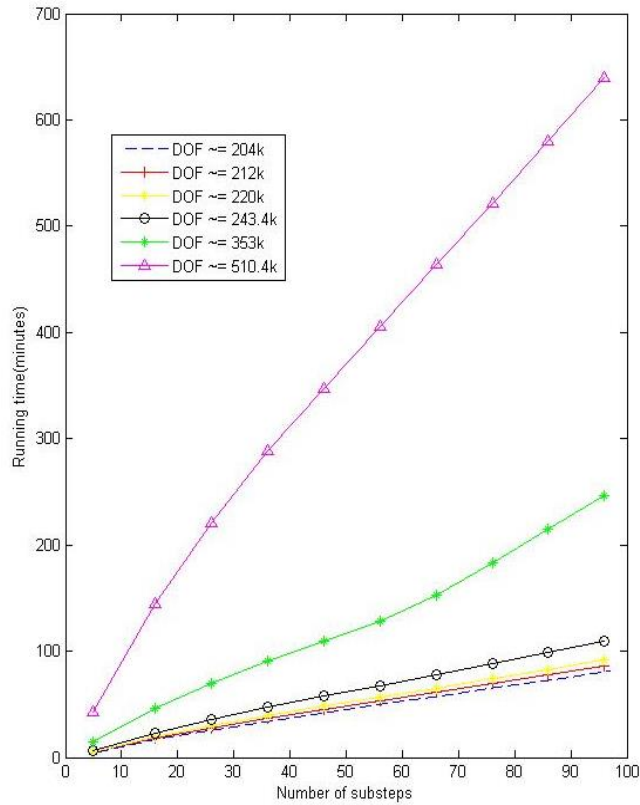
coordinates follow ASTM standard terminology [112].

5.6.2.3 Results and Discussion

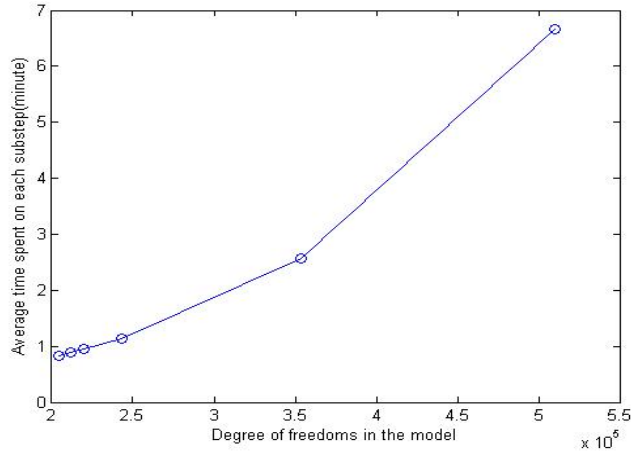
A three dimensional model built in ANSYS using the above-mentioned discretization and overall dimensions ranges from 204k to 714k degrees of freedom (DOFs). The number of DOFs linearly increase as the number of layers increase. Figure 53 shows the time to simulate various sub-portions of the model for different layers on a Dell Precision T1650 desktop computer with a processor speed of 3.2GHz and 8GB of RAM. Each model ran for the first ten laser offsets for each layer of simulation (it was not possible to finish running even one layer in an acceptable amount of time).

The way laser offsets are modelled are different in ANSYS versus 3DSIM. The dynamic mesh developed for this problem has a fine mesh region that is stationary with respect to the coarse mesh for several time substeps as the laser energy traverses the fine mesh. Once the laser has crossed a pre-determined location in the fine mesh, the fine mesh moves in the direction of laser motion so that the melt pool remains within the fine mesh region. In the ANSYS model, this is approximated by causing the point of laser exposure to remain virtually stationary at the center of the fine mesh between time substeps until the laser position should have reached the fine mesh boundary (Figure 52 (b)) leading to an advancement of the fine mesh by one coarse mesh distance in the direction of laser travel. In the 3DSIM model, the laser exposure changes location within the fine mesh region every time substep. The result of this difference is that 3DSIM more accurately captures temperature variations. Since this experiment was designed to test the speed difference of 3DSIM versus ANSYS, no detailed analysis of accuracy was done.

In Figure 53(a), the ANSYS execution time is plotted against the number of substeps for different DOF scenarios. In Figure 53 (b), the average ANSYS time per substep is plotted against the number of DOFs. In order to predict the time needed for larger problems, the execution speed of the model using different computational configurations was tested and is shown in Figure 54 for two cases of approximately 204k and 510k DOFs respectively. It was observed from these test results that the model runs fastest using the combination of 1 GPU and 2 CPU cores. The corresponding results for average time spent per substep w.r.t. DOFs is shown in Figure 55.



(a) Running time versus number of substeps



(b) Average time per substep versus DOFs ($\times 10^5$)

Figure 53 ANSYS sub-model run time on an ordinary desktop computer

In order to estimate the time for the execution of an entire part model in ANSYS, the results shown in Figure 55 have been used for extrapolation. From Figure 55, the time to solve an increasing number of DOFs was assumed to be a linear function for DOFs

exceeding 220k, and the data was fitted using a linear function. Using this linear estimation methodology, the execution time for ANSYS to fully simulate the small test peg model using 321,160 substeps (representing a solution of the laser for every 12.5 μm of laser travel) would be about 61.5 years.

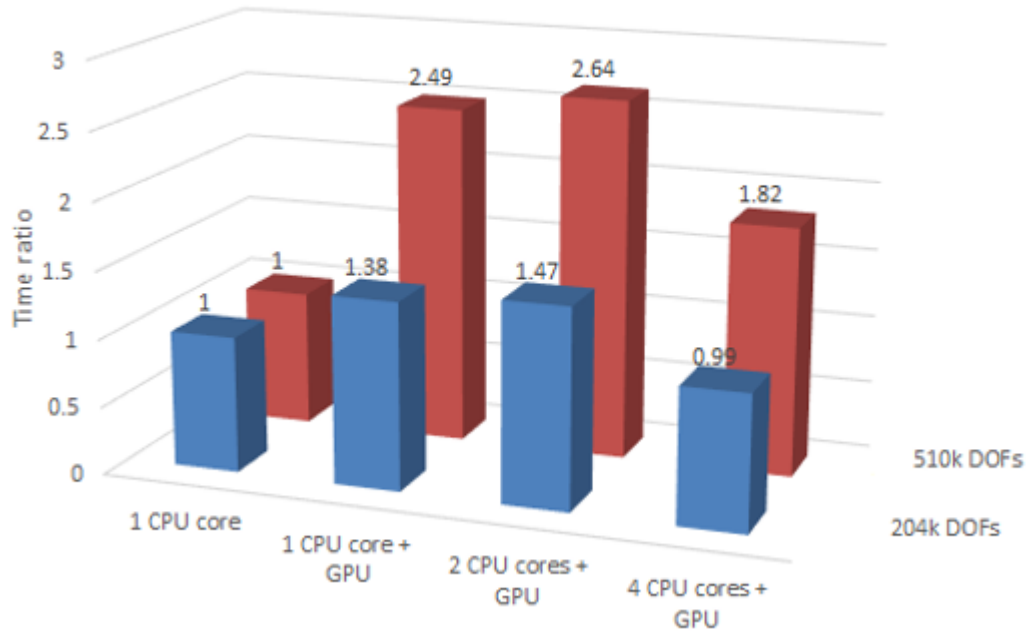


Figure 54 Different computational configurations comparison

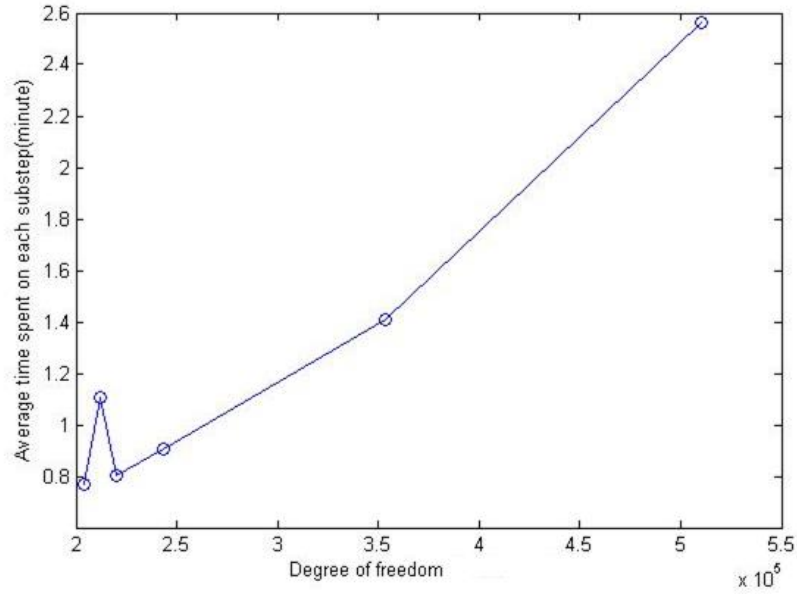


Figure 55 ANSYS model running time for multiple GPU processors

In order to compare the computational speed of the ANSYS model with its 3DSIM counterpart, a model with three elements in the Z direction was executed using 3DSIM. The execution time for finishing one layer with about 200K time steps are shown in Table 1 for both 3DSIM and ANSYS. A previous case study reported in SFF 2013 showed that the Matlab version of 3DSIM's algorithms was about 66 times faster than ANSYS [5]. From the results in Table 1, the initial (non-optimized) C++ 3DSIM model used for this study is about 294 times faster.

Table 1 3DSIM Processing Time for the model with 3 elements in the Z direction

	Time steps	Offsets	s/time step	s/offset	Total(hours)
3DSIM	200244	11779	0.2	0.5	12.8
ANSYS	200584	N/A	67.54	0	3763.2

5.7 Conclusions and future work

A dynamic mesh framework has been developed to provide an efficient computational method for simulation and modeling of SLM using ANSYS. This framework provides very large computational speed and model size advantages compared to other FEM approaches in the literature. The accuracy of interpolation of nodal temperatures from one fine mesh configuration to the next has been tested and was found to be reliable since the converged thermal field in the previous fine mesh configuration matches well with the initial condition thermal field in the next mesh configuration. A comparison of ANSYS solutions with experimental results for melt pool size and shape indicate the model accurately simulates the process.

The ANSYS approach to dynamic meshing, however, is still not as fast as required due to the node renumbering and reassembly required in ANSYS and the need for finer time steps for convergence. ANSYS is arguably the best existing commercial tool for solving SLM thermal problems. Using ANSYS, however, to simulate even a relatively small SLM thermal problem requires many years of computational time.

A comparison between ANSYS and 3DSIM show that both methods can be used to accurately simulate the thermal transformations in SLM. The set of algorithms and software tools being developed by 3DSIM show an initial advantage for speed, and thus capability, for simulating AM problems. So 3DSIM could be adapted to provide temperature and thermal stress results for support structure design and optimization.

CHAPTER 6 EVALUATION OF EFFECTIVE THERMAL CONDUCTIVITY APPROACHES FOR SUPPORT STRUCTURES

6.1 Introduction

Selective laser melting (SLM) is an Additive Manufacturing (AM) technology whereby a part is built by melting successive layers of metal powder. The part is typically built upon a plate in an enclosed chamber. Support structures are designed during the build setup process. These structures are commonly built using process parameters different from part fabrication parameters since the objective of their fabrication is to withstand the thermal stress due to the part fabrication followed by their easy removal post-fabrication. These structures typically resemble a truss-like structure such that the material usage can be reduced [3]. Although support structures play a critical role in SLM processing, the complexities related to thermal phenomena in SLM and the need for fast simulations leads one to consider how to minimize computational time when including support structures in a thermo-mechanical model [5, 113].

Simulations capable of predicting the complex thermal behavior which occurs in a SLM process would help design and manufacturing engineers build more optimum designs in a reliable manner. A multiscale generalized feed forward adaptive refinement and de-refinement (FFD-AMRD solver for 3DSIM) finite element framework for SLM has been developed to achieve fast thermomechanical field solutions [45]. Support structures fabricated during SLM to overcome thermal stress induced part distortion are a key part of the process, and a representation of these support structures in a finite element

framework must be considered. If support structures could be designed with minimal material usage while still maintaining an ability to withstand the thermal stresses generated during the part fabrication, this would significantly impact industrial use of SLM. In order to reduce the computational cost and maintain the speed of the simulations, the use of effective thermal properties for support structures is evaluated in this paper within the above-mentioned framework. The effective material properties have been computed using the Representative Volume Element (RVE) approach.

The effective thermal properties of support structures can be represented using thermal homogenization. The effective thermal properties of the support structures have been found to be a function of their geometry, anisotropy and constituent independent thermal properties. The results from this study have been compared against standard models and a good match has been found. The objective of this work is to derive effective thermal property functions which could be directly incorporated in the FFD-AMRD framework mentioned above to enhance computational speed.

6.2 Background

The theory of homogenization was developed in the 1970s [114-117]. This method was developed to obtain the effective physical properties of a periodic structure using an RVE of the structure such that the property value under consideration converges to a specific value as a function of an increasing number of periodic unit cells. The theory of homogenization uses asymptotic expansion and assumes periodicity to substitute for differential equations and obtain limiting solutions asymptotically close to the original solutions [116, 118]. Replacing the fine spatially detailed model with an

equivalent model such as an RVE is a computationally cheap way to dimensionally reduce the size of a detailed model.

Examples of homogenization based dimensional reduction have been illustrated for a variety of computational problems. A finite element based micromechanical model was developed to study the compressive deformation response of an RVE designed for a truss-based cellular solid [119]. In order to solve this RVE, periodic boundary conditions were applied to the fine spatially detailed model. The mechanical parameters of interest including the stiffness and strength were studied by changing various inputs such as volume fraction and size of the RVE. Similarly, another example of homogenization is a numerical procedure built in ANSYS with a FORTRAN subroutine to parametrically change input variables of the simulation. The objective of this work was to study the effective material coefficients of piezoelectric fiber composites [120]. Periodic boundary conditions were applied to the model to keep each composite RVE in the same deformation mode; which means there was no separation and overlap between the neighboring RVEs. The opposite surfaces were meshed in such a way that the corresponding nodes were coupled with the same number of nodes on both surfaces.

There is no prior work reported on effective thermal conductivity for support structures in SLM. However, effective thermal conductivity of fiber reinforced composites and honeycomb structures similar to SLM support structures in shape, form and geometrical aspects have been studied in the literature. A boundary collocation scheme for 2D periodic arrays of a composite comprising extrusions with circular and square bases has been developed to compute the effective thermal conductivity [121]. This led to a study of the influence of inclusion volume fraction and conductivity ratio on

the effective thermal conductivity of these composites. Similar to the previous study, a 2D transverse cross-section of fiber reinforced composites was studied and the effective thermal conductivity was computed using four different types of periodic boundary conditions applied for a representative FEM [122]. The boundary conditions used for this study are (a) prescribed constant boundary temperature on both vertical boundaries, (b) prescribed constant temperature and a constant heat flux at the vertical boundaries, (c) prescribed constant heat flux at both vertical boundaries and (d) prescribed constant vertical boundary temperatures and a linearly varying thermal field in between opposite horizontal boundaries. The effective thermal conductivity results computed using FEM were compared against available analytical and experimental results for both circular and square cross-section fibers. Another numerical investigation was performed to study effective thermal conductivity as a function of monolith honeycomb structures such as a hollow hexagon, circle or square periodic arrays coated with washcoat [123] at the internal periphery. The axial and transverse effective thermal conductivities were computed for these monolith structures and compared against parallel and series spring model counterparts.

6.3 Description of the problem

Figure 56 shows the most commonly used block support structures for SLM when using an EOS M270 direct metal laser sintering machine. Figure 57 shows the physical 3D model and RVE of the support structures along with the substrate. The substrate is usually a one-inch thick plate. The support structure is scanned, melted and solidified during the fabrication process. The fabrication of these structures leaves residual powder trapped inside the support channels. Therefore, the fabricated part is held in its desired

shape using a mixture of powder and solidified truss-like support structures on top of the base plate. It is therefore required to model both the solidified support structures along with the powder trapped inside them to arrive at an RVE and efficient thermal properties to be directly integrated into a thermomechanical solver.

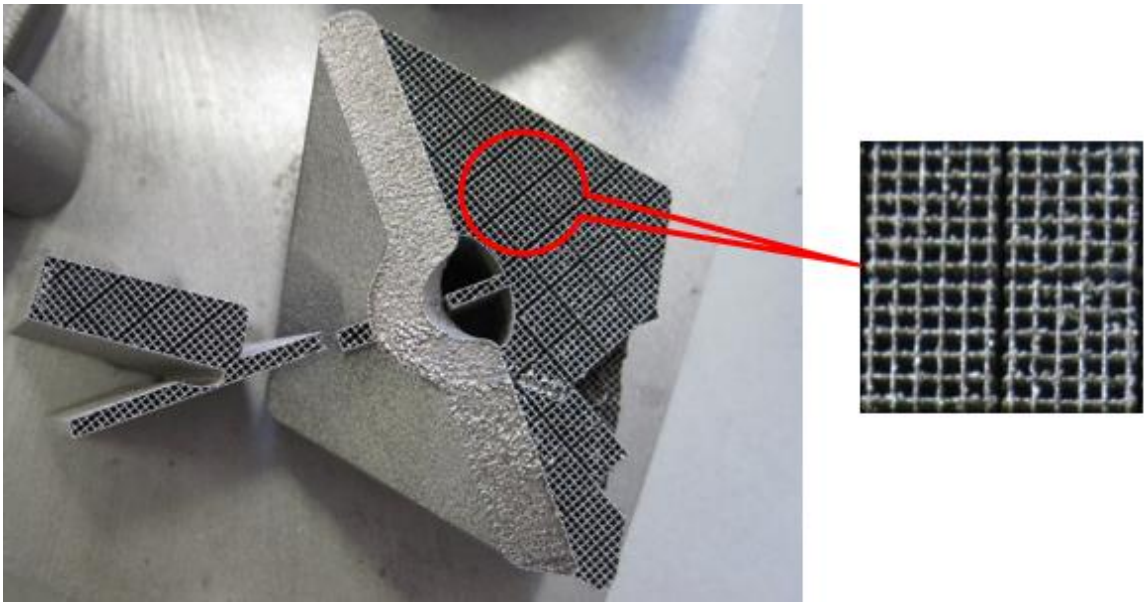


Figure 56 Support structure built using an EOS M270 machine

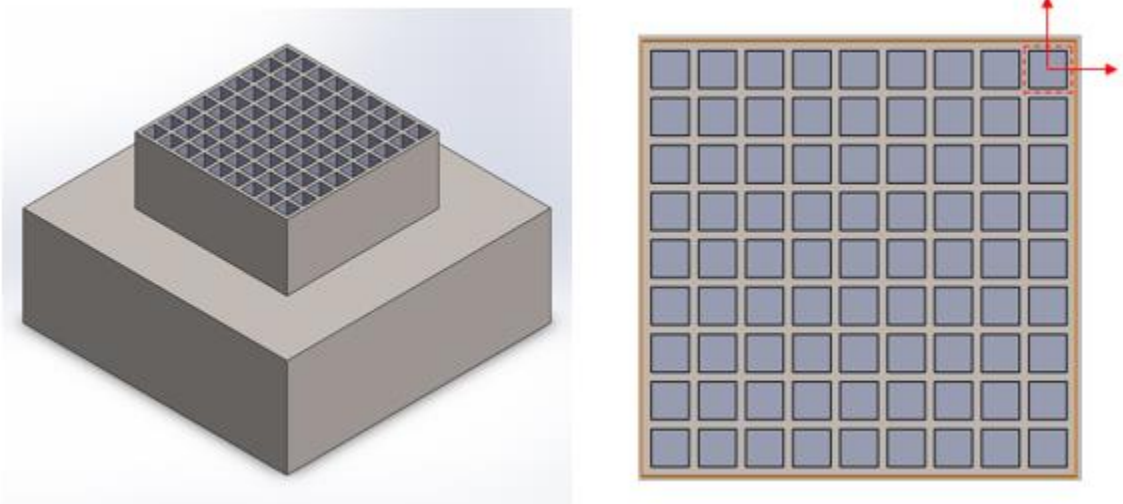


Figure 57 3D model with support structure and RVE of support structure

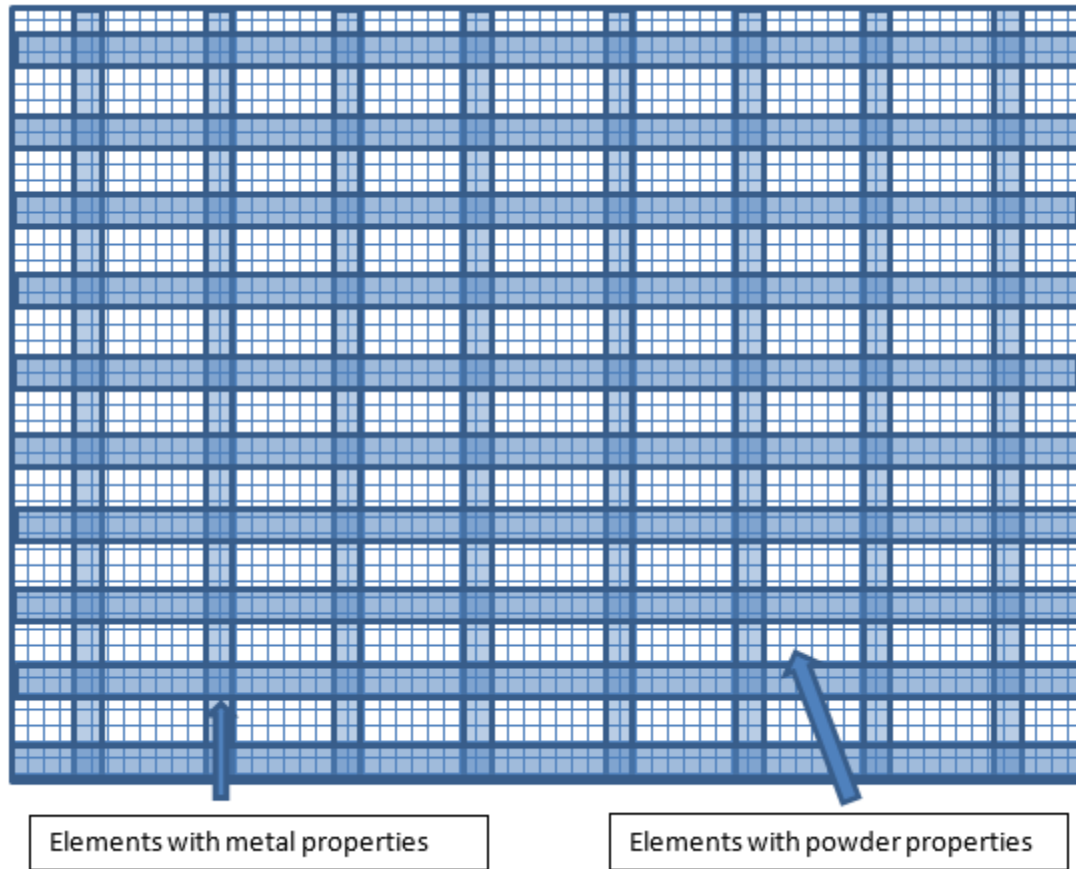


Figure 58 View of the XY plane of an example mesh

A cross-section of the mesh with solidified thin wall geometries and trapped powder inside the intercellular space is shown in Figure 58. The support structure domain consists of elements with different material properties for solidified material and powder. The current FFDAMRD process solver adopts a predefined coarse and fine moving mesh strategy to capture the different scales of thermal behavior [43], and inhomogeneous material properties of the support structure increase the complexity of the problem. In order to avoid this complexity, an effective thermal conductivity for the combined solid-powder support structure is studied in this paper. An RVE was designed to replicate the combined solid-powder structure with periodic boundary conditions applied to it. The influence of volume fraction and the number of unit cells affecting the effective thermal

properties was analyzed. Both temperature-independent and temperature dependent thermal properties such as thermal conductivity have been used to perform a steady state thermal analysis of the RVE.

6.4 Numerical method

The addition of support structures made up of solid ribs filled with powder in the intercellular spaces into the FFDAMRD finite element framework makes it more complicated and increases its computational burden. The main purpose of the method is to find a globally homogeneous media equivalent to the original structure, where the heat energy stored is approximately the same [124]. Hence an RVE has been designed such

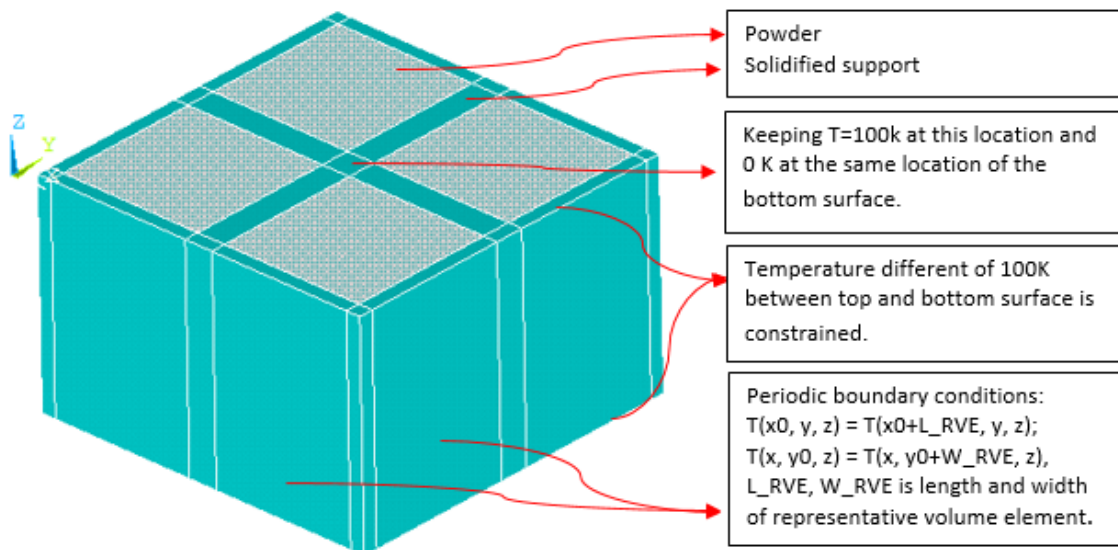


Figure 59 Representative Volume Element for the support structure with defined boundary conditions

that an equivalent model could be derived as a function of support structure geometry, volume fractions of the intercellular powder and solidified supports, and thermal loading direction. The periodic boundary conditions shown in Figure 59 were applied to the RVE. The average heat flux and temperature gradient was evaluated based on the thermal results from running the RVE in ANSYS. The equivalent model results in the prediction

of an effective thermal conductivity of the support structure in the z-axis by performing a finite element simulation with its results validated against a parallel model for springs [125].

6.4.1 Linear Temperature-Independent Material Property Case Study Results

Figure 59 shows the initially chosen model geometry to represent the support structure for evaluating the effective thermal conductivity. A constant temperature of 100K and 0K were prescribed at the center nodes of the top and bottom surfaces respectively as boundary conditions in the finite element model. Other nodes on the top and bottom surfaces were constrained to maintain a temperature difference of 100K between the top and bottom surfaces. The intent of this simulation was to create a representative model and to perform a finite element simulation with periodic boundary conditions such that the opposite faces of the model domain perpendicular to the x- and y-axis have exactly the same temperatures. The thermal solution has been obtained in ANSYS by subjecting the model geometry to the above-mentioned boundary conditions and surface constraints. An effective thermal conductivity was then calculated based on the heat equation shown in Equation (13)

$$q = -k \frac{dT}{dz} \quad (13)$$

where q is the heat flux, k is the thermal conductivity, T is the temperature and z is the distance in the z direction.

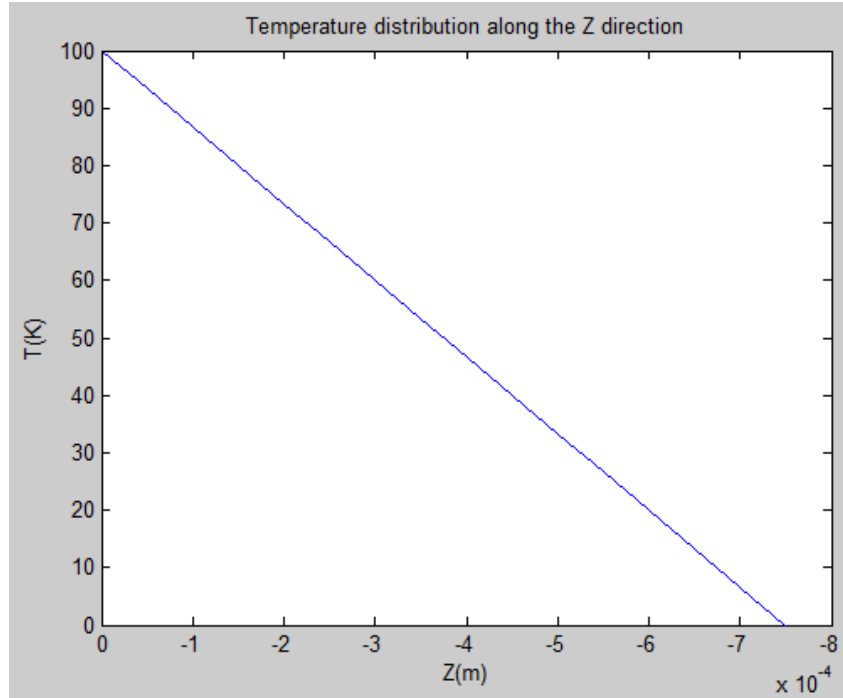


Figure 60 Temperature distribution along the z direction

The temperature difference in the z direction is 100K, which is predefined as the boundary condition. The temperature gradient in the z direction can be obtained through an integration of Equation (13). As shown in Figure 60, the temperature distribution along the z direction is linearly distributed, thus the temperature gradient could be easily calculated in this case. The heat flux for all elements with different properties (powder and solidified sections) through the z direction is stored in the ANSYS result list. The total heat flux input in the z direction for the surface is the sum of the result for all elements. The effective thermal conductivity is calculated through the z direction by using the average temperature gradient available from temperature values in the z-direction and retrieved heat flux.

The influence of the total number of cells in the support structure and the volume fraction of the solidified material and entrapped powder in the representative volume element were studied. According to the literature, series and parallel spring models for

studying the effective properties of a composite material are commonly used [125] to establish a relationship between average and local thermal conductivities. The parallel model was chosen over the series model to verify the numerical model in this study since the powder and solidified support structures were lying side-by-side. The effective thermal conductivity of the parallel composite described above is shown in equation (14).

$$K_{effective} = K_{solid} * \theta + K_{powder} * (1 - \theta) \quad (14)$$

where K_{solid} and K_{powder} are the thermal conductivity for the solidified support and powder respectively and θ is the volume fraction of solidified support w.r.t. the combined structure comprising solidified truss-like geometries and entrapped powder.

Since the increase in the number of support structure cells does not necessarily change the volume fraction of the solidified support material, the effective thermal conductivity converges to a constant value regardless of the number of unit cells. The effective thermal conductivity does not change with increasing number of support structure cells. However, with an increase in the volume fraction of the solidified material, the effective thermal conductivity increases, as shown in Figure 61. Both results show that the numerical effective thermal conductivity matches the results obtained from the parallel spring model.

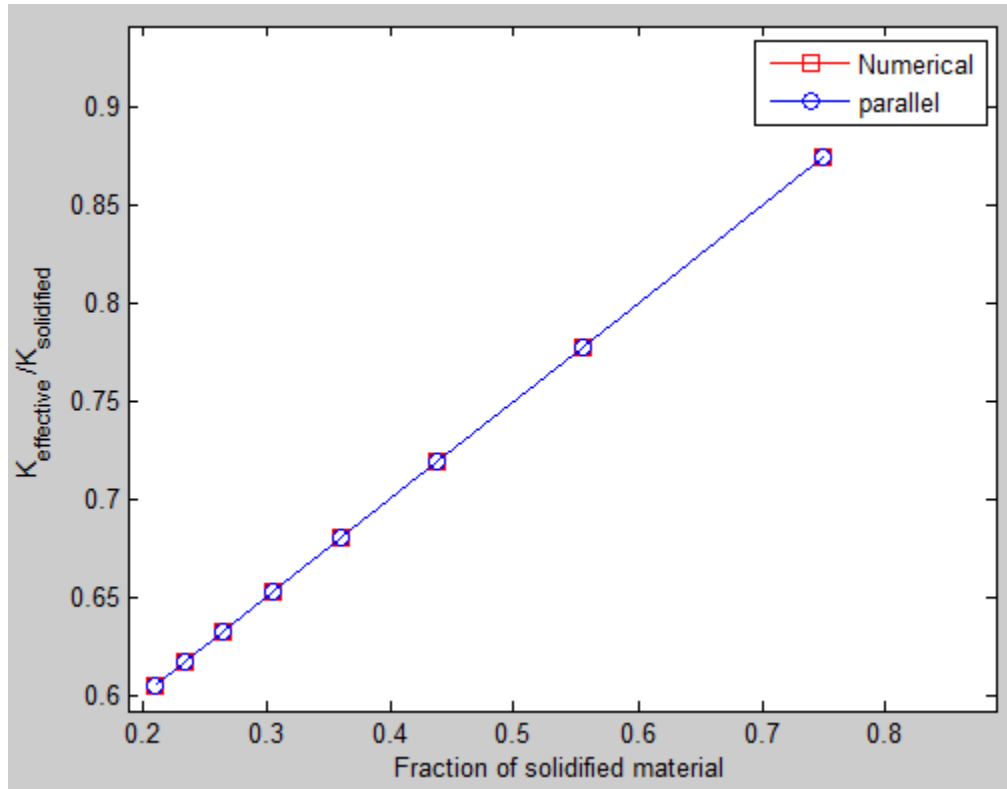


Figure 61 $K_{\text{effective}}/K_{\text{solidified}}$ vs the fraction of solidified material

6.4.2 Nonlinear Temperature-Dependent Material Property Case Study Results

In general, the thermal properties of common materials are temperature dependent and nonlinear in nature. In this case, the temperature difference between the central nodes at the top and bottom surfaces has been set to be the exact value of the prescribed temperature difference with an added constraint that the thermal conductivity of the material will change as a function of temperature rather than remaining constant throughout the thermal range. When solving a linear material property case problem, temperature variation doesn't influence the results because the thermal conductivity is assumed to be temperature independent. However, the temperature at the central bottom surface node and the temperature difference between the top and bottom surface are required to be selected carefully for nonlinear thermal conductivity scenarios where a

change in thermal conductivity across the supports is significant. In order to set the boundary conditions, the temperature of the entire domain is assumed to be the same as the temperature of the central bottom surface node followed by a temperature difference of 1 K between the top and bottom surfaces. This results in the effective thermal conductivity of the combined support comprised of the solid and entrapped powder material as a function of individual volume fractions, geometry and the base-line temperature. The effective thermal conductivity for a critical temperature, such as the beta transus temperature or melting point, was evaluated. The procedure to calculate the effective thermal conductivity for each selected temperature in this case is exactly the same as has been described for the linear material case using Equation (14).

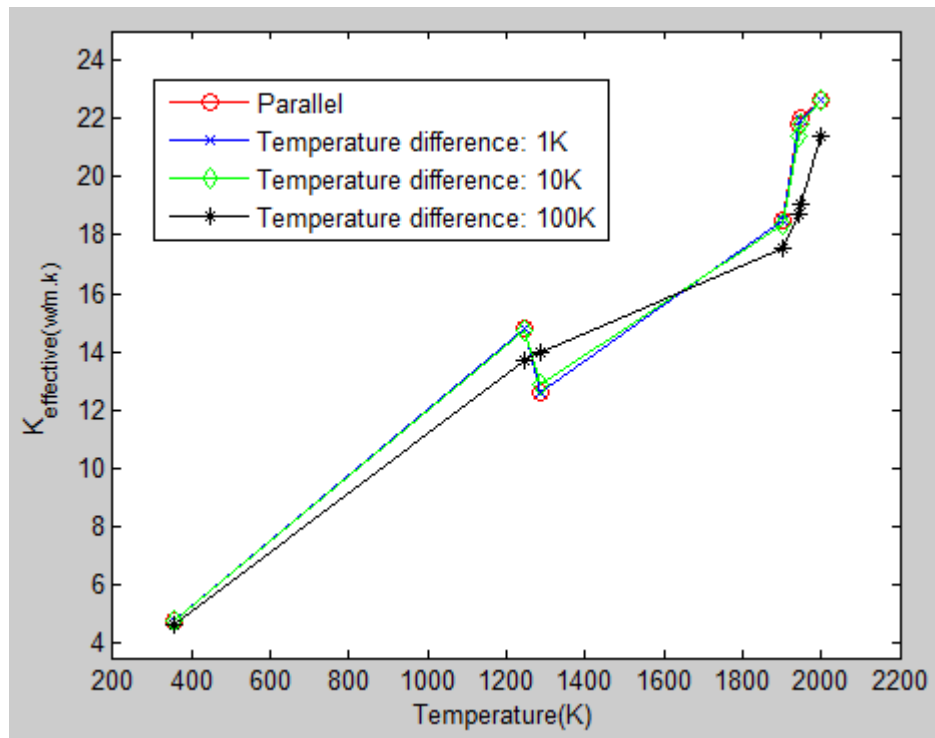


Figure 62 Effective conductivity vs temperature for temperature-dependent Ti64 properties at various temperature gradients

The influence of the temperature difference on the volume fraction of solidified material has been studied to gauge the nonlinear effective thermal conductivity as shown

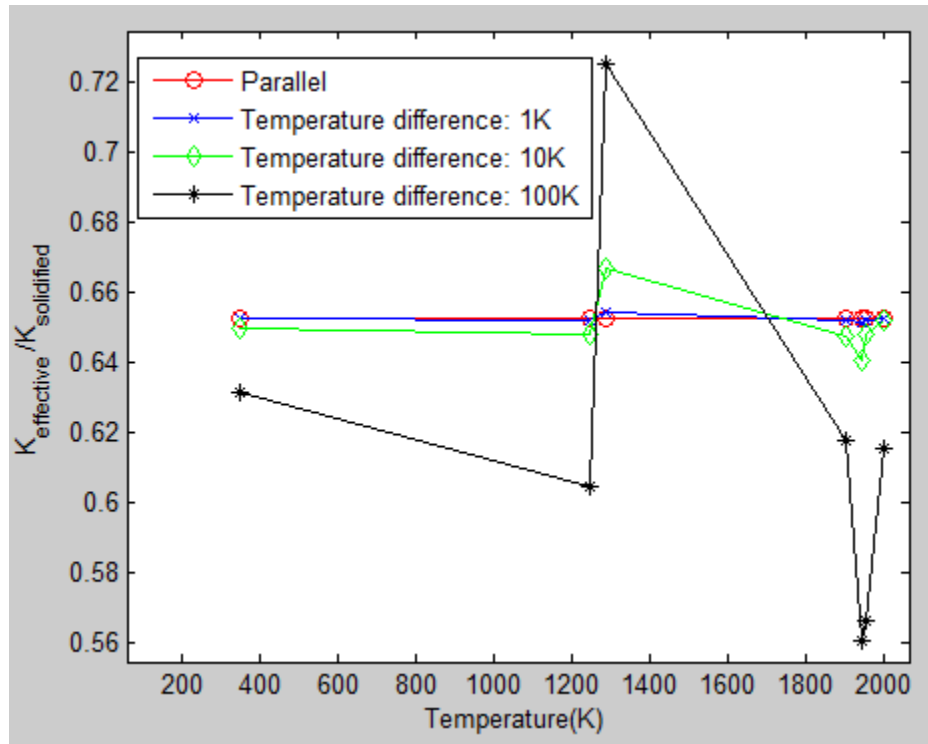


Figure 63 Effective conductivity ratio vs temperature for temperature dependent Ti64 properties at different temperature gradients

in Figure 62 and Figure 63 using temperature-dependent properties for Ti64 [105], a common SLM alloy. Figure 62 and Figure 63 show the effective thermal conductivity with respect to the temperature difference between the top and bottom surface. The effective thermal conductivity jump between the temperature regions of 1247~1287K shows the beta transus, and the temperature between 1874~1933K is considered the melting zone for Ti64 bulk material. Three scenarios have been illustrated in Figure 62 and Figure 63 with 1, 10 and 100 K temperature difference between the top and bottom surface and how they compare against the parallel spring model. These three scenarios illustrate the effects of boundary conditions on the effective results. The effective thermal conductivity matches well with the parallel spring model for a temperature difference of

1K with increasing deviations w.r.t the theoretical spring model as a function of increasing temperature difference between the top and bottom surfaces. These differences become clearer in Figure 63 which plots the ratio of effective thermal conductivity compared to solid thermal conductivity as a function of temperature. The nonlinear effective thermal conductivity is calculated for each critical temperature point. This illustrates that there is an imprecise transition in the effective thermal conductivity plot when temperature difference is large. It can be concluded that the effect of boundary conditions such as the temperature difference between the top and bottom surfaces and the initial temperature has a huge influence on the effective thermal conductivity if thermal conductivities are assumed to be non-linear and temperature dependent.

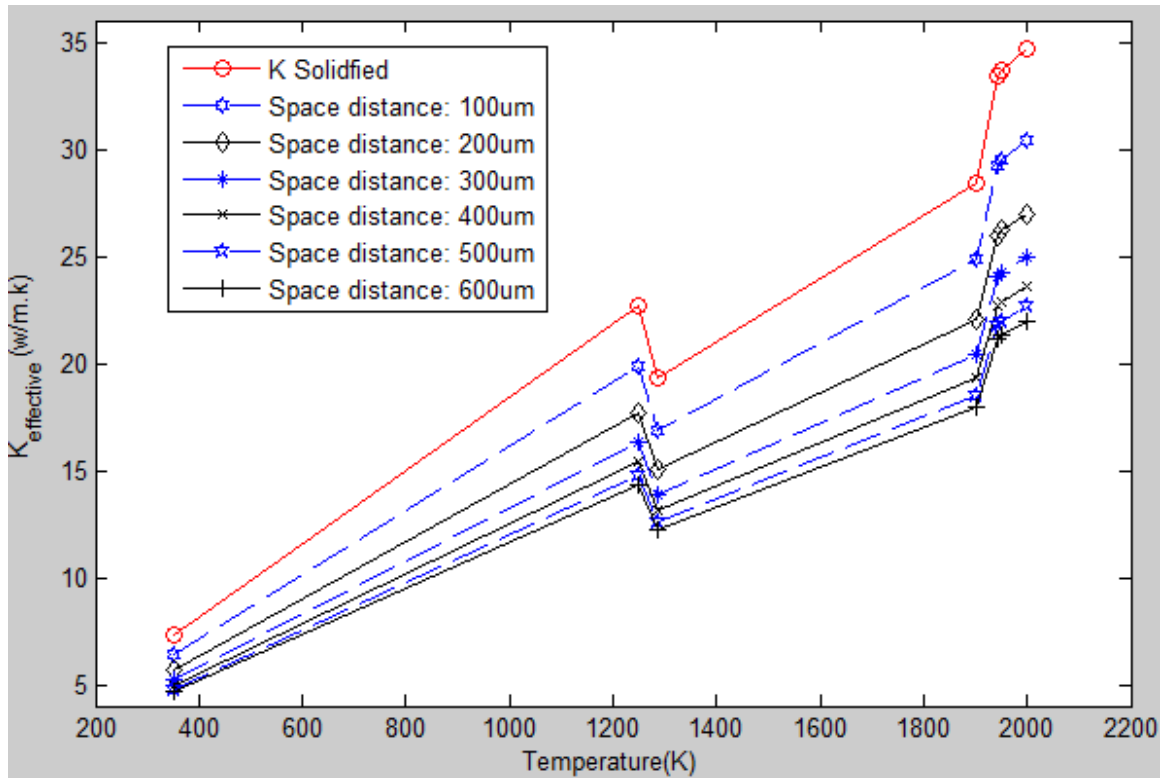


Figure 64 Effective thermal conductivity vs Temperature for temperature-dependent Ti64 properties at different support structure space distances

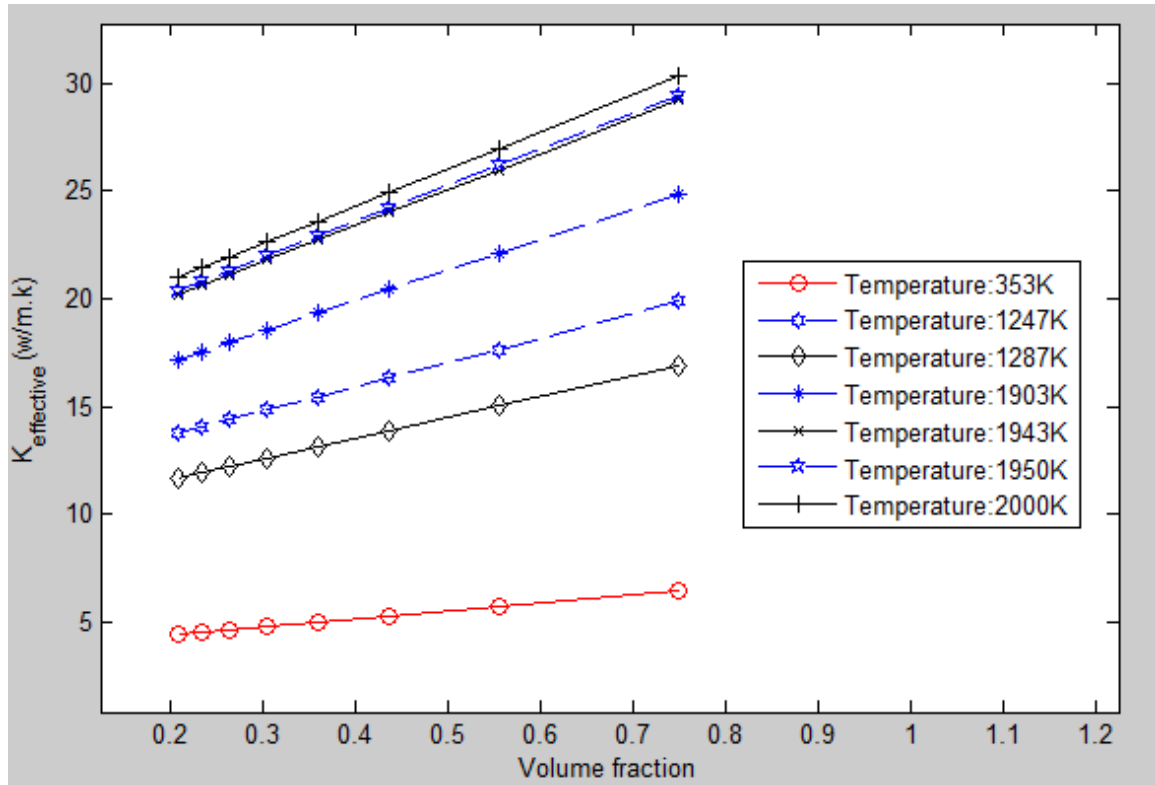


Figure 65 Effective thermal conductivity vs Volume fraction for temperature-dependent Ti64 properties

As shown in Figure 61, effective thermal conductivity increases with increasing volume fraction of solidified material. Figure 64 shows nonlinear effective thermal conductivity w.r.t. varying space distance. The space distance is a representation of the distance between the opposite surfaces of the hollow square prism entrapping the powder. It can be observed that the effective nonlinear thermal conductivity is proportional to the volume fraction of the solidified material. Figure 65 shows the nonlinear effective thermal conductivity as a function of volume fraction of the solidified support material at different temperatures. It can be observed that at any given temperature, the effective thermal conductivity increases as a function of increasing solid volume fraction.

6.5 Validation of the results of effective thermal properties

A comparative study of the temperature distribution between two scenarios is shown in Figure 66 and Figure 67. The two scenarios differ from one another by different thermal conductivity assumptions which have been applied at the element integration point. The original support structure is composed of a solidified wall and trapped power. The bulk material properties and the powder thermal conductivities were input to the model respectively. The comparison study aims to verify that thermal distribution due to effective and the real thermal conductivity are the same. Figure 66 with a linear thermal

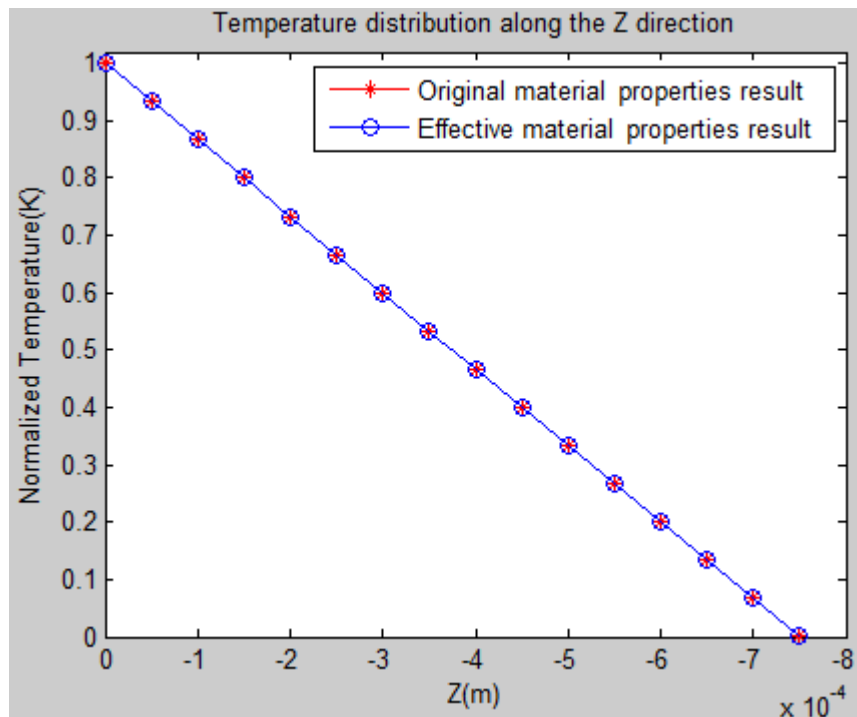


Figure 66 Temperature distribution of the RVE for linear material property conductivity assumption shows that the thermal distributions resulting from effective and original thermal conductivities are identical. On the other hand, in Figure 67 with non-linear thermal conductivity assumptions, the thermal distributions differ from each other by a relative maximum standard deviation of 3.5%. The thermal distribution curve shapes

as a function of distance from the top plane in the $-z$ direction show that the curvature and order of the effective and original thermal conductivity assumptions match.

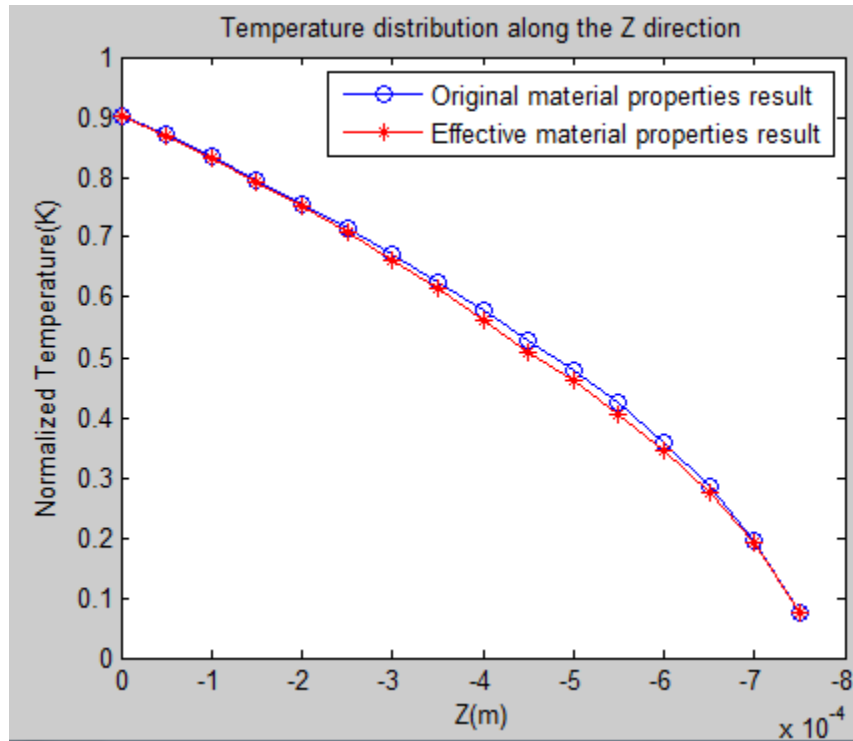


Figure 67 Temperature distribution of the RVE for nonlinear thermal conductivity

6.6 Conclusion and future work

The finite element model built in ANSYS successfully illustrated a manner to calculate the effective thermal conductivity of support structures in SLM consisting of a solidified material and entrapped powder in the intercellular spaces. The theories of homogenization and periodic boundary conditions were applied to study the steady state thermal behavior of the RVE. Both temperature independent (linear) and dependent (nonlinear) thermal property assumptions were studied in the model. The influence of volume fraction, number of cells in the RVE and boundary conditions on linear and nonlinear thermal assumptions were analyzed. The effective thermal properties of the support structure were compared against a parallel spring thermal counterpart and shown

to have a good match. The method has thus provided an efficient method for prediction of temperature by using an effective thermal conductivity to reduce the complexity of finite element analyses.

Support structures used for real parts should be optimized such that a minimum amount of supports to withstand thermal stress induced distortion should be added to a part. This would result in local property variations and anisotropy in the X, Y and Z directions. A method to apply an effective thermal conductivity for support structure with non-uniform wall thickness and spacing was shown to be accurate and thus merits further study.

CHAPTER 7 SUPPORT STRUCTURE DESIGN AND OPTIMIZATION FRAMEWORK

7.1 Introduction

The support structures generated by support generation modules of AM specific design software such as Magics are geometry and pattern driven and do not place support structures based upon any knowledge of the thermal stresses generated by the thermal field in metal powder bed fusion processes. Thus, support structure generation becomes a trial and error process driven primarily by a user's experience with similar geometries. This results in a waste of material and machine time. The lead time for successfully developing strategies for building parts using SLM is largely increased due to the trial and error process of support design and placement. A support structure optimization and design framework is being developed to overcome the difficulty of dealing with support structure in SLM. This chapter introduces the method and steps for a support structure optimization and design framework. Both analytical solutions and FEM are applied to optimize the support structure parameters.

As shown in Figure 68, the support structure generation module will be incorporated into the current thermomechanical process solver. The support structure is taken into consideration in the thermomechanical solver along with the input of process parameters, material properties and scan strategies. The goal is to create a force/strength map on the lower surfaces of a part to be built that guides the fitting of an optimized support structure to that force/strength map. One approach that is explored in this chapter

includes placing an “initial” support structure into the thermomechanical model along with the part geometry. An example of this initially assumed support structure is a block

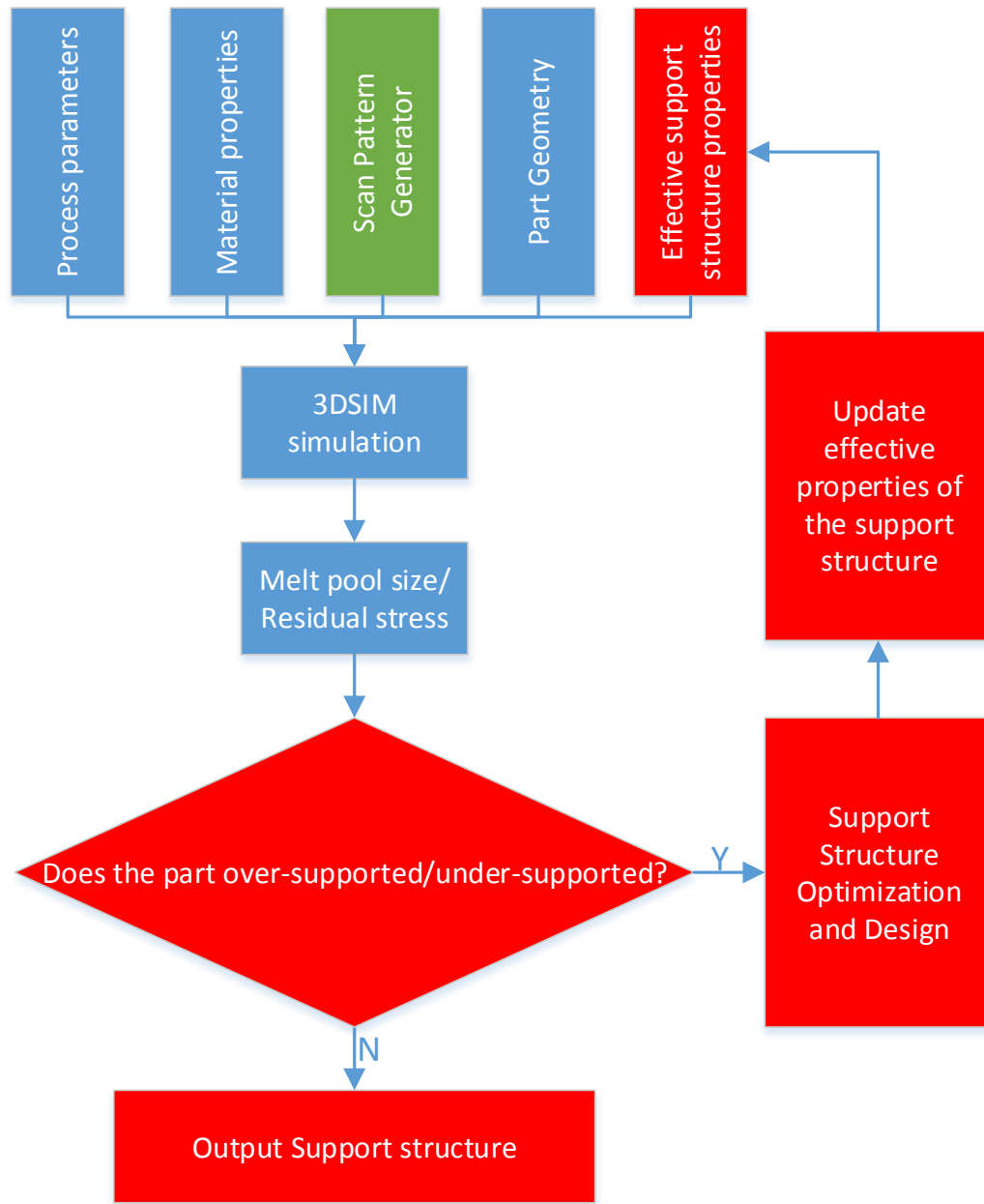


Figure 68 Support structure optimization and design flowchart for incorporation with 3DSIM

structure with powder in the intercellular spaces as shown in Figure 56. This block structure will be used to support the fabricated part on the substrate. The solidified

support and the powder trapped inside the support structure will be modeled using appropriate effective thermophysical properties as described in chapter 6. A cross-section of the mesh with solidified struts and trapped powder inside the intercellular space is shown in Figure 58. This model will be solved using a thermomechanical eigenmodal strategy layer-by-layer with a contact model to account for snapping of supports at their interface with the baseplate and/or the part. At the end of each simulation, the dimensions of the solidified struts will be periodically updated as a function of layer-by-layer buildup of the fabricated structure. In the meanwhile, it results in updated element properties from powder to solid with an updated total stiffness matrix.

7.2 The Support Structure Optimization and Design Framework

Figure 69 shows the framework for support structure optimization and design. It consists of two categories of algorithms, CAD operations and stress calculations shown in purple and red dotted boxes respectively. As explained in Figure 68, for a given ‘initial’ support structure, the thermal stress can be calculated and stored in a file format such as a CSV file. The algorithm starts with reading the part and thermal stress information in STL and CSV file formats respectively. The appropriate areas where support structures are necessary is determined based on some general rules of support structure generation. Based on empirical rules or user-directed inputs, a default support structure is calculated. Thermally induced stress is calculated using 3DSIM tools and optimized support parameters are calculated based on either analytical solutions or FEM. For different types of thermal stress, the maximal support structure parameters calculated from each scenario are recorded. The final support structure parameters are the maximal value of all scenarios and it is updated iteratively.

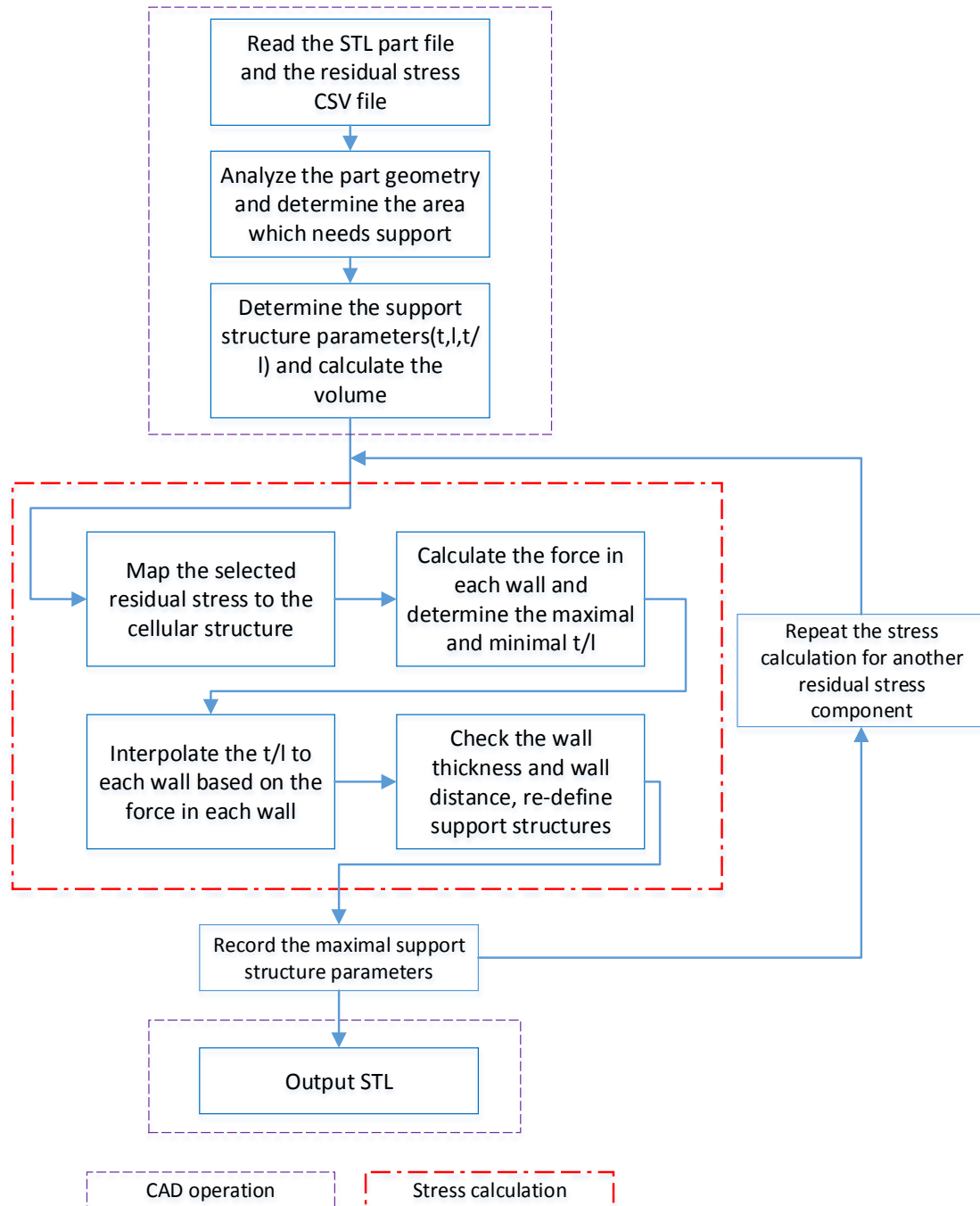


Figure 69 support structure optimization and design framework

All the steps of the support structure optimization and design framework are described in detail in this section. Both analytical solutions from a square Honeycomb structure and FEM are applied to calculate the support structure parameters. The

application of analytical solutions to support structure optimization is introduced in this chapter along with the steps of the methodology. The FEM method and its implementation is introduced in a new section.

7.2.1 Supporting Area Detection

For a given arbitrary part, the location and mass of support structures must be determined. Each part has a bounding box defined, as defined by ASTM standard terminology for Additive Manufacturing-Coordinate systems and test methodologies [126]. The bounding box provides the area for which support structures might be necessary and is defines the maximal support region. Some general empirical design rules could be used to reduce the support region. The surface angle with respect to the XY plane is one possible rule. This could be seen as a criterion and applied to eliminate unnecessary support areas.

The example below is a thick hemispherical dome structure as shown in Figure 22 and Figure 70 is the STL model in 2D. It is clear that the area to be considered for supporting this part is a circular area in 2D, and the dimensions of the bounding box varies dependent on the selection of surface angles. The diameter of the bounding area for the part is 190.48mm. A surface angle threshold of 45° was selected for this example. Surfaces having an angle of 45° and more with respect to the horizontal plane are considered not to need support structures and are not included in the supporting area.

Equation (15) represents a surface in three dimensional space where a, b, c and d are the coefficients for coordinates x, y, z and a constant respectively. These are determined by solving linear equations using the vertices of the triangles in an STL file. The surface angle is calculated using triangle normal $\mathbf{n} = (a, b, c)$ subtracted by 90° . After

applying the angle criterion to all the triangles in the STL file, the supporting area is reduced to a circular area with diameter of 130mm which can be seen from Figure 70.

$$a * x + b * y + c * z + d = 0 \quad (15)$$

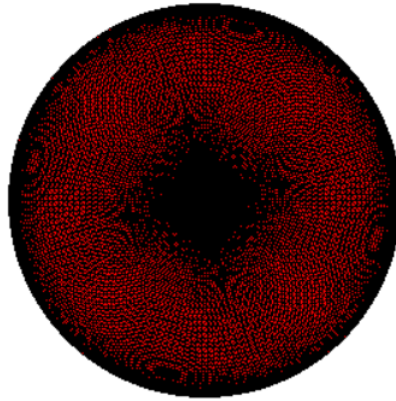


Figure 70 STL file representation of the part in 2D

7.2.2 Support Structure Default Parameters Determination

The support structure is set to the default parameters so as to decide the location of the supporting walls in the first stage. The support structure explored in this paper is the commonly used block support structure which is shown in Figure 71 [127] in the XYZ coordinate system. The basic structure has three primary parameters: t (thickness), l (spacing) and h (height of the structure). The value for parameters t and l is continuous with an interval which is defined by the resolution of the machine and the physical possibility for material processing. A minimal number of support walls is used to setup the default support structure, calculated using the dimensions of the bounding box divided by the maximal possible multiplications of t and l in both X and Y directions.

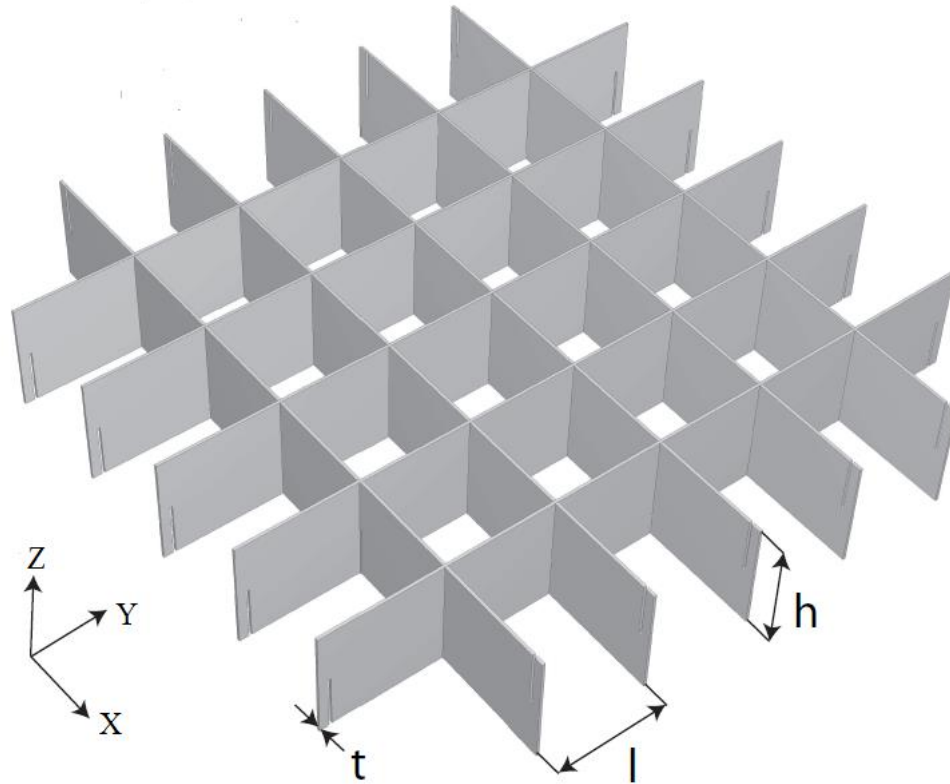


Figure 71 Square honeycomb structure [127]

7.2.3 Support Structure Volume Calculation

The height of the supporting walls in each cell must be provided in order to calculate the volume of the support structure. In addition, the extrusion of the support structure also needs the coordinates of the common line which the downward surface and the support structure walls intersect. Figure 72 is the flow chart applied to calculate the support structure volume. For the block support structure, each cell is a square and the supporting walls in one direction are vertical to the other direction. The first step is to find all triangle intersects with the current wall. Each triangle has a bounding box using the maximal and minimal coordinate of the vertices. The wall is considered to intersect the triangle if the coordinate of the wall is in the range of the bounding box. The plane and triangle intersection equation shown in Equation (8) is carried out to find the

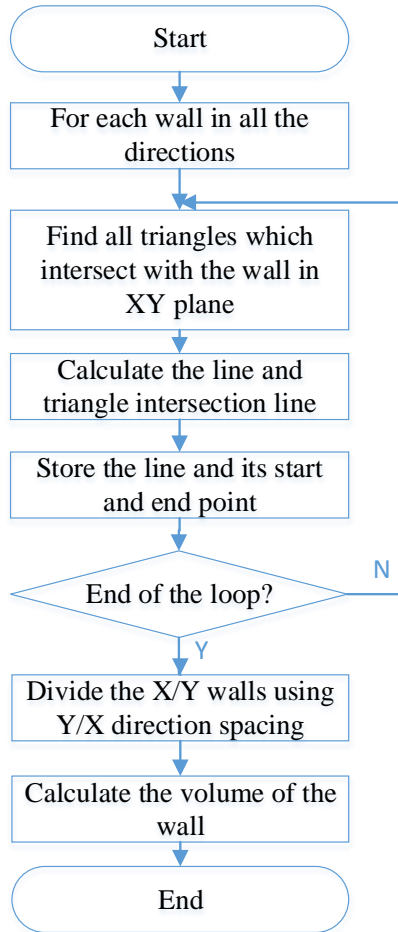


Figure 72. Flow chart for finding the support wall and triangle intersection line intersection lines for all the walls in 3D. Since the wall is simplified as a line when it is projected in the 2D plane, the line and triangle intersection is used to find the intersection line in 2D and the Z coordinate is interpolated based on the X and Y coordinates. Possible plane intersections with different lines are shown in Figure 73 (c, d, e, and f). The intersection could be also a single point as shown in (a, b). Different scenarios are dealt with independently in the algorithm. All the intersection lines for each triangle are sorted and the support wall is formed by connecting the lines sequentially. The support structure wall is divided into each cell by using the coordinate in the vertical direction since each cell might have a different thickness.

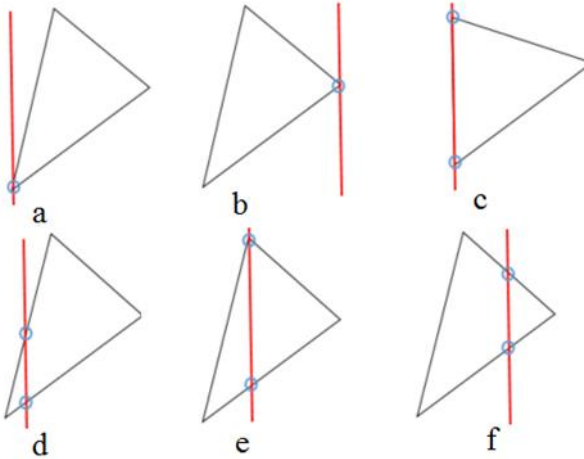


Figure 73. Line and triangle intersections

7.2.4 Non-Uniform Localized Support Design

The support structure shown in Figure 71 is designed to be uniform in thickness and spacing for the walls. However, for the given thermal stress, the force might be not uniformly distributed and so the support structure may not be uniform. The primary principles are to make sure that the support structure will not fail in large thermal stress areas and that the part is not over-supported in small thermal stress areas. Figure 74 elaborates the idea of non-uniform support structures. The blue square stands for the boundary of the part which could be random in shape. The green and red color defines the contour map of the thermal stress. The yellow color is the support structure wall and it has non-uniform thickness for the walls in the same X/Y location. The cell in the support structure allows for different parameters t_1, t_2, t_3, t_4 for the walls. Suppose that the thermal stress decreases from the red to the green area. In this case the support structure wall thickness should show a similar tendency of reducing the wall thickness from the red to the green area.

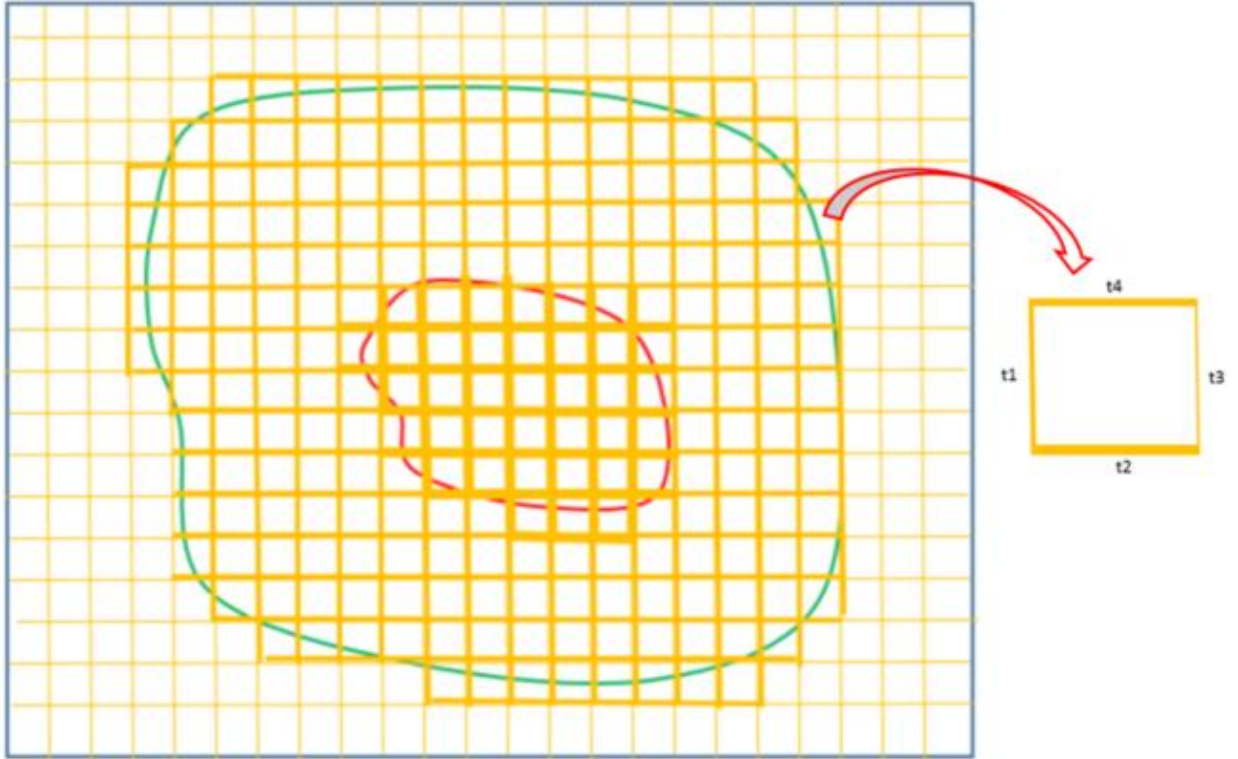


Figure 74 Non-uniform support structure where blue represents the part boundary, green/red represent thermal stress contour plot lines and yellow represents the support structure walls.

7.2.5 Linear Programming (LP) Method

As shown in Figure 74, each element cell has six independent variables, which are thickness for each strut t_1 , t_2 , t_3 , and t_4 and inter-strut distance d_1 , and d_2 which are predefined. Two sets of parameters tx_i and ty_j are defined for struts in both x and y directions in order to formulate the problem using an LP method from Equations (16) to (25):

$$\text{Min: } \sum_i \sum_p (t_{xi} * d_{yp} * h_{ip}) + \sum_i \sum_p (t_{yi} * d_{xp} * h_{pi}) \quad (16)$$

S.T.

$$d_{min} \leq dx_{i+nj} - (tx_{i+(j-1)n} + tx_{i+n+(j-1)n}) \leq d_{max} \quad (17)$$

$$i = 1, 2, \dots, n ; j = 1, 2, \dots, m$$

$$t_{min} \leq tx_{i+(j-1)n} + tx_{i+n+(j-1)n} \leq t_{max} \quad (18)$$

$$i = 3, 4, \dots, n-1; w = 3, 4, \dots, m-1$$

$$d_{min} \leq dx_{i+nj} - (tx_{i+(j-1)n} + tx_{i+n+(j-1)n}) \leq d_{max} \quad (19)$$

$$i = 1, 2, \dots, n; j = 1, 2, \dots, m$$

$$t_{min} \leq tx_{i+(j-1)n} + tx_{i+n+(j-1)n} \leq t_{max} \quad (20)$$

$$i = 3, 4, \dots, n-1; w = 3, 4, \dots, m-1$$

$$d_{min} \leq dy_{j+mi} - (ty_{j+(i-1)m} + ty_{j+m+(i-1)m}) \leq d_{max} \quad (21)$$

$$i = 1, 2, \dots, n; j = 1, 2, \dots, m$$

$$t_{min} \leq ty_{j+(i-1)m} + ty_{j+m+(i-1)m} \leq t_{max} \quad (22)$$

$$i = 3, 4, \dots, n-1; w = 3, 4, \dots, m-1$$

$$d_{min} \leq dy_{j+mi} - (ty_{j+(i-1)m} + ty_{j+m+(i-1)m}) \leq d_{max} \quad (23)$$

$$i = 1, 2, \dots, n; j = 1, 2, \dots, m$$

$$t_{min} \leq ty_{j+(i-1)m} + ty_{j+m+(i-1)m} \leq t_{max} \quad (24)$$

$$i = 3, 4, \dots, n-1; w = 3, 4, \dots, m-1$$

$$\frac{\iint \sigma_q dx dy}{area} \leq \sigma_{allowable} \quad (25)$$

where all the variables are non-negative and m and n are numbers of walls in x and y directions respectively.

The above problem is expressed in matrix format from Equation (26) to (28).

$$\text{Min: } \vec{f}\vec{x} \quad (26)$$

$$\text{S.T: } A\vec{x} \leq b \quad (27)$$

$$\vec{x}_{min} \leq \vec{x} \leq \vec{x}_{max} \quad (28)$$

Where

$$\vec{x} = [tx_1, tx_2, \dots, tx_{i+(j-1)n}, ty_1, ty_2, \dots, ty_{j+(i-1)m}]'$$

\vec{f} is the coefficient of the objective function with size $2*n*m$ by 1

A is the coefficient matrix of the constraint equation with size $2*n*m$ by $2*n*m$

The dimension of b is $2*n*m$ by 1

$\vec{x}_{min}, \vec{x}_{max}$ are the lower and upper boundaries of the variables.

The number of variables in this LP problem is $6*m*n$ which makes it extremely difficult to solve when the dimensions of the part becomes large. Even though the LP problem is solvable using methods such as Simplex or Interior point [128], the results are not consistent with the thermal stress distribution. The anticipated optimized support structure result should have a similar distribution to the thermal stress distribution. The correlation of support structure parameters and thermal stress distribution for different supporting walls is found by using the same ratio of thermal stress. The assumption helps to reduce the number of variables in the LP problem to two which are the minimal and maximal t/l ratio corresponding to minimal and maximal thermal stress.

7.2.6 Minimal Cross-Section Area

Equation (29) is the cross-sectional area of the support structure. If n_x and n_y from Equation (30) are substituted into Equation (29) and then both the denominator and numerator are divided by l^2 , the cross-sectional area is in proportion to the ratio t/l . The minimal cross-section is found when t/l is minimal.

$$Area = n_x * n_y * 4 * (t * l + t^2) \quad (29)$$

$$n_x = \left\lfloor \frac{A}{t + l} \right\rfloor, \quad n_y = \left\lfloor \frac{B}{t + l} \right\rfloor \quad (30)$$

The variable Area in Equation 29 is the area of the cross-section, n_x is the number of cells in the X direction, n_y is the number of cells in the Y direction, A and B are the size of the support structure, the operator $[n]$ is rounded to the nearest integer in the negative direction, t is the thickness and l is the length between walls.

7.2.7 Thermal Stress Mapping to Support Structures

The thermal stress is stored in the multi-scale mesh from the simulation. The thermal stress is mapped to the cellular support structure using iso-parametric interpolation, and the 1st order shape function is applied [4].

The thermal stress is a numerically distributed force in each node. As shown in Figure 75 [129], the concentrated force and centroid of the force in each cell is calculated using Equations (31) and (32). The trapezoidal integration method is applied to evaluate the integration in the equations.

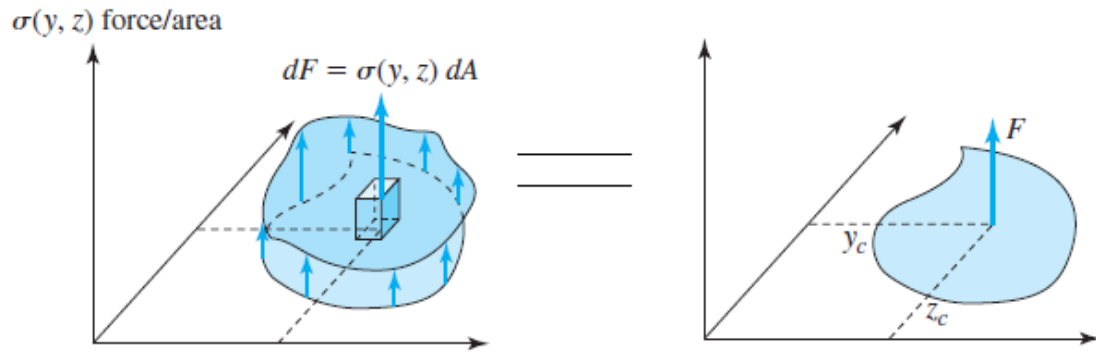


Figure 75 Static equivalency for a distributed force on a surface [129]

$$F = \iint_A \sigma(y, z) dydz \quad (31)$$

$$y_c = \frac{\iint_A y\sigma(y, z) dydz}{F}, \quad z_c = \frac{\iint_A z\sigma(y, z) dydz}{F} \quad (32)$$

7.2.8 t/l Ratio Calculation Based on Thermal Stress

7.2.8.1 Simple Structure Surface (SSS) Method

In order to calculate the equivalent force acting in each wall of a cell, the Simple Structure Surface (SSS) method is used. The SSS method is widely used in designing plane, box or van structure such as vehicle panel/frame structures [130]. It is used to convert the concentrated thermal stress F in each cell into four components which are the support structure walls. Figure 76 [131] illustrates the force working on the support structure and how to calculate the force each walls experiences. Suppose the centroid of the force is in the middle of the cell, all the K_i are the same. However, the centroid is dependent on the thermal stress distribution and Equations (41), (42), (43), and (44) are used to calculate the K_i . The derivatives are described as follows [131].

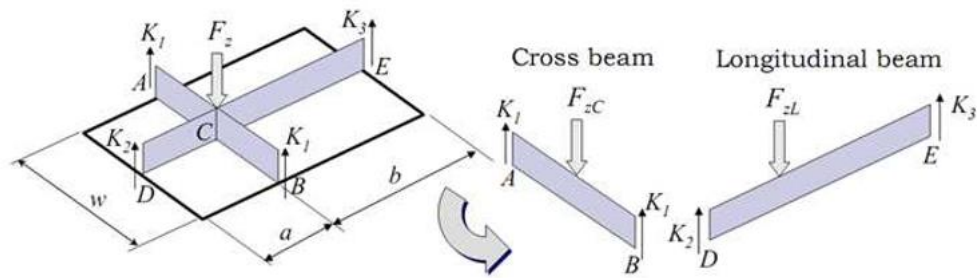


Figure 76 Load distribution for each wall [131]

Equilibrium & Compatibility equations

$$\delta_{Cross-beam} = \delta_{longi-beam} \quad (33)$$

$$K_1 + K_2 + K_3 + K_4 = F_{ZL} \quad (34)$$

$$K_1 w_1 = K_2 w_2 \quad (35)$$

$$K_3 a = K_4 b \quad (36)$$

$$w_1 + w_2 = w \quad (37)$$

The moment of the inertia of both beams AB and DE are I_C and I_L .

$$I_C = \frac{hw^3}{12} + hw \left(\frac{w_1 - w_2}{2} \right)^2 \quad (38)$$

$$I_L = \frac{hL^3}{12} + hL \left(\frac{a - b}{2} \right)^2 \quad (39)$$

And

$$\frac{K_1 + K_2}{K_3 + K_4} = \frac{I_C}{I_L} \quad (40)$$

The solution for Ks are:

$$K_4 = \frac{F_{ZL}}{\left(1 + \frac{b}{a}\right) \left(1 + \frac{w^3 + 3w(w_1 - w_2)^2}{l^3 + 3l(a - b)^2}\right)} \quad (41)$$

$$K_3 = \frac{b}{a} K_4 \quad (42)$$

$$K_2 = \frac{1 + \frac{b}{a}}{1 + \frac{w_2}{w_1}} * \frac{w^3 + 3w(w_1 - w_2)^2}{l^3 + 3l(a - b)^2} K_4 \quad (43)$$

$$K_1 = \frac{w_2}{w_1} K_2 \quad (44)$$

7.2.8.2 Analytical Solutions for Calculation of t/l

The maximal and minimal support structure t/l ratio is determined using the mechanical failure formulations from square honeycomb structures. As shown in Figure 71, the force in the plane XY is noted as in plane and the plane XZ/YZ is noted as out of

plane. The in plane shear force and out of plane tensile and compression forces are taken into consideration.

Tensile strength out of plane (Z direction) [127, 132]

Experiments and simple analyses have shown that their out of plane elastic properties scale linearly with the relative density $\bar{\rho}$ [127] which is shown in Equation (45).

$$\bar{\rho} = \frac{2t}{l} \quad (45)$$

The measured true tensile stress versus logarithmic strain response may be approximated as an elastic, linearly hardening solid [132]. The ratio of the yield stress and material yield strength is in Equation (46):

$$\frac{\sigma_{pl}^*}{\sigma_{ys}} = \frac{\rho^*}{\rho_s} = \frac{2t}{l} \quad (46)$$

where σ_{ys} is the out of plane plastic yield strength of the cellular structure, σ_{pl}^* is the solid cell wall material yield strength, ρ^* is the density of cellular material, and ρ_s is the solid cell wall material.

Compression strength out of plane (Z direction) [132]

The peak compressive strength of the honeycomb is governed by a competition between elastic buckling and plastic micro-buckling of the cell walls [132]. It is supposed that the cell walls are treated as plates and simply supported along their vertical edges. The elastic buckling load is as shown in Equation (47).

$$P_c = \frac{k\pi^2}{6(1-\nu)} G \frac{t^3}{l} \quad (47)$$

For simply supported boundary conditions along the top and bottom edges, $k \approx 4$ provided that $\frac{H}{l} > 1$. H and l are the height of the plate and spacing of the cell.

When k is chosen as 4, the elastic bifurcation stress σ_c^e of the square honeycomb becomes

$$\sigma_c^e = \frac{4\pi^2}{3(1-\nu)} G \left(\frac{t}{l}\right)^3 \quad (48)$$

Shear stress in the plane (XY direction) [127]

Elastic shear buckling strength of a clamped plate is given by Equation (49) [133]:

$$\tau_c = \frac{k\pi^2 E}{12(1-\nu)} \left(\frac{t}{l}\right)^2 \quad (49)$$

where k varies from 8.99 to 12.88 depending on the ratio of $\frac{t}{l}$, E is the elastic modulus, and ν is the poisson ratio. Note that for a honeycomb with aspect ratio 1, and clamped edges along $Z = 0$ and $Z = h$, $k = 12.28$ [127].

The maximum allowable shear stress of the square honeycomb made from an elastic, ideally plastic solid is described in Equation (50).

$$\tau_{3n}^p = \begin{cases} \frac{k\pi^2 E}{96(1-\nu^2)} \bar{\rho}^3, & \text{if } \bar{\rho} < \sqrt{\frac{48(1-\nu^2)\sigma_y}{\sqrt{3}k\pi^2 E}} \\ \frac{\sigma_y}{2\sqrt{3}} \bar{\rho} & , \quad \text{otherwise} \end{cases} \quad (50)$$

The plastic shear buckling stress of clamped plates is estimated from Equation (51)

where G_s is the secant shear modulus from Equation (52).

$$\tau_c^p = \frac{k\pi^2 G_s}{6(1-\nu)} \left(\frac{t}{l}\right)^2 \quad (51)$$

$$G_s = \frac{\tau}{\gamma} = \frac{\sigma}{3\epsilon} \quad (52)$$

The shear strength of the square honeycomb is simplified in Equation (53) assuming that the square honeycomb collapse when either the wall parallel to the X axis or Y axis plastically buckles.

$$\tau_{3n}^p = \frac{\tau_c^p}{2} \bar{\rho} \quad (53)$$

7.2.9 t/l Interpolation

The minimal t/l ratio is calculated for a specific thermal stress as well as the interval of the minimal t/l ratio for a given thermal stress distribution. For each scenario described above, the lower and upper bounds for the minimal t/l ratio are calculated and the max operation is carried out to find the safest minimal t/l interval. Since the force K in each wall is calculated based on the SSS method, its t/l ratio is interpolated using the maximal and minimal t/l ratio and also the corresponding maximal and minimal K. Once the t/l ratio is determined for each support structure wall, the t and l are found by solving the two variable linear equations since the sum of t and l is also known.

7.2.10 Post-processing

The value of variable thickness (t) and spacing (l) is constrained by practical physical limitations for support structure fabrication. The minimal value of the thickness is dependent on the resolution of the machine and diameter of the powder. The maximal value is determined by considering difficulties in removal during the post-processing stage. It is necessary to adjust results from interpolation by applying rules based upon user-defined or machine-specific boundaries for variables.

7.2.11 STL Output

The readable file for support structures in SLM machines is an STL file. Each wall surface is triangulated and written into an STL file.

7.2.12 Example

Distortion results from literature [134] are cited to generate thermal stresses for support structure optimization. Figure 77 [134] shows the deformation of a twin cantilever structure after cutting from the support structure. According to the curvature of the deformation in the plotting, the thermal stress is assumed to be a 1D quadratic function in the X direction and constant in the Y direction, as shown in Figure 78.

The minimal and maximal wall thickness (t) and wall spacing (l) used for this part is explored in chapter 8. Based on the calculation, it is assumed that there are 40x5 walls in the X and Y directions respectively in this case study. The results for the support structure wall thickness in X and Y directions are shown in Figure 79 and Figure 80 respectively. The wall thickness in the X direction shows a similar distribution to the thermal stress except for the edges. However, the wall thickness in the Y direction are all the same. This is because the thermal stress is assumed to be 1D and uniform in the Y direction.

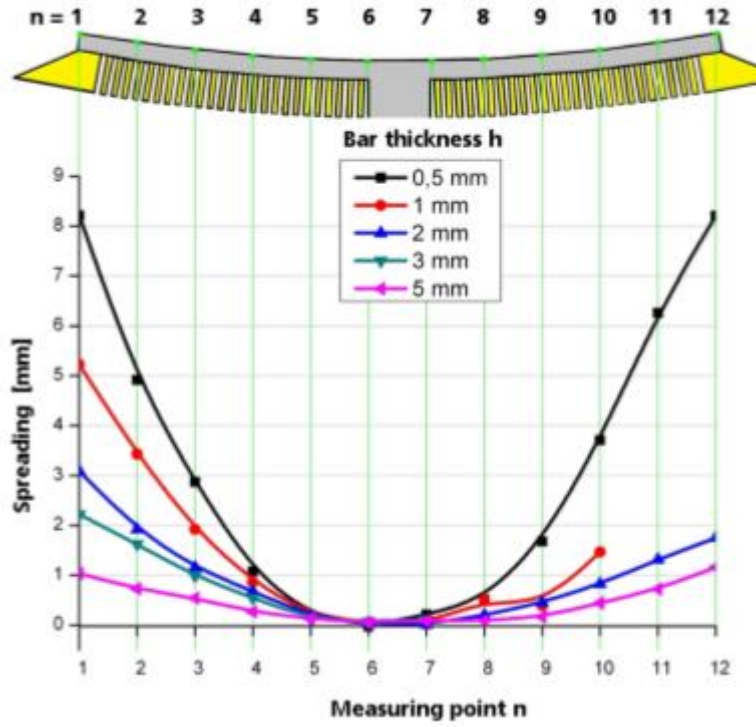


Figure 77 Spreading of the twin cantilever depending on bar thickness (h) and measurement point (n) [134]

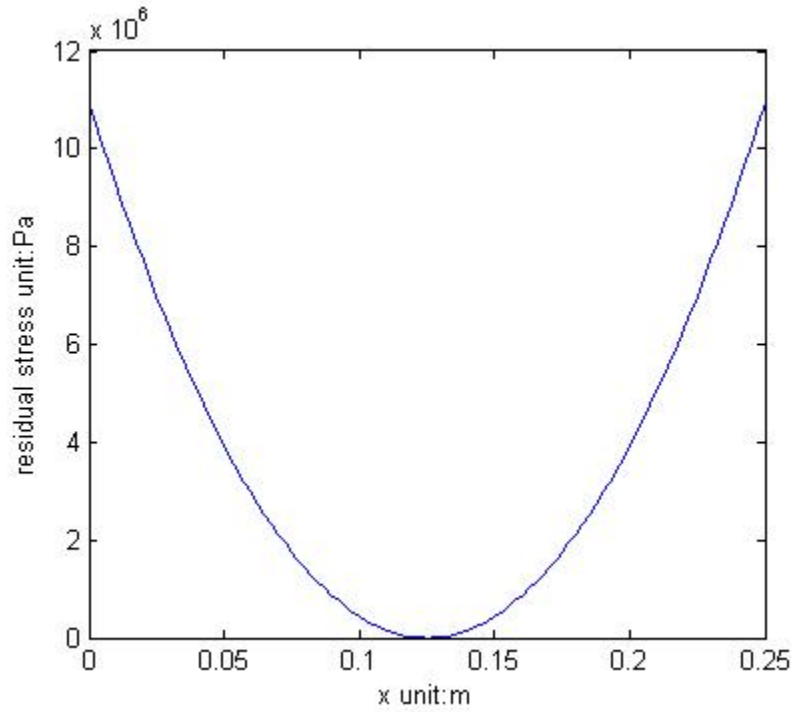


Figure 78 Assumed quadratic thermal stress

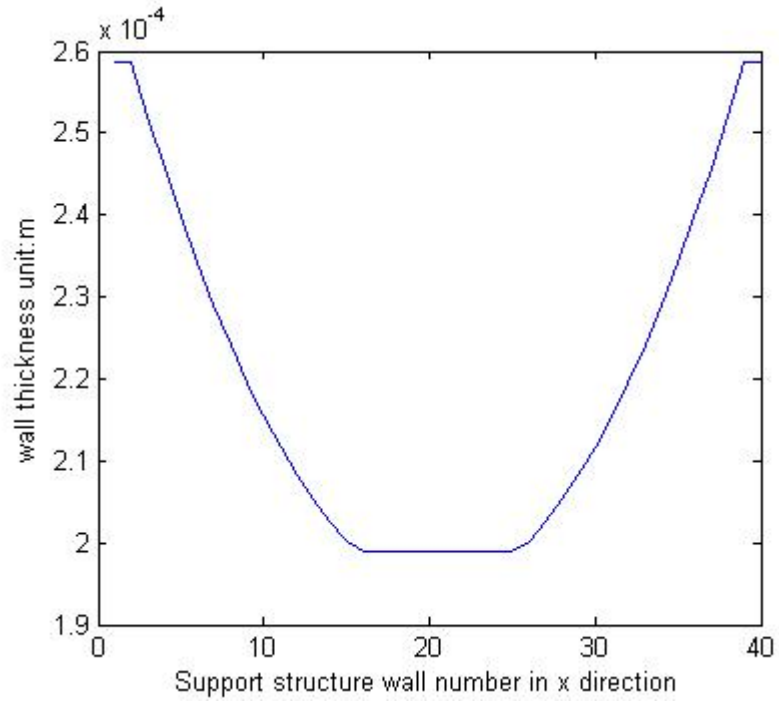


Figure 79 Optimized wall thickness in the X direction

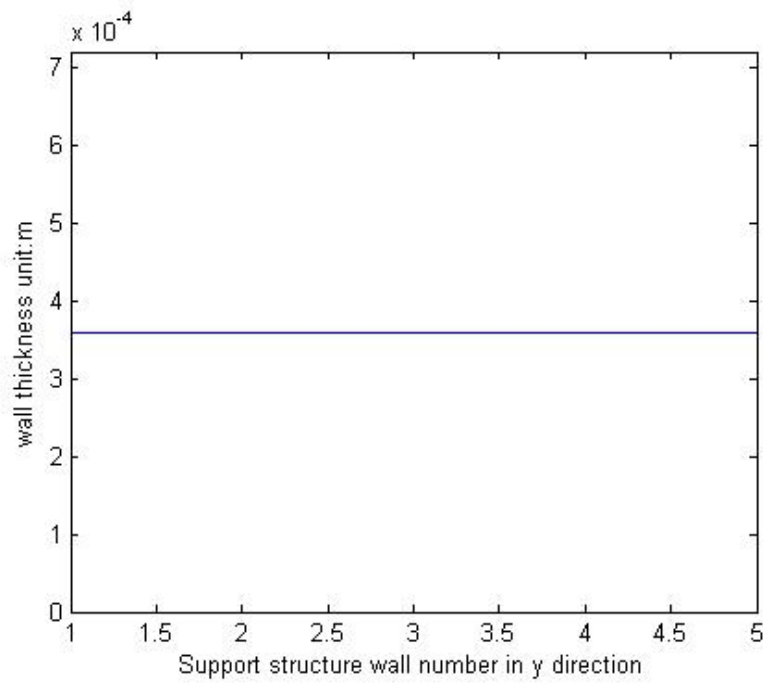


Figure 80 Optimized wall thickness in the Y direction

7.3 FEM Based Support Structure Optimization

FEM is applied to simulate part distortion under thermal stress boundary conditions. Figure 81 shows the flow chart of FEM analysis for support structure optimization. It starts with applying the thermal stress and other boundary conditions. In each iteration, the maximal stress/distortion is checked so as to see if it exceeds the allowed criterion. The corresponding degree of freedom (DOF) is set to zero on the node which behaves as the support structure walls. The location of the node and its stress is kept for further configuration of the support structure.

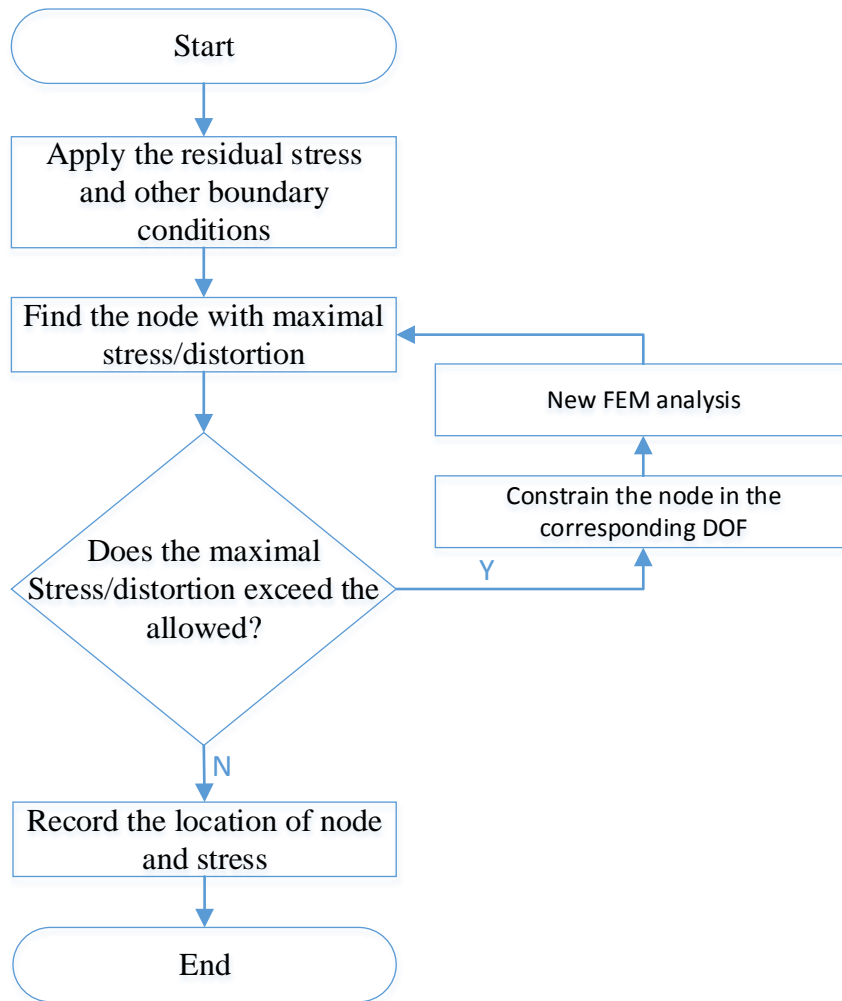


Figure 81 Flow chart of FEM analysis for support structure optimization

7.3.1 FEM Formulation

Support structure optimization for a thin plate structure was analyzed. The 1D, 2D and 3D representation of a cantilever beam structure is shown in Figure 82, Figure 83 and Figure 84.

7.3.1.1 1D Formulation

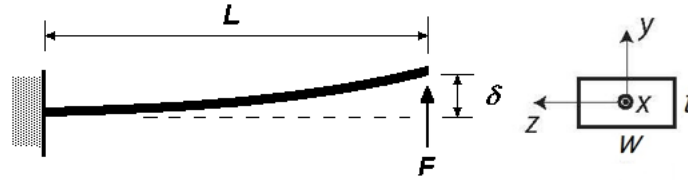


Figure 82 1D representation of the structure

The 2 nodes beam element is used and element stiffness matrix becomes:

$$k = \frac{EI}{l^3} \begin{bmatrix} Al^2/I & 0 & 0 & -Al^2/I & 0 & 0 \\ 0 & 12 & 6l & 0 & -12 & 6l \\ 0 & 6l & 4l^2 & 0 & -6l & 2l^2 \\ -Al^2/I & 0 & 0 & Al^2/I & 0 & 0 \\ 0 & -12 & -6l & 0 & 12 & -6l \\ 0 & 6l & 2l^2 & 0 & -6l & 4l^2 \end{bmatrix} \quad (54)$$

7.3.1.2 2D Formulation

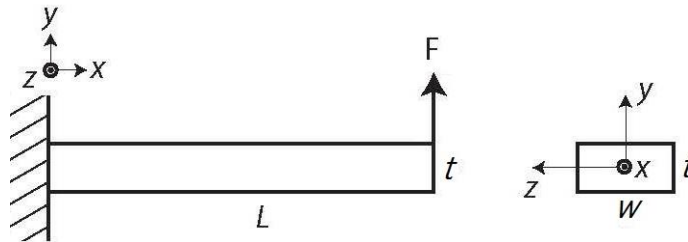


Figure 83 2D representation of the structure

The 4 nodes bilinear quadrilateral element is used and the shape function becomes:

$$N_1 = \frac{1}{8}(1 - \xi)(1 - \eta) \quad N_2 = \frac{1}{8}(1 + \xi)(1 - \eta) \quad (55)$$

$$N_3 = \frac{1}{8}(1 + \xi)(1 + \eta) \quad N_4 = \frac{1}{8}(1 - \xi)(1 + \eta)$$

7.3.1.3 3D Formulation

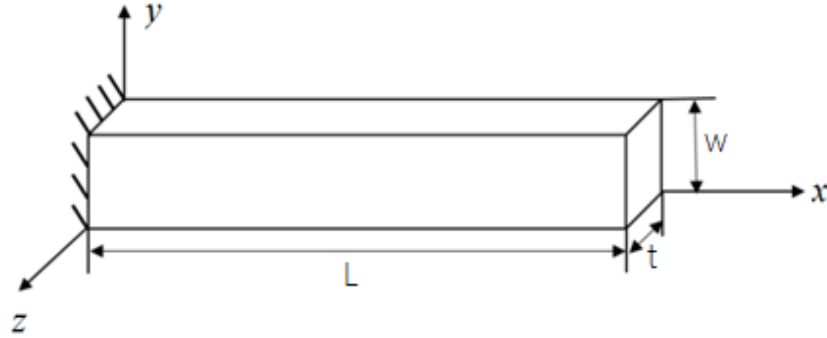


Figure 84 3D representation of the structure

The 8 nodes hexahedron element is used and the shape function becomes:

$$\begin{aligned}
 N_1 &= \frac{1}{8}(1 - \xi)(1 - \eta)(1 - \varsigma) & N_2 &= \frac{1}{8}(1 + \xi)(1 - \eta)(1 - \varsigma) \\
 N_3 &= \frac{1}{8}(1 + \xi)(1 + \eta)(1 - \varsigma) & N_4 &= \frac{1}{8}(1 - \xi)(1 + \eta)(1 - \varsigma) \\
 N_5 &= \frac{1}{8}(1 - \xi)(1 - \eta)(1 + \varsigma) & N_6 &= \frac{1}{8}(1 + \xi)(1 - \eta)(1 + \varsigma) \\
 N_7 &= \frac{1}{8}(1 + \xi)(1 + \eta)(1 + \varsigma) & N_8 &= \frac{1}{8}(1 - \xi)(1 + \eta)(1 + \varsigma)
 \end{aligned} \tag{56}$$

7.3.1.4 B-Bar Method [135]

Two Gaussian points were chosen to numerically calculate the integration for the 2D and 3D FEM formulations. However, various finite element schemes result in poor observed convergence rate. This is due to the so called ‘locking’ effect, especially for the analysis of elastic problems when the material is nearly incompressible [136]. The B-Bar method is to build a new appropriate and approved B matrix by splitting the B matrix into dilatational and deviatoric parts.

The B matrix of the element is:

$$B = \begin{bmatrix} B_1 & 0 & 0 \\ 0 & B_2 & 0 \\ 0 & 0 & B_3 \\ 0 & B_3 & B_2 \\ B_3 & 0 & B_1 \\ B_2 & B_1 & 0 \end{bmatrix} \quad (57)$$

And the dilatational part of B is:

$$B^{dil} = \frac{1}{3} \begin{bmatrix} B_1 & B_2 & B_3 \\ B_1 & B_2 & B_3 \\ B_1 & B_2 & B_3 \\ 0 & 0 & 0 \\ 0 & 0 & 0 \\ 0 & 0 & 0 \end{bmatrix} \quad (58)$$

The deviatoric part B is:

$$B^{dev} = B - B^{dil} \quad (59)$$

To achieve an effective formulation for nearly incompressible applications, \bar{B}^{dil} is the approved B^{dil} .

$$\bar{B}^{dil} = \frac{1}{3} \begin{bmatrix} \bar{B}_1 & \bar{B}_2 & \bar{B}_3 \\ \bar{B}_1 & \bar{B}_2 & \bar{B}_3 \\ \bar{B}_1 & \bar{B}_2 & \bar{B}_3 \\ 0 & 0 & 0 \\ 0 & 0 & 0 \\ 0 & 0 & 0 \end{bmatrix} \quad (60)$$

So the new B-bar is:

$$\bar{B} = B^{dev} + \bar{B}^{dil} = \begin{bmatrix} B_5 & B_6 & B_8 \\ B_4 & B_7 & B_8 \\ B_4 & B_6 & B_9 \\ 0 & B_3 & B_2 \\ B_3 & 0 & B_1 \\ B_2 & B_1 & 0 \end{bmatrix} \quad (61)$$

where:

$$B_4 = \frac{\bar{B}_1 - B_1}{3}, B_5 = B_1 + B_4, B_6 = \frac{\bar{B}_2 - B_2}{3}, \quad (62)$$

$$B_7 = B_2 + B_6, B_8 = \frac{\bar{B}_3 - B_3}{3}, B_9 = B_3 + B_8$$

7.3.2 Sensitivity Analysis

The analytical solution for the maximum deflection for 1D and 2D FEM is shown in Equations (63) and (64).

$$\delta_{\max} = \frac{PL^3}{3EI} \quad (63)$$

$$\delta_{\max} = \frac{PL^3}{3EI} + \frac{6PL}{5GA} \quad (64)$$

P is the uniform shearing force for the tip of the beam, L is the length of beam, A is the cross-sectional area, E is the elastic modulus, G is the shearing modulus, and I is the moment of inertia.

A thin plate is used to validate the accuracy and convergence of the code. The part dimension is: L = 50mm, W = 5mm and t = 2mm. The material properties are: E = 1.138E11, $\nu = 0.342$, and the force P = 4x10⁵N. Three sets of results from Matlab code with full integration and B bar method, and ANSYS using default FEM schemes are compared.

Figure 85 shows the result comparison of ANSYS and Matlab analytical integration for the 1D problem. The maximal deflection is 0.04394mm using Equation (63) and there is no error for the Matlab code since it is using the analytical integration.

Figure 86 shows the result comparison for the 2D problem. The maximal deflection is 0.044mm using Equation (64). The full integration result matches ANSYS, however, the B bar result has better accuracy than both. The result is converging to the maximal deflection with a relative error of 0.45% for the B bar method when the element division is 150x6.

Figure 87 shows the result comparison for the 3D problem. The maximal deflection results from Equation (64) were used in the 3D comparison as well. The B bar method result matches the ANSYS result which both have better accuracy than the full integration result. The B bar result is converging to the maximal deflection with a relative error of 1.59% when the element division is 100x10x4.

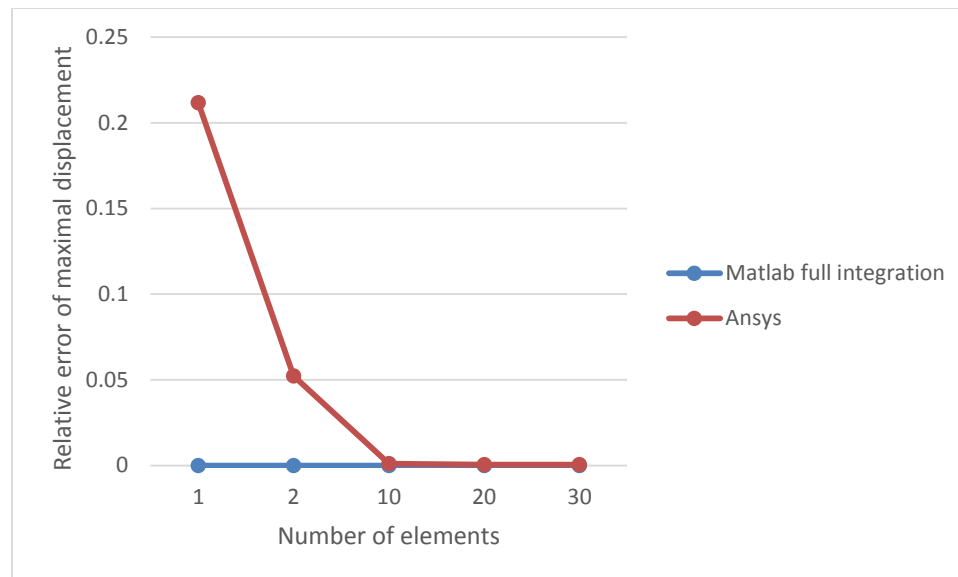


Figure 85 Sensitivity analysis of 1D FEM result

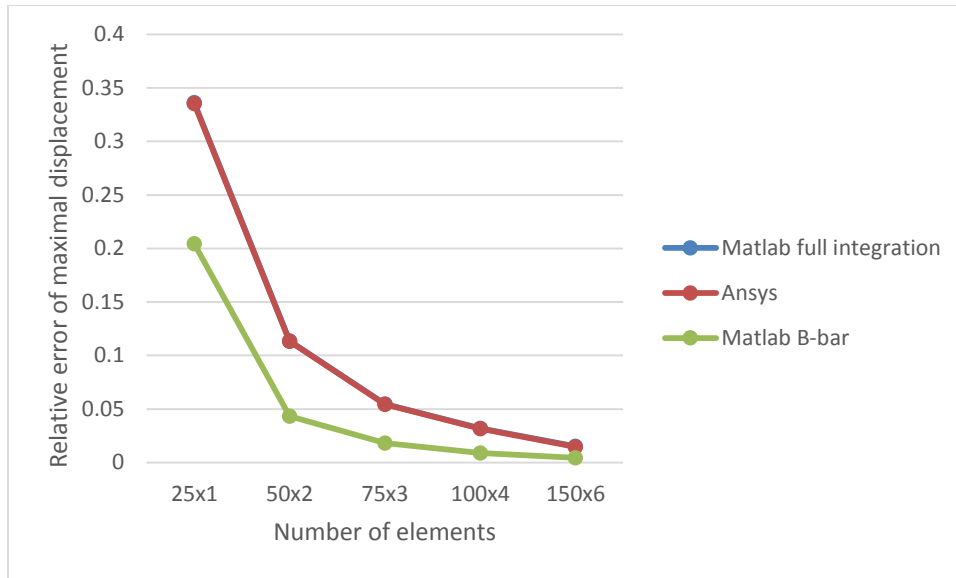


Figure 86 Sensitivity analysis of 2D FEM result

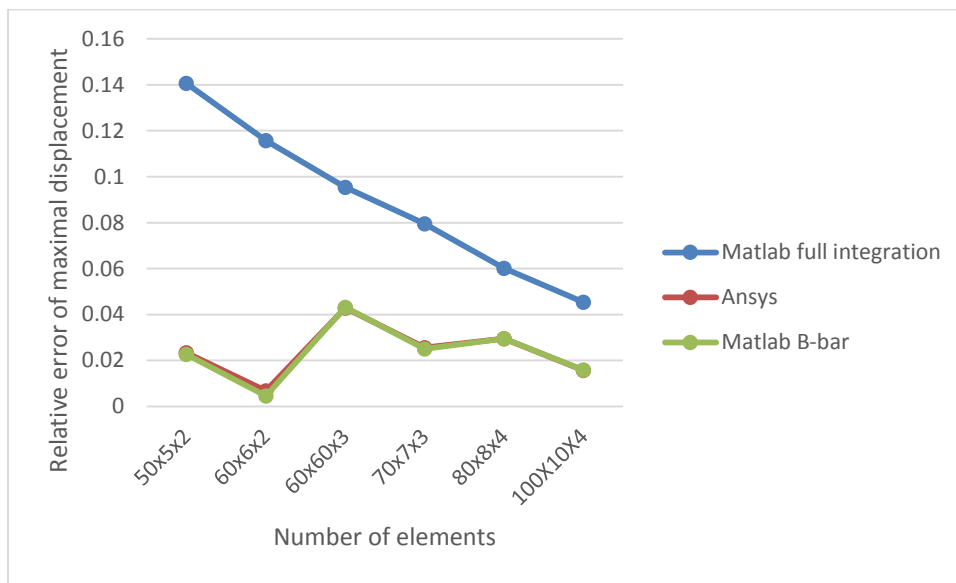


Figure 87 Sensitivity analysis of 3D FEM result

7.3.3 Support Structure Optimization Example Based on FEM Results

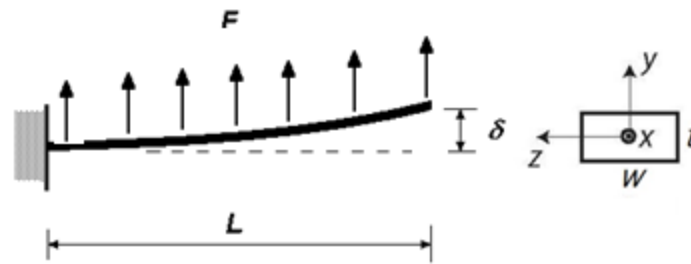


Figure 88 The uniform distributed force cantilever beam

In this case study, the dimension of the part is the same as the example above. However, the force F with magnitude of $5 \times 10^7 \text{N}$ is uniformly distributed over the top surface and the maximal deflection is calculated using Equation (65).

$$\delta_{\max} = \frac{FL^3}{8EI} = 2.0595 \text{mm} \quad (65)$$

As shown in Figure 81, the determination of support structures is iteratively calculated based on FEM until the deflection of the plate is under the requirement.

Figure 89, Figure 90, Figure 91 and Figure 92 show steps to find the support structure locations for the 1D cantilever problem. The maximal deflection as shown in Figure 89 is 2.0603mm.

Figure 93, Figure 94, Figure 95 and Figure 96 show steps to find the support structure locations for the 2D cantilever problem. The maximal deflection as shown in Figure 93 is 2.0702mm.

Figure 98, Figure 99, Figure 100 and Figure 101 show steps to find the support structure locations for the 3D cantilever problem. The maximal deflection as shown in Figure 98 is 2.0827mm.

The location of support structures found from the FEM procedure could be fit into the support structure optimization framework in the future. The parameters for each support structure wall is determined by the corresponding stress at the specific node.

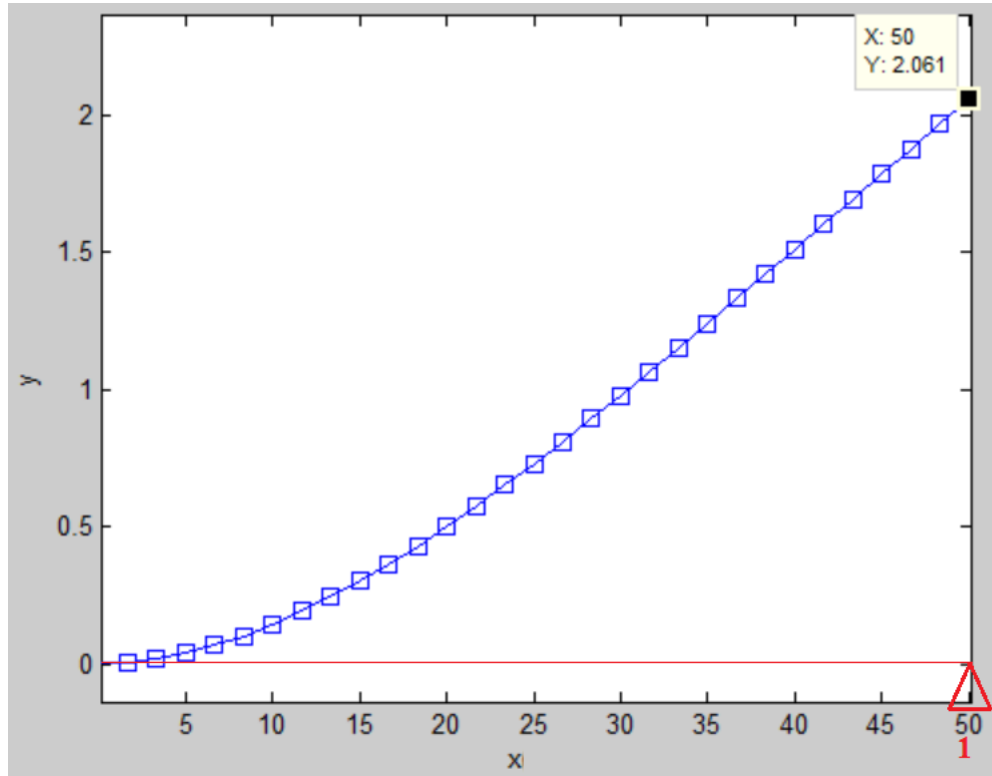


Figure 89 1st step for a 1D support structure (Unit: mm)

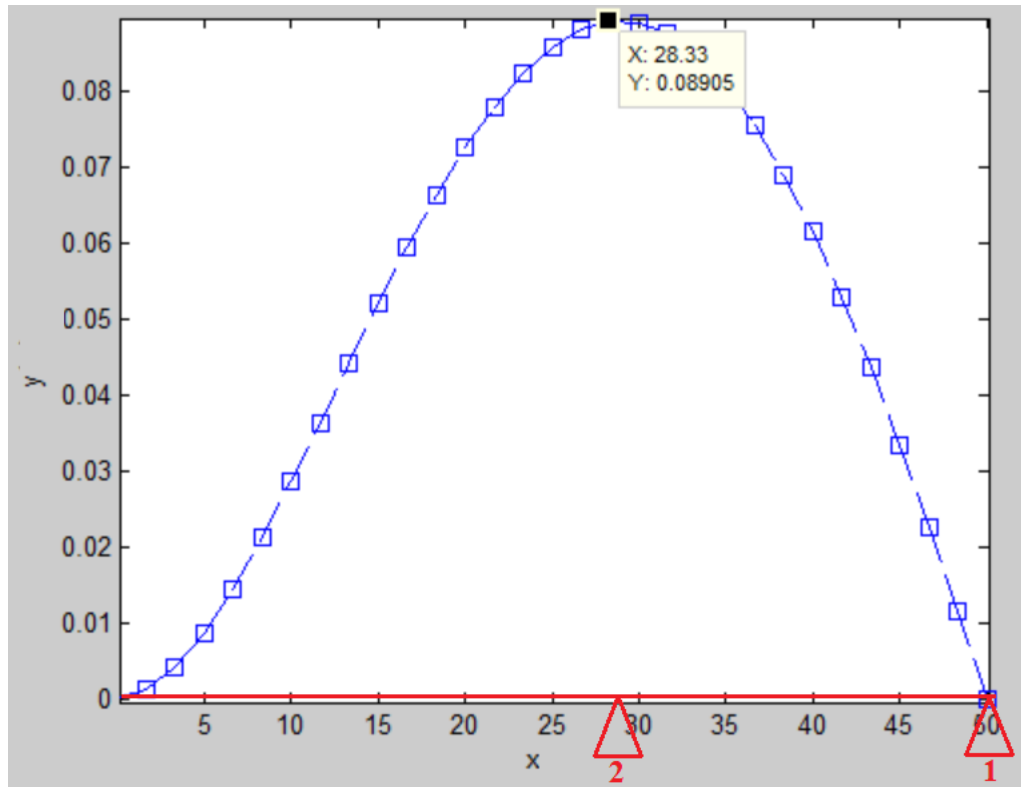


Figure 90 2nd step for a 1D support structure (Unit: mm)

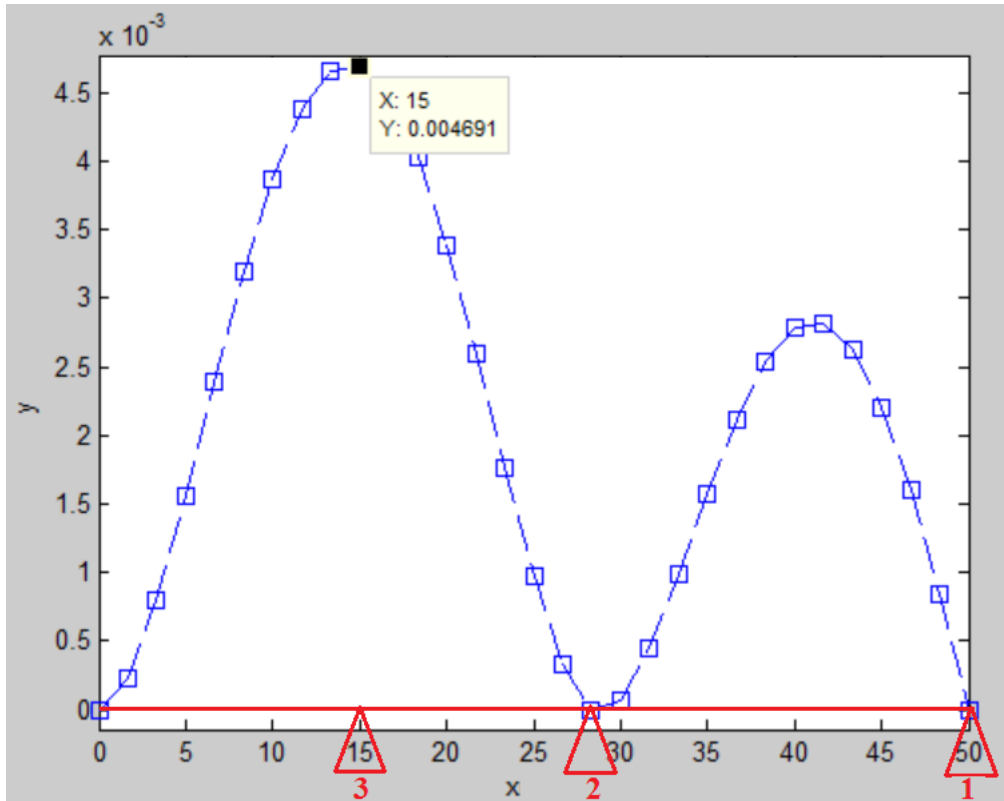


Figure 91 3rd step for a 1D support structure (Unit: mm)

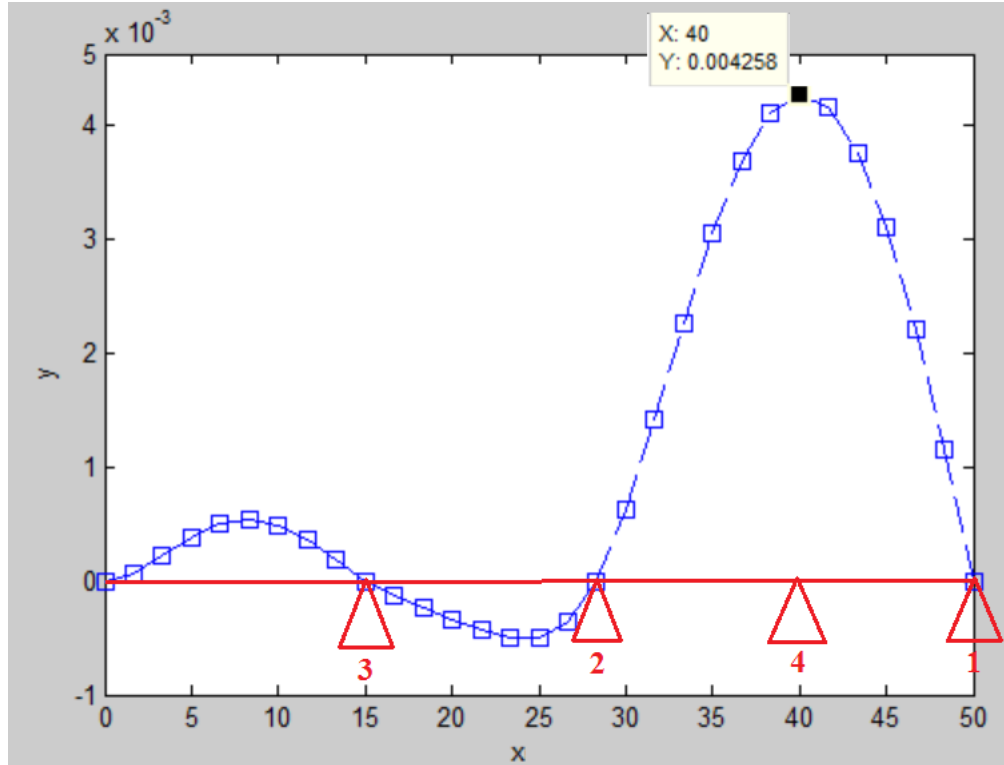


Figure 92 4th step for a 1D support structure (Unit: mm)

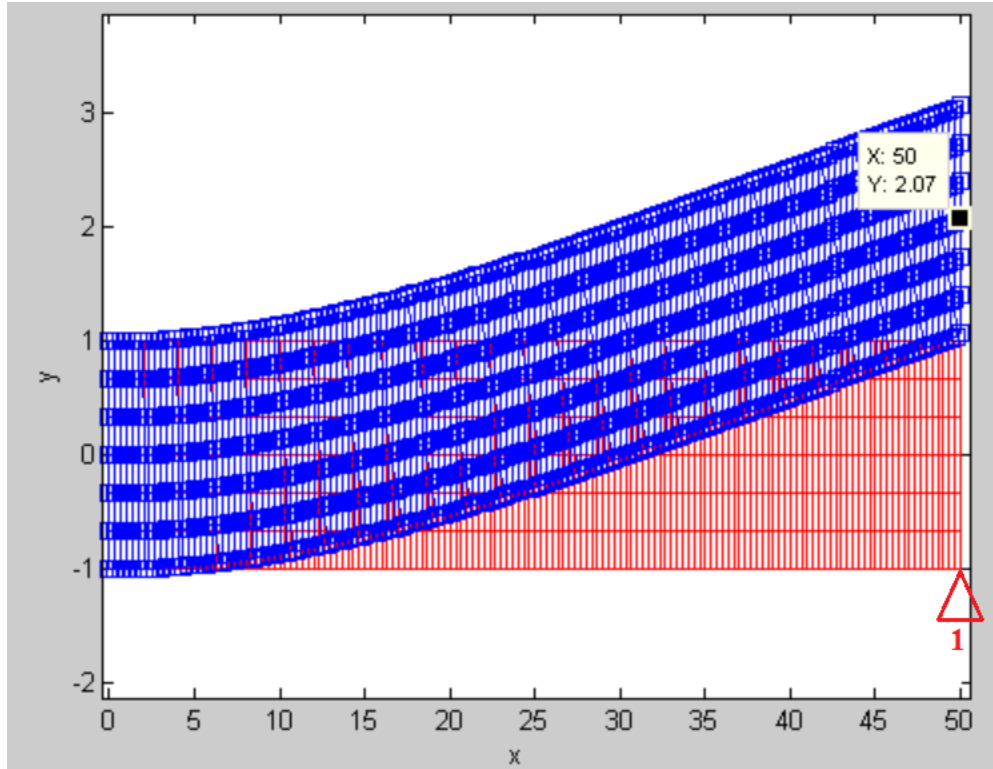


Figure 93 1st step for support structure design in 2D (Unit: mm)

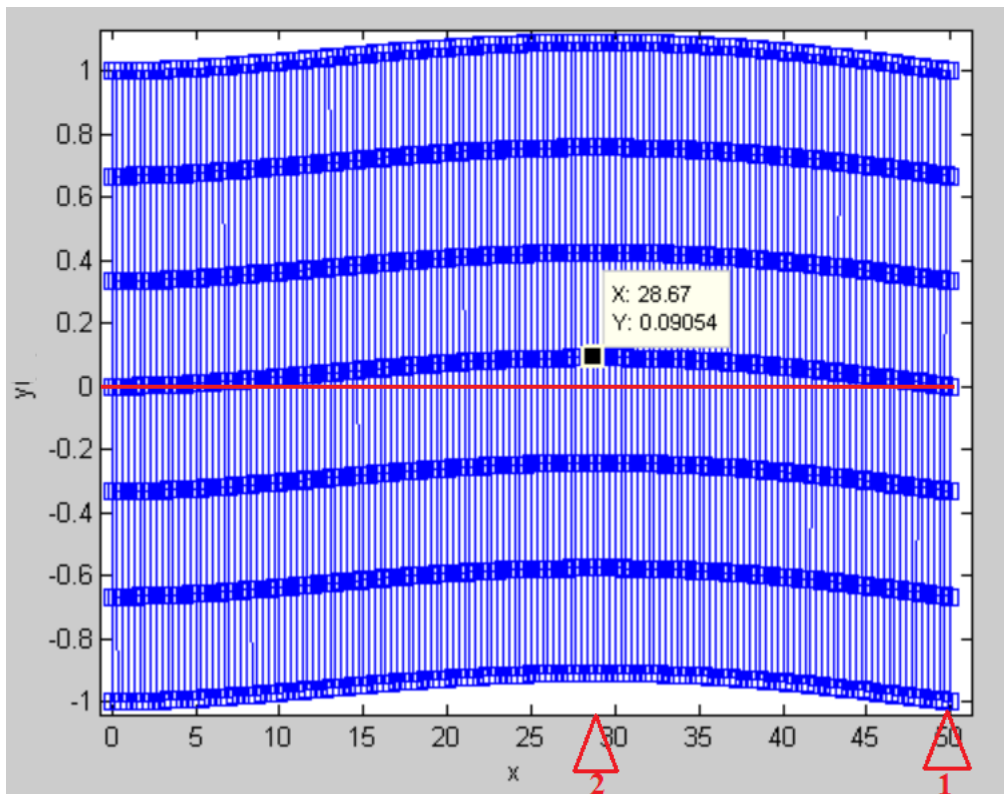


Figure 94 2nd step for support structure design in 2D (Unit: mm)

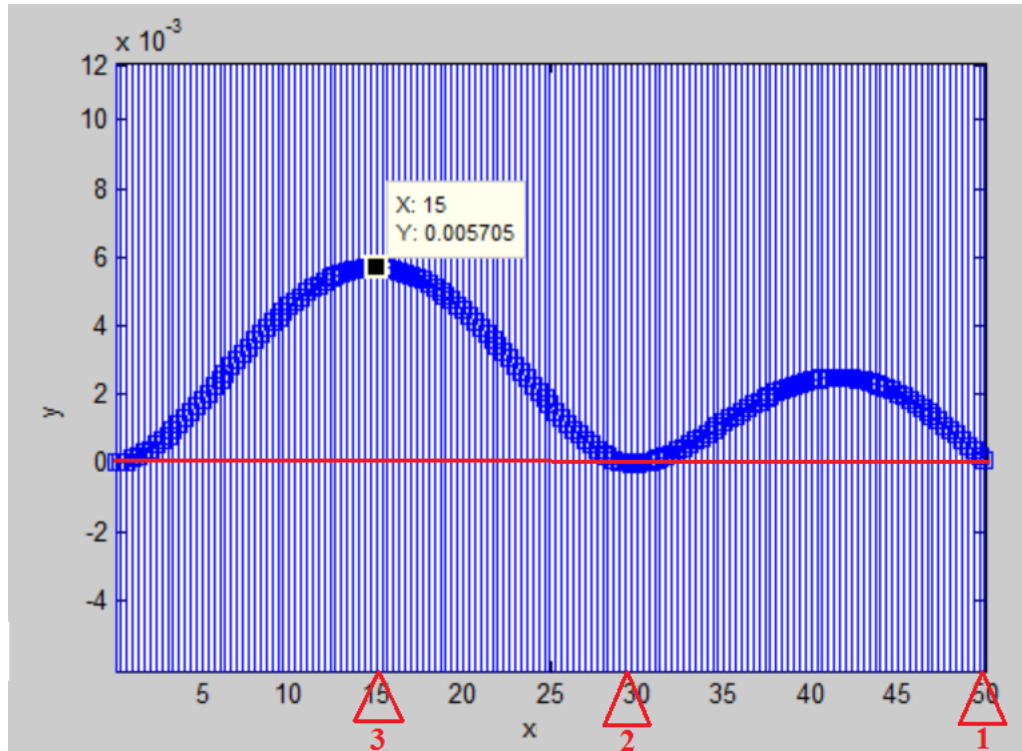


Figure 95 3rd step for support structure design in 2D (Unit: mm)

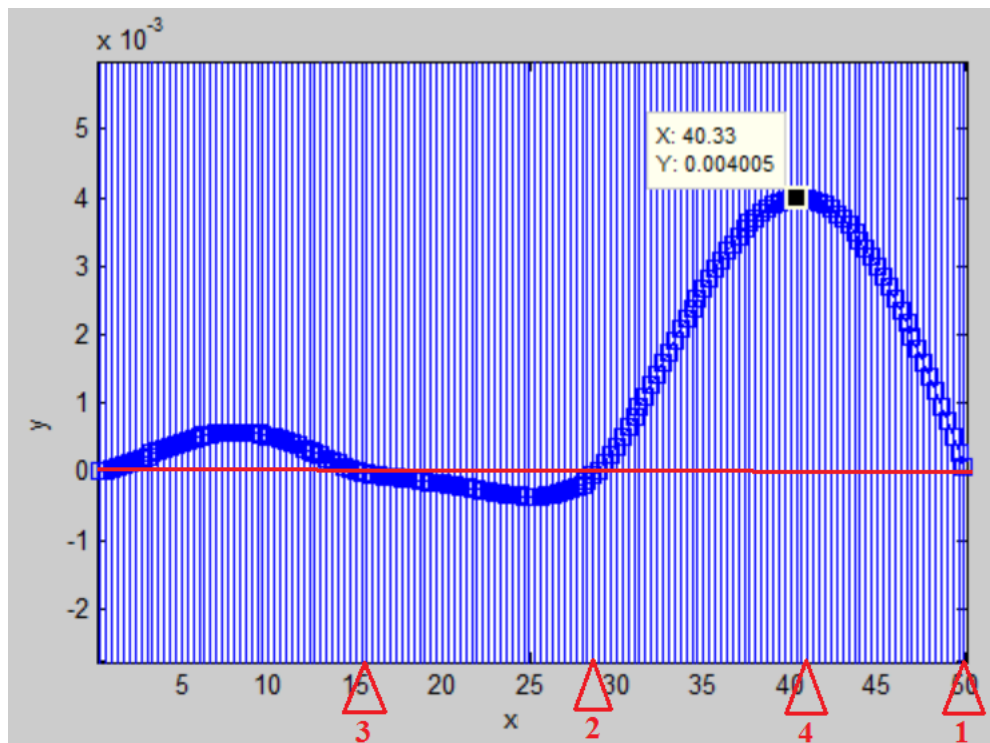


Figure 96 4th step for support structure design in 2D (Unit: mm)

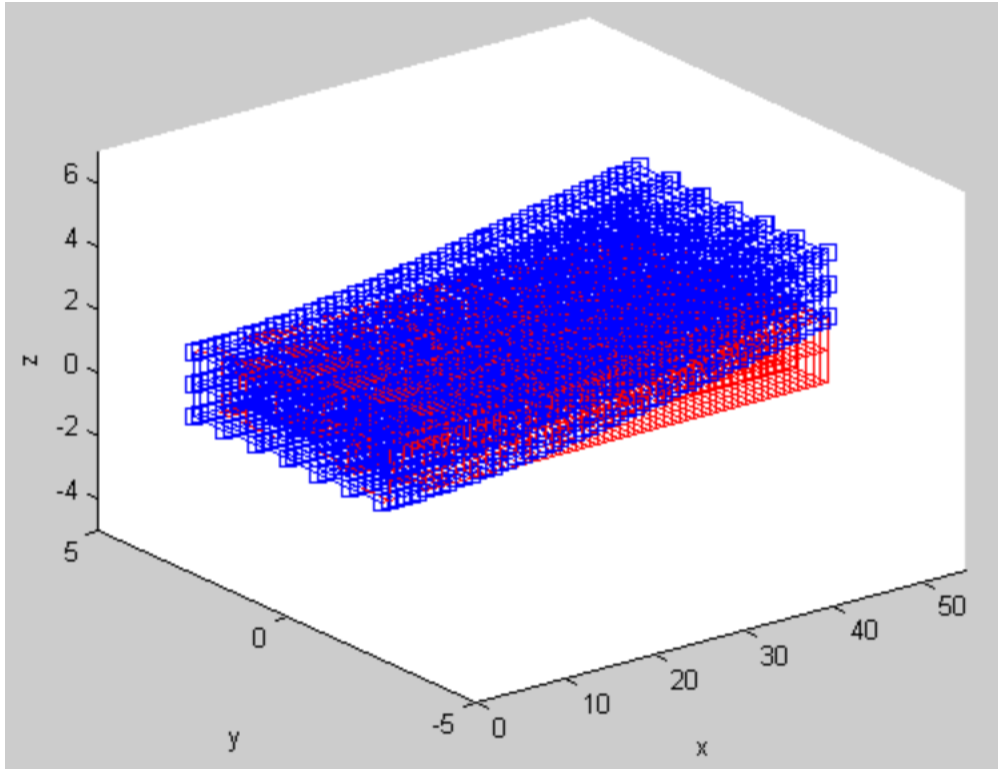


Figure 97 Beam deformation in 3D (Unit: mm)

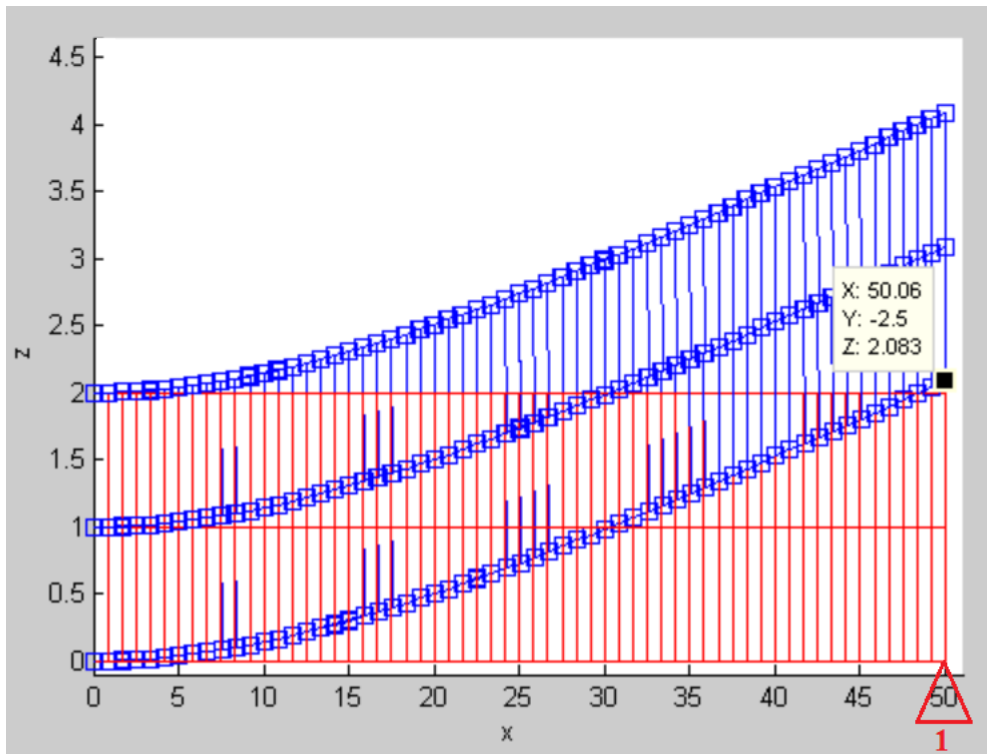


Figure 98 1st step for support structure design in 3D (Unit: mm)

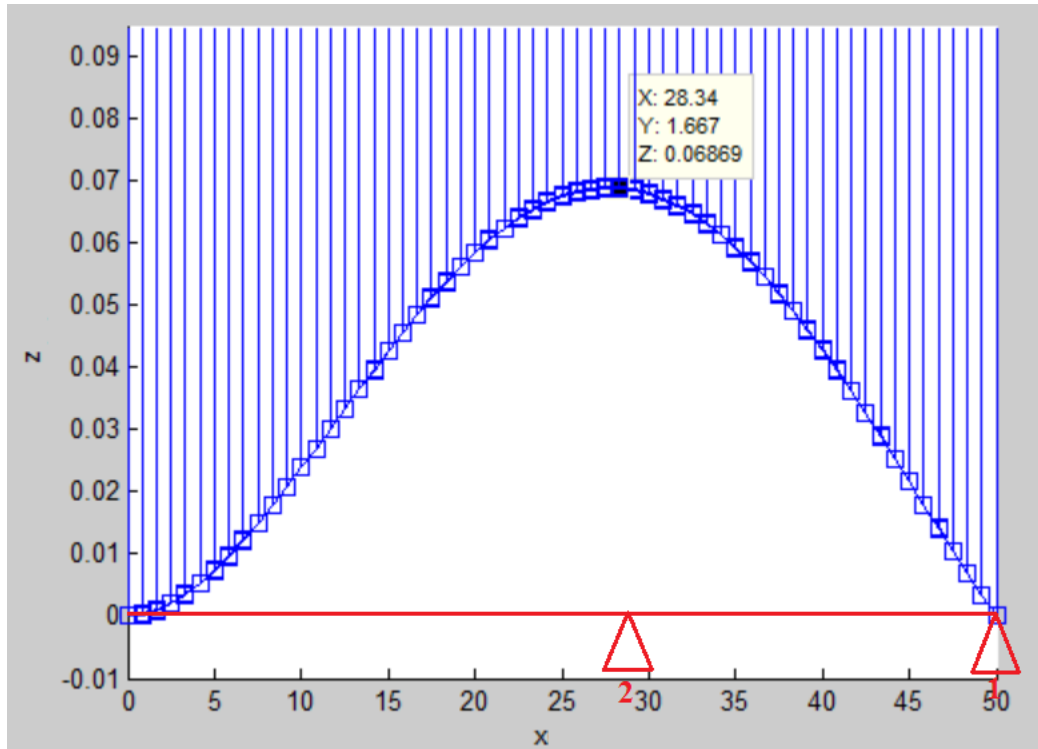


Figure 99 2nd step for support structure design in 3D (Unit: mm)

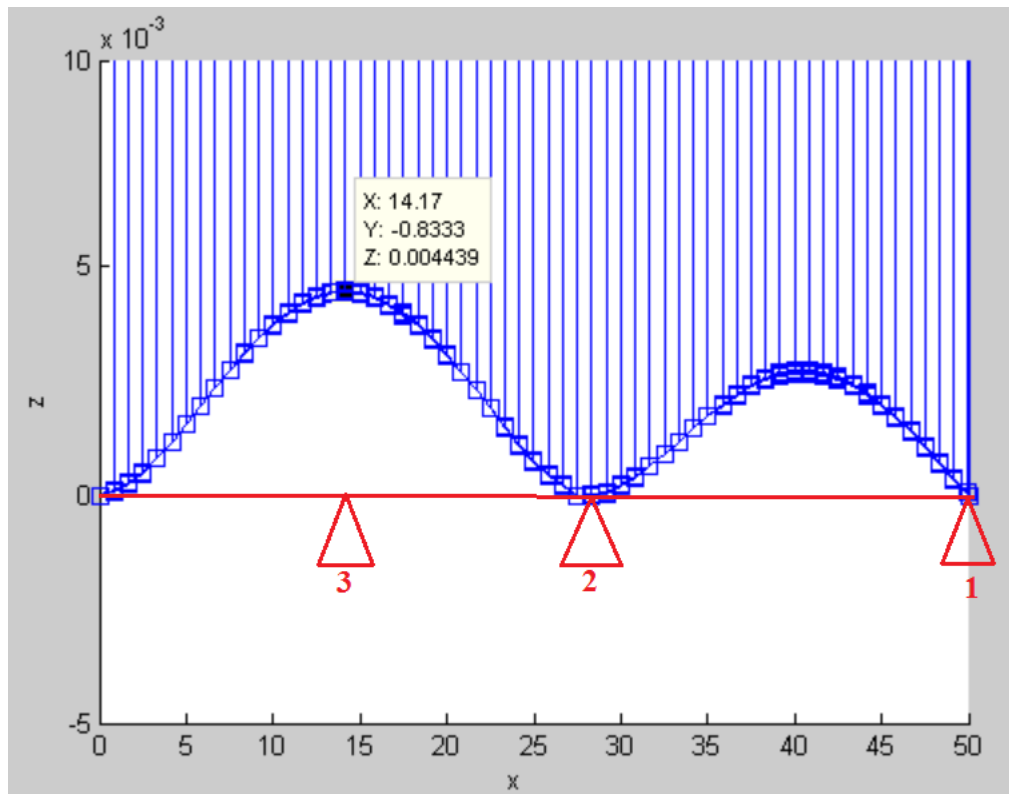


Figure 100 3rd step for support structure design in 3D (Unit: mm)

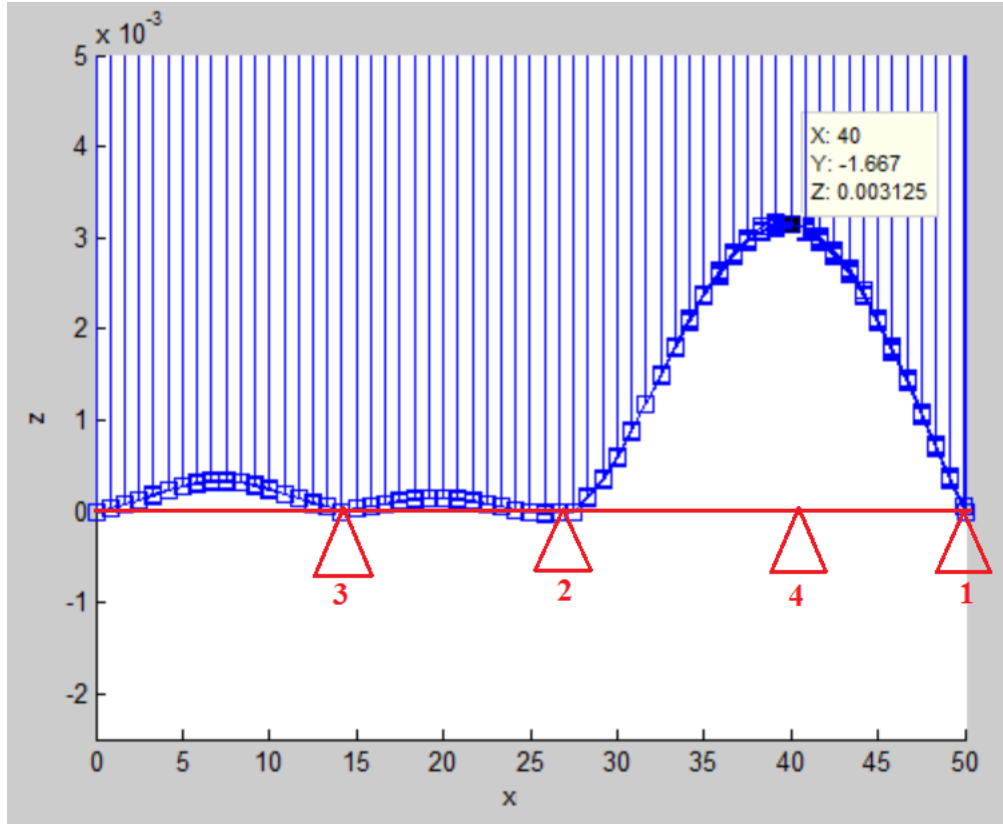


Figure 101 4th step for support structure design in 3D (Unit: mm)

7.4 Conclusions

A general framework for a support structure optimization and design tool has been developed. The support structure optimization problem is formulated using an LP method and is solved using an alternative way which applies the thermal stress density to the support structure wall t/l ratio. Analytical solutions based on square honeycomb structures are used to calculate the boundaries for t/l ratio and interpolated later to the overall structure. An FEM based simulation was also developed which searches for locations in which a support structure are necessary. This FEM method can be used in the general support optimization framework in future work.

CHAPTER 8 SUPPORT STRUCTURE EXPERIMENTS WITH Ti64

8.1 Introduction

Experiments were conducted to investigate thresholds for support structure density in an EOS M270 machine when building parts from Ti64. A qualitative experimental design was utilized based upon observed failure for a large set of support structure densities, without replicates. Two part geometries were investigated: 40x5x2mm and 20x20x2mm part with 4mm support structures respectively. A layer thickness of 30 μm was utilized, with the support structure scanned once every other layer and the part scanned once each layer. The surface quality of the base plate and the location of the part on the base plate were neglected as variables.

For standard support structures, machine parameters such as laser power, scan speed and scan strategy can be different than that used for the part. In an EOS machine, the support structure is simplified as a line without thickness. Single beam scans every other layer using default EOS parameters which are unknown to the user are utilized. For non-uniform support structures, the thickness of the support structure is customized and an EOS machine no longer considers it as a support structure. It is scanned as a solid part using EOS default parameters for Ti64 parts. This difference is not taken into consideration in this analysis.

8.2 Design of Experiment and Observation of Results

Seven sets of experiments were investigated for a 40x5x2mm thin plate and a 20x20x2mm part with uniform and non-uniform supports.

8.2.1 Experiment 1: Investigation the Support Structure for a 40x5x2mm Part

8.2.1.1 Experimental Design

The first experimental design built eight samples with different sets of configurations, as shown in Table 2. The layout of the samples is shown in Figure 102. The experiment was designed to see the influence of support structure height, large hatch space and the difference between cellular and bulk supports. As seen from the experiment layout and configuration, two different support structure heights, 5mm and 2mm respectively, three different hatch spacing, 0.8mm, 2mm and 12.5mm respectively, and two types of support structures, block and bulk, were used in the experiment.

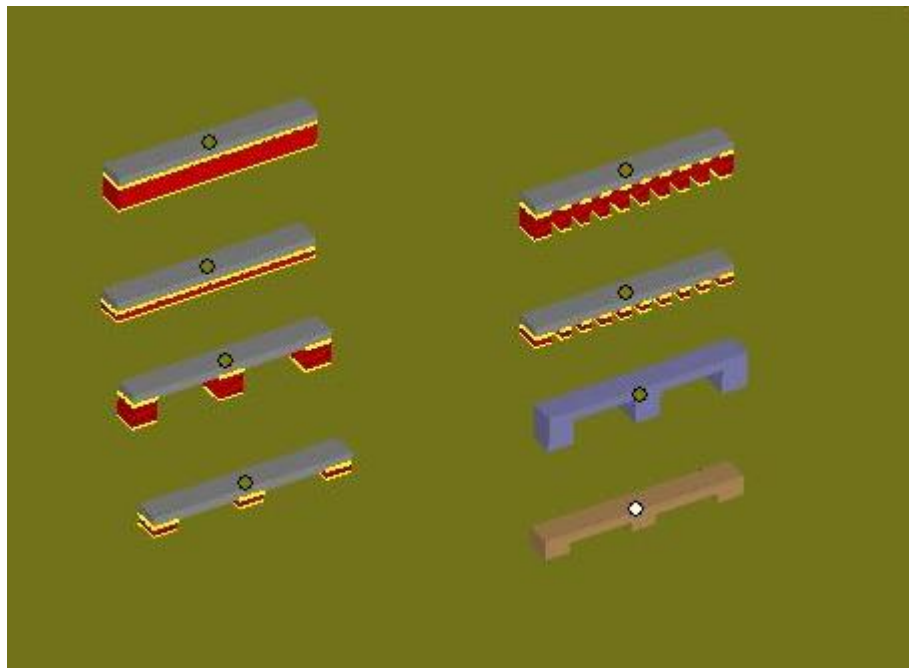


Figure 102 Experiment 1 layout

Table 2 Configurations for design of experiment

Configuration Sample #	Support height		Hatch space			Support type	
	5mm	2mm	0.8mm	2mm	12.5mm	block	bulk
1	√		√			√	
2		√	√			√	
3	√			√		√	
4		√		√		√	
5	√				√	√	
6		√			√	√	
7	√				√		√
8		√			√		√

8.2.1.2 Result observation for experiment 1

Figure 103 shows defects on bottom surfaces caused by large support structure hatch spacing. The support structure with EOS default parameters did not show any defects for the bottom surface. However, the part's bottom surface has obvious damage for hatch spacing of 2mm and 12.5mm, which is worse at larger spacing. A part of the bottom surface is nearly detached from the part. Figure 104 shows that the powder melting and defects when the laser scans the support structure with 12.5mm hatch spacing. Due to the overlarge hatch space, the powder, rather than support structure, is underneath the part in large areas when the laser scans the first several layers. The strength of the powder and the reduced thermal conductivity results in an accumulation of defects in the first few layers as shown in Figure 103. The other samples in the

experiment show that the height of the support structure and the types of support do not affect the building of the part. As a result, further experiments were designed to focus on searching for a threshold for hatch spacing for the same part.

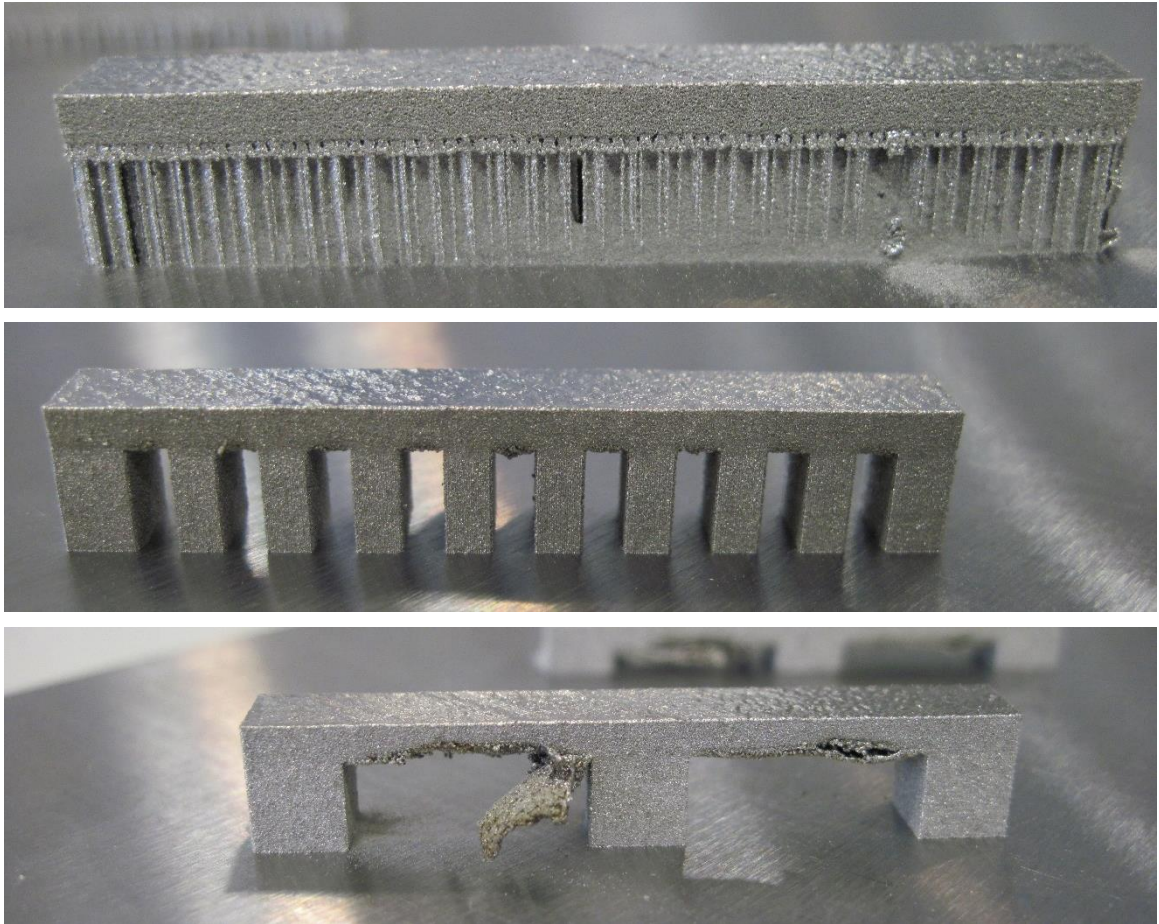


Figure 103 Defects observed for different support structures
(Top: EOS default support structure (0.8mm hatch space); middle: 2mm hatch space;
bottom: 12.5mm hatch space.)

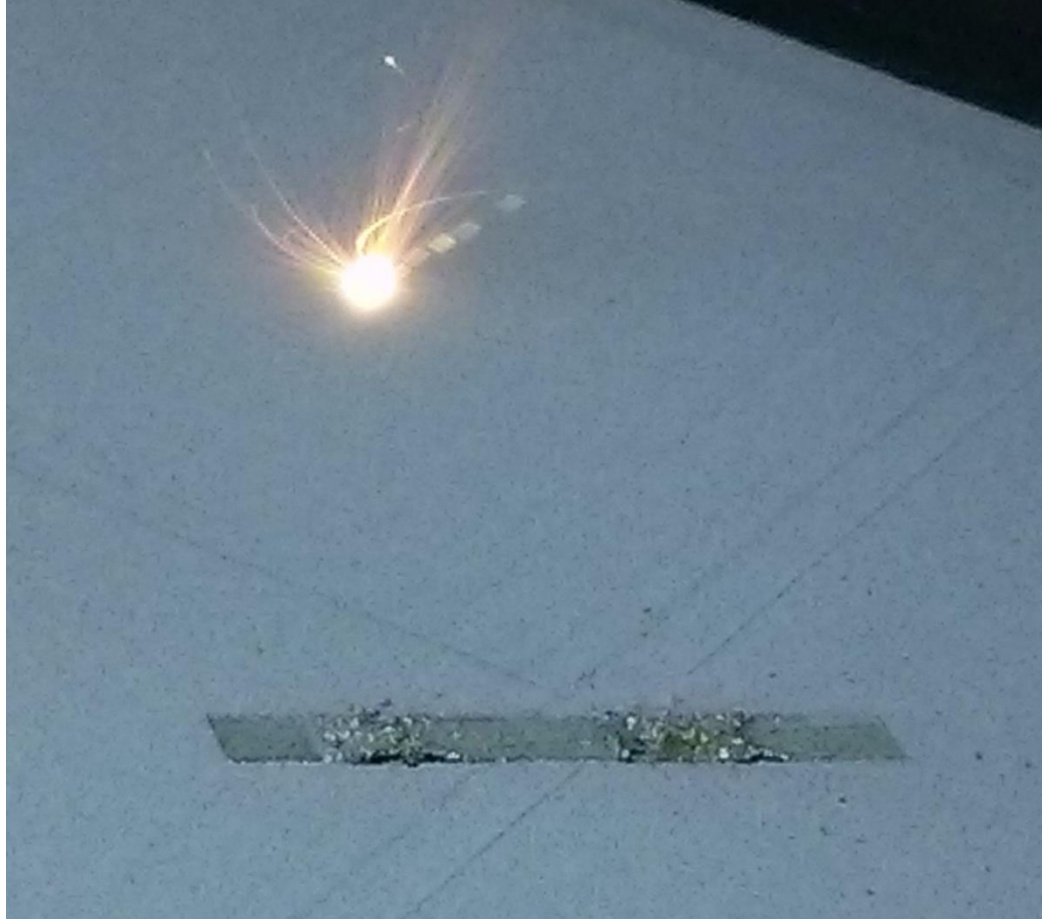


Figure 104 Surface defects during scanning of parts with large hatch spacing

8.2.2 Experiments 2&3: Uniform Hatch Spacing Support Structure Design for the 40x5x2mm Part

8.2.2.1 Experimental Design

Figure 105 shows the layout of the uniform support structure design with parts built at an orientation of 30° with respect to the +X axis. Parts with 0° orientation were also built. The support spacing was from 0.8 to 10mm and from 0.8 to 2.8mm in the length direction and width direction respectively, as shown in Table 3.

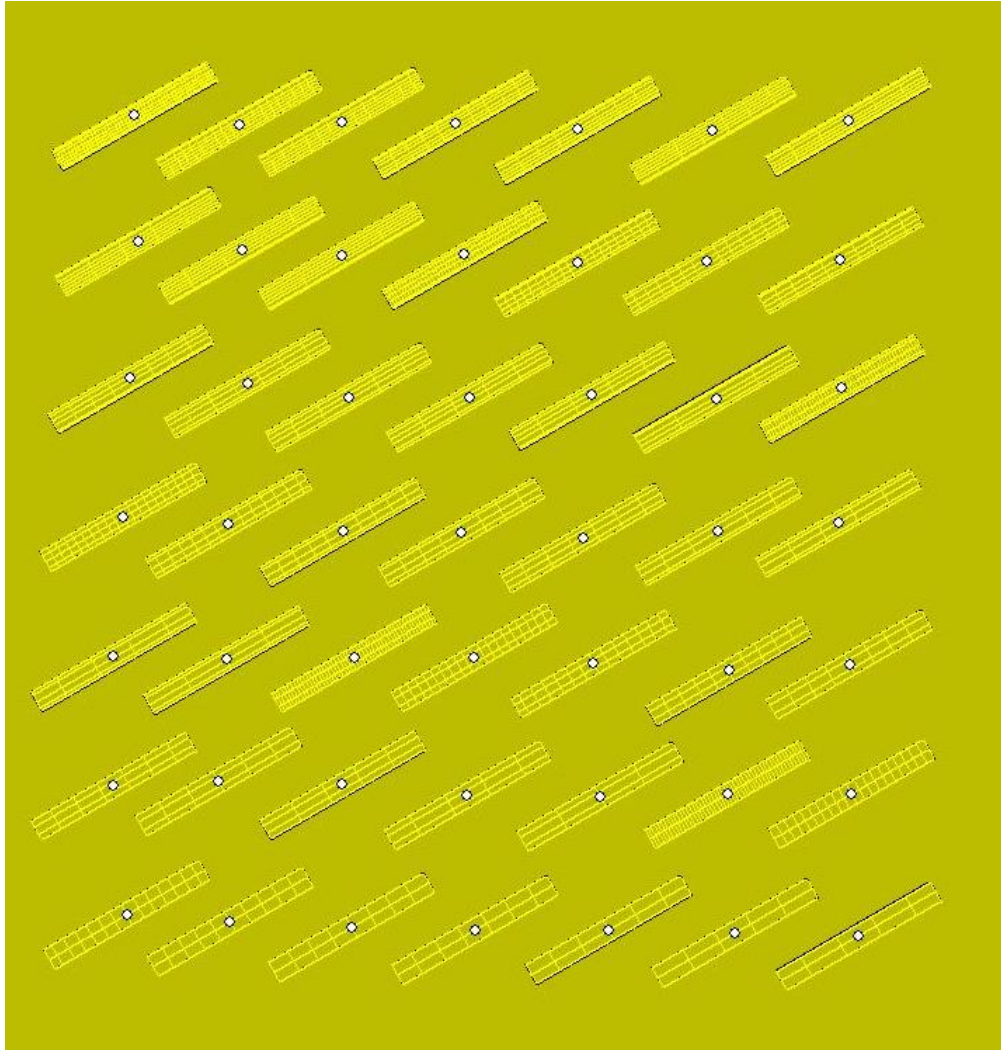


Figure 105 Uniform support structure design layout

Table 3 Support spacing in the length and width direction

Width (mm) \ Length (mm)	0.8	2	3	4	5	6	7	8	9	10
	0.8	√	√	√	√	√	√	√	√	√
1.2	√	√	√	√	√	√	√	√	√	√
1.6	√	√	√	√	√	√	√	√	√	√
2.0	√	√	√	√	√	√	√	√	√	√
2.4	√	√	√	√	√	√	√	√	√	√
2.8	√	√	√	√	√	√	√	√	√	⊗

8.2.2.2 Experimental Results

The main defects from these experiments was support structure cracking where the support structure attached to the base plate. Different degrees of failure are shown in Figure 106. From part 1 to part 3, the cracking worsens, and one of the ends of part 3 is completely detached from the base plate. The crack for part 2 is obviously observable. The detached part warps in the +Z direction with large deformations which result in the part and blade crashing during the powder delivery and distribution process. The machine stopped due to blade crashing, and several parts failed during the build process. All the samples with width direction support spacing from 1.6mm to 2.8mm failed because of



Figure 106 Support structure cracking at the bottom

blade crashing. The deformation for the first group of the samples where the width direction spacing was 0.8mm was less than the group with 1.2mm spacing. The larger the hatch spacing in length direction, the greater the deformation for the part. From the experimental results, it was found that parts with hatch spacing less than 1.2mm in both width and length directions had no cracks and defects. Parts oriented with an angle of 30° had much less deformation than parts aligned with the +X axis. So all the parts in the further experiment were placed at 30° angle and Table 4 has the spacing parameter from 0.8mm to 1.2mm for all the parts further built.

8.2.3 Experiment 4: Refinement of Experiments 2&3

Following experiments 2&3, another set of parts was built to further investigation the spacing from 0.8mm to 1.2mm. The layout of the parts in the experiment are shown in Figure 107 and Table 4 is the support spacing configuration.

The experiment showed no obvious cracks and defects for the parts. In conclusion, the threshold for uniform support spacing in order to successfully build parts with dimension of 40x5x2mm is 1.2mm.

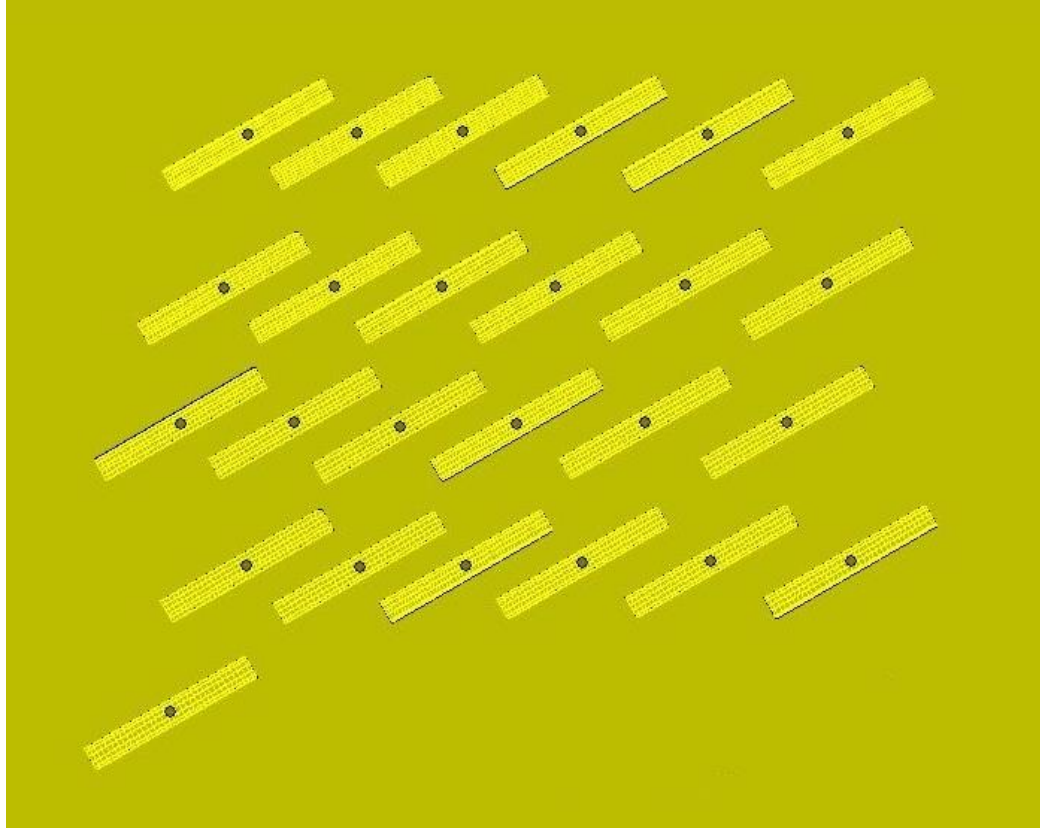


Figure 107 Uniform support structure design layout

Table 4 Hatch spacing in the width and length direction

Length (mm) \ Width (mm)	Width (mm)				
	0.8	0.9	1.0	1.1	1.2
0.8	√	√	√	√	√
0.9	√	√	√	√	√
1.0	√	√	√	√	√
1.1	√	√	√	√	√
1.2	√	√	√	√	√

8.2.4 Experiment 5: Non-uniform Supports for a 40x5x2mm Part

Assume the wall distance a_n is the arithmetic sequence shown in Equation (66).

$$a_n = a_1 + (n - 1)d \quad (66)$$

The 1st parameter a_1 is the initial value and the 2nd parameter d is the difference between two consecutive terms. There are a number (n) of default walls put on each end of the part to make both ends strong enough to resist the deformation.

Figure 108 is the non-uniform hatch space support structure design. Both ends of the part have n default supporting walls and the support spacing increases with a value of d for consecutive walls. Table 5 shows the configuration of parameters for all the parts in the experiment. a_1 is 0.8mm, 1.0mm and 1.2mm, d is set as $a_1/2$ and n is from 1 to 7.

The experimental results shows that all the parts are built successfully, although a few of them showed evidence of crack initiation barely observed by the naked eye.

Table 5 Parameters for experiment design

$a_1(d)$ mm \ n	1	2	3	4	5	6	7
0.8(0.4)	×	×	√	√	√	√	√
1.0(0.5)	√	√	√	√	√	√	×
1.2(0.6)	√	√	√	√	√	√	×

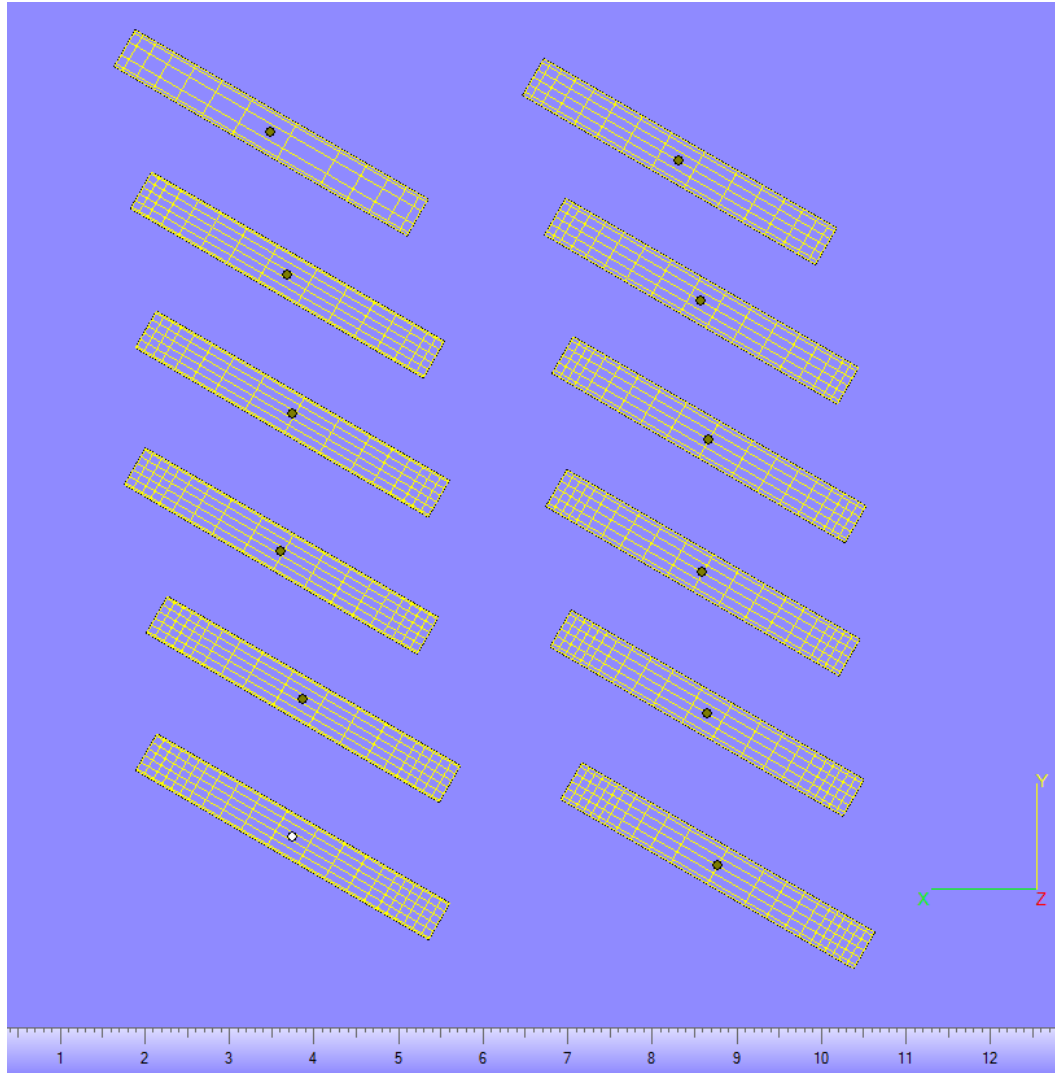


Figure 108 Non-uniform support structure layout

8.2.5 Experiment 6: Non-uniform Wall Thickness Support Structure for 40x5x2mm

Part

8.2.5.1 EOS Default Support Structure Wall Thickness

The thickness of the supporting structure wall scanned with EOS default support structures was measured from previously built samples. 10 samples were collected and three sample points for each part were measured. All the collected data is shown in Table 6. The average wall thickness was calculated as 0.1963mm.

Table 6 Support structure wall thickness measurement data (unit: mm)

Part number Sample point	1	2	3	4	5	6	7	8	9	10
1	0.2	0.21	0.2	0.17	0.2	0.2	0.19	0.21	0.18	0.21
2	0.18	0.2	0.19	0.19	0.2	0.21	0.23	0.18	0.18	0.2
3	0.2	0.2	0.2	0.17	0.21	0.2	0.19	0.19	0.19	0.21

8.2.5.2 Experimental Design and Result

The default wall thickness and wall spacing ratio, t/l , is calculated using the measured thickness and the support spacing (0.8mm, 1.0mm and 1.2mm) used in the previous experiments. Three different t/l ratios (0.2450, 0.1960 and 0.1634) with respect to the three support spacings were investigated. In this design of experiments, spacing from 1 to 5mm and the full configuration of parameters is shown in Table 7. Figure 109 shows the layout of part in the experiment.

The experimental results showed that all parts were built successfully and none of them showed evidence of crack initiation visible to the naked eye.

Table 7 Parameters for experimental design

t/l \ l(mm)	1	1.5	2	2.5	3	3.5	4	4.5	5
0.2450	0.245	0.368	0.49	0.613	0.735	0.858	0.98	1.103	1.225
0.1960	0.196	0.294	0.392	0.49	0.588	0.686	0.784	0.882	0.98
0.1634	X	0.245	0.327	0.408	0.49	0.572	0.653	0.735	0.817

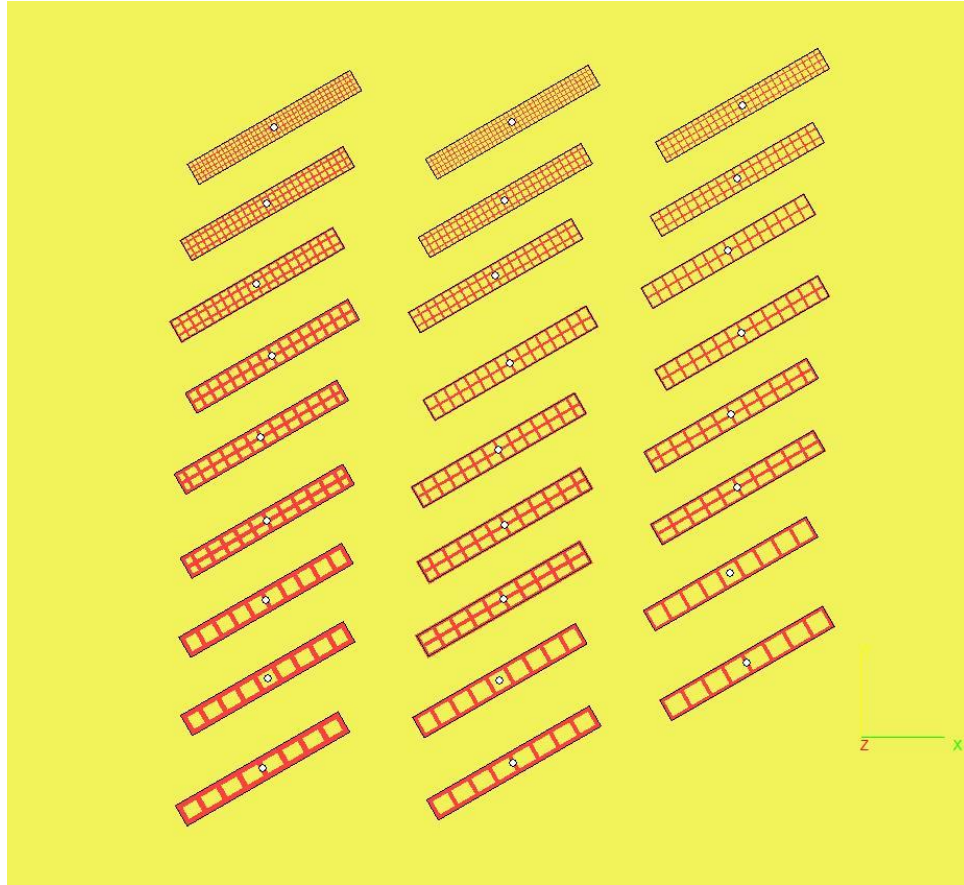


Figure 109 Customized support structure design layout

8.2.6 Experiment 7: Support Structure Investigation for a 20x20x2mm Part

8.2.6.1 Experimental Design

Both uniform and non-uniform support structure spacing was investigated for parts with dimension of 20x20x2mm. For the uniform hatch space support structure, 0.6mm, 0.8mm, 1mm, 2mm, 3mm, 4mm, 5mm, 6mm, 7mm, 8mm, 9mm and 10mm were utilized. For the non-uniform support structure, the configuration of parameters a_1 , d and n are shown in Table 8.

Table 8 Support spacing for the 20mmx20mmx2mm non-uniform support structure parts

$a_1(d)$ mm \ n	4
0.6(0.3)	√
0.7(0.35)	√
0.8(0.4)	√

8.2.6.2 Experimental Results

Figure 110 shows some typical failures for part observed from the experiment. The uniform hatch spacing support structures showed obvious defects among which the part with 0.8mm hatch spacing had the least defects. It was observed from the experiment that cracking starts growing from corners as seen in Figure 105. Other severely damaged part are circled with a red 2 in the same Figure. Figure 111 shows the results for non-uniform hatch support structures, which did not have obvious defects/cracks.

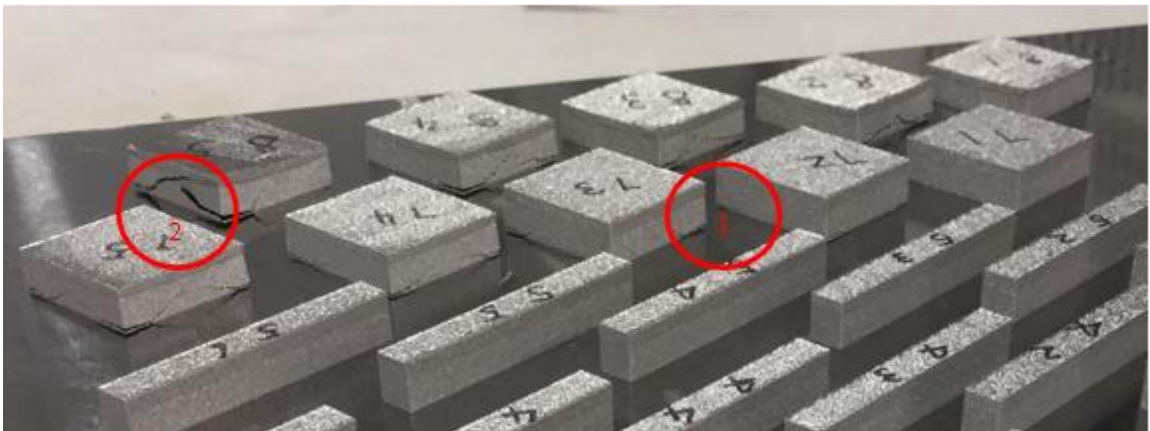


Figure 110 Uniform hatch space support structure cracking at the bottom

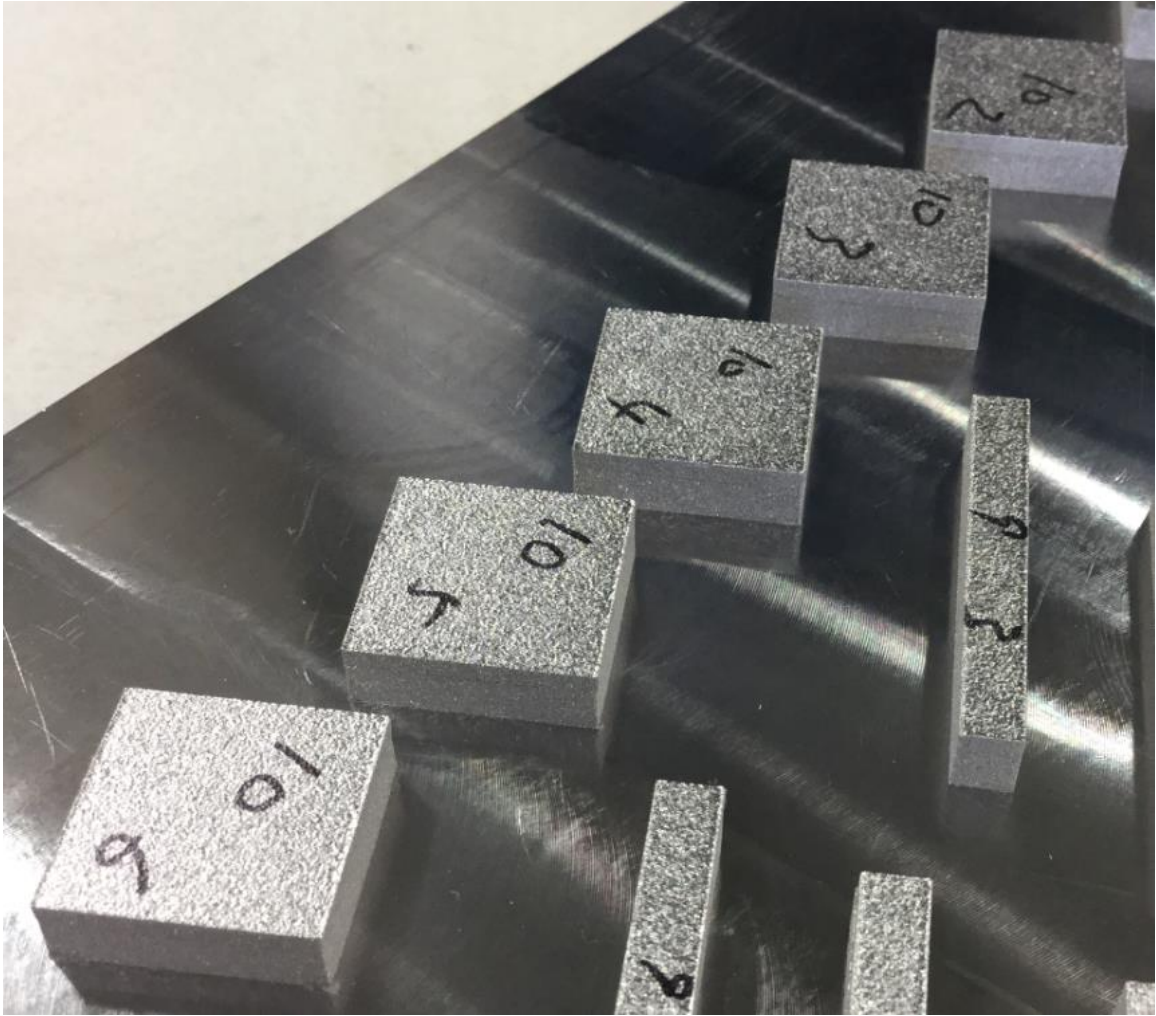


Figure 111 Non-uniform support structures

In conclusion, support spacing should be at most 0.8mm in order to successfully build the 20x20x2mm part. Since the defects initiate from the corner of the part, it is suggested to put dense support structures around the corner, while the rest of the area could be supported less densely. The non-uniform support structure experiment indicates that loose support structures far away from the corners would have no negative effects on a part.

8.3 Conclusion

This chapter focused on support structure experiments to explore the influence of support spacing and thickness on the successfully building of two parts with dimensions of 40x5x2mm and 20x20x2mm, in an EOS M270 machine made using Ti64. Seven sets of experiments were performed and conclusions were drawn as follows:

- Surface finish is poor and even damaged when using large support spacing for parts with a large surface area.
- For parts with dimensions of 40x5x2mm
 - The failure happens on the short end of the part. The support structure detaches from the base plate due to large thermal stress/deformation.
 - The maximal support spacing for uniform support structures for a successful part is around 1.2mm.
 - For non-uniform support structures, an arithmetic sequence with threshold value for all parameters were found to be $a_1(1.2\text{mm})$ and $n(6)$ for successfully building parts.
 - For non-uniform wall thickness support structures, the threshold value for all parameters are t/l of 0.1634 and l of 5mm for successfully building a part.
- For the part with dimensions of 20x20x2mm
 - The failure initiates from one of the corners of the part and further results in cracking and detachment of the edges from the base plate.
 - The maximal support spacing for uniform support structures in order to build a successful part is around 0.8mm.

- For non-uniform support structures using an arithmetic sequence, the suggested threshold value for all parameters are a_1 (0.8mm) and n (4) for successfully building a part.

CHAPTER 9 CONCLUSION AND FUTURE WORK

9.1 Conclusion

The goal of this research work was to develop support structure generation tools based on real scan patterns and thermo-mechanical simulation tools for SLM developed at the University of Louisville and being commercialized by 3DSIM, LLC. In order to achieve the goal, five objectives corresponding to five major parts of the simulation required for support structure generation have been achieved. First of all, the scan pattern which is one of the key parameters in SLM is investigated and input to the model in order to fully simulate the SLM process. 3DSIM simulation tools are adapted to generate residual stress results for the support structure design and optimization, thus benchmarking of the 3DSIM against a dynamic thermal model built in commercial software ANSYS is successfully compared. The geometry of support structures could be complex and it takes much more computational time and resources to simulate SLM when considering the support structure. So the problem is mitigated by using an effective thermal conductivity approach. The support structure design and optimization framework has been developed using two sets of methods which are an analytical solution and FEM. In the meanwhile, an experimental investigation of support structures for two specific parts has been carried out with Ti64.

9.1.1 Scan Pattern Generation Tool

A scan pattern generation module capable of providing various real scan patterns to the 3DSIM simulation environment has been developed. The module focuses on

generation of the real scan strategies including the scan orientation, scan space, scan pattern, etc. The traditional raster scan strategy is reversed engineered from the EOS machine based on study of scanning orientation and scan pattern. The scan strategy generation tool is able to create real scan path information and is applied to the simulation. Both traditional raster scan and chessboard scan strategies are available in the tool.

9.1.2 A dynamic Moving Mesh Model Development in ANSYS and 3DSIM against ANSYS Benchmark

A dynamic mesh framework has been developed to provide an efficient computational method for simulation and modeling of SLM using ANSYS. This framework provides very large computational speed and model size advantages compared to other FEM approaches in the literature. The accuracy of interpolation of nodal temperatures from one fine mesh configuration to the next has been tested and was found to be reliable since the converged thermal field in the previous fine mesh configuration matches well with the initial condition thermal field in the next mesh configuration. A comparison of ANSYS solutions with experimental results for melt pool size and shape indicate the model accurately simulates the process.

A comparison between ANSYS and 3DSIM show that both methods can be used to accurately simulate the thermal transformations in SLM. The set of algorithms and software tools being developed by 3DSIM show an initial advantage for speed, and thus capability, for simulating AM problems. So 3DSIM could be adapted to provide temperature and thermal stress results for the support structure design and optimization in this study.

9.1.3 Support Structure Optimization and Design Framework

An effective thermal conductivity model has been developed in order to consider the influence of support structures on the thermal field in the thermal model. The method has thus provided an efficient method for prediction of temperature by using an effective thermal conductivity to reduce the complexity of finite element analyses. The effective thermal conductivity of support structures is compared with parallel model results and both show good match.

A support structure optimization and design framework is able to generate support structures with the minimum volume/mass needed for a given part orientation to meet a set of user-specified constraint conditions. Both analytical solutions from square Honeycomb structures and FEM have been applied to design the support structure. The minimum volume/mass is computed based upon the amount of support structure needed to satisfy the constraint equations for a computed thermal stress pattern resulting from a user-specified combination of process parameters, material, support structure geometry/type and scan pattern. The support structure is exported as an STL file in the final stage.

9.1.4 Experiment to Investigate the Block Support Structure for Ti64

An experiment has been carried out to investigate block support structure behavior for Ti64 in an EOS M270 machine. The threshold of support structure parameters has been found by fabrication of two parts: 40x5x2mm and 20x20x2mm respectively which could be applied to other materials by considering the material properties.

9.2 Future work

The ANSYS approach to dynamic meshing, however, is still not as fast as required due to the node renumbering and reassembly required in ANSYS and the need for finer time steps for convergence. ANSYS is arguably the best existing commercial tool for solving SLM thermal problems. Using ANSYS, however, to simulate even a relatively small SLM thermal problem requires many years of computational time. More efforts has to be put in order to speed up the model. The thermomechanical model needs to be implemented into ANSYS in the future work as well.

This study of scan pattern is solely reverse engineered from an EOS M 270 machine. In order to enable simulations using real scan strategies, more efforts should be put into issues such as exploring scan strategies in other SLM machines and processes in the future work.

In the effective thermal property study, a method to apply an effective thermal conductivity for support structures with non-uniform wall thickness and spacing, requires further study and investigations. Support structures used for real parts should be optimized such that a minimum amount of supports to withstand thermal stress induced distortion should be added to a part. This would result in local property variations and anisotropy in the X, Y and Z directions.

The support structure optimization and design framework has been designed based on the assumption of a block support structure. In order to satisfy the needs of different support structure types, such as line, point, contour, etc., more efforts and research must be done. What is more, the tool should be improved so as to be capable of comparing the effects of part orientation on support volume, build time, and thermal

stress to enable future multi-objective optimization experiments to be conducted. The framework needs to be implemented into 3DSIM, and proper iteration and termination criterion chosen. After the framework is completely implemented into 3DSIM, the results have to be validated and more experiments need to be investigated.

REFERENCES

1. Wong, K.V. and A. Hernandez, A review of additive manufacturing. ISRN Mechanical Engineering, 2012. **2012**.
2. Scott, J., et al., Additive manufacturing: Status and opportunities. Science and Technology Policy Institute, 2012: p. 1-29.
3. Gibson, I., D.W. Rosen, and B. Stucker, Additive manufacturing technologies:3D Printing, Rapid Prototyping, and Direct Digital Manufacturing. 2010: Springer.
4. Patil, N., A Novel Numerical Framework For Simulation Of Multiscale Spatio-Temporally Non-Linear Systems In Additive Manufacturing Processes. 2014, University of Louisville.
5. Zeng, K., et al., A New Dynamic Mesh Method Applied to the Simulation of Selective Laser Melting. Proceedings of the Solid Freeform Fabrication Symposium, 2013.
6. Quarshie, R., et al., Shaping our National Competency in Additive Manufacturing. The Additive Manufacturing Special Interest Group for the Technology Strategy Board, 2012.
7. EOSINT, EOSINT M270 Basic Training And Introduction Manual. 2008.
8. Gong, H., Generation And Detection Of Defects In Metallic Parts Fabricated By Selective Laser Melting And Electron Beam Melting And Their Effects On Mechanical Properties. PhD Thesis, 2013. **University of Louisville**.

9. Kruth, J.-P., et al. Part and material properties in selective laser melting of metals. in Proceedings of the 16th International Symposium on Electromachining. 2010.
10. Zaeh, M.F. and G. Branner, Investigations on residual stresses and deformations in selective laser melting. Production Engineering, 2010. **4**(1): p. 35-45.
11. Wang, D., et al., Research on the fabricating quality optimization of the overhanging surface in SLM process. The International Journal of Advanced Manufacturing Technology, 2013. **65**(9-12): p. 1471-1484.
12. Kempen, K., et al., PRODUCING CRACK-FREE, HIGH DENSITY M2 HSS PARTS BY SELECTIVE LASER MELTING: PRE-HEATING THE BASEPLATE. 2013.
13. Kruth, J.-P., et al., Binding mechanisms in selective laser sintering and selective laser melting. Rapid prototyping journal, 2005. **11**(1): p. 26-36.
14. Roberts, I., et al., A three-dimensional finite element analysis of the temperature field during laser melting of metal powders in additive layer manufacturing. International Journal of Machine Tools and Manufacture, 2009. **49**(12): p. 916-923.
15. Carslaw, H.S. and J.C. Jaeger, Conduction of heat in solids. Oxford: Clarendon Press, 1959, 2nd ed., 1959. **1**.
16. Crafer, R.C. and P.J. Oakley, Laser processing in manufacturing. 1992: Springer.
17. Ready, J., Effects of high-power laser radiation. 2012: Elsevier.
18. Dai, K. and L. Shaw, Finite element analysis of the effect of volume shrinkage during laser densification. Acta materialia, 2005. **53**(18): p. 4743-4754.

19. Wang, X., et al., Direct selective laser sintering of hard metal powders: experimental study and simulation. *The International Journal of Advanced Manufacturing Technology*, 2002. **19**(5): p. 351-357.
20. Rosenthal, D. *The theory of moving sources of heat and its application to metal treatments*. 1946. ASME.
21. Eagar, T. and N. Tsai, Temperature fields produced by traveling distributed heat sources. *Welding Journal*, 1983. **62**(12): p. 346-355.
22. Dowden, J.M., *The mathematics of thermal modeling: an introduction to the theory of laser material processing*. 2001: CRC Press.
23. JunChang, L., C. Langlade, and A. Vannes, Evaluation of the thermal field developed during pulsed laser treatments: semi analytical calculation. *Surface and Coatings Technology*, 1999. **115**(1): p. 87-93.
24. Labudovic, M., D. Hu, and R. Kovacevic, A three dimensional model for direct laser metal powder deposition and rapid prototyping. *Journal of materials science*, 2003. **38**(1): p. 35-49.
25. Dai, K. and L. Shaw, Thermal and stress modeling of multi-material laser processing. *Acta Materialia*, 2001. **49**(20): p. 4171-4181.
26. Dai, K. and L. Shaw, Thermal and mechanical finite element modeling of laser forming from metal and ceramic powders. *Acta Materialia*, 2004. **52**(1): p. 69-80.
27. Gusarov, A., et al., Heat transfer modelling and stability analysis of selective laser melting. *Applied Surface Science*, 2007. **254**(4): p. 975-979.

28. Patil, R.B. and V. Yadava, Finite element analysis of temperature distribution in single metallic powder layer during metal laser sintering. *International Journal of Machine Tools and Manufacture*, 2007. **47**(7): p. 1069-1080.
29. Fischer, P., et al., Temperature measurements during selective laser sintering of titanium powder. *International Journal of Machine Tools and Manufacture*, 2004. **44**(12): p. 1293-1296.
30. Kolossov, S., et al., 3D FE simulation for temperature evolution in the selective laser sintering process. *International Journal of Machine Tools and Manufacture*, 2004. **44**(2): p. 117-123.
31. Dong, L., et al., Three-dimensional transient finite element analysis of the selective laser sintering process. *Journal of materials processing technology*, 2009. **209**(2): p. 700-706.
32. Zhang, D., et al., Select laser melting of W–Ni–Fe powders: simulation and experimental study. *The International Journal of Advanced Manufacturing Technology*, 2010. **51**(5-8): p. 649-658.
33. Song, B., et al., Process parameter selection for selective laser melting of Ti6Al4V based on temperature distribution simulation and experimental sintering. *The International Journal of Advanced Manufacturing Technology*, 2012. **61**(9-12): p. 967-974.
34. Childs, T., et al. Simulation and experimental verification of crystalline polymer and direct metal selective laser sintering. in *Proc. SFF Symp.*, Austin. 2000.

35. Hauser, C., et al. Direct selective laser sintering of tool steel powders to high density, Part A: Effects of laser beam width and scan strategy. in Proceedings of the 2003 Solid Freeform Fabrication Symposium. 2003.
36. Childs, T., C. Hauser, and M. Badrossamay, Mapping and modelling single scan track formation in direct metal selective laser melting. *CIRP Annals-Manufacturing Technology*, 2004. **53**(1): p. 191-194.
37. Taylor, C.M., Direct laser sintering of stainless steel: thermal experiments and numerical modelling. 2004, The University of Leeds.
38. Ibraheem, A.K., B. Derby, and P.J. Withers. Thermal and Residual Stress Modelling of the Selective Laser Sintering Process. in *MATERIALS RESEARCH SOCIETY SYMPOSIUM PROCEEDINGS*. 2003. Cambridge Univ Press.
39. Roberts, I.A., Investigation of residual stresses in the laser melting of metal powders in additive layer manufacturing. 2012.
40. Huang, W. and R.D. Russell, Adaptive moving mesh methods. Vol. 174. 2010: Springer.
41. ANSYS, C., ANSYS CFX. Academic Research Release, 2006. 11.
42. Shiomi, M., et al., Finite element analysis of melting and solidifying processes in laser rapid prototyping of metallic powders. *International Journal of Machine Tools and Manufacture*, 1999. **39**(2): p. 237-252.
43. Patil, N., et al., A generalized feed forward dynamic adaptive mesh refinement and de-refinement finite element framework for spatiotemporally periodic

- localized boundary conditions: Application to Metal Laser Sintering. International Journal of Thermal Sciences, xxx, xxxxxx, 2013.
44. Patil, N., D. Pal, and B. Stucker. A New Finite Element Solver using Numerical Eigen Modes for Fast Simulation of Additive Manufacturing Processes. in Proceedings of the Solid Freeform Fabrication Symposium. 2013.
 45. D. Pal, N.P., K. Rafi H, K. Zeng, A. Moreland, A. Hicks, D. Beeler and B. E Stucker, A generalized feed forward dynamic adaptive mesh refinement and de-refinement finite element framework for Metal Laser Sintering: Part II (Non-linear thermal simulations and validations). Journal of Manufacturing Science and Engineering, 2014. **In process**.
 46. Hauser, C., Selective laser sintering of a stainless steel powder. 2003, University of Leeds.
 47. Kruth, J.-P., et al., Selective laser melting of iron-based powder. Journal of Materials Processing Technology, 2004. **149**(1): p. 616-622.
 48. Mercelis, P. and J.-P. Kruth, Residual stresses in selective laser sintering and selective laser melting. Rapid Prototyping Journal, 2006. **12**(5): p. 254-265.
 49. Thijs, L., et al., Fine-structured aluminium products with controllable texture by selective laser melting of pre-alloyed AlSi10Mg powder. Acta Materialia, 2013. **61**(5): p. 1809-1819.
 50. Beal, V., et al., Scanning strategies and spacing effect on laser fusion of H13 tool steel powder using high power Nd: YAG pulsed laser. International journal of production research, 2008. **46**(1): p. 217-232.

51. Zhang, W., et al., Consecutive sub-sector scan mode with adjustable scan lengths for selective laser melting technology. *The International Journal of Advanced Manufacturing Technology*, 2009. **41**(7-8): p. 706-713.
52. Bo, Q., et al., The helix scan strategy applied to the selective laser melting. *The International Journal of Advanced Manufacturing Technology*, 2012. **63**(5-8): p. 631-640.
53. Jhabvala, J., Study of the consolidation process under macro-and microscopic thermal effects in selective laser sintering and selective laser melting. 2010, Ph. D. thesis, EPFL, p 4609.
54. Matsumoto, M., et al., Finite element analysis of single layer forming on metallic powder bed in rapid prototyping by selective laser processing. *International Journal of Machine Tools and Manufacture*, 2002. **42**(1): p. 61-67.
55. Ma, L. and H. Bin, Temperature and stress analysis and simulation in fractal scanning-based laser sintering. *The International Journal of Advanced Manufacturing Technology*, 2007. **34**(9-10): p. 898-903.
56. Mohanty, S., C.C. Tutum, and J.H. Hattel. Cellular scanning strategy for selective laser melting: Evolution of optimal grid-based scanning path & parametric approach to thermal homogeneity. in *Proc. of SPIE Vol. 2013*.
57. Ramaswami, K., *Process planning for shape deposition manufacturing*. 1997, Citeseer.
58. Choi, K.-H., et al., Novel scan path generation method based on area division for SFFS. *Journal of mechanical science and technology*, 2009. **23**(4): p. 1102-1111.

59. Papadakis, L., et al. Numerical modeling of heat effects during thermal manufacturing of aero engine components. in Proceedings of the World Congress on Engineering. 2012.
60. Krol, T., et al. Development of a Simulation-Based Process Chain-Strategy for Different Levels of Detail for the Preprocessing Definitions. in ASIM. 2011.
61. Pohl, H., et al. Thermal stresses in direct metal laser sintering. in Proceedings of the Solid Freeform Fabrication Symposium. 2001.
62. Wright, S. 3D Printing Titanium & the Bin of Broken Dreams (Part 1). 2015 [cited 2015 06/07]; Available from: <http://3dprintingindustry.com/2015/03/10/3d-printing-titanium-the-bin-of-broken-dreams-part-1/>.
63. Wright, S. 3D Printing Titanium & the Bin of Broken Dreams (Part 2). 2015 [cited 2015 06/07]; Available from: <http://3dprintingindustry.com/2015/03/11/3d-printing-titanium-the-bin-of-broken-dreams-part-2/>.
64. Wright, S. 3D Printing Titanium & the Bin of Broken Dreams (Part 3). 2015 [cited 2015 06/07]; Available from: <http://3dprintingindustry.com/2015/03/12/3d-printing-titanium-the-bin-of-broken-dreams-part-3/>.
65. Mumtaz, K., P. Vora, and N. Hopkinson. A method to eliminate anchors/supports from directly laser melted metal powder bed processes. in SOLID FREEFORM FABRICATION PROCEEDINGS. 2011.
66. Alexander, P., S. Allen, and D. Dutta, Part orientation and build cost determination in layered manufacturing. Computer-Aided Design, 1998. **30**(5): p. 343-356.

67. Rickenbacher, L., A. Spierings, and K. Wegener, An integrated cost-model for selective laser melting (SLM). *Rapid Prototyping Journal*, 2013. **19**(3): p. 208-214.
68. Jacobs, P.F., *Rapid prototyping & manufacturing: fundamentals of stereolithography*. 1992: Sme.
69. SMART3D.NET. Available from: <http://www.smart3d.net/supportgenerator>.
70. Hussein, A., et al., Advanced lattice support structures for metal additive manufacturing. *Journal of Materials Processing Technology*, 2013. **213**(7): p. 1019-1026.
71. M. Cloots, A.B.S., K. Wegener, Assessing New Support Minimizing Strategies for the Additive Manufacturing Technology. *Proceedings of the Solid Freeform Fabrication Symposium*, 2013.
72. Yan, C., et al., Evaluations of cellular lattice structures manufactured using selective laser melting. *International Journal of Machine Tools and Manufacture*, 2012. **62**: p. 32-38.
73. Frank, D. and G. Fadel, Expert system-based selection of the preferred direction of build for rapid prototyping processes. *Journal of Intelligent Manufacturing*, 1995. **6**(5): p. 339-345.
74. Majhi, J., et al. Multi-criteria geometric optimization problems in layered manufacturing. in *Proceedings of the fourteenth annual symposium on Computational geometry*. 1998. ACM.

75. Jain, P.K., P.M. Pandey, and P. Rao, Effect of delay time on part strength in selective laser sintering. *The International Journal of Advanced Manufacturing Technology*, 2009. **43**(1-2): p. 117-126.
76. Hussein, A., et al., Preliminary investigation on cellular support structures using SLM process. et al., *Innovative Developments in Virtual and Physical Prototyping*, Taylor & Francis Group, London, 2011: p. 609-612.
77. Strano, G., et al., A new approach to the design and optimisation of support structures in additive manufacturing. *The International Journal of Advanced Manufacturing Technology*, 2013. **66**(9-12): p. 1247-1254.
78. T. A. Krol, M.F.Z.a.C.S., Optimization of Supports in Metal-Based Additive Manufacturing by Means of Finite Element Models. *proceedings of the Solid Freeform Fabrication Symposium*, 2012.
79. Krol, T., et al., Verification of structural simulation results of metal-based additive manufacturing by means of neutron diffraction. *Physics Procedia*, 2013. **41**: p. 842-850.
80. Seireg, S., *Optimizing the shape of mechanical elements and structures*. Vol. 105. 1997: CRC Press.
81. Eschenauer, H.A. and N. Olhoff, Topology optimization of continuum structures: A review*. *Applied Mechanics Reviews*, 2001. **54**(4): p. 331-390.
82. Kodiyalam, S., *Geometry and optimization techniques for structural design*. 1993: Computatio.
83. ANSYS, C., *Theory Guide Release 12.0* ANSYS. 2009, Inc.

84. Allaire, G. and F. Jouve, Minimum stress optimal design with the level set method. *Engineering analysis with boundary elements*, 2008. **32**(11): p. 909-918.
85. Xia, Q., M.Y. Wang, and T. Shi, A level set method for shape and topology optimization of both structure and support of continuum structures. *Computer Methods in Applied Mechanics and Engineering*, 2014.
86. Wang, M.Y. and L. Li, Shape equilibrium constraint: a strategy for stress-constrained structural topology optimization. *Structural and Multidisciplinary Optimization*, 2013. **47**(3): p. 335-352.
87. Guo, X., et al., Stress-related topology optimization via level set approach. *Computer Methods in Applied Mechanics and Engineering*, 2011. **200**(47): p. 3439-3452.
88. Osher, S. and J.A. Sethian, Fronts propagating with curvature-dependent speed: algorithms based on Hamilton-Jacobi formulations. *Journal of computational physics*, 1988. **79**(1): p. 12-49.
89. Zhao, H., K. Long, and Z.-D. Ma, Homogenization topology optimization method based on continuous field. *Advances in Mechanical Engineering*, 2011. **2010**.
90. Bendsoe, M.P. and N. Kikuchi, Generating optimal topologies in structural design using a homogenization method. *Computer methods in applied mechanics and engineering*, 1988. **71**(2): p. 197-224.
91. He, Q., Z. Kang, and Y. Wang, A topology optimization method for geometrically nonlinear structures with meshless analysis and independent density field interpolation. *Computational Mechanics*, 2014: p. 1-16.

92. Brackett, D., I. Ashcroft, and R. Hague. Topology optimization for additive manufacturing. in 22nd Annual International Solid Freeform Fabrication Symposium. 2011.
93. Fred van Keulen , M.L.a.G.E.v.B., Topology Optimization and Additive Manufacturing, Natural Counterparts for Precision Systems - State-of-the-Art and Challenges. 2014 ASPE Spring Topical Meeting, 2014.
94. Sundararajan, V.G., Topology optimization for additive manufacturing of customized meso-structures using homogenization and parametric smoothing functions. 2011.
95. Li, Y. and Y. Chen. Beam structure optimization for additive manufacturing based on principal stress lines. in Solid Freeform Fabrication Proceedings. 2010.
96. Sunday, D. Intersections of Rays and Triangles (3D). 2012 [cited 2015 06/07]; Available from: http://geomalgorithms.com/a06-_intersect-2.html.
97. Common Layer Interface (CLI). [cited 2015 06/07]; Available from: https://www.forwiss.uni-passau.de/~welisch/papers/cli_format.html.
98. Bineli, A.R.R., et al. Direct metal laser sintering (DMLS): Technology for design and construction of microreactors. in 6th Congress Brasileiro De Engenharia De Fabrica Çã. 2011.
99. Shellabear, M. and O. Nyrhil ä DMLS-Development history and state of the art. Laser Assisted Netshape Engineering 4, Proceedings of the 4th LANE, 2004: p. 21-24.
100. Nikoukar, M., et al. Methods for Enhancing the Speed of Numerical Calculations for the Prediction of the Mechanical Behavior of Parts Made Using Additive

- Manufacturing. in Proceedings of the Solid Freeform Fabrication Symposium. 2013.
101. Rombouts, M., J.-P. Kruth, and L. Froyen, Impact of physical phenomena during selective laser melting of iron powders. Proceedings of The Minerals, Metals & Materials Society (TMS): Fabrication, Materials, Processing and Properties, 2009. **1**: p. 397-404.
 102. Attar, E., Simulation of selective electron beam melting processes. 2011, Ph. D. Thesis.
 103. Körner, C., A. Bauereiß, and E. Attar, Fundamental consolidation mechanisms during selective beam melting of powders. Modelling and Simulation in Materials Science and Engineering, 2013. **21**(8): p. 085011.
 104. APDL, A.M., Mechanical applications Theory reference. ANSYS Release, 2010. **13**.
 105. Mills, K.C., Recommended values of thermophysical properties for selected commercial alloys. 2002: Woodhead Publishing.
 106. Zeng, K., D. Pal, and B. Stucker. A review of thermal analysis methods in Laser Sintering and Selective Laser Melting. in Solid Freeform Fabrication Symposium. 2012.
 107. Verhaeghe, F., et al., A pragmatic model for selective laser melting with evaporation. Acta Materialia, 2009. **57**(20): p. 6006-6012.
 108. Cook, R.D., Concepts and applications of finite element analysis. 2007: Wiley.com.
 109. ANSYS, C., Release 13.0-User Manual. 2010, November.

110. Cervera, G.B.M. and G. Lombera, Numerical prediction of temperature and density distributions in selective laser sintering processes. *Rapid Prototyping Journal*, 1999. **5**(1): p. 21-26.
111. Pal, D., et al., An Integrated Approach to Additive Manufacturing Simulations Using Physics Based, Coupled Multiscale Process Modeling. *Journal of Manufacturing Science and Engineering*, 2014. **136**(6): p. 061022.
112. Standard, A., F2792. 2012. Standard Terminology for Additive Manufacturing Technologies. ASTM F2792-10e1.
113. Zeng, K., et al., Comparison of 3DSIM thermal modelling of selective laser melting using new dynamic meshing method to ANSYS. *Materials Science and Technology*, 2014.
114. Cioranescu, D. and J.S.J. Paulin, Homogenization in open sets with holes. *Journal of mathematical analysis and applications*, 1979. **71**(2): p. 590-607.
115. Sánchez-Palencia, E. Non-homogeneous media and vibration theory. in *Non-homogeneous media and vibration theory*. 1980.
116. Hassani, B. and E. Hinton, A review of homogenization and topology optimization I—homogenization theory for media with periodic structure. *Computers & Structures*, 1998. **69**(6): p. 707-717.
117. Bensoussan, A., J.-L. Lions, and G. Papanicolaou, Asymptotic analysis for periodic structures. Vol. 374. 2011: American Mathematical Soc.
118. Oleinik, O.A., On homogenization problems, in *Trends and Applications of Pure Mathematics to Mechanics*, P. Ciarlet and M. Roseau, Editors. 1984, Springer Berlin Heidelberg. p. 248-272.

119. Rosario, M.J., Finite Element Based Micromechanical Modeling of Periodic Compition Structure. Master Thesis, 2010. **Masschusets Institute of Technology**.
120. Berger, H., et al., An analytical and numerical approach for calculating effective material coefficients of piezoelectric fiber composites. *International Journal of Solids and Structures*, 2005. **42**(21): p. 5692-5714.
121. Lu, S.-Y., The effective thermal conductivities of composites with 2-D arrays of circular and square cylinders. *Journal of composite materials*, 1995. **29**(4): p. 483-506.
122. Islam, M.R. and A. Pramila, Thermal conductivity of fiber reinforced composites by the FEM. *Journal of Composite Materials*, 1999. **33**(18): p. 1699-1715.
123. Hayes, R., A. Rojas, and J. Mmbaga, The effective thermal conductivity of monolith honeycomb structures. *Catalysis Today*, 2009. **147**: p. S113-S119.
124. Kari, S., et al., Computational evaluation of effective material properties of composites reinforced by randomly distributed spherical particles. *Composite Structures*, 2007. **77**(2): p. 223-231.
125. Carson, J.K., et al., Thermal conductivity bounds for isotropic, porous materials. *International Journal of Heat and Mass Transfer*, 2005. **48**(11): p. 2150-2158.
126. ASTM52921-13, A.I., Standard Terminology for Additive Manufacturing-Coordinate Systems and Test Methodologies. 2013, ASTM International, West Conshohocken, PA.

127. Cote, F., V. Deshpande, and N. Fleck, The shear response of metallic square honeycombs. *Journal of Mechanics of Materials and Structures*, 2006. **1**(7): p. 1281-1299.
128. Winston, W.L., M. Venkataramanan, and J.B. Goldberg, Introduction to mathematical programming. Vol. 1. 2003: Thomson/Brooks/Cole.
129. Vable, M., Intermediate mechanics of materials. 2008: Oxford University Press New York, NY.
130. Happian-Smith, J., An introduction to modern vehicle design. 2001: Elsevier.
131. Husain, N.b.A. Introduction to the simple structural surfaces (SSS) method. 2011 [cited 2015 06/03]; Available from: <http://www.fkm.utm.my/~arahim/SSS%20method.pdf>.
132. Cote, F., et al., The out-of-plane compressive behavior of metallic honeycombs. *Materials Science and Engineering: A*, 2004. **380**(1): p. 272-280.
133. Timoshenko, S., Gere. JM: Theory of elastic stability. McGraw-Hill New York 1961, 1961. **294**.
134. Buchbinder, D., et al., Investigation on reducing distortion by preheating during manufacture of aluminum components using selective laser melting. *Journal of Laser Applications*, 2014. **26**(1): p. 012004.
135. Hughes, T.J., The finite element method: linear static and dynamic finite element analysis. 2012: Courier Corporation.
136. Babuška, I. and M. Suri, Locking effects in the finite element approximation of elasticity problems. *Numerische Mathematik*, 1992. **62**(1): p. 439-463.

APPENDIXCES

Zeng, Kai

From: Brent Stucker <brent.stucker@3DSIM.com>
Sent: Friday, June 26, 2015 2:52 PM
To: kai.zeng@louisville.edu
Subject: Re: Permission for including papers in my PhD thesis

Yes you have my permission.

On Jun 26, 2015 2:31 PM, "kai.zeng@louisville.edu" <kai.zeng@louisville.edu> wrote:
Hello, Dr. Stucker

I am planning to include list of papers as given below in my PhD thesis. I need your kind permission for including these articles in my thesis. Please reply to this email with your response.

1. Zeng, K., Pal, D., Gong, H. J., Patil, N., & Stucker, B. (2015). Comparison of 3DSIM thermal modelling of selective laser melting using new dynamic meshing method to ANSYS. *Materials Science and Technology*, 31(8), 945-956.
2. Zeng, K., Pal, D., Teng, C., & Stucker, B. E. (2015). Evaluations of effective thermal conductivity of support structures in selective laser melting. *Additive Manufacturing*, 6, 67-73.
3. Zeng, K., Teng, C., Xu, S., Sublette, T., Patil, N., Pal, D., & Stucker, B. E. (2014, August). A Comparison of the Computational Speed of 3DSIM versus ANSYS Finite Element Analyses for Simulation of Thermal History in Metal Laser Sintering. In *Proceedings of the Solid Freeform Fabrication Symposium, Austin, TX, Aug* (pp. 1205-1212).

Thanks!

Kai Zeng
PhD candidate
Department of Industrial Engineering
University of Louisville

Zeng, Kai

From: Sally Xu <sally.xu@3DSIM.com>
Sent: Friday, June 26, 2015 2:49 PM
To: kai.zeng@louisville.edu
Subject: RE: Permission for including papers in my PhD thesis

Sure. I didn't know my name was on the paper.

From: kai.zeng@louisville.edu [mailto:kai.zeng@louisville.edu]
Sent: Friday, June 26, 2015 4:45 PM
To: Sally Xu
Subject: Permission for including papers in my PhD thesis

Hello, Dr. Xu

I am planning to include list of papers as given below in my PhD thesis. I need your kind permission for including these articles in my thesis. Please reply to this email with your response.

1. Zeng, K., Teng, C., Xu, S., Sublette, T., Patil, N., Pal, D., & Stucker, B. E. (2014, August). A Comparison of the Computational Speed of 3DSIM versus ANSYS Finite Element Analyses for Simulation of Thermal History in Metal Laser Sintering. In *Proceedings of the Solid Freeform Fabrication Symposium, Austin, TX, Aug* (pp. 1205-1212).

Thanks!

Kai Zeng
PhD candidate
Department of Industrial Engineering
University of Louisville

Zeng, Kai

From: Chong Teng <chong.teng@3DSIM.com>
Sent: Friday, June 26, 2015 2:47 PM
To: kai.zeng@louisville.edu
Subject: RE: Permission for including papers in my PhD thesis

Dear Kai,

You definitely have my permission to include these two papers in your thesis. Good luck with your final defense.

Regards,

Chong Teng, Ph.D.

Senior Research Engineer



www.3dsim.com

From: kai.zeng@louisville.edu [mailto:kai.zeng@louisville.edu]
Sent: Friday, June 26, 2015 2:43 PM
To: Chong Teng
Subject: Permission for including papers in my PhD thesis

Hello, Dr. Teng

I am planning to include list of papers as given below in my PhD thesis. I need your kind permission for including these articles in my thesis. Please reply to this email with your response.

1. Zeng, K., Pal, D., Teng, C., & Stucker, B. E. (2015). Evaluations of effective thermal conductivity of support structures in selective laser melting. *Additive Manufacturing*, 6, 67-73.
2. Zeng, K., Teng, C., Xu, S., Sublette, T., Patil, N., Pal, D., & Stucker, B. E. (2014, August). A Comparison of the Computational Speed of 3DSIM versus ANSYS Finite Element Analyses for Simulation of Thermal History in Metal Laser Sintering. In *Proceedings of the Solid Freeform Fabrication Symposium, Austin, TX, Aug* (pp. 1205-1212).

Thanks!

Kai Zeng
PhD candidate
Department of Industrial Engineering
University of Louisville

Zeng, Kai

From: hajjun.gong@louisville.edu
Sent: Friday, June 26, 2015 2:42 PM
To: kai.zeng@louisville.edu
Subject: RE: Permission for including papers in my PhD thesis

Dear Kai Zeng,

I hereby give permission to you to reprint the requested article in your dissertation.

Wish you all the best for your defense!

Best regards,

Haijun Gong
Dept. of Industrial Engineering
University of Louisville
Louisville, KY 40292

From: kai.zeng@louisville.edu [mailto:kai.zeng@louisville.edu]
Sent: Friday, June 26, 2015 4:36 PM
To: hajjun.gong@louisville.edu
Subject: Permission for including papers in my PhD thesis

Hello, Dr. Gong

I am planning to include list of papers as given below in my PhD thesis. I need your kind permission for including these articles in my thesis. Please reply to this email with your response.

1. Zeng, K., Pal, D., Gong, H. J., Patil, N., & Stucker, B. (2015). Comparison of 3DSIM thermal modelling of selective laser melting using new dynamic meshing method to ANSYS. *Materials Science and Technology*, 31(8), 945-956.

Thanks!

Kai Zeng
PhD candidate
Department of Industrial Engineering
University of Louisville

Zeng, Kai

From: Nachiket Patil <nachiket.patil@3DSIM.com>
Sent: Friday, June 26, 2015 2:40 PM
To: kai.zeng@louisville.edu
Subject: RE: Permission for including papers in my PhD thesis

Kai

Feel free to use them for your thesis.

Thanks
Nachiket

From: kai.zeng@louisville.edu [mailto:kai.zeng@louisville.edu]
Sent: Friday, June 26, 2015 2:38 PM
To: Nachiket Patil
Subject: Permission for including papers in my PhD thesis

Hello, Dr. Patil

I am planning to include list of papers as given below in my PhD thesis. I need your kind permission for including these articles in my thesis. Please reply to this email with your response.

1. Zeng, K., Pal, D., Gong, H. J., Patil, N., & Stucker, B. (2015). Comparison of 3DSIM thermal modelling of selective laser melting using new dynamic meshing method to ANSYS. *Materials Science and Technology*, 31(8), 945-956.
2. Zeng, K., Teng, C., Xu, S., Sublette, T., Patil, N., Pal, D., & Stucker, B. E. (2014, August). A Comparison of the Computational Speed of 3DSIM versus ANSYS Finite Element Analyses for Simulation of Thermal History in Metal Laser Sintering. In *Proceedings of the Solid Freeform Fabrication Symposium, Austin, TX, Aug* (pp. 1205-1212).

Thanks!

Kai Zeng
PhD candidate
Department of Industrial Engineering
University of Louisville

Zeng, Kai

From: Tim Sublette <tim.sublette@3DSIM.com>
Sent: Monday, June 29, 2015 7:57 AM
To: kai.zeng@louisville.edu
Subject: RE: Permission for including papers in my PhD thesis

Absolutely. You have my permission to use the paper.

Tim

From: kai.zeng@louisville.edu [mailto:kai.zeng@louisville.edu]
Sent: Friday, June 26, 2015 2:43 PM
To: Tim Sublette
Subject: Permission for including papers in my PhD thesis

Hello, Tim

I am planning to include list of papers as given below in my PhD thesis. I need your kind permission for including these articles in my thesis. Please reply to this email with your response.

1. Zeng, K., Teng, C., Xu, S., Sublette, T., Patil, N., Pal, D., & Stucker, B. E. (2014, August). A Comparison of the Computational Speed of 3DSIM versus ANSYS Finite Element Analyses for Simulation of Thermal History in Metal Laser Sintering. In *Proceedings of the Solid Freeform Fabrication Symposium, Austin, TX, Aug* (pp. 1205-1212).

Thanks!

Kai Zeng
PhD candidate
Department of Industrial Engineering
University of Louisville

Zeng, Kai

From: deepankar.pal@louisville.edu
Sent: Friday, June 26, 2015 5:00 PM
To: kai.zeng@louisville.edu; deepankar.pal@louisville.edu
Subject: RE: Permission for including papers in my PhD thesis

When did I become Dr. Pal. Yeah please use the papers.

From: kai.zeng@louisville.edu [kai.zeng@louisville.edu]
Sent: Friday, June 26, 2015 4:34 PM
To: deepankar.pal@louisville.edu
Subject: Permission for including papers in my PhD thesis

Hello, Dr. Pal

I am planning to include list of papers as given below in my PhD thesis. I need your kind permission for including these articles in my thesis. Please reply to this email with your response.

1. Zeng, K., Pal, D., Gong, H. J., Patil, N., & Stucker, B. (2015). Comparison of 3DSIM thermal modelling of selective laser melting using new dynamic meshing method to ANSYS. *Materials Science and Technology*, 31(8), 945-956.
2. Zeng, K., Pal, D., Teng, C., & Stucker, B. E. (2015). Evaluations of effective thermal conductivity of support structures in selective laser melting. *Additive Manufacturing*, 6, 67-73.
3. Zeng, K., Teng, C., Xu, S., Sublette, T., Patil, N., Pal, D., & Stucker, B. E. (2014, August). A Comparison of the Computational Speed of 3DSIM versus ANSYS Finite Element Analyses for Simulation of Thermal History in Metal Laser Sintering. In *Proceedings of the Solid Freeform Fabrication Symposium, Austin, TX, Aug* (pp. 1205-1212).

Thanks!

Kai Zeng

PhD candidate

Department of Industrial Engineering

University of Louisville

CURRICULUM VITA

Kai Zeng

Contact Information

1841 S 2300 E
Salt Lake City, UT 84108

Cell: (502)8307009
Email: kaizeng1211@gmail.com

Education

- **Ph.D. in Industrial Engineering, University of Louisville, August, 2015**
 - Thesis: Optimization of Support Structures for Selective Laser Melting
- **M.S. in Mechanical Engineering, University at Buffalo, State University of New York, June, 2011**
 - Project: A framework for the development of multi-hazard LFRD for bridge design
- **B.S. in Mechanical Engineering, Northwest A&F University, June, 2007**
 - Research: Development of a serial communication program debugging software using VB6.0 and MSP430F149 single-chip platform to control communication between upper and lower PC.

Publication

"A review of thermal analysis methods in Laser Sintering and Selective Laser Melting."

Kai Zeng, Deepankar Pal, and Brent Stucker. In Proceedings of Solid Freeform Fabrication Symposium Austin, TX. 2012.

"An Integrated Approach to Additive Manufacturing Simulations Using Physics Based, Coupled Multiscale Process Modeling." Deepankar Pal, Nachiket Patil, Kai Zeng, and

Brent Stucker. *Journal of Manufacturing Science and Engineering* 136, no. 6 (2014): 061022.

"An integrated approach to cyber-enabled additive manufacturing using physics based, coupled multi-scale process modeling." Deepankar Pal, Nachiket Patil, Mohammad Nikoukar, Kai Zeng, Khalid Haludeen Kutty, and Brent Stucker. In *Proceedings of SFF Symposium*, Austin, TX, Aug, pp. 12-14. 2013.

"A new dynamic mesh method applied to the simulation of selective laser melting." Kai Zeng, Deepankar Pal, Nachiket Patil, and Brent Stucker. In *Proceedings of the Solid Freeform Fabrication Symposium*, Austin, TX, Aug, pp. 12-14. 2013.

"Layer by layer validation of geometrical accuracy in additive manufacturing processes." Kai Zeng, Nachiket Patil, Hengfeng Gu, Haijun Gong, Deepankar Pal, Tomas Starr, and Brent E. Stucker. In *Proceedings of the Solid Freeform Fabrication Symposium*, Austin, TX, Aug, pp. 12-14. 2013.

"Enhancing Simulations of Additive Manufacturing Processes using Spatiotemporal Multiscaling." Deepankar Pal, Nachiket Patil, Kai Zeng, Chong Teng, Sally Xu, Tim Sublette, and Brent E. Stucker. In *Proceedings of the Solid Freeform Fabrication Symposium*, Austin, TX (2014).

"A Comparison of the Computational Speed of 3DSIM versus ANSYS Finite Element Analyses for Simulation of Thermal History in Metal Laser Sintering." Kai Zeng, Chong Teng, Sally Xu, Tim Sublette, Nachiket Patil, Deepankar Pal, Brent Stucker. In *Proceedings of the Solid Freeform Fabrication Symposium*, Austin, TX (2014).

"Comparison of 3DSIM thermal modelling of selective laser melting using new dynamic meshing method to ANSYS." Kai Zeng, Deepankar Pal, Haijun Gong, Nachiket Patil, and Brent Stucker. *Materials Science and Technology* 31, no. 8 (2015): 945-956.

"Melt pool characterization for selective laser melting of Ti-6Al-4V pre-alloyed powder." Haijun Gong, Hengfeng Gu, Kai Zeng, J. J. S. Dilip, Deepankar Pal, Brent Stucker, Daniel Christiansen, Jack Beuth, and John J. Lewandowski. In *Proceedings of the Solid freeform fabrication symposium*, Austin, TX (2014).

"Evaluations of effective thermal conductivity of support structures in selective laser melting. Kai Zeng, Deepankar Pal, Chong Teng, and Brent E. Stucker. *Additive Manufacturing* 6 (2015): 67-73.

"A study of transverse laser modes using a novel multi-scale simulation architecture for laser-based manufacturing technologies." Nachiket Patil, Deepankar Pal, Chong Teng, Kai Zeng, Tim Sublette, and Brent Stucker. In *SPIE LASE*, pp. 935313-935313. International Society for Optics and Photonics, 2015.

"An Efficient Multi-Scale Simulation Architecture for the Prediction of Performance Metrics of Parts Fabricated Using Additive Manufacturing." Deepankar Pal, Nachiket Patil, Kai Zeng, Chong Teng, and Brent Stucker. *Metallurgical and Materials Transactions A*: 1-12.